SIMULATION AND DAMAGE MODELS FOR PERFORMANCE ASSESSMENT OF REINFORCED CONCRETE BEAM-COLUMN JOINTS

A DISSERTATION

SUBMITTED TO THE DEPARTMENT OF CIVIL AND ENVIRONMENTAL ENGINEERING

AND THE COMMITTEE ON THE GRADUATE STUDIES

OF STANFORD UNIVERSITY

IN PARTIAL FULFILLMENT OF THE REQUIREMENTS

FOR THE DEGREE OF

DOCTOR OF PHILOSOPHY

Arash Altoontash

August 2004

I certify that I have read this dissertation and that, in my opinion, it is fully adequate in scope and quality, as a dissertation for the degree of Doctor of Philosophy.

Gregory G. Deierlein
(Principal Adviser)

I certify that I have read this dissertation and that, in my opinion, it is fully adequate in scope and quality, as a dissertation for the degree of Doctor of Philosophy.

Helmut Krawinkler

I certify that I have read this dissertation and that, in my opinion, it is fully adequate in scope and quality, as a dissertation for the degree of Doctor of Philosophy.

Eduardo Miranda

Approved for the University Committee on Graduate Studies.

Abstract

Performance based earthquake Engineering requires robust analytical tools for obtaining the structural response, damage assessment, as well as for performing reliability analysis. This research effort advances the numerical modeling of reinforced concrete structures by enabling simulation of inelastic beam-column joint behavior and reduced load carrying capacity of structural frames resulting from joint damage. The behavior of beam-column joints has been researched extensively over the past forty years through experimental studies on isolated joints in reinforced concrete subassemblies. This study focuses on the influence of joints on the overall frame behavior and the effect of modeling uncertainties on the response prediction. The analytical models proposed in this research are implemented in the OpenSees environment. Joint elements are formulated to simulate the nonlinear response of joints in two and three-dimensional models under cyclic loading. Proposed joint elements capture both geometric and material nonlinearities. A collection of nonlinear constitutive rules with cyclic deterioration are implemented to facilitate modeling the inelastic behavior associated with shear panel deformations and the slip of longitudinal reinforcement anchored in the joint. A generic damage model is proposed and implemented following the object-oriented architecture of OpenSees. The damage model incorporates existing damage formulations for representing deteriorating parameters in component force-deformation relationships and for component performance assessment. Calibrated modeling parameters are provided for seismically detailed code-conforming joints, and with minor calibration the same methods are used for modeling older (non-conforming) designs. The generic damage model allows one to present the damage indices as the engineering demand parameters and define limit-state boundaries for reliability analysis based on component damage. The sensitivity of the joint response and the nonlinear materials to modeling parameters are formulated for application through the reliability analysis toolbox of OpenSees. Applications of the proposed performance modeling tools are demonstrated through reliability simulations to compute the probabilistic distribution of damage in the joints, considering variability in both modeling and material parameters.

Acknowledgements:

I would like to dedicate my greatest gratitude to my academic Advisor, Professor Deierlein. This research effort would not be possible without his guidance, support, and brilliant suggestions. Serving as his research assistant was a fortunate opportunity for me to improve my knowledge and abilities. I am well confident whatever I learnt from him is going to have a great influence on my career and my personal life.

I will always remember Professor Helmut Krawinkler as an impressive teacher, and a great academic advisor whose suggestions and constructive criticism significantly improved my research. Parts of my research on modeling force-deformation relationships for reinforce concrete was based on the findings of Professor Krawinkler and one of his former students, Dr. Luis Ibarra, whose work is highly appreciated.

I am deeply indebted to Professor Drew V. Nelson for chairing my doctoral dissertation committee. I also appreciate Professor Sarah Billington's willingness to participate in my doctoral dissertation committee and providing me valuable feedback. Professor Eduardo Miranda's comments were greatly appreciated who spent a lot of his time to patiently review my dissertation and contributed to the quality of my work.

I need to acknowledge Professor Laura N. Lowes and the role she had in my academic research. Her mentorship during my first years at Stanford University made my transition to the Ph.D. program smooth and pleasant. She inspired my research on the reinforced concrete beam-column joint elements and helped me with academic writing and publishing.

Dr. Frank McKenna, the creator of OpenSees, helped me significantly with my programming issues. I really appreciate him taking his time and driving to Stanford several times to resolve my modeling and programming issues.

This research would not be complete without the experimental data, provided by Professor Dawn Lehman, Professor John Stanton, and Steven Walker from University of Washington, whose help is highly appreciated.

I greatly appreciate the role other faculty members of the structural program at Stanford University had on my academic progress – including Professors Law, Professor Kiremidjian, Professor Menun, and Professor Borja who have provided me with very useful advice and information from time to time.

I would also want to say special thank to Racquel Hagen who has been a great friend and a wonderful help with handling many of the administrative aspects of this study.

Support of this work was provided primarily by the Earthquake Engineering Research Centers Program of the National Science Foundation, under Award Number EEC-9701568 through the Pacific Earthquake Engineering Research Center (PEER). I am very grateful to the PEER center, Professor Deierlein, and Stanford University for funding me for the whole period of my studies.

The John A. Blume Research Center was not only a professional environment for me; it was a place where I developed personal relationships with many colleagues, specially my friends in the Deierlein research group, Amit Kanvinde, Paul Cordova, Rohit Kaul, and Scott Hamilton who are amongst the smartest of structural engineering brains and the finest of people. I will carry away good memories with me, of great times I had at the Blume center with dear friends of mine – Bert Sweetman, Luise Ibarra, Babak Alavi, Farzin Zareian,, Jerry Lynch, Sameh Mehanny, Ashraf Ayoub, Dimitrious Vamvatsikous, Fatemeh Jalayer, Tina Kashef, Shahram Taghavi, , Ricardo Medina, Hesaam Aslani, Pooya Sarabandi, Toko Hitaka, Curt Haselton, Burak Tuncer, Gee Liek Yeo, Jack Baker, the list goes on, and I thank each one of them

I need to mention the influence the Persian Student Association at Stanford University had on my life at Stanford. I thank all my dear Iranian friends at Stanford specially my dear friend Sina Zahedi and his family for all their support.

I need to thank my beloved Helaleh, who was patiently beside me for the whole period I was working on this dissertation, and gave me all her affection and support. The last but not the least, I need to give all my gratitude and love to my family for their unconditional support, who patiently endured years of distance to let me reach for the dream of my life.

Table of contents:

List of tables:

List of Figures:

1 Introduction

1.1 *Motivation for study*

The ultimate goal of earthquake engineering is design and construction of economical earthquake resistant structures. In practice, an optional economic design solution can be difficult to find, given the numerous sources of uncertainty that may obstruct the path toward a unique, earthquake-resistant design that satisfies all the serviceability and safety expectations. One of the key attributes of new performance-based approaches to earthquake engineering is dealing with the inherent uncertainties in a systematic approach.

Earthquakes are probabilistic phenomena, with uncertainties in the location of the source, the ground motion characteristics, and the occurrence rate. Geotechnical conditions of the building site and soil-structure interaction add to the variability of the earthquake hazard. Uncertainties in proportions and behavior of the structure itself further complicate the problem. Uncertainties due to the lack of knowledge or modeling capabilities are sometimes referred to as epistemic uncertainties. Other sources of uncertainty which are unavoidable due to the underlying physics or lack of information to the design phase, such as the inherent material characteristics or construction tolerances, are referred to as aleatory variability. Distinctions between the epistemic uncertainties in engineering models and the aleatory variability is useful in formulation an engineering approach for earthquake resistant design.

The engineering approach for dealing with a complex problem with numerous unknowns, constraints, and input variability can be described as breaking the main problem to smaller problems to deal with a limited number of variables for each piece of problem. Each subsection of the main problem is then solved more conveniently and the partial solutions are integrated to form the global solution.

This study incorporates such as approach to investigate the design and behavior of Reinforced Concrete (*RC*) frames. The RC frame is divided to individual structural

components, including beam-column elements, wall elements, floor diaphragms and connections between these elements. This research focuses on beam-column joints, which comprise the volume of the structure defined by beam and column intersection. Figure 1-1 shows damage in an exterior and an interior RC beam-column joint subjected to cyclic loading which resulted in severe loss in load bearing capacity. Damage of this sort has been observed in post-earthquake evaluations of reinforced concrete buildings subjected to large earthquakes.

Behavior of the reinforced concrete beam-column joints has been extensively studied over the past 40 years, but there are still many unresolved issues regarding the joint performance. Both experimental and analytical investigations of the beam-column joint behavior have been a challenge since beam-column joints are relatively small and geometrically complex regions of the structure with high force gradients, resulting in local nonlinearities and damage. The nonlinear behavior of beam-column joints increases the variability and complexity of the overall structural behavior. In recent years, the use of high strength concrete has resulted in smaller sections and proportionally larger reinforcement bars which will place more demands on the joints, particularly as they undergo cyclic deformations into the inelastic range.

1.2 *Impression of performance-based earthquake engineering*

Modern methodologies and improved knowledge about earthquake phenomena and the structural response have accelerated the development of earthquake engineering. Performance based earthquake engineering (*PBEE*) is a recent focus of research and development to permit more informed decision making on structural design, to meet desired performance expectations for possible earthquake hazards (Krawinkler and Miranda, 2004).

Since the seismic demands and capacities cannot be predicted with complete certainty, PBEE allows a more comprehensive approach by achieving a more predictable performance, considering multiple hazard levels and performance objectives in the design

process. Each performance objective is associated with an earthquake hazard level based on the owner's expectations and budget.

The performance objectives are chosen based on the owner's expectations such as immediate occupation and limited downtime along with a performance limitation for collapse prevention and life safety. The approach used by Pacific Earthquake Engineering Research (*PEER*) Center for *PBEE* divides the performance assessment to four intermediate processes to relate the earthquake intensity to the structural performance (Cornell and Krawinkler, 2001; Deierlein, 2003; Moehle, 2003). As shown in Figure 1-2, the intermediate variables used in *PBEE* are listed as, the Engineering Demand Parameters (*EDP*), the Damage Measures (*DM*), and the Decision Variable (*DV*).

The earthquake occurrence and its characteristics are probabilistic in nature, and definition of the earthquake hazard is one of the primary sources of uncertainty in estimating structural performance. The earthquake hazard is subdivided to specific hazard levels, where each hazard level is defined by the occurrence rate of earthquakes smaller than the specified intensity. The intensity measure (*IM*) describes the severity of the ground motion hazard in a probabilistic manner. *IMs* are typically identified by single parameter variables, such as spectral acceleration or spectral displacement. Calculating *IMs* is involved with the geological characteristics of the region including the building site characteristics and nearby active faults.

In addition to the earthquake intensity, there are design and construction factors involved with the uncertainties of evaluating the performance of the structure. These factors depend on the technical knowledge, construction techniques and quality, and uncertainties in the building materials.

Referring to Figure 1-2, the first process in the PEER methodology relates the earthquake intensity measure (*IM*) to the engineering demand parameters. The parameters that quantitatively express the structural response are the so-called Engineering Demand Parameters (*EDP*), which are computed by structural analysis procedures such as nonlinear time-history analysis. The *EDPs* are selected based on the type of structural

system, the performance expectations, and how the *EDPs* relate to the damage measures. Typical *EDPs* include inter-story drifts, component inelastic deformations, or floor accelerations; although, cumulative damage indices are also possible.

The Damage Measures (*DM*) are qualitative states that describe the extent of structural and non-structural damage to the structure and its components. The damage indices introduced in this research are used to facilitate the process of relating the *EDPs* to *DMs*. The damage measures are defined based on the consequences of the damage on safety, continued functionality, and the required repair procedures.

Information from the damage measures are used to determine the Decision Variables (*DV*) to evaluate potential economical and life loss, as well as repair time. The decision variables, usually defined in a probabilistic manner, are used for performance assessment and risk management decisions.

The performance assessment process deals with variability in the *IM*, *EDP*, *DM*, *DV,* and their inter-relationships. The total probability theorem is used in the PEER methodology to integrate the generalized variables to describe the outcome of possible earthquake occurrence (Deierlein et al. 2003). The mean annual frequency of the decision variable exceeding a pre-specified value, $\upsilon(dv > DV)$, is calculated by the following equation:

$$\upsilon(dv > DV) = \int_{dm}\int_{edp}\int_{im} P(dv > DV \,|\, dm = DM)\cdot dP(dm > DM \,|\, edp = EDP)\cdot dP(edp > EDP \,|\, im = IM)\cdot \frac{d\upsilon(IM)}{dIM} dIM \tag{1.1}$$

where $P(dv > DV \,|\, dm = DM)$, $P(dm > DM \,|\, edp = EDP)$, and $P(edp > EDP \,|\, im = IM)$ are conditional probabilities and $\frac{d\upsilon(IM)}{dIM}$ is the derivative of the seismic hazard curve, relating the intensity measure to its mean annual frequency of exceedence. The underlying assumptions behind Equation (1.1) are that these conditional probabilities are independent of each other.

The *DM-EDP* relationship is dependent on the uncertainties in modeling knowledge, component properties (e.g. material quality of construction etc.), and loading history. Comparisons between the predicted damage, based on the theoretical damage models, and the actual damage observed form laboratory tests or detailed models provide data to establish the *DM-EDP* relationship at the component level. The damage models proposed in this research will facilitate establishment of the *DM-EDP* relationship.

1.2.1 Structural analysis for PBEE

To achieve the full vision of the Performance Based Earthquake Engineering, all of the significant details that may contribute to the structural response should be represented by the analysis model. The analysis must accurately characterize the engineering demand parameters and consequently the structural performance for various seismic hazard levels up to the collapse point. The analytical tools developed in this research will contribute to this vision of PBEE by enhancing the structural modeling technologies through:

- Development and implementation of new beam-column joint elements to more accurately simulate nonlinear frame response, which include cyclic strength and stiffness degradation and large displacement (geometric) nonlinear effects.
- Implementation of hysteretic nonlinear material models with strength and stiffness deterioration.
- Development and implementation of models and tools for post processing and tracking structural component damage
- Implementation and application of reliability models to assess the influence of modeling uncertainties.

1.2.2 Reinforced concrete frame behavior under dynamic loading

Behavior of RC frames is governed by many factors, including the initial characteristics of the structure, the time dependent effects such as creep and shrinkage, the environments and the loading history. RC components are usually expected to crack under service loadings. The dynamic behavior of RC frames is even more complex since load reversals

may accelerate the strength and stiffness degradation and change the load bearing mechanisms. The inelastic deformations in reinforced concrete are associated with rebar yielding, bond-slip, rebar pullout, crack opening and possible concrete crushing or cover spalling (Figure 1-3). The amount and details of longitudinal and transverse reinforcement both in beams and columns, the detailing of the beam-column joints, slab connections, laps and splices, rebar discontinuities can influence the structural performance under seismic loading.

The behavior is also highly dependent on the design and detailing requirements which have changed considerably over past decades. Prior to early 1970's, buildings were designed mainly for gravity loads, with limited capacity to sustain inelastic lateral load reversals. Design details of the pre-70's structures do not provide adequate confinement in the joint zone, which can result in severe beam-column joint damage, where the structure is subjected to inelastic cyclic loading. Discontinuities in beam longitudinal reinforcements increase the tendency of rebar pullout at joint zones. In more recent years (1980, and later), the components are designed with somewhat reduced strength capacity compared to the older designs, but with ductile reinforcement detailing. Ductile detailing for the RC components allows larger plastic deformation capacity, which sustains the structural resistance out to large deformation and results in increased energy dissipation capacity. Current design standards (ACI318-02 and ACI352-02 for joints) are highly dependent on ductile detailing to provide confinement, anchorage and plastic deformation capacity.

Issues associated with older design methodologies have been addresses and studied in detail (e.g. Townsend and Hanson, 1977; Bracci et al., 1995; Beres et al., 1996; Elmorsi et al., 1998; Pantelides et al., 2002; Lehman et al., 2004; Walker et al., 2004). Bracci et al. (1995) considered the following deficiencies in an experimental study in the performance of RC structures designed based on older codes:

- Columns with flexural capacity smaller than that of the joining beam(s), which may result in a soft-story collapse due to the formation of plastic hinges in the columns instead of in the beams.

- Minimal transverse reinforcement for shear and confinement in the beams and columns, especially in the hinge zones.
- Lap splices located at the potential hinge zones, directly above the floor slab.
- Minimal or no transverse reinforcement in beam-column joints.
- Positive (bottom) flexural reinforcement of the beams that is typically very small and often discontinued in the joint zone.

Rigorous analysis of reinforced concrete structures should take into account of all these details and possible mechanisms. Computer analysis programs must be able to model the behavior of beams and columns, consider the interaction of different loading modes at the component level, smaller plastic deformations and account for change of component characteristics due to the plastic deformations. To the extend that slabs contribute to the lateral capacity of the system, the effects of slabs must also be considered. Finite-element modeling, fiber models, and generalized hinge approaches are among the general approaches for modeling RC beam-columns. The two-dimensional and three-dimensional joint models developed in this research permit improved modeling of the beam-column joint deformation and the cyclic deterioration of joint shear capacity, both of which effect overall frame behavior.

1.3 *Reinforced concrete beam-column joint behavior*

The behavior of beam-column joints and the influence they may have on the overall structure is actively under investigation, but there are still gaps in the research literature for comprehensive experimental data that can explain different aspects of joint behavior. In particular, there is a need for developing a robust formulation to describe the joints monotonic and cyclic nonlinear response and to predict its damage states.

The models and formulations proposed in this research cover the behavior of joints designed based on both the older and the current reinforced concrete provisions according to American Concrete Institute guidelines and recommendations. In the older (prior to 1976) design provisions, there was little, if any thought given to the joint behavior. The ACI 352-76 report was the beginning of the effort that led to the current standards. The

1976 report began to articulate the role of the joints in providing development length for the beam rebar. The 1976 provisions did not anticipate significant inelastic deformations, and the deformation demand was not assessed quantitatively. The 1976 provisions established the joint strength to enforce strong-column weak-beam design concept. The design guidelines required the joint strength to be evaluated based on the nominal strength of the frame elements connected to it. For this purpose, the beam reinforcement stress is increased to account for possible over strength resulting from strain hardening, and the joint must be strong enough to sustain the forces associated with the development of the beam flexural strength. Ratio of the column height h_c to the beam bar diameter d_b must be adequate to limit the bond stress demand. The joints designed to meet ACI352-76 recommendations are assumed to remain essentially elastic. Therefore they can experience rapid strength and stiffness deteriorates due to high levels of cyclic joint shears and bond stresses imposed by seismic loads within the structural life span. The cyclic damage of the joints will be a matter of concern for the performance evaluation of the older structures.

The latest ACI joint design recommendations (ACI352-R02) anticipate inelastic deformation in the joint zone. The current joint design and detailing provisions provide resistance for gravity loads, the seismic effects, and for the interaction of the multidirectional forces transferred to the joint by adjacent frame members. Use of high strength materials, which result in smaller sections and larger reinforcement bars is anticipated, and attention is focused on the joints to provide proper ductility under deformation reversals into the inelastic range. Adequate development length and confinement in the panel zone are provided to guarantee a minimum plastic deformation capacity and enhanced cyclic behavior. The shear forces considered for the joint design are not limited to the forces determined by the nominal strengths of the adjacent members and the analysis results must also be taken into account.

Accurate seismic assessment and design of RC frames requires an analytical tool for representing the nonlinear behavior of the beam-column joints. A rational, but easy to use beam-column joint model for frame structures does not exist in most of the existing structural analysis programs. Most of the knowledge on the joints has been acquired

through experimental studies on reinforced concrete beam-column subassemblies, and less attention has been paid to the influences of the joints on the frame behavior and the effects of uncertainties on performance. In this research, new joint elements are developed to fill this gap in structural analysis and enable engineers to asses the effects of the joint strength, stiffness, inelastic deformations and softening on the structural response.

Four variations to the joint element are introduced in this research. The joint elements consist of a finite size shear panel, which can undergo shear deformations. The connection between the shear-panel to adjacent members allows for either a rigid or flexible (inelastic) connection. The joint elements represent the finite-size and axial and flexural rigidity of the joint panel. Any type of frame element can be attached to the joint, and the joint element can be calibrated to simulate RC, steel, or composite frame systems, since they all share similar kinematics of the panel zone and frame-joint connections.

1.4 *Damage models and applications in cyclic joint behavior*

The older joint design concepts used forces (or stresses) as the main design parameter and the ratio of the maximum applied force to the nominal capacity as a damage predictor. New seismic provisions focus more explicitly on ductility demand, where deformation (or distortion) capacities for inelastic deformations under seismic loading are considered. Current performance based assessment methodologies focus on displacements as the primary parameter to evaluate structural performance, where the deformations are loosely translated to performance targets related to life-safety, serviceability, repair cost and down-time. As a more detailed approach, the component deformation and the inter-story drifts are related to the overall damage of the structure.

Pervious research on damage in RC frames (Park et al, 1985b; Kratzig et al., 1989; Florez and Lopez, 1995; Fajfar and Gaspersic, 1996) investigated a variety of approaches to numerically estimate the overall structural damage by focusing on damages at component level. The experimental outcome of the beam-column joint behavior under various types

of loading is used to study the relation of engineering demand parameters and the damage states of the reinforced concrete joints.

The peak deformation demand is not general enough to fully describe the cyclic damage process. Therefore a variety of cyclic damage models are suggested for predicting structural damage (Park and Ang, 1985a; Kratzig et al., 1989; Williams and Sexsmith, 1995; Williams et al., 1997; Dube et al., 1996; Hindi et al. 2001; Mehanny and Deierlein 2000).

A generic damage model is developed and introduced for computing the damage indices to relate to the damaged state of structural components. The damage indices will facilitate the process of integrating the structural component damages, to determine the overall structural performance.

1.5 *Overview of OpenSees*

OpenSees, *Open System for Earthquake Engineering Simulation*, is a structural analysis program developed by Pacific Earthquake Engineering Research Center (McKenna, 1997; McKenna and Fenves, 2002; OpenSees, 2004). The OpenSees platform is designed to enable the earthquake engineering research community to implement their analysis models while utilizing general solution procedures of the framework. OpenSees is written in C++ with an object-oriented architecture, where the analysis components are defined as separate objects. The analysis model is introduced as the *domain* object, which contains analysis components such as nodes, material models, elements, constraints, loading patterns, solver algorithms, integrators, constraint handlers, and recorders. The domain is created by the user for each application through an interface script using Tcl. Tcl is a simple programming language which is used as the command interpreter for OpenSees to read the input files. Figure 1-4 shows the hierarchy of the main objects, which comprise a structural analysis model. The OpenSees terminology used in this research is reviewed and explained in Appendix A.

1.6 *Objectives*

The contributions of this research to performance based earthquake engineering and structural analysis are summarized by the following objectives:

- Develop analytical tools for modeling beam-column joints in two and three dimensional structures, and implement them in the object oriented OpenSees platform.
- Develop hierarchical models for processing engineering demand parameters and local damage measures, with emphasis on applications to beam-column joint models.
- Calibrate the joint models based on analytical and experimental studies, and verify the results by comparison with laboratory data.
- Quantify the variability in the proposed joint analysis models for use in reliability analysis.
- Provide capabilities for reliability simulation of RC joints by incorporating the new joint element into the OpenSees reliability toolbox, which was previously developed by Haukaas and Der Kiureghian (2000).
- Formulate the structural response sensitivity to modeling (beam-column joint) parameters, i.e. the gradient of structural response with respect to the joint characteristics.
- Demonstrate the simulation models, damage models, and reliability tools through application to the performance assessment of a RC frame, i.e. obtain the probability of joint damage, considering the effects of model variability, $P\left[EDP < edp \middle| IM = im,\ ground\ motion \right]$ and the failure probability, $P\left[EDP < edp \right]$
- Present recommendations for analysis and joint behavior assessment.

1.7 *Scope*

Results of a comprehensive literature review on the cyclic behavior, design and analysis of reinforced concrete beam-column joints are summarized in Chapter 2 (Paulay et al.,

1978; Soleimani et al., 1979; Filippou and Popov, 1984; Durrani and Wight, 1985; Ehsani and Wight, 1985; Alameddine et al., 1991; Gentry and Wight, 1994; Mazzoni, 1997; Naito et al., 2001; Walker et al., 2004). The mechanisms and parameters that influence the joint behavior are identified and categorized, and the modeling parameters are calibrated for a joint with pre-defined properties. The previously published models and techniques for modeling RC joint are reviewed (El-Metwally and Chen, 1988; Alath and Kunnath, 1995; Modeling inelastic shear deformation Fleury et. al., 1996; Uma and Prasad, 1996; Kunnath, S. K., 1998; Deng et al., 1999; Fleury et al., 2000; Lowes, 2001; Lowes and Altoontash, 2003a), and the force transfer mechanisms are summarized. The physical behavior of the joint is simplified to an idealized mechanism which provided the basis for a versatile numerical joint element model for a versatile joint element. Implementation of the resulting joint models in OpenSees is described.

The performance based methodology requires tools for damage assessment and study on the states of structural damage. This research leads to the application of damage indices (with focus on beam-column joints) to relate the analysis results to damage measures. In Chapter 3, a generic damage object class for OpenSees is introduced. This damage class is then used to implement several damage indices that have been published in the literature (Park and Ang, 1985a; Kratzig et al., 1989; Rahnama and Krawinkler, 1993; Mehanny and Deierlein 2000). The damage indices are used for recording beam-column joint damage and modeling response deterioration.

Previously proposed hysteretic material models with parameter deterioration were reviewed (Rahnama and Krawinkler, 1993; Kunnath et al., 1996; Mostaghel, 1999; Sivaselvan and Reinhorn, 2000; Ibarra, 2003; Ibarra et al, 2004) to provide deteriorating hysteretic models to simulate different mechanisms of the *RC* joint behavior. The models are also used to test out and evaluate use of the damage models as a deterioration parameter. Three hysteretic material models with strength and stiffness degradation (Ibarra et al, 2004) are studied and implemented in OpenSees.

In Chapter 4, the mechanical behavior of RC beam-column joints is reviewed based on previous experimental and analytical researches to identify and characterize the

parameters that determine the force-deformation joint response (Higashi and Ohwada, 1969; Ehsani and Wight, 1985; Leon and Jirsa, 1986; Paulay, 1989; Bonacci and Pantazopoulou, 1993; Pantazopoulou and Bonacci, 1994; Scott, 1996). The main mechanisms that govern the joint response are identified as the shear response of the panel zone, and the member-end-rotations due to bond-slip. Analytical methods for modeling the shear panel behavior (Vecchio and Collins, 1986; Stevens et al., 1991; Shiohara, 2001) and bond-slip (Eligenhausen et al., 1983; Leon, 1989) are discussed. The Modified Compression Field Theory (Vecchio and Collins, 1986) is reviewed and modified to model the RC joint response. A new approach is proposed for modeling the joint interface rotations based on a fiber section analysis for a modified section that incorporates the bond-slip behavior. Calibration information is provided for older beam-column joint designs with inadequate transverse reinforcement in the joint zone. The modeling and calibration information are used to create computer models to simulate a series of RC subassembly tests, which provide the basis for validating the proposed models. The verification problems include a test on a series of beam-column subassemblies (Walker et. al, 2004) and a two-third scale 2-story RC frame (Tsai et al., 2000). The recorded damage indices and reported observed damages are used to evaluate the new damage models in OpenSees and to provide the probabilistic distributions that relate the damage indices to the damage state.

The probabilistic aspects of the joint behavior and its response sensitivity are studied in Chapter 5. To study the influence of the joints on the structural reliability, the variability of modeling parameters are studied and probability distributions are suggested for the joint behavior. The comparison of the analytical models and the experimental results are used to estimate the variability in the proposed model and to provide probabilistic distribution for model variability. An approach for defining the limit-state functions in terms of the damage indices is discussed, i.e. the target engineering demand parameters are presented in the form of damage indices; and the structural performance is related to limit-state functions described using the damage indices.

The general concept and formulation of response sensitivity is reviewed (Zhang and Der Kiureghian, 1991; Conte et al., 1999; Conte 2001), and a sensitivity formulation for the

joint element and the hysteretic material models are derived and implemented. The sensitivity of the limit-state functions to the modeling random variables are formulated as response gradient vectors. The OpenSees reliability toolbox (Haukaas and Der Kiureghian, 2000; Haukaas, 2003a) is used to perform a variety of reliability simulations. FORM, MVFOSM, and Monte Carlo simulations are performed to estimate the failure (exceeding the limit-state function) probability, and derive fragility curves for individual joint damage.

The contributions, recommendations and suggestions for further research are summarized in Chapter 6.

Figure 1-1: Damage in RC exterior (Pantelides et al., 2002) and interior (Walker, 2001) joints

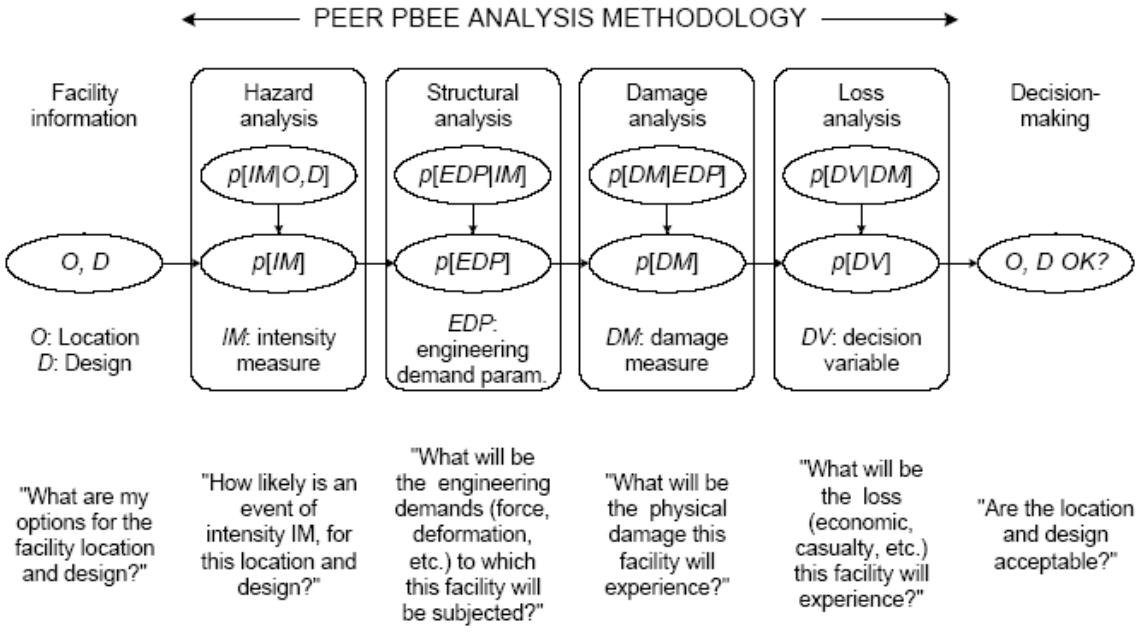

Figure 1-2: PEER PBEE methodology (Porter et al., 2002)

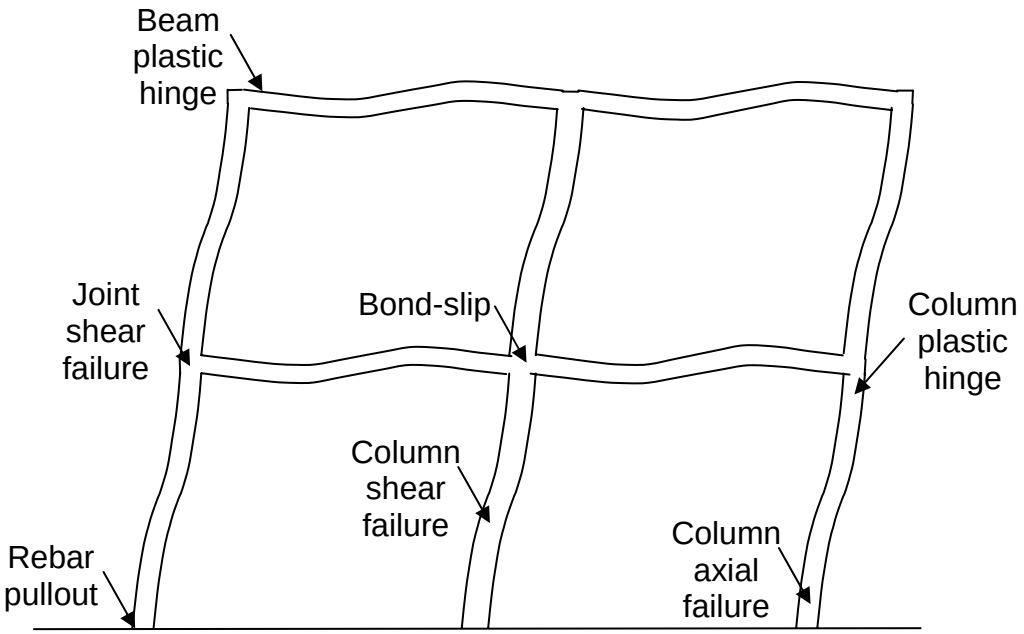

Figure 1-3: Inelastic failure modes in a laterally deformed RC frame

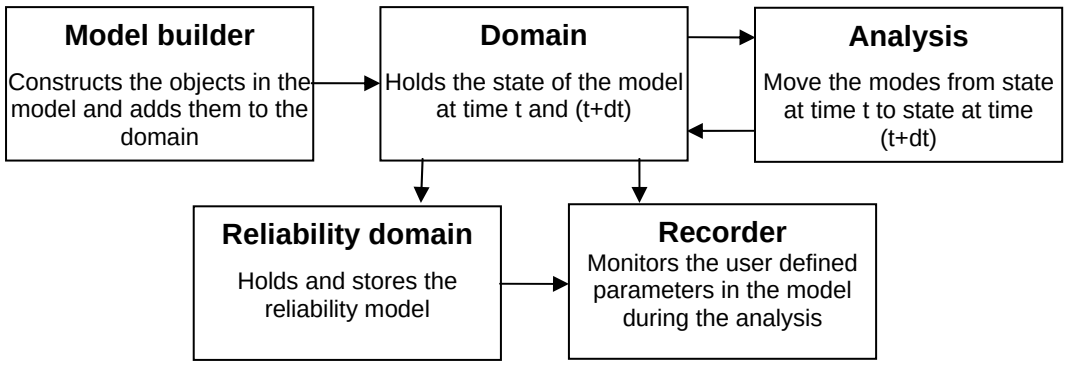

Figure 1-4: The *OpenSees* hierarchical structure (OpenSees, 2004)

2 Beam-column joint model formulation and implementation

Previous research confirms the importance of beam-column joints response on the overall structural performance, including the influence of beam-column joints on the frame elastic stiffness, and nonlinear dynamic response (ACI-352 2002; Pantazopoulou and Bonacci, 1994). Figure 2-1 illustrates the comparison between the laboratory reading (Tsai et al. 2000), and two sets of analytical results, one for a center-line model without considering the effects of joint and one for a model with beam-column joint elements (the model details will be discussed later in chapter 4). In this chapter, the detailed mechanical behavior of the beam-column joints in reinforced concrete moment-resisting frames is discussed and characterized through idealized force-transfer mechanisms. These mechanisms are then used as the basis for a numerical model to simulate beam-column joint response.

2.1 *Introduction and definitions*

Joints in framed structures are defined as the volume of the structure formed by intersection of beams the columns. The American Concrete Institute committee 352 was organized in 1966 to develop and report information on the design and detailing of joints and connections in monolithic concrete structures. The latest edition of design recommendations by ACI-352 (2002) has a more exact definition for cases where the beam width is smaller than the column width, where the joint is defined as the portion of the column within the depth of the beam(s), which frame into the column. The role of the joint is to maintain the equilibrium and compatibility by transferring member-end forces between the beam(s) and column(s).

For convenience in understanding the beam-column joints behavior, the joint can be visualized as combination of two separate zones, the panel zone and connection interfaces. The connection interfaces refer to region connecting the beams and columns to the panel zone, and the panel zone is the common (core) region that transfer shear forces between adjacent frame members. In steel frames, the panel zone and the connection interfaces are easily distinguished by their visible mechanical components, while in the

reinforced concrete joints, these zones are not as apparent and must be defined by some conceptual interpretations. These idealized mechanisms are discussed at length later in this chapter.

Joints exist in different types and forms in frame structures. The joint type is determined by the number and the configuration of the frame elements connected to it. ACI-352 (2002) distinguishes joints as having interior or exterior categorizations for the purpose of specifying design strengths. Figure 2-2 shows the configuration of interior joint, exterior, corner and roof interior-joints in a simple two dimensional frame. The figure also shows a schematic diagram of how the joints would be represented in an analysis model using the four-node beam-column element developed in this thesis. The interior joints connect two beams and two columns. Exterior joints connect one beam to two columns, while roof-interior (tee) joints connect two beams to a column. Corner (knee) joints are located at the corners, connecting only one beam to one column. As shown in Figure 2-3, this categorization is more complex for three dimensional space frames, where the out-of-plane framing conditions must be considered.

The details of the mechanical behavior of the interior, exterior, corner and roof joints are slightly different, and the similarities and differences of various joint types must be carefully observed to provide evidence that their behavior can be accurately modeled by a single type of joint element. The basic joint element proposed in this research is one model that is configured for internal joints (with for external nodes, see Figure 2-2), but it can also represent cases with fewer connecting members. The differences in behavior of joints with different configuration will be handled by using separate modeling parameters for different joint types.

2.2 *Physical behavior of RC beam-column joints*

The ACI-352 (2002) report for the design of reinforced concrete joints offer simplified provisions based on limitations to average shear stress applied to the joint. The nominal average joint shear stress for joints effectively confined on three vertical faces, or two opposite vertical faces is limited to $20\sqrt{f_c'}(psi)$ for interior joints and $15\sqrt{f_c'}(psi)$ for

exterior joints. For joints with effective confinement on all four vertical faces, these amounts are increased to $24\sqrt{f_c'}(psi)$ and $15\sqrt{f_c'}(psi)$ for interior and exterior joints, respectively. The critical section for the shear forces within the joint is a horizontal plane at the mid height of the joint. The analytical model is configured accordingly to use shear equivalent loading and deformation as the primary analytical characteristics. The details of calculating the average joint stress and effective joint area are specified in ACI-352 (2002).

The kinematics of the panel zone shows similarities for reinforced concrete, steel, or composite steel-concrete joints, while the member-end rotations have different mechanisms. Figure 2-4, Figure 2-5, and Figure 2-6 show the deformed shape of three joints in RC, steel and RCS moment resisting frames, respectively.

The panel zone usually has higher stiffness and strength compared to the connected frame elements. The finite joint size also affects the frame response, primarily by reducing the column and beam lengths. These two influences collectively, result in more accurate, and usually higher calculated initial stiffness for the frame, which affects both static and dynamic analysis results. In frames where the joints are not properly designed, the stiffness and strength of the joint may degrade rapidly due to high force and moment gradient within the panel zone.

The beam-column joints are subjected to various loading modes. A convenient way to study the joint physical behavior is to observe each mode separately and then focus on their combinations. Loads are transferred to the joint by adjacent beam-column elements, whose local forces include axial force, shear force, and bending on the joint. In theory the beam-column joint would, therefore, have axial, bending, and shear modes along with the member-end rotations (see Figure 2-7). However, the joint proportions and properties are such that the axial and bending deformation of the joint are usually assumed to be negligible.

The design and detailing recommendations for the joints are associated with joint shear deformation which results from applied shear forces and anti-symmetric bending

moments. Compared to axial and bending deformations, the shear stresses impose the most significant deformations to the joint core that can influence the overall frame behavior. The joint size is usually significantly small, compared to the attached beam and column members, such that the axial and bending deformations in the joint can be ignored. Thus the shear deformation contributes the most to the joint behavior. Additionally, depending on the connection details, the connected rotation at the connection point of the beams and columns (usually referred to herein as the interface rotations) may also affect in the behavior and should be considered in the model.

2.2.1 The joint equilibrium and force transfer paths

Joints are loaded with a force and moment vector at each face. For a two dimensional frame model, the standard frame nodes have three degrees of freedom (two displacements and one rotation) with corresponding force components. Thus, two dimensional joints are loaded by two force components and a moment component at each face. The applied forces to a two-dimensional beam-column joint can be decomposed to the axial, shear, and the symmetric and anti-symmetric flexural modes. Since the number of independent loading modes must be equal to the number of undetermined nodal forces, these four basic modes can be reduced to three independent modes. The anti symmetric bending and the shear modes are the only ones that cause shear deformation in the shear panel. As shown in Figure 2-8, the basic deformation modes from Figure 2-7 manifest themselves under the idealized symmetric gravity and anti-symmetric lateral loading. In three dimensional joints, the torsional mode must be considered along with the other modes. The external forces applied to a two-dimensional joint are illustrated in Figure 2-9. The external forces can be decomposed as leading to following deformation modes:

Axial mode: In this case the beam or column axial forces (in either the vertical or horizontal directions) are directly transferred through the joint panel. Unbalanced axial forces are transferred as symmetric shear forces to the adjacent frame members. There will not be any shear or flexural deformation involved in this mode (Figure 2-10).

Flexural mode: Once a moment is applied to any face of the joint, the joint is loaded in the Flexural mode. The flexural loading in each direction can be decomposed to two separate symmetric and anti-symmetric bending modes. In the symmetric bending, the flexural moment applied to opposite faces are equal and they balance each other, such that there is not any shear deformation (Figure 2-11). On the other hand, the anti-symmetric bending moments and shears (Figure 2-12) lead to large shear force transfer through the panel zone.

Pure shear mode: In this case, the joint is loaded with shear forces on every side as shown in Figure 2-13. The shear forces in this case are balanced and do not impose any unbalance moment on the joint. Nevertheless, the pure shear mode can lead to large shear deformation. Note, however, that the pure shear mode in not likely to happen alone and it is usually accompanied by flexural loading to balance the shear forces (Figure 2-13).

Figure 2-14 summarizes the superposition of forces in the different load/deformation modes and the nodal force equilibrium.

2.2.2 Elastic and inelastic force transfer mechanisms in RC joints

Previous research on beam-column connections has identified different mechanisms contributing to joint deformations. The primary components of joint deformations are mostly observed as the joint-panel shear distortion and rotations at the joint interfaces (Park and Ruitong 1988; Paulay, 1989; ACI-352, 2002; Pantazopoulou et al., 1994; Shiohara, 2001). As noted previously, axial elongation is also possible but can usually be ignored. Thus the shear panel and interface rotations are the only deformation modes considered in the proposed model (Paulay 1989; Uma et al., 1996; Fleury et al. 1996). Length and dimensions of a joint-panel are normally smaller compared to the attached beam and column members. Shorter flexural and axial length and higher stiffness limit flexural and axial deformations of the joint to a negligible level. In the event that axial joint deformations are deemed to be significant, they can be included by modifying the axial rigidity of the frame elements connected to the joint, rather than modeling the axial deformations inside the joint core itself.

The major sources of joint damage are related to the damage in the load transfer path to the shear panel and the shear panel damage itself. Bond loss is one of the major causes of damage in the load transfer path (as evident in the interface deformations, see Figure 2-4), while concrete crushing, transverse rebar yielding and slip along the shear cracks are the possible causes of shear panel damage (Pantazopoulou, 1994). These damage sources are represented by the shear panel and member-end rotational springs, which lose their stiffness and strength after large loading reversals, causing softening behavior in the joint.

2.2.3 **The joint kinematics idealization and simplification**

For analysis purposes, the beam-column joint behavior is idealized here by a joint panel and member-end interface zones (Figure 2-15). The axial and shear deformation of the member-end interface zones are presumed insignificant, while the rotation of these interfaces due to extension of flexural loading is accounted for.

In a planar frame, the shear panel is defined as a parallelogram with axially rigid sides, where an angel change between the sides allows let the shear panel to deform in the shear mode. The adjacent frames are connected to the mid points of every side. The shear panel can move as a rigid body in the two-dimensional space, while the shear deformation adds an additional degree of freedom. Thus, the shear panel has four kinematic degrees of freedom. Three degrees of freedom are associated with the rigid body motion of the shear panel and the fourth degree of freedom is related to the shear distortion angle. A rotational spring is used to represent the shear force-deformation based on the calculated shear resistance of the shear panel.

In space frames, the panel zone takes the form of a block subjected to tri-directional shear deformations. The block is represented as a parallelepiped with rigid faces, in which the angle between sides may vary to let the joint block deform in the shear modes. The adjacent beam-column elements are connected to the centroid of each side. The 3Djoint block has nine kinematic degrees of freedom. Six degrees of freedom are associated with the rigid body motion of the joint and the remaining three degrees of freedom define the

shear deformation. Three rotational springs, representing the force-deformation rules, provide the shear resistance in each orthogonal direction of the 3D joint.

2.3 *Previously proposed analytical models for joints*

Previous research provides several approaches to modeling the inelastic response of beam-column joints. Early work to simulate the response of reinforced-concrete frames relied on calibration of the "plastic hinges" introduced at the ends of beam-column line elements to represent inelastic joint action as well as frame member flexural response (e.g., Otani 1974; Anderson and Townsend 1977). The next generation of models decoupled the inelastic response of the beams, columns, and joints by introducing zero-length rotational spring elements to connect the rotational degrees of freedom of beam and column elements (e.g., El-Metwally and Chen 1988). Calibration of these models was accomplished using experimental data characterizing the response of joint subassemblages. Refinements to this concept include the addition of rigid zones at the end of the beams and columns (Alath and Kunnath 1995) or the addition of very stiff beam-column elements between the central node and the external nodes (Deng et al, 2000). These models are illustrated in Figure 2-16. This approach does not completely satisfy the joint kinematics, while the addition of rigid end-offsets resulted in more realistic models.

While these approaches provide a computationally efficient means of simulating joint response, the development of objective, transparent models is challenging because the effects of multiple inelastic response mechanisms are combined into a single moment-rotation relationship.

More recently, researchers have begun using continuum-type elements to represent the response of reinforced-concrete joints in combination with transition interface elements that are used to maintain compatibility with beam-column line elements. These models offer the potential for accurate simulation of inelastic response mechanisms at the price of increased computational effort. However, to date, only simple continuum idealizations of the joint region have been proposed (Elmorsi et al. 2000; Fleury et al. 2000). A joint

model previously proposed by the author (Lowes and Altoontash 2003) explicitly represents the mechanisms that may determine inelastic joint action. This model offers the potential for objectivity and transparency in modeling the joint response. Figure 2-18 shows the schematic representation of the model with separate springs to represent individual bond-slip and rebar pullout mechanisms. Though this model offers the potential for a more accurate and transparent representation of the joint, it requires detailed information on bond-slip response which is not currently available The simplifications and assumptions of an alternative (more simplified) joint model, presented in this study (Figure 2-15), were inspired by the detailed joint element of Figure 2-18.

2.4 *Proposed Joint 2D models*

In this section, the shear panel and the connection interfaces are represented in the form of new two-dimensional joint elements, based on the simplifications and assumptions mentioned previously. The basic two-dimensional joint element is generally referred to as Joint2D. The version of the joint element with member-end rotations and five springs is named Joint2D-SPR5 (Figure 2-19), and the joint element with rigid member-end connections and one shear spring is referred to as Joint2D-1SPR (Figure 2-23). Joint2D, like any regular structural analysis element, imports the nodal deformations and exports the element stiffness matrix and nodal forces. In addition, Joint2D is responsible for imposing geometric constraints to satisfy the compatibility.

As shown in Figure 2-17, the Joint2D model is introduced into the OpenSees platform as a new element, which interfaces with the standard OpenSees element class. Included in the element implementation are extensions to the multipoint constraint (MP_Constraint) and node (Node) classes of OpenSees (refer to Appendix A for more details on the OpenSees classes). The primary operation of the joint element is creating a central node and connecting this central node to the external node by means of kinematic constraints (see Figure 2-19 and Figure 2-22). The central node is located at the center point of this parallelogram. For the two-dimensional frame model, the central node has four degrees of

freedom, the three standard degrees of freedom and one extra degree of freedom for the shear deformation.

The four external nodes are those where the joint element is connected to the adjoining beam-column elements. The kinematic constraints are decomposed to four multipoint constraints. Each multipoint constraint connects the degrees of freedom between one exterior node and the central node. Uniaxial (single degree-of-freedom) material objects are used to assign the joint shear stiffness and the joint-to-member interface stiffness (in Joint2D-5SPR).

The joint element is developed for symmetric joints with beam center lines passing through the column centroid, so it is essential that the initial layout of the exterior nodes constructs a parallelogram.

2.4.1 **Element characteristics and formulation**

The two dimensional beam-column joint is idealized as a parallelogram shaped shear panel with adjacent elements connected to its mid-points. The midpoints of the parallelogram sides are referred to as external nodes. These nodes are the only analysis components that connect the joint element to the surrounding structure.

The foundation of kinematic formulation of the shear panel is the geometric features of a parallelogram. The shear panel maintains its parallelogram shape as it moves and deforms in the planar system. The parallelogram shape is maintained by the kinematic constraints between the external nodes and the central node.

A parallelogram is a four-sided plane figure that has two sets of opposite parallel sides. There are three unique geometric features that differentiate a parallelogram from any other quadrilateral figure. The sides on the opposite sides of a parallelogram have equal length, they are parallel, and the diagonals bisect each other, i.e. they intersect at their mid-points. Since there is no restriction applied to the corner angles, the parallelogram can deform in the shear mode by changing the angle between adjacent sides, without changing the size, or imposing any axial or flexural deformation on the joint.

For the two dimensional formulation discussed here, the nodes are tagged in a counter-clockwise order, beginning with the node on the right side of the element. The initial location of the external nodes is defined as vectors of size two:

$$\underline{X}_1^{\,0} = \begin{Bmatrix} x_1^0 \\ y_1^0 \end{Bmatrix} \quad \underline{X}_2^{\,0} = \begin{Bmatrix} x_2^0 \\ y_2^0 \end{Bmatrix} \quad \underline{X}_3^{\,0} = \begin{Bmatrix} x_3^0 \\ y_3^0 \end{Bmatrix} \quad \underline{X}_4^{\,0} = \begin{Bmatrix} x_4^0 \\ y_4^0 \end{Bmatrix} \tag{2.1}$$

The nodal displacement field is defined by two translations and one rotation. The nodal displacements are time dependent vectors with three degrees of freedom. The initial displacements at step $i = 0$ are zero.

The nodal deformation vectors for the load step i are defined as:

$$\underline{\Delta}_1^{\,i} = \begin{Bmatrix} u_1^i \\ v_1^i \\ \theta_1^i \end{Bmatrix} \quad \underline{\Delta}_2^{\,i} = \begin{Bmatrix} u_2^i \\ v_2^i \\ \theta_2^i \end{Bmatrix} \quad \underline{\Delta}_3^{\,i} = \begin{Bmatrix} u_3^i \\ v_3^i \\ \theta_3^i \end{Bmatrix} \quad \underline{\Delta}_4^{\,i} = \begin{Bmatrix} u_4^i \\ v_4^i \\ \theta_4^i \end{Bmatrix} \tag{2.2}$$

The updated locations of nodes for the time-step i are calculated by adding the nodal deformations to the initial coordinates:

$$\underline{X}_1^{\,i} = \begin{Bmatrix} x_1^i \\ y_1^i \end{Bmatrix} = \begin{Bmatrix} x_1^0 + u_1^i \\ y_1^0 + v_1^i \end{Bmatrix} \quad \underline{X}_2^{\,i} = \begin{Bmatrix} x_2^i \\ y_2^i \end{Bmatrix} = \begin{Bmatrix} x_2^0 + u_2^i \\ y_2^0 + v_2^i \end{Bmatrix}$$

$$\underline{X}_3^{\,i} = \begin{Bmatrix} x_3^i \\ y_3^i \end{Bmatrix} = \begin{Bmatrix} x_3^0 + u_3^i \\ y_3^0 + v_3^i \end{Bmatrix} \quad \underline{X}_4^{\,i} = \begin{Bmatrix} x_4^i \\ y_4^i \end{Bmatrix} = \begin{Bmatrix} x_4^0 + u_4^i \\ y_4^0 + v_4^i \end{Bmatrix} \tag{2.3}$$

The first set of equations for satisfying the parallelogram geometric constraints correspond to the location of the intersection of the parallelogram diagonals, or the parallelogram centroid. The lines that connect midpoints of the opposite sides are referred to as main chords. For this formulation, the two main chords connect the first node to the third node and the second node to the fourth node respectively. The two diagonals of a parallelogram and both main chords bisect exactly at the same location, which establishes

the location of the central node. The coordinates of the parallelogram centroid, $\underline{X}_c^i$ are thus calculated as follows:

$$\underline{X}_c^i = \frac{1}{2}\cdot(\underline{X}_1^i + \underline{X}_3^i) = \frac{1}{2}\cdot(\underline{X}_2^i + \underline{X}_4^i) \tag{2.4}$$

or in expanded form,

$$\underline{X}_C^i = \begin{Bmatrix} x_C^i \\ y_C^i \end{Bmatrix} = \begin{Bmatrix} x_C^0 + u_C^i \\ y_C^0 + v_C^i \end{Bmatrix} = \begin{Bmatrix} \frac{1}{2}\cdot\left(x_1^0 + x_3^0 + u_1^i + u_3^i\right) \\ \frac{1}{2}\cdot\left(y_1^0 + y_3^0 + v_1^i + v_3^i\right) \end{Bmatrix} = \begin{Bmatrix} \frac{1}{2}\cdot\left(x_2^0 + x_4^0 + u_2^i + u_4^i\right) \\ \frac{1}{2}\cdot\left(y_2^0 + y_4^0 + v_2^i + v_4^i\right) \end{Bmatrix} \tag{2.5}$$

The system of equations can also be presented as:

$$\begin{cases} \underline{X}_1^i - \underline{X}_C^i = \underline{X}_C^i - \underline{X}_3^i \\ \underline{X}_2^i - \underline{X}_C^i = \underline{X}_C^i - \underline{X}_4^i \end{cases} \tag{2.6}$$

The second geometric feature used in this formulation is the length of the parallelogram sides. It is possible to prove that the length of each main chord is equal to the length of the side parallel to it. To maintain the joint panel size during the analysis, the length of the vectors connecting the nodes on opposite sides must remain constant and equal to the initial size:

$$\begin{gathered} \left\| \underline{X}_1^i - \underline{X}_3^i \right\| = \left\| \underline{X}_1^0 - \underline{X}_3^0 \right\| \\ \textit{and} \\ \left\| \underline{X}_2^i - \underline{X}_4^i \right\| = \left\| \underline{X}_2^0 - \underline{X}_4^0 \right\| \end{gathered} \tag{2.7}$$

The expanded form of (2.7) is calculated as (2.8) and (2.9) to be later used for the length correction algorithm:

$$\left(x_1^0 - x_3^0 + u_1^i - u_3^i\right)^2 + \left(y_1^0 - y_3^0 + v_1^i - v_3^i\right)^2 = \left(x_1^0 - x_3^0\right)^2 + \left(y_1^0 - y_3^0\right)^2 \tag{2.8}$$

$$\left(x_2^0 - x_4^0 + u_2^i - u_4^i\right)^2 + \left(y_2^0 - y_4^0 + v_2^i - v_4^i\right)^2 = \left(x_2^0 - x_4^0\right)^2 + \left(y_2^0 - y_4^0\right)^2 \tag{2.9}$$

The external nodes are rigidly constrained to the midpoints of each side of the parallelogram. Therefore, the rotation of the external nodes is equal to the rotation of the parallelogram side and the parallel main chord. The rotation of each external node is described using the cross product of the updated main chord and the main chord at its initial position:

$$\sin\left(\theta_2^i\right) = \sin\left(\theta_4^i\right) = \frac{\left(\underline{X}_1^i - \underline{X}_3^i\right) \times \left(\underline{X}_1^0 - \underline{X}_3^0\right)}{\left\|\underline{X}_1^i - \underline{X}_3^i\right\| \cdot \left\|\underline{X}_1^0 - \underline{X}_3^0\right\|} = \sin\left(\alpha^i\right) \tag{2.10}$$

$$\sin\left(\theta_1^i\right) = \sin\left(\theta_3^i\right) = \frac{\left(\underline{X}_2^i - \underline{X}_4^i\right) \times \left(\underline{X}_2^0 - \underline{X}_4^0\right)}{\left\|\underline{X}_2^i - \underline{X}_4^i\right\| \cdot \left\|\underline{X}_2^0 - \underline{X}_4^0\right\|} = \sin\left(\beta^i\right) \tag{2.11}$$

where the α and β angles are the rotation of each main chord with respect to their initial alignment (Figure 2-20). The coordinates of the parallelogram center can be written in expanded form as:

$$\sin\left(\theta_2^i\right) = \sin\left(\theta_4^i\right) = \sin\left(\alpha^i\right) = \sin\left(\alpha^0\right) + \frac{\left(u_1^i - u_3^i\right) \cdot \left(y_1^0 - y_3^0\right) - \left(v_1^i - v_3^i\right) \cdot \left(x_1^0 - x_3^0\right)}{\left(x_1^0 - x_3^0\right)^2 + \left(y_1^0 - y_3^0\right)^2} \tag{2.12}$$

$$\sin\left(\theta_1^i\right) = \sin\left(\theta_3^i\right) = \sin\left(\beta^i\right) = \sin\left(\beta^0\right) + \frac{\left(u_2^i - u_4^i\right) \cdot \left(y_2^0 - y_4^0\right) - \left(v_2^i - v_4^i\right) \cdot \left(x_2^0 - x_4^0\right)}{\left(x_2^0 - x_4^0\right)^2 + \left(y_2^0 - y_4^0\right)^2} \tag{2.13}$$

Using the expanded equations (2.5), (2.8), (2.9), (2.12), and (2.13), all the nodal deformations can be explicitly derived as functions of x_C^i, y_C^i, α^i, β^i, which are the translations and rotations of the central node.

The constraint equations in OpenSees and most response history structural analysis programs are enforced in piecewise linear form. The incremental piecewise linear formulation of the multipoint constraints is necessary because the geometric information

is available only for the beginning of the step, when the step size is unknown. In OpenSees, the initial state of each load step is known and the incremental form of the constraint equations are used to predict the next step. Assuming that the steps are fairly small, a first order Taylor expansion of the rotation angles is valid.

The piecewise-linear incremental form of the equations can be achieved by chain differentiating the equations:

$$\begin{Bmatrix} \delta u_C \\ \delta v_C \end{Bmatrix} = \begin{Bmatrix} \frac{1}{2}\cdot\left(\delta u_1 + \delta u_3\right) \\ \frac{1}{2}\cdot\left(\delta v_1 + \delta v_3\right) \end{Bmatrix} = \begin{Bmatrix} \frac{1}{2}\cdot\left(\delta u_2 + \delta u_4\right) \\ \frac{1}{2}\cdot\left(\delta v_2 + \delta v_4\right) \end{Bmatrix} \tag{2.14}$$

$$\left(x_1^i - x_3^i\right)\cdot\left(\delta u_1 - \delta u_3\right) + \left(y_1^i - y_3^i\right)\cdot\left(\delta v_1 - \delta v_3\right) = 0 \tag{2.15}$$

$$\left(x_2^i - x_4^i\right)\cdot\left(\delta u_2 - \delta u_4\right) + \left(y_2^i - y_4^i\right)\cdot\left(\delta v_2 - \delta v_4\right) = 0 \tag{2.16}$$

$$\cos\left(\alpha^i\right)\delta\alpha = \frac{\left(y_1^0 - y_3^0\right)}{\left(x_1^0 - x_3^0\right)^2 + \left(y_1^0 - y_3^0\right)^2}\left(\delta u_1 - \delta u_3\right) + \frac{\left(x_1^0 - x_3^0\right)}{\left(x_1^0 - x_3^0\right)^2 + \left(y_1^0 - y_3^0\right)^2}\left(\delta v_1 - \delta v_3\right) \tag{2.17}$$

$$\cos\left(\beta^i\right)\delta\beta = \frac{\left(y_2^0 - y_4^0\right)}{\left(x_2^0 - x_4^0\right)^2 + \left(y_2^0 - y_4^0\right)^2}\left(\delta u_2 - \delta u_4\right) + \frac{\left(x_2^0 - x_4^0\right)}{\left(x_2^0 - x_4^0\right)^2 + \left(y_2^0 - y_4^0\right)^2}\left(\delta v_2 - \delta v_4\right) \tag{2.18}$$

Using the definition of the inner product of two vectors, $\cos\left(\alpha^i\right)$ and $\cos\left(\beta^i\right)$ can be calculated as:

$$\cos\left(\alpha^i\right) = \frac{\left(\underline{X}_1^{\,i} - \underline{X}_3^{\,i}\right)\bullet\left(\underline{X}_1^{\,0} - \underline{X}_3^{\,0}\right)}{\left\|\underline{X}_1^{\,i} - \underline{X}_3^{\,i}\right\|\cdot\left\|\underline{X}_1^{\,0} - \underline{X}_3^{\,0}\right\|} = \frac{\left(x_1^i - x_3^i\right)\cdot\left(x_1^0 - x_3^0\right) + \left(y_1^i - y_3^i\right)\cdot\left(y_1^0 - y_3^0\right)}{\left(x_1^0 - x_3^0\right)^2 + \left(y_1^0 - y_3^0\right)^2} \tag{2.19}$$

$$\cos\left(\beta^i\right) = \frac{\left(\underline{X}_2^{\,i} - \underline{X}_4^{\,i}\right)\bullet\left(\underline{X}_2^{\,0} - \underline{X}_4^{\,0}\right)}{\left\|\underline{X}_2^{\,i} - \underline{X}_4^{\,i}\right\|\cdot\left\|\underline{X}_2^{\,0} - \underline{X}_4^{\,0}\right\|} = \frac{\left(x_2^i - x_4^i\right)\cdot\left(x_2^0 - x_4^0\right) + \left(y_2^i - y_4^i\right)\cdot\left(y_2^0 - y_4^0\right)}{\left(x_2^0 - x_4^0\right)^2 + \left(y_2^0 - y_4^0\right)^2} \tag{2.20}$$

The differential form of equations (2.17) and (2.18) can be rearranged in the form of a system of equations as:

$$\left[\left(x_1^i - x_3^i\right)\cdot\left(x_1^0 - x_3^0\right) + \left(y_1^i - y_3^i\right)\cdot\left(y_1^0 - y_3^0\right)\right]\delta\alpha = \left(y_1^0 - y_3^0\right)\left(\delta u_1 - \delta u_3\right) - \left(x_1^0 - x_3^0\right)\left(\delta v_1 - \delta v_3\right) \tag{2.21}$$

$$\left[\left(x_2^i - x_4^i\right)\cdot\left(x_2^0 - x_4^0\right) + \left(y_2^i - y_4^i\right)\cdot\left(y_2^0 - y_4^0\right)\right]\delta\beta = \left(y_2^0 - y_4^0\right)\left(\delta u_2 - \delta u_4\right) - \left(x_2^0 - x_4^0\right)\left(\delta v_2 - \delta v_4\right) \tag{2.22}$$

By substituting the coordinate and the displacement of the central point, and splitting the equations for each external degree of freedom:

$$\begin{aligned}
&\delta u_1 = \delta u_C + \left(y_1^i - y_C^i\right)\delta\alpha \qquad \delta v_1 = \delta v_C - \left(x_1^i - x_C^i\right)\cdot\delta\alpha \qquad \delta\theta_1 = \delta\beta \\
&\delta u_2 = \delta u_C + \left(y_2^i - y_C^i\right)\delta\beta \qquad \delta v_2 = \delta v_C - \left(x_2^i - x_C^i\right)\delta\beta \qquad \delta\theta_2 = \delta\alpha \\
&\delta u_3 = \delta u_C + \left(y_3^i - y_C^i\right)\delta\alpha \qquad \delta v_3 = \delta v_C - \left(x_3^i - x_C^i\right)\delta\alpha \qquad \delta\theta_3 = \delta\beta \\
&\delta u_4 = \delta u_C + \left(y_4^i - y_C^i\right)\delta\beta \qquad \delta v_4 = \delta v_C - \left(x_4^i - x_C^i\right)\delta\beta \qquad \delta\theta_4 = \delta\alpha
\end{aligned} \tag{2.23}$$

The relation of deformation increments of external nodes and the ones of the central node are represented in matrix form in equation (2.24). The Joitn2D-1SPR with rigid member-end interfaces will incorporate equation (2.24) as its compatibility relations.

$$\begin{Bmatrix} \delta u_1 \\ \delta v_1 \\ \delta \theta_1 \\ \delta u_2 \\ \delta v_2 \\ \delta \theta_2 \\ \delta u_3 \\ \delta v_3 \\ \delta \theta_3 \\ \delta u_4 \\ \delta v_4 \\ \delta \theta_4 \end{Bmatrix} = \begin{bmatrix} 1 & 0 & \left(y_1^i - y_C^i\right) & 0 \\ 0 & 1 & -\left(x_1^i - x_C^i\right) & 0 \\ 0 & 0 & 0 & 1 \\ 1 & 0 & 0 & \left(y_2^i - y_C^i\right) \\ 0 & 1 & 0 & -\left(x_2^i - x_C^i\right) \\ 0 & 0 & 1 & 0 \\ 1 & 0 & \left(y_3^i - y_C^i\right) & 0 \\ 0 & 1 & -\left(x_3^i - y_C^i\right) & 0 \\ 0 & 0 & 0 & 1 \\ 1 & 0 & 0 & \left(y_4^i - y_C^i\right) \\ 0 & 1 & 0 & -\left(x_4^i - y_C^i\right) \\ 0 & 0 & 1 & 0 \end{bmatrix} \times \begin{Bmatrix} \delta u_C \\ \delta v_C \\ \delta \alpha \\ \delta \beta \end{Bmatrix} \tag{2.24}$$

Next, the stiffness relationships are introduced to the model, which describe the shear panel and member-end rotations. The deformation of the shear panel in shear mode corresponds to the change of the angle between the main chords. The variation of the angle between the main chords is quantified as $\left(\delta\alpha - \delta\beta\right)$. The shear stiffness is introduced as a rotational spring connecting the two rotational degrees of freedom of the central node. Conceptually, the resultant moments of this spring are nonlinear functions of $\left(\delta\alpha - \delta\beta\right)$:

$$\begin{Bmatrix} M_\alpha \\ M_\beta \end{Bmatrix} = \begin{Bmatrix} M_C\left(\alpha - \beta\right) \\ M_C\left(\beta - \alpha\right) \end{Bmatrix} \tag{2.25}$$

or, in piecewise-linear incremental form:

$$\begin{Bmatrix} \delta M_\alpha \\ \delta M_\beta \end{Bmatrix} = \begin{bmatrix} K_C & -K_C \\ -K_C & K_C \end{bmatrix} \times \begin{Bmatrix} \delta\alpha \\ \delta\beta \end{Bmatrix} \tag{2.26}$$

Equations (2.25) and (2.26) will define the resultant force vector and the tangent matrix for Joint2D-1SPR. In the Joint2D-5SPR model with the member-end rotations to the model, the kinematic constraints between the rotational degree of freedom of the external node and the central node must be released. This is possible by removing the row related to the rotational degree of freedom from the constraint matrix. The released constraints

are replaced by rotational springs. The resultant constraint matrix and stiffness matrix are presented in :

$$\delta \underset{\sim}{U}_{external}^{constrained} = \underline{\underline{C}} \times \delta \underset{\sim}{U}_{central} \tag{2.27}$$

where $\underline{\underline{C}}$ is the assembled matrix of the individual constraint matrices that connect each external node to the central node (Figure 2-22), and $\delta \underset{\sim}{U}_{external}^{constrained}$ and $\delta \underset{\sim}{U}_{central}$ are increments of deformation vectors of constrained and retained degrees of freedom.

$$\begin{Bmatrix} \delta u_1 \\ \delta v_1 \\ \delta u_2 \\ \delta v_2 \\ \delta u_3 \\ \delta v_3 \\ \delta u_4 \\ \delta v_4 \end{Bmatrix} = \begin{bmatrix} 1 & 0 & \left(y_1^i - y_C^i\right) & 0 \\ 0 & 1 & -\left(x_1^i - x_C^i\right) & 0 \\ 1 & 0 & 0 & \left(y_2^i - y_C^i\right) \\ 0 & 1 & 0 & -\left(x_2^i - x_C^i\right) \\ 1 & 0 & \left(y_3^i - y_C^i\right) & 0 \\ 0 & 1 & -\left(x_3^i - x_C^i\right) & 0 \\ 1 & 0 & 0 & \left(y_4^i - y_C^i\right) \\ 0 & 1 & 0 & -\left(x_4^i - x_C^i\right) \end{bmatrix} \times \begin{Bmatrix} \delta u_C \\ \delta v_C \\ \delta \alpha \\ \delta \beta \end{Bmatrix} \tag{2.28}$$

The nodal moment increment for the Joint2D-5SPR element is computed as:

$$\delta \underline{M}^{unconstrained} = \underline{\underline{K}} \times \delta U_{rotational} \tag{2.29}$$

or

$$\begin{Bmatrix} \delta M_1 \\ \delta M_2 \\ \delta M_3 \\ \delta M_4 \\ \delta M_\alpha \\ \delta M_\beta \end{Bmatrix} = \begin{bmatrix} K_1 & 0 & 0 & 0 & 0 & -K_1 \\ 0 & K_2 & 0 & 0 & -K_2 & 0 \\ 0 & 0 & K_3 & 0 & 0 & -K_3 \\ 0 & 0 & 0 & K_4 & -K_4 & 0 \\ 0 & -K_2 & 0 & -K_4 & K_C + K_2 + K_4 & -K_C \\ -K_1 & 0 & -K_3 & 0 & -K_C & K_C + K_1 + K_3 \end{bmatrix} \times \begin{Bmatrix} \delta \theta_1 \\ \delta \theta_2 \\ \delta \theta_3 \\ \delta \theta_4 \\ \delta \theta_\alpha \\ \delta \theta_\beta \end{Bmatrix} \tag{2.30}$$

The nodal moments for the joint element are computed as:

$$\begin{Bmatrix} M_1 \\ M_2 \\ M_3 \\ M_4 \\ M_\alpha \\ M_\beta \end{Bmatrix} = \begin{Bmatrix} M_1(\theta_1 - \theta_\beta) \\ M_2(\theta_2 - \theta_\alpha) \\ M_3(\theta_3 - \theta_\beta) \\ M_4(\theta_4 - \theta_\alpha) \\ M_\alpha(\theta_\alpha - \theta_\beta) \\ M_\beta(\theta_\beta - \theta_\alpha) \end{Bmatrix} \tag{2.31}$$

It needs to be mentioned if any of the frame elements are rigidly connected to the joint, the rotational degree of freedom at the connection node must be constrained to the corresponding degree of freedom and its referring column and row must be removed off the stiffness matrix. The element Joint2D-1SPR has all four frame elements rigidly connected to the joint element. The internal components of the Joint2D-1SPR (Figure 2-23), its deformed shape (Figure 2-24), the external degrees of freedom (Figure 2-25), and the modified constraint matrix are presented (Figure 2-26).

2.4.2 **Implementation in OpenSees**

The OpenSees features and the object oriented terminology related to the Joint2D implementation are briefly described in this section. A more detailed description of the OpenSees components and structure is provided in Appendix A. The OpenSees platform is designed around an object oriented architecture, which facilitates using the existing classes to develop new components. The analytical model in OpenSees is divided to two objects, referred to as the analysis and domain objects. The domain refers to the object responsible for storing the model components and the analysis is responsible for performing the calculations. The joint elements are introduced as a member of the domain.

Conventional elements (such as the beam-column elements) do not modify the domain; they only import the nodal displacements from the domain and return the stiffness matrix

and nodal forces to the domain. The situation is a bit different for the Joint2D elements, which modify the analytical model (domain) by adding several other components.

Joint2D adds a central node and a series of four multipoint constraints to the domain, and then constructs itself as an element over the four external nodes and the central node (Figure 2-19 and Figure 2-23). The central node and the constraints use the existing OpenSees class definitions with some modifications to satisfy the joint formulation. Implementation of the Joint2D formulation is explained in three parts: defining the joint element subcomponents, implementing the multi-point constraints, constructing the Joint2D.

Defining the joint element subcomponents: The central node and four multipoint constraint objects are sub-components, which the joint element constructs and adds to the domain. Since the multipoint constraints connect the central node to the external nodes, the central node and its properties are discussed first. Each node is specified by a unique tag. The tag assignment for the external node is arbitrary, while the tag assignment of external node tags must be sequential in a clockwise or counter-clockwise order.

The central node is introduced to the domain by the joint element, not the user. In the element command interface, the user is only required to provide a tag for the central node. The location of the central node is determined by the joint element based on the location of the four external joint nodes. The central node is located on a two dimensional coordinate system, exactly at the intersection point of the mains chords. As mentioned in the element specifications, it is required that main chords bisect each other, so that a virtual parallelogram can be constructed centered at the central node, with external nodes located at the midpoint of its sides. The displacement field for the external nodes is defined by two translations and one rotation; i.e. the standard three degrees of freedom for a regular two-dimensional frame model. The central node has four degrees of freedom, two translations and two rotations. The joint shear deformation is defined between these two rotations (Figure 2-20 and Figure 2-24).

The constraint equations are defined in equation (2.28) as a matrix, relating the external nodal displacements to the central node displacement. To comply with the object oriented structure of OpenSees, the constraint equations are separately defined between each set of two nodes, as shown in Figure 2-22. Four sets of multi-point constraint objects maintain the external node positions on a parallelogram, and they reduce the extra degrees of freedom, associated with the external nodes. The five nodes of Joint2D have a total of 16 degrees of freedom; of those 8 degrees of freedom (for Joint2D5-SPR) and 12 degrees of freedom (for Joint2D-1SPR) are constrained to the central node.

Implementing the multi-point constraints: The multipoint constraint connects the central node to each external joint node. The central node is referred to as the retained node since its motion is independent, while the external node is referred to as the constrained node. The displacement components of the constrained (external) node that are controlled by the constraint equations are called constrained degrees of freedom. The constraint on the rotational degree of freedom of the external node is decided based on the rotational fixity defined at the external nodes. The independent displacement components of the retained (central) node that control the motion of the constrained node are referred to as retained degrees of freedom. The retained and constrained degrees of freedom are introduced as two vectors to the multipoint constraint object.

For the case when the member-end rotation is allowed at the external nodes (i.e. Joint2D-5SPR):

$$ConstrainedDOF = \begin{Bmatrix} u_{ext} \\ v_{ext} \end{Bmatrix} \tag{2.32}$$

$$RetainedDOF = \begin{Bmatrix} u_{cen} \\ v_{cen} \\ \alpha_{cen} \\ \beta_{cen} \end{Bmatrix} \tag{2.33}$$

where the subscripts refer to the external and central nodes respectively. When the frame element is rigidly connected to the external node, i.e. no member-end rotation in Joint2D1SPR:

$$ConstrainedDOF = \begin{Bmatrix} u_{ext} \\ v_{ext} \\ \theta_{ext} \end{Bmatrix} \tag{2.34}$$

$$RetainedDOF = \begin{Bmatrix} u_{cen} \\ v_{cen} \\ \alpha_{cen} \\ \beta_{cen} \end{Bmatrix} \tag{2.35}$$

The multipoint constraint formulation for the joint element is similar to a rigid link. One of the two rotations of the retained node determines the rigid body rotation of the rigid link. This rotation is called the primary rotational degree of freedom of the retained node (Figure 2-22 and Figure 2-26). The other rotation of the retained node, the auxiliary rotational degree of freedom, determines the rotation of the constrained node. For programming purposes, a single formulation is introduced, where the primary and auxiliary rotational degrees of freedom will switch places for each node (see Table 2-1).

Table 2-1: Central node primary and auxiliary degrees of freedom for Joint2D

Node	Primary Rotation	Auxiliary Rotation
1	α_{cen}	β_{cen}
2	β_{cen}	α_{cen}
3	α_{cen}	β_{cen}
4	β_{cen}	α_{cen}

MP_joint2D-15SPR and MP_joint2D-1SPR are the names for the multipoint constraint class for the two dimensional joint element. The constrained and retained node tags and degrees of freedom, along with the primary rotation degree of freedom, are declared in

the MPjoint2D constructor. The implementation of Joint2D allows the user to arbitrarily set each member-end rotation as rigid (for more details on the Joint2D command refer to Appendix B). Two additional variables are used to indicate the fixity of the member-end rotation and the large deformation condition.

The constraint formulation is defined in the form of a linear system of equations, and the resulting constraint matrix is exported to the analysis object. Depending on the large deformation formulation specified by the user, the constraint matrix is either constant or time varying. The constraint matrix formulation is defined and calculated as:

$$\delta \underline{U}_C = \underline{\underline{C}} \times \delta U_R \tag{2.36}$$

where $\delta \underline{U}_C$ refers to the displacement increments of the constrained degrees of freedom of the constrained external node, $\underline{\underline{C}}$ is the constraint matrix, given by equation (2.37) or (2.38), and δU_R represents the displacement increments of the retained degrees of freedom at the retained (central) node. The general form of the constraint equations is introduced by defining primary and auxiliary rotations.

In the case where any or all of the external nodes are released to permit member-end rotation (i.e. when the external node rotation is connected through a rotational spring to the central node) the rotational degree of freedom of the external node is not constrained. In such cases, the constraint formulation is modified to the following:

$$\begin{Bmatrix} \delta u_C \\ \delta v_C \end{Bmatrix} = \begin{bmatrix} 1 & 0 & \left(y_C^i - y_R^i\right) \\ 0 & 1 & -\left(x_C^i - x_R^i\right) \end{bmatrix} \times \begin{Bmatrix} \delta u_R \\ \delta v_R \\ \delta \theta_R^{Primary} \end{Bmatrix} \tag{2.37}$$

For cased without member-end rotations (Joint2D-1SPR or Joint2D-5SPR with selected constraints), the constraint formulation is:

$$\begin{Bmatrix} \delta u_C \\ \delta v_C \\ \delta \theta_C \end{Bmatrix} = \begin{bmatrix} 1 & 0 & \left(y_C^i - y_R^i\right) & 0 \\ 0 & 1 & -\left(x_C^i - x_R^i\right) & 0 \\ 0 & 0 & 0 & 1 \end{bmatrix} \times \begin{Bmatrix} \delta u_R \\ \delta v_R \\ \delta \theta_R^{Primary} \\ \delta \theta_R^{Auxilary} \end{Bmatrix} \tag{2.38}$$

Constructing the Joint2D: In OpenSees, the elements are stored as domain components in the domain object. The Joint2D is a subclass of element and consequently a subclass of the domain component. The domain components of each class are identified by a unique tag. Beside the tag, the elements also require specification of the nodal connectivity and the material information. Joint2D invokes a pointer to the domain to add the central node and multipoint constraints to the domain it belongs to. The following arguments are imported at the constructor level of the Joint2D element:

- A unique element tag for the joint element
- The tags of four external nodes.
- An unused tag for the central node
- One uniaxial material model for the shear panel and up to four more uniaxial material models for member-end rotations
- A pointer to the domain that the joint element belongs to. The pointer is sent by the Model Builder and used for adding new components to the domain.
- The tag for the large deformation condition

The user-specified tags of the external nodes are used to retrieve the nodal pointer from the domain. The nodal pointers in turn provide access to the coordinates of external nodes. An error check is performed on the location of the intersection point of the main chords. The intersection point of the main chords must be located within the radius of $\left(1.0e-6\times JointSize\right)$ from the centroid of the imaginary parallelogram constructed on the external nodes. Here the joint size is the minimum length of the main chords. The commands for creating the joint elements are presented in Appendix B. The number of degrees of freedom of the external nodes is also checked.

The domain is checked to make sure the user-specified central node tag is not already used by another node. Then the central node is constructed at the location of parallelogram centroid, with four degrees of freedom. The central node is added to the domain, so it will be involved in the analysis.

A copy of the material models that the user provides to the joint are stored as element private data. If the member-end rotation materials are not specified, a rigid connection at the external node is assumed as the default condition. Otherwise, uniaxial material models introduced by the user are assigned to the rotational springs for the joint element. These material models simulate the nonlinear joint shear or interface behavior by updating the stiffness matrix and the resisting nodal forces for every load step. The matrix and vectors are dynamically allocated for the element stiffness matrix and nodal forces.

The last step in constructing the Joint2D element is the construction of the multipoint constraints and addition of them to the domain. The constrained and retained degrees of freedom are determined based on the fixity at the external nodes. The constrained and retained nodal degrees of freedom and the element specified tags for the primary rotation (see Table 2-1) and large deformation condition are sent to the multipoint constraint constructor and the constraint object is added to the domain.

Once the element is created and introduced as a part of the domain, it is included as part of the analysis, so at each analysis iteration, the analysis object requests the tangent stiffness matrix and nodal forces from the joint element. The joint element retrieves the nodal displacements and calculates the deformations for each rotational spring based on the current geometry. The rotational deformations are submitted to the uniaxial material models (representing the joint shear and interface springs), which returns the resisting moment and tangent stiffness to the joint element. These values are then applied to the joint element stiffness matrix and residual forces vector, per the derivation presented in the previous formulation section. For the rigid connections, the multi-point constraint enforces the rigidity, and uniaxial material information does not apply (zero values are assumed for the uniaxial material model stiffness and resultant force).

A series of damage models (as described in chapter 3) are also implemented in OpenSees. These damage models calculate the structural or component damages based on the forces, deformations, energy, or a combined formulation. The joint element can invoke the damage models to calculate and record the structural damage that the joint undergoes. The damage models are generated in the input file and they are introduced as supplementary arguments to the joint element. The damage of each spring in the joint model will be recorded as element output. Based on the damage model used, the joint damage can be calculated as a function of the total deformation, plastic deformation, or another combination of the force/deformation of the rotational springs.

2.4.3 **Validation cases for 2D joint models**

As part of the implementation process, an analytical model of a simple subassembly with the joint element and elastic frame elements was created to check the model implementation. The sizes and material properties in the example are arbitrary, but they were selected in a manner to facilitate hand calculation of the system under different loading modes. The subassembly model was then monotonically loaded in axial, shear and asymmetric modes, and the equilibrium of the joint zone and the whole structure was examined. The compatibility was checked for both the joint and the frame elements connected to the joint. The joint stiffness matrix was also tested by comparing the analysis results with hand calculations.

The joint element was subjected to cyclic loading and large deformations for verifying the performance of multi-point constraints. The joint element maintained the initial size and the external nodes were located at the expected location on the deformed parallelogram.

The joint was subjected to a rigid body rotation in small increments and the results were compared with the case for one large step. The large displacement formulation with length correction (described in Section 2.6) gave identical results for both cases. For observing the $P-\Delta$ effects, a highly distorted joint was subjected to axial forces and the

resulting $P-\Delta$ moment was detected in the shear panel was checked for equilibrium in the deformed geometry.

2.5 *Joint3D*

Basic assumptions regarding the deformation modes for the two-dimensional model are simple to extend for the three dimensional model. The three dimensional joint is viewed as a block with frame elements connected to the centroid of each face, Figure 2-27. This block is assumed to be flexible in shear and rigid in the axial and flexural modes; hence, it will be referred to as shear block. The sizes and dimensions of the shear block do not change through the process. The shear block is modeled by a parallelepiped, a polyhedron whose faces are parallelograms lying in pairs of parallel planes (Figure 2-28).

The shear block is subjected to six force components at each face, Figure 2-29, but, only the shear forces can deform the shear block. The shear resistance is provided by three rotational springs, each defined along a local axis. The 3D joint implementation is limited to cases where adjacent beam-column members are rigidly connected to the joint (i.e. comparable to the Joint2D-1SPR element). Where necessary, the end rotations can be added separately by rotational springs.

2.5.1 Element characteristics

Joint3D is a three dimensional extension of the Joint2D-1SPR model which represents the shear block in three dimensional the analysis models. The Joint3D is constructed over six external nodes. An imaginary parallelepiped is constructed on external nodes in a sense that each node is located at the center of one of the parallelepiped faces. In Joint2D model all the rotations and deformations occur in a single fixed plane, i.e. the rotation vectors all have a constant direction, whereas in Joint3D the direction of rotation vector varies. A local coordinate system is defined to signify the direction of rotation vectors for the joint shear deformation. The local coordinate system is defined by the external nodes at two opposite sides of the block. The order for tagging the external nodes is done such that the local x' axis is defined by nodes 1 and 2, the local y' axis is defined by nodes 3

and 4 define, and nodes 5 and 6 define the local z' axis (Figure 2-28). The order of the nodal tags does not necessarily imply the local axes are orthogonal, and the formulation is developed for large deformations where the local axes may not remain orthogonal. The nodal locations in the normalized local coordinate system are defined as:

$$\begin{aligned} x_1' &= (-1,0,0) \quad x_2' = (1,0,0) \\ x_3' &= (0,-1,0) \quad x_4' = (0,1,0) \\ x_4' &= (0,0,-1) \quad x_6' = (0,0,1) \end{aligned} \tag{2.39}$$

The external nodes have six degrees of freedom each, three translations and three rotations. The movements of external nodes are constrained to the central node by multipoint constraints and move attached to the shear block. The adjacent members are rigidly connected to the external nodes, so the displacement of the external nodes directly determines the global deformations of the connected beam-column members. The central node controls both rigid body motion and shear deformation of the element with its 9 degrees of freedom (6 degrees for the rigid-body motion and 3 degrees for shear distortion).

2.5.2 **Formulation**

The formulation of the Joint3D element depends on the geometric features of parallelepipeds. A principal plane is defined as a plane parallel to one of the faces that passes through the parallelepiped centroid. Three principal planes are defined for a parallelepiped, which divide the parallelepiped to eight equal parallelepipeds (Figure 2-28). Each principal plane is identified by a normal vector and the central node, i.e. centroid of the volume. The intersection of principal planes with the volume of the parallelepiped is a parallelogram in three-dimensional space. The external nodes are defined by the intersections of two principal planes and the parallelepiped face. The assumptions of axial and flexural rigidity of the parallelepiped imply that the size of these three principal parallelograms can not change and their deformability is limited only to shear distortion (change of angle). The local coordinate system is defined by three vectors connecting the external nodes on each two opposite faces (Figure 2-28). The main chord

is a line that connects two nodes on two opposite faces of parallelepiped. The central node is located at the centroid of the parallelepiped where the principal planes intersect and main chords bisect each other.

The rigid-body motion of the Joint3D element is prescribed by the displacements and rotations of the central node, while the three shear deformation modes are determined by the relative rotation between the principal planes. The magnitude of the shear deformations is expressed by shear angles in the local coordinate system. The shear angles are scalar values and they are stored as nodal rotations. The central node has three extra degrees of freedom for storing these shear angles.

The initial location of an external node n is defined as a vector of size three, defined to have zero initial displacements at step $i = 0$:

$$\underline{X}_n^{\,0} = \begin{Bmatrix} x_n^0 \\ y_n^0 \\ z_n^0 \end{Bmatrix} \tag{2.40}$$

The nodal displacements are time variant vectors with six degrees of freedom, three translations and three rotations. The nodal deformation vectors for the load step i are defined as:

$$\underline{\Delta}_n^{\,i} = \begin{Bmatrix} u_n^i \\ v_n^i \\ w_n^i \\ \alpha_n^i \\ \beta_n^i \\ \chi_n^i \end{Bmatrix} \tag{2.41}$$

The updated locations of nodes for the time-step i are calculated by adding the nodal deformations to the initial coordinates:

$$\underline{X}_n^i = \begin{Bmatrix} x_n^0 + u_n^i \\ y_n^0 + v_n^i \\ z_n^0 + w_n^i \end{Bmatrix} \tag{2.42}$$

As the element deforms in shear, all the joint dimensions remain constant through the analysis and only the angle between the principal planes may change. This means the main chords always intersect at the centroid and they bisect each other. The location of the central node, $\underline{X}_c^i$, can be calculated based on the position of the external nodes.

$$\underline{X}_c^i = \begin{Bmatrix} x_c^i \\ y_c^i \\ z_c^i \end{Bmatrix} = \begin{Bmatrix} x_c^0 + u_c^i \\ y_c^0 + v_c^i \\ z_c^0 + w_c^i \end{Bmatrix} = \begin{Bmatrix} \frac{1}{2}\left(x_1^i + x_2^i\right) \\ \frac{1}{2}\left(y_1^i + y_2^i\right) \\ \frac{1}{2}\left(z_1^i + z_2^i\right) \end{Bmatrix} = \begin{Bmatrix} \frac{1}{2}\left(x_3^i + x_4^i\right) \\ \frac{1}{2}\left(y_3^i + y_4^i\right) \\ \frac{1}{2}\left(z_3^i + z_4^i\right) \end{Bmatrix} = \begin{Bmatrix} \frac{1}{2}\left(x_5^i + x_6^i\right) \\ \frac{1}{2}\left(y_5^i + y_6^i\right) \\ \frac{1}{2}\left(z_5^i + z_6^i\right) \end{Bmatrix} \tag{2.43}$$

The following nine equations satisfy the condition that main chords bisect each other:

$$\frac{1}{2}\cdot(\underline{X}_1^i + \underline{X}_2^i) = \frac{1}{2}\cdot(\underline{X}_3^i + \underline{X}_4^i) = \frac{1}{2}\cdot(\underline{X}_5^i + \underline{X}_6^i) \tag{2.44}$$

The next geometric feature used in this formulation is that the length of the parallelepiped main chords must remain constant to maintain the axial and flexural rigidity. This feature can be expressed in the form of three equations.

$$\begin{cases} \left\| \underline{X}_1^i - \underline{X}_2^i \right\| = \left\| \underline{X}_1^0 - \underline{X}_2^0 \right\| \\ \left\| \underline{X}_3^i - \underline{X}_4^i \right\| = \left\| \underline{X}_3^0 - \underline{X}_4^0 \right\| \\ \left\| \underline{X}_5^i - \underline{X}_6^i \right\| = \left\| \underline{X}_5^0 - \underline{X}_6^0 \right\| \end{cases} \tag{2.45}$$

The other feature used here is that the faces remain parallel. The external nodes are rigidly connected to each face of the parallelepiped; therefore the rotation vector of two external nodes on the opposite faces of the parallelepiped are identical and they must be

equal to the rotation of the normal vector of the principal plane parallel to the parallelepiped face. This feature is captured by the following equations:

$$\begin{Bmatrix} \alpha_1^i \\ \beta_1^i \\ \chi_1^i \end{Bmatrix} = \begin{Bmatrix} \alpha_2^i \\ \beta_2^i \\ \chi_2^i \end{Bmatrix} \qquad \begin{Bmatrix} \alpha_3^i \\ \beta_3^i \\ \chi_3^i \end{Bmatrix} = \begin{Bmatrix} \alpha_4^i \\ \beta_4^i \\ \chi_4^i \end{Bmatrix} \qquad \begin{Bmatrix} \alpha_5^i \\ \beta_5^i \\ \chi_5^i \end{Bmatrix} = \begin{Bmatrix} \alpha_6^i \\ \beta_6^i \\ \chi_6^i \end{Bmatrix} \tag{2.46}$$

The fixed set of equations required for the model relates nodal displacements to nodal rotations. Formulating the general three-dimensional rotation of principal planes requires careful adherence to a correct notation. For minimizing the number of redundant parameters in this formulation, the rotation of a main chord is only allowed to occur in its corresponding principal plane. This rotation will cause the principal parallelogram deform locally in the principal plane is defined on. The rotation of the main chord will cause the main chord end nodes move, and the other two nodes in that principal plane rotate. Figure 2-31 shows a principal parallelogram of the joint, and how its deformation affects the nodal deformations. The rotation of each main chord imposes a deformation component to the nodes at two ends of the main chord, resulting in 18 equations to relate the rotation of mains chords to external nodes.

In a two-dimensional plane with three degrees of freedom, the rotation vector is always parallel to the z-axis and it maintains a constant direction. In three-dimensional space with six degrees of freedom, there is no guarantee that the rotational vectors maintain their initial direction. For large deformations analysis, it is essential to consider the change in direction of the rotation vectors. Calculating the general rotation of a vector in three dimensions is a delicate task since superposition can not be used for large deformations. If a number of 3D rotations are applied, the result depends on the order rotations are applied, which means that the element formulation can not be based on total rotations for large deformations (and rotations). This is one of the reasons that most structural analysis platforms use incremental formulations for enforcing the kinematic constraints, since for small incremental rotations the rotation can be approximated as vectors. Since the behavior of the Joint3D element relies on the superposition of different deformation modes, the formulation is based on the deformation increments, rather than

total deformations. For infinitesimal rotations, the rotation of a vector will be simply calculated by the outer product of the vectors, Figure 2-30.

All the deformation modes of the joint parallelepiped can be explicitly derived as functions of central node motion and the shear deformation in principal planes. The shear deformation angles in principal planes are added as supplemental degrees of freedom to the central node, so the central node deformation are expressed in the form of three translations, $\left(u_c^i, v_c^i, w_c^i\right)$ three rotations $\left(\alpha_c^i, \beta_c^i, \chi_c^i\right)$, and three shear deformations $\left(\gamma_{x'}^i, \gamma_{y'}^i, \gamma_{z'}^i\right)$ all defined along the local axes.

$$\underline{\Delta}_{center}^i = \left\{ u_c^i \quad v_c^i \quad w_c^i \quad \alpha_c^i \quad \beta_c^i \quad \chi_c^i \quad \gamma_{x'}^i \quad \gamma_{y'}^i \quad \gamma_{z'}^i \right\}^T \tag{2.47}$$

To summarize, the displacement of each external node is governed by the rigid body motion of the central node $\left(\delta RB\right)$, and the shear distortion of two principal planes passing through the node. The shear distortions are described in the form of a rotation due to shear deformation of one of the principal planes $\left(\delta Rot\right)$ and a translation due to shear deformation of the other plane $\left(\delta Disp\right)$. The normal vector of the principal plane that governs the rotation is defined as $\eta_{rot} = \left(\eta_x^{rot}, \eta_y^{rot}, \eta_z^{rot}\right)$ and the rotation angle of this plane is γ_{rot}. The normal vector of the principal plane that governs the displacement is defined as $\eta_{disp} = \left(\eta_x^{disp}, \eta_y^{disp}, \eta_z^{disp}\right)$ and the rotation angle of this plane is γ_{disp}. The vector that connects the central node to the external node is defined as $\Delta = \left(\Delta_x, \Delta_y, \Delta_z\right)$. In equation form, these relationships are described as follows:

$$\delta node = \delta RB + \delta Rot + \delta Disp \tag{2.48}$$

$$\underline{\Delta}_n^i = \begin{Bmatrix} u_n^i \\ v_n^i \\ w_n^i \\ \alpha_n^i \\ \beta_n^i \\ \chi_n^i \end{Bmatrix} = \begin{bmatrix} 1 & 0 & 0 & 0 & \Delta_z & -\Delta_y \\ 0 & 1 & 0 & -\Delta_z & 0 & \Delta_x \\ 0 & 0 & 1 & \Delta_y & -\Delta_x & 0 \\ 0 & 0 & 0 & 1 & 0 & 0 \\ 0 & 0 & 0 & 0 & 1 & 0 \\ 0 & 0 & 0 & 0 & 0 & 1 \end{bmatrix} \times \begin{Bmatrix} u_c^i \\ v_c^i \\ w_c^i \\ \alpha_c^i \\ \beta_c^i \\ \chi_c^i \end{Bmatrix} + \gamma_{Rot} \times \begin{Bmatrix} 0 \\ 0 \\ 0 \\ \eta_x^{rot} \\ \eta_y^{rot} \\ \eta_z^{rot} \end{Bmatrix} + \gamma_{Rot} \times \begin{Bmatrix} \Delta_z \cdot \eta_y^{disp} - \Delta_y \cdot \eta_z^{disp} \\ \Delta_x \cdot \eta_z^{disp} - \Delta_z \cdot \eta_x^{disp} \\ \Delta_y \cdot \eta_x^{disp} - \Delta_x \cdot \eta_y^{disp} \\ 0 \\ 0 \\ 0 \end{Bmatrix} \tag{2.49}$$

With the nodal deformation relationships established, the joint shear stiffness relationships are introduced next. In the 2D formulation for the shear panel, a spring was introduced between the internal degrees of freedom. In the 3D formulation the internal degrees of freedom lying in each principal plane are connected in a similar manner. The nodal forces in the global system are defined as follows:

$$\begin{Bmatrix} M_{\gamma x'} \\ M_{\gamma x'} \\ M_{\gamma x'} \end{Bmatrix} = \begin{Bmatrix} M_{\gamma x'}\left(\gamma_{x'}\right) \\ M_{\gamma y'}\left(\gamma_{y'}\right) \\ M_{\gamma z'}\left(\gamma_{z'}\right) \end{Bmatrix} \tag{2.50}$$

Or in the piece-wise linear incremental form:

$$\begin{Bmatrix} \delta M_{\gamma x'} \\ \delta M_{\gamma x'} \\ \delta M_{\gamma x'} \end{Bmatrix} = \begin{bmatrix} K_{x'} & 0 & 0 \\ 0 & K_{y'} & 0 \\ 0 & 0 & K_{z'} \end{bmatrix} \begin{Bmatrix} \delta\gamma_{x'} \\ \delta\gamma_{y'} \\ \delta\gamma_{z'} \end{Bmatrix} \tag{2.51}$$

where $K_{x'}$, $K_{y'}$, and $K_{z'}$ are the tangent stiffness of the rotational springs defined along x', y', and z' axes respectively.

2.5.3 **Implementation**

The Joint3D uses the same modeling concepts used in the two dimensional model. Joint3D has six external nodes and one central node. The central node has 3 extra degrees of freedom (9 DOF total) to represent the joint shear deformations. External nodes are connected to the central node by special MP_Joint3D multipoint constraints, allowing large deformation capability. Three rotational springs provide shear resistance for the

shear modes. The springs are introduced along the main chords and their moment is effective on the principal plane they are normal to.

The central node is introduced in the same manner as the two dimensional element. The location of the central node is determined based on the midpoint of main chords and an error check procedure guarantees the mid point of all main chords are coincident.

The constraint equations are defined to relate the external nodal displacements to the central node. The MP_Joint3D is the multipoint constraint object developed for this purpose, and six sets of multi point constraint objects provide the constraint equations. Joint3D has 45 degrees of freedom, but 36 of these are constrained to the central node, resulting in 9 free degrees of freedom.

Implementing the multi-point constraints: The implementation of multipoint constraints for the 3D case is different than two dimensional case since two nodes are required to define the direction of principal planes passing through the retained node, Figure 2-33. The central node is the retained node, and the external node is the constrained node. As mentioned in the formulation section, two out of three principal planes pass through each external node. Shear deformation in one of these planes, γ_{disp}, causes displacement (i.e. the translation of the constrained node is only related to γ_{disp}), and the shear deformation in the second plane, γ_{rot}, causes rotation (i.e. rotations of the constrained node are only related to γ_{rot}). The normal vectors of these planes are parallel to the local coordinate system and they are defined by a normalized vector connecting the central node to a specified external node. The information for creating the multipoint constraint (i.e. the local axes used for rotating or translating the external nodes) is summarized in Table 2-2.

Based on the constraint formulation, all the translational and rotational degrees of freedom of the external nodes are constrained to eight degrees of freedom of the retained (central) node (i.e. for each external node, one of the rotational degrees of freedom of the central node is excluded as a retained degree of freedom). The constrained and retained degrees of freedom for the Joint3D multi-point constraint are summarized as:

$$constrainedDOF = \begin{Bmatrix} u_{ext} \\ v_{ext} \\ w_{ext} \\ \alpha_{ext} \\ \beta_{ext} \\ \gamma_{ext} \end{Bmatrix} \tag{2.52}$$

$$retainedDOF = \begin{Bmatrix} u_{cen} \\ v_{cen} \\ w_{cen} \\ \alpha_{cen} \\ \beta_{cen} \\ \chi_{cen} \\ \gamma_{rot} \\ \gamma_{disp} \end{Bmatrix} \tag{2.53}$$

Table 2-2: Rotation vectors for Joint3D nodal displacement and rotation

Node	Rotation Node	Rotation Angle	Displacement Node	Displacement Angle
1	6 (local z' axis)	$\gamma_{z'}$	4 (local y' axis)	$\gamma_{y'}$
2	6 (local z' axis)	$\gamma_{z'}$	4 (local y' axis)	$\gamma_{y'}$
3	2 (local x' axis)	$\gamma_{x'}$	6 (local z' axis)	$\gamma_{z'}$
4	2 (local x' axis)	$\gamma_{x'}$	6 (local z' axis)	$\gamma_{z'}$
5	4 (local y' axis)	$\gamma_{y'}$	2 (local x' axis)	$\gamma_{x'}$
6	4 (local y' axis)	$\gamma_{y'}$	2 (local x' axis)	$\gamma_{x'}$

MP_joint3D is constructed automatically by Joint3D element, based on the tags specified by Joint3D element for: (1) the constrained and retained nodes, (2) a node that signifies

the direction for γ_{rot} and the central node degree of freedom for γ_{rot} , (3) a node and degree of freedom for γ_{disp} , and (4) a indicator for large deformation formulation.

The constrained and retained degrees of freedom are formed by two vectors and they are returned to the main analysis algorithm along with the constraint matrix. Depending on the large deformation condition, the constraint matrix is either selected to be constant or time varying (see section 2.6 for more details on the time varying constraint). The constraint matrix formulation is defined and calculated as:

$$\delta \underline{U}_C = \underline{\underline{C}} \times \delta U_R \tag{2.54}$$

$$\begin{Bmatrix} \delta u_{con} \\ \delta v_{con} \\ \delta w_{con} \\ \delta \alpha_{con} \\ \delta \beta_{con} \\ \delta \chi_{con} \end{Bmatrix} = \begin{bmatrix} 1 & 0 & 0 & 0 & \Delta_z & -\Delta_y & 0 & \Delta_z \cdot \eta_y^{disp} - \Delta_y \cdot \eta_z^{disp} \\ 0 & 1 & 0 & -\Delta_z & 0 & \Delta_x & 0 & \Delta_x \cdot \eta_z^{disp} - \Delta_z \cdot \eta_x^{disp} \\ 0 & 0 & 1 & \Delta_y & -\Delta_x & 0 & 0 & \Delta_y \cdot \eta_x^{disp} - \Delta_x \cdot \eta_y^{disp} \\ 0 & 0 & 0 & 1 & 0 & 0 & \eta_x^{rot} & 0 \\ 0 & 0 & 0 & 0 & 1 & 0 & \eta_y^{rot} & 0 \\ 0 & 0 & 0 & 0 & 0 & 1 & \eta_z^{rot} & 0 \end{bmatrix} \times \begin{Bmatrix} u_{cen} \\ v_{cen} \\ w_{cen} \\ \alpha_{cen} \\ \beta_{cen} \\ \chi_{cen} \\ \gamma_{rot} \\ \gamma_{disp} \end{Bmatrix} \tag{2.55}$$

The approach for handling large or small deformation is the same as the 2D model. The small deformation formulation uses the constraint matrix calculated at the initial step, while the large deformation formulation updates the constraint matrix at each committed step based on the current nodal configuration. The user chooses between these methods through a flag for large deformations and length correction.

Constructing the Joint3D: The constructor of the Joint3D element is quite similar to the 2D element. The Joint3D adds the central node and multipoint constraints to the domain, where the element is generated. The following user-defined arguments are imported at the constructor level of the Joint3D element:

- A unique element tag for the joint element
- The tags of six external nodes

- An unused tag for the central node
- Three uniaxial material models for the shear block deformations
- A pointer to the domain
- The tag for the large deformation condition

The command line for creating the Joint3D elements in OpenSees is presented in Appendix B.

2.5.4 **Validation cases for the 3D joint model**

A 3D beam-column subassembly was created with a single joint in the center, with are located along x and y axes and a column located along z axis. The bottom of the column is hinged and end of all four beams are rollers allowing displacements in *xy* plane. A displacement history was applied to the top of the column. The joint formulation was then checked for the following cases:

- The central point is always located at the middle point of every two front nodes.
- Every two front planes always remain parallel .
- Joint size remains constant.
- For the constant constraint matrix, the nodes locally move only on their corresponding normal plane.
- Penalty and transformation constraint handlers result in identical answers.
- The external reactions must satisfy the equilibrium equations of the system.
- Apply the displacement history to each separate shear mode and observe the interaction between modes. For rollers at each beam end, the x-x and y-y displacements do not interact with each other and they only load y’ and x’ shear modes.
- Equilibrium of force transfer between shear modes for various support conditions.

2.6 *Large deformation formulation for the multi-point constraints*

For small deformation models the configuration of the system is assumed to be constant and the constraint matrix is calculated based on the initial configuration. When deformations become larger, then constant constraint matrix, if not updated for every step, will lead to change in the multi point constraint length, and an incorrect path for constrained node. The error associated with the constant constraint matrix does not allow the element to capture the second order results for geometric nonlinearity, see Figure 2-35. Fortunately, this error is not cumulative for cyclic loading and, since the joint returns to its exact size whenever it is positioned in its original configuration.

A more accurate solution can be achieved by using a time varying constraint matrix. As shown in Figure 2-36, the time varying constraint matrix results in a more accurate path for the constrained node, but the length of the multi-point constraint will be constantly increasing. The increasing length error will be a cumulative error that may become excessive after several large cycles. The increasing length error can be eliminated by a length correction scheme, whereby the constrained node is displaced at the end of each load step to maintain the initial multi point constraint length. For the 2D joint, the length correction factors are calculated by (2.8) and (2.9) to be multiplied by the main chords to relocate the external nodes:

$$\underline{X}^{i}_{1or3} \leftarrow \frac{\left(x_1^0 - x_3^0\right)^2 + \left(y_1^0 - y_3^0\right)^2}{\left(x_1^0 - x_3^0 + u_1^i - u_3^i\right)^2 + \left(y_1^0 - y_3^0 + v_1^i - v_3^i\right)^2} \times \left(\underline{X}^{i}_{1or3} - \underline{X}^{i}_{c}\right) + \underline{X}^{i}_{c} \qquad (2.56)$$

$$\underline{X}^{i}_{2or4} \leftarrow \frac{\left(x_2^0 - x_4^0\right)^2 + \left(y_2^0 - y_4^0\right)^2}{\left(x_2^0 - x_4^0 + u_2^i - u_4^i\right)^2 + \left(y_2^0 - y_4^0 + v_2^i - v_4^i\right)^2} \times \left(\underline{X}^{i}_{2or4} - \underline{X}^{i}_{c}\right) + \underline{X}^{i}_{c} \qquad (2.57)$$

The OpenSees implementation permits the user to choose any one of three constraint schemes- (a) constant, (b) time varying without the length correction, and (c) time varying with length correction.

2.7 *Numerical methods for handling multipoint constraints*

The analysis object applies the piecewise linear constraint formulation to the system of equations by constraint handler classes. The details of the large deformation formulation, how the constraints are handled, and the global formulation of the joint element will be discussed later in this section.

The transformation or penalty constraint formulations provide two alternative approaches for applying the multi-point constraints to the analysis model. Since the joint element formulation highly depends on multipoint constraints, the constraint handling method determines how the joint element influences the solution. The advantages and disadvantages of using each of these methods depend on the nature of the problem, modeling details, and solution algorithms. There is no general rule for choosing one of these methods, and it is left to the user to determine which may fit the problem better. However, some guidelines based on testing of the joint is provided later in section 2.8

2.7.1 **The transformation handler**

The transformation constraint formulation replaces the constrained degrees of freedom by the transformed retained degrees of freedom, hence it reduces the size of system of equations. It also modifies the stiffness matrix and the load vector of all elements that are connected to the constrained node. The transformation method is quite efficient, particularly for the linear problems, but in the OpenSees implementation, it has some limitations for complicated models with multiple constraint equations and time varying incremental problems. One of the major limitations of the OpenSees transformation implementation is that it does not permit “chained” multiple constraints where one retained node is constrained to third node. This limitation is observed for cases such as when the joint elements and rigid-body diaphragms apply kinematic constraints to a common node.

The transformation formulation for handling a multipoint constraint is discussed here. Consider a simple case that two nodes are constrained by a multipoint constraint, with an elastic element that connects the constrained node to a third unconstrained (free) node

(Figure 2-34). The displacement field for the retained node, constrained node, and the unconstrained (free) nodes are defines as:

$$\underline{\Delta}_{ret} = \begin{Bmatrix} \underline{u}^{R}_{ret} \\ \underline{u}^{F}_{ret} \end{Bmatrix} \tag{2.58}$$

$$\underline{\Delta}_{con} = \begin{Bmatrix} \underline{u}^{C}_{con} \\ \underline{u}^{F}_{con} \end{Bmatrix} \tag{2.59}$$

$$\underline{\Delta}_{free} = \begin{Bmatrix} \underline{u}^{F}_{free} \end{Bmatrix} \tag{2.60}$$

In which the subscripts refer to the node name and the superscript of R, C, and F refer to retained, constrained and free degrees of freedom. The constraint relationship is defined as:

$$\underline{u}^{C}_{con} = \underline{\underline{C}} \times \underline{u}^{R}_{ret} \tag{2.61}$$

The nodal deformations for the element are defined by the constrained node and the free node as:

$$\underline{\Delta}_{elem} = \begin{Bmatrix} \underline{u}^{C}_{con} \\ \underline{u}^{F}_{con} \\ \underline{u}^{F}_{free} \end{Bmatrix} = \begin{bmatrix} \underline{\underline{C}} & 0 & 0 \\ 0 & \underline{\underline{I}} & 0 \\ 0 & 0 & \underline{\underline{I}} \end{bmatrix} \times \begin{Bmatrix} \underline{u}^{R}_{ret} \\ \underline{u}^{F}_{con} \\ \underline{u}^{F}_{free} \end{Bmatrix} = \underline{\underline{T}} \times \begin{Bmatrix} \underline{u}^{R}_{ret} \\ \underline{u}^{F}_{con} \\ \underline{u}^{F}_{free} \end{Bmatrix} = \underline{\underline{T}} \times \underline{\Delta}_{trns} \tag{2.62}$$

Note that the orders of $\underline{\Delta}_{elem}$ and $\underline{\Delta}_{trns}$ are not the same, and using (2.62) the transformed degrees of freedom $\underline{\Delta}_{trns}$ replace the element nodal deformations in the global system of equations.

The energy function of the element is defined as:

$$\Phi_{elem} = \frac{1}{2}\underline{\Delta}^{T}_{elem} \times \underline{\underline{K}} \times \underline{\Delta}_{elem} + \underline{\Delta}^{T}_{elem} \times \underline{F}_{elem} = \frac{1}{2}\underline{\Delta}^{T}_{trns} \times \underline{\underline{T}}^{T} \times \underline{\underline{K}} \times \underline{\underline{T}} \times \underline{\Delta}_{trns} + \underline{\Delta}^{T}_{trns} \times \underline{\underline{T}}^{T} \times \underline{F}_{elem} \tag{2.63}$$

To enforce the equilibrium, the energy function must be minimized with respect to deformations:

$$\frac{\partial \Phi_{elem}}{\partial u} = 0 \tag{2.64}$$

$$\underline{\underline{T}}^T \times \underline{\underline{K}} \times \underline{\underline{T}} \times \underline{\Delta}_{trns} + \underline{\underline{T}}^T \times \underline{F}_{elem} = 0 \tag{2.65}$$

So the system of equations must be solved for $\underline{\Delta}_{trns}$ and constrained degrees of freedom $\underline{u}^C_{con}$ are thereby removed from the solution.

The element stiffness matrix and nodal forces are calculated as:

$$\underline{\underline{K}}_{trns} = \underline{\underline{T}}^T \times \underline{\underline{K}} \times \underline{\underline{T}} \tag{2.66}$$

and

$$\underline{F}_{trns} = \underline{\underline{T}}^T \times \underline{F}_{elem} \tag{2.67}$$

In the transformation method, the constraint matrix must be multiplied by the stiffness matrix of connected elements at every single step, as part of the assembly of the global stiffness matrix.

2.7.2 **The penalty handler**

The penalty approach is a numerical method for enforcing the constraint equations on the system of equations. The penalty method minimizes the difference between the actual displacements of constraint degrees of freedom and the calculated values based on the constraint equations. This difference is expressed as a vector for each multipoint constraint, calculated as:

$$\underline{u}^C_{con} - \underline{\underline{C}} \times \underline{u}^R_{ret} = \underline{D} \tag{2.68}$$

Where $\underline{u}_{con}^{C}$ and $\underline{u}_{ret}^{R}$ are the actual deformations at the constrained and retained degrees of freedom, respectively. The physical representation of the penalty method is achieved by adding stiff springs between $\underline{u}_{con}^{C}$ and $\underline{\underline{C}} \times \underline{u}_{ret}^{R}$ vectors.

To formulate the penalty method, the difference vector $\underline{D}$ is added to the energy equation, using a penalty matrix. The penalty matrix is a diagonal matrix with very large values, or numerical infinity. In concept, it is possible to use a separate penalty value for each constrained degree of freedom, but typically a unique penalty value is used for the whole problem. So the constraint term in the energy equation will be:

$$\Phi_C = \frac{1}{2} \underline{D}^T \times \underline{\underline{PM}} \times D \tag{2.69}$$

where $\underline{\underline{PM}} = PV \cdot \underline{\underline{I}}$, and PV is the penalty value (the notations $\underline{\underline{M}}$ and $\underline{V}$ refer to matrices and vectors, respectively).

$$\Phi_C = \frac{1}{2}\left(\underline{u}_{con}^{C} - \underline{\underline{C}} \times \underline{u}_{ret}^{R}\right)^T \times \underline{\underline{PM}} \times \left(\underline{u}_{con}^{C} - \underline{\underline{C}} \times \underline{u}_{ret}^{R}\right) = \frac{PV}{2} \begin{Bmatrix} \underline{u}_{con}^{C} \\ \underline{u}_{ret}^{R} \end{Bmatrix}^T \begin{bmatrix} \underline{\underline{I}} & -\underline{\underline{C}} \\ -\underline{\underline{C}}^T & \underline{\underline{C}}^T \underline{\underline{C}} \end{bmatrix} \begin{Bmatrix} \underline{u}_{con}^{C} \\ \underline{u}_{ret}^{R} \end{Bmatrix} \tag{2.70}$$

To enforce the equilibrium, all terms of the energy function must be minimized with respect to deformations, so:

$$\frac{\partial \Phi_C}{\partial u} = PV \begin{bmatrix} \underline{\underline{I}} & -\underline{\underline{C}} \\ -\underline{\underline{C}}^T & \underline{\underline{C}}^T \underline{\underline{C}} \end{bmatrix} \begin{Bmatrix} \underline{u}_{con}^{C} \\ \underline{u}_{ret}^{R} \end{Bmatrix} = 0 \tag{2.71}$$

To summarize, in the penalty method the extra stiffness terms (2.71) are added to the system of equations along with the normal element stiffness matrices. This method does not have the limitation against “chained” constraints that the transformation method has. This is because it does not remove the constrained degrees of freedom and instead solves the full system of equations. Depending on the penalty value (PV), there will be some degree of flexibility in the constraints, which is not present in the transformation method.

2.8 *Accuracy, convergence stability and solution rate*

The force-deformation formulation of the joint elements is fairly straightforward and is comparable in many respects to a multi-directional zero-length spring. Both of the joint models do not perform any nonlinear equation solution within the element, Instead, they instead rely on the global solution algorithms. The main burden of the joint elements is related to the extra degrees of freedom and multi-point constraints. The number of additional degrees of freedom imposed to the system depends on the handling method that one chooses for multi-point constraints (i.e. penalty versus transformation).

The transformation method for handling the constraints reduces the size of the system of equations by removing the constrained degrees of freedom. For a 2D joint model, 16 degrees of freedom are reduced to 4, and for a 3D joint model 45 degrees of freedom are reduced to 9. This reduction in the size of the system of equation is quite significant. The multipoint constraints handled by transformation method are replaced by mathematical relations that make the constraints absolutely rigid. The transformation method is more accurate and efficient for linear problems. Since the accuracy of the joint element response depends directly on how accurately the multipoint constraints are handled, the joint element will be quite precise when it is used with transformation constraint handler. One possible source of inaccurate response will be due to large deformations. This problem is handled by updating the constraint matrix and length correction. The transformation constraint handler may not be efficient for some nonlinear problems, since the rigid constraints may cause large force imbalances that may lead to convergence problems.

The penalty constraint handler on the other hand does not reduce the size of the linear system of equation, so the size of the linear system of equation is larger. For small models, the size of the linear system of equation does not have a considerable influence the run time, while as the number of degree of freedom grows, the extra degrees of freedom in the linear system of equation may have a considerable influence. Switching to penalty constraint handler did not have a negative influence on the run time and accuracy for the validation problems (chapter 4) with limited degrees of freedom.

Choosing the penalty value is a delicate task, since the penalty value must not be small to make the right constraint flexible, and the penalty values must not be too large so as to exceed the computer precision and lead to an ill-conditioned stiffness matrix. As a rough estimate, the penalty value is suggested as the larger of either $1.0e12$ or $1.0e3$ times the largest value of the stiffness matrix (but not greater than the typical machine precision of $1.0e16$).

2.9 *Recording analysis outputs for joint elements*

An element recorder object monitors the state of an element during the analysis. The element recorder writes the element converged state at the end of each load step to a file or to a database. The response of joint elements can also be recorded using the element recorder. The valid inquiries to a Joint2D element when creating an element recorder are:

- The displacements of the central node will be recorded as a vector. The displacement of the central node can be used for calculating the rigid-body motion of the joint.
- The joint size returns the distance of the nodes on opposite sides of the joint. The joint size value can be used to monitor the constraints under large cyclic deformation. If the change in the joint size is larger than expected, the length correction algorithm can be used.
- The joint deformation as the spring rotation at external nodes and at the panel.
- The joint force as the spring moment at external nodes and at the panel.
- The plastic rotation of the springs. The Plastic rotation at external nodes and at the shear panel is calculated by subtracting the elastic component of the rotation. The elastic part of the rotation is calculated based on based on initial or unloading stiffness.
- The joint stiffness matrix

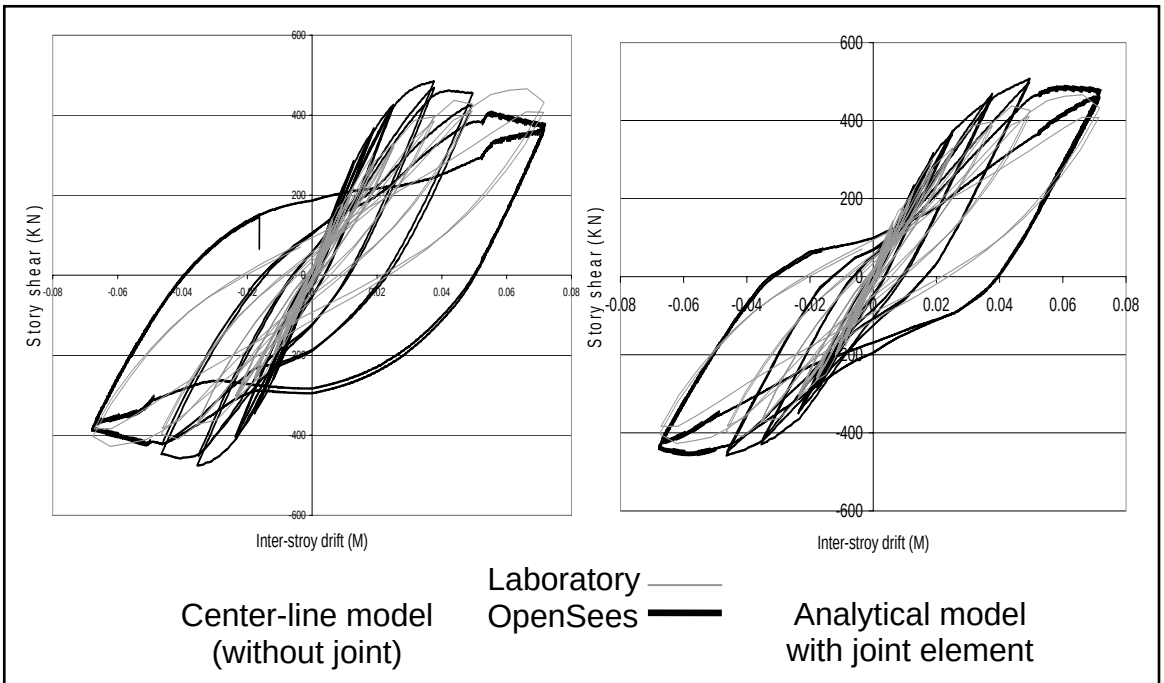

Figure 2-1: Influence of the joint on the analysis results (Tsai et al., 2000)

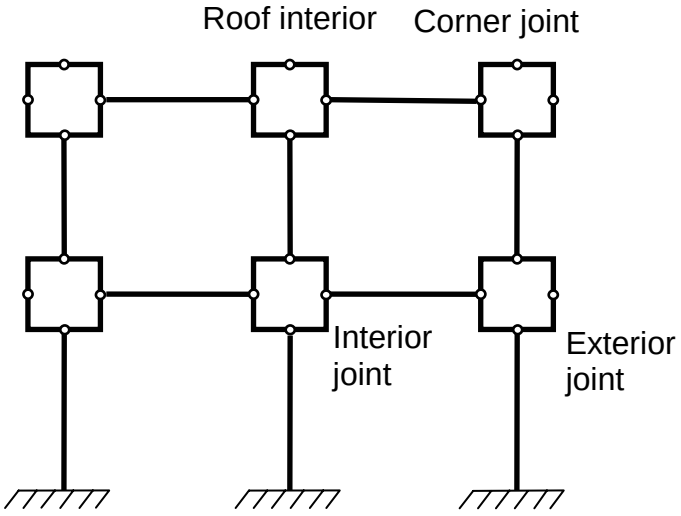

Figure 2-2: Joint types in a 2D RC frame model

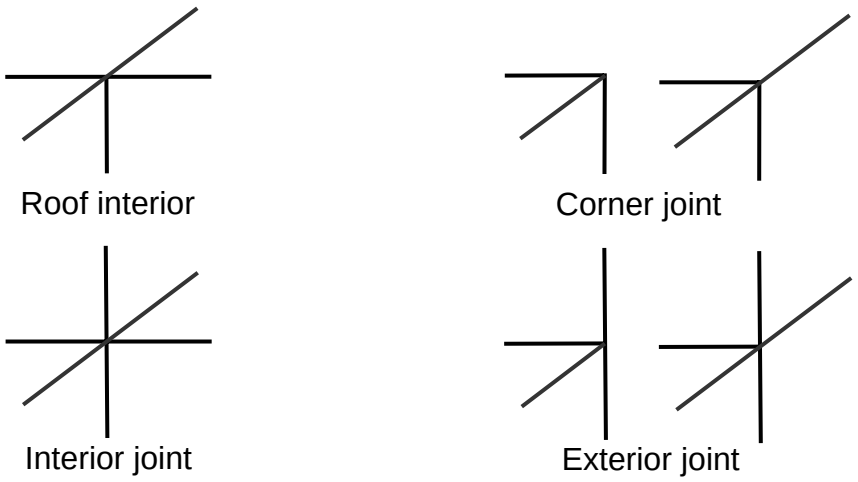

Figure 2-3: Joint types in a 3D RC frame model (ACI-352)

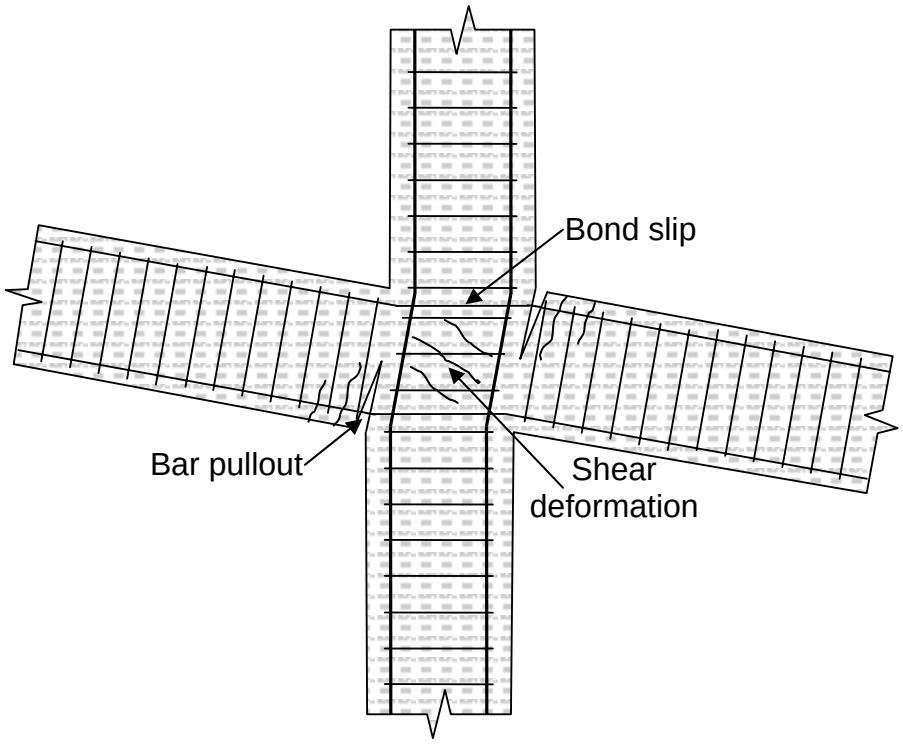

Figure 2-4: Deformed reinforced concrete joint

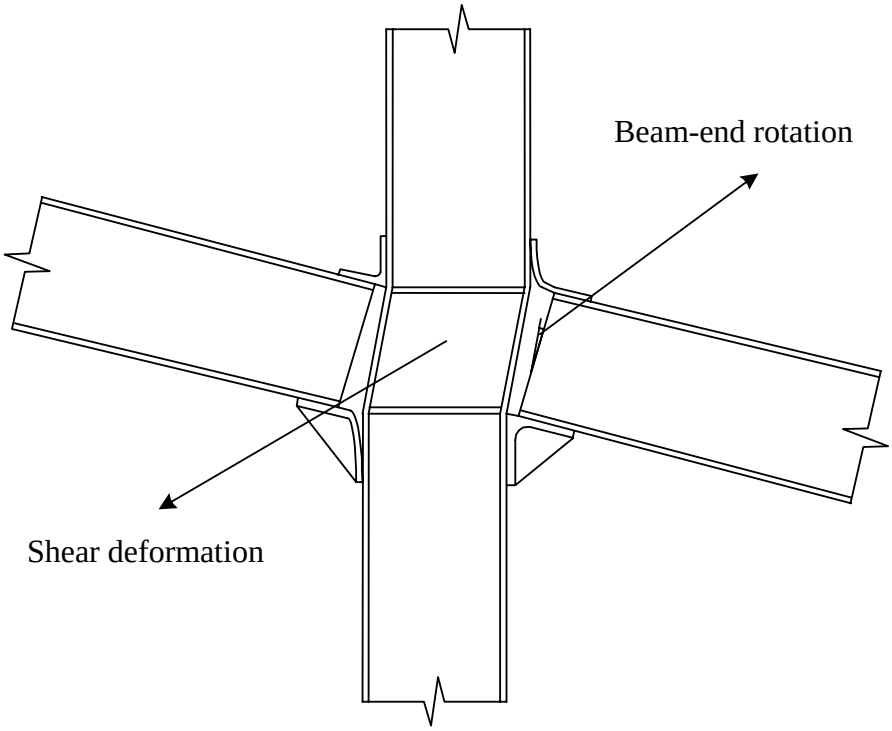

Figure 2-5: Deformed steel moment resisting joint

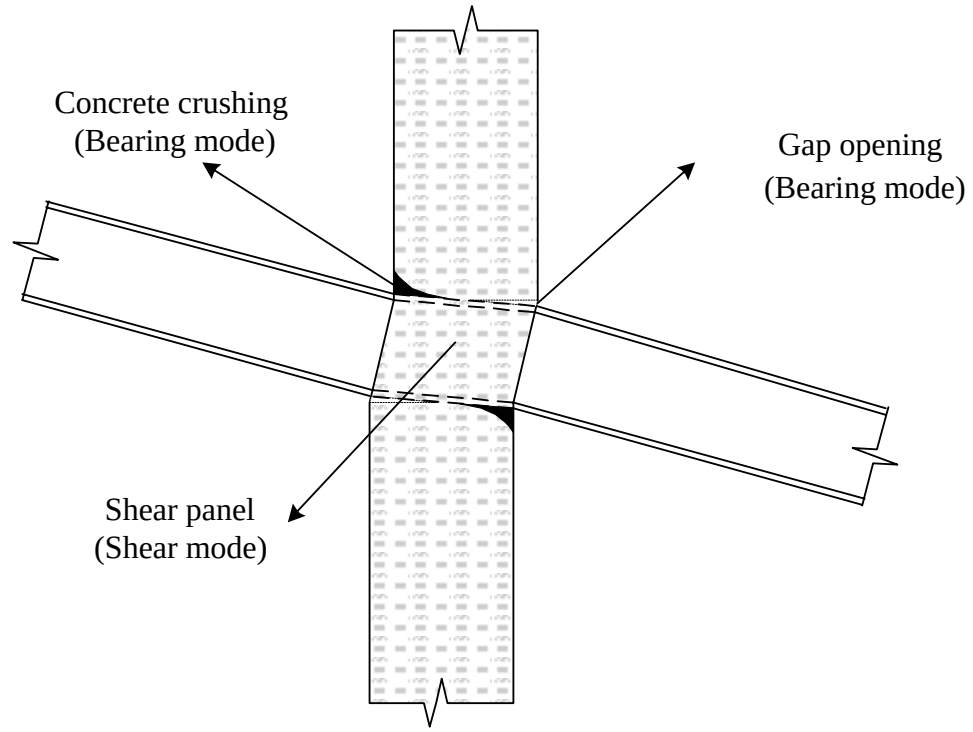

Figure 2-6: Deformed RCS joint

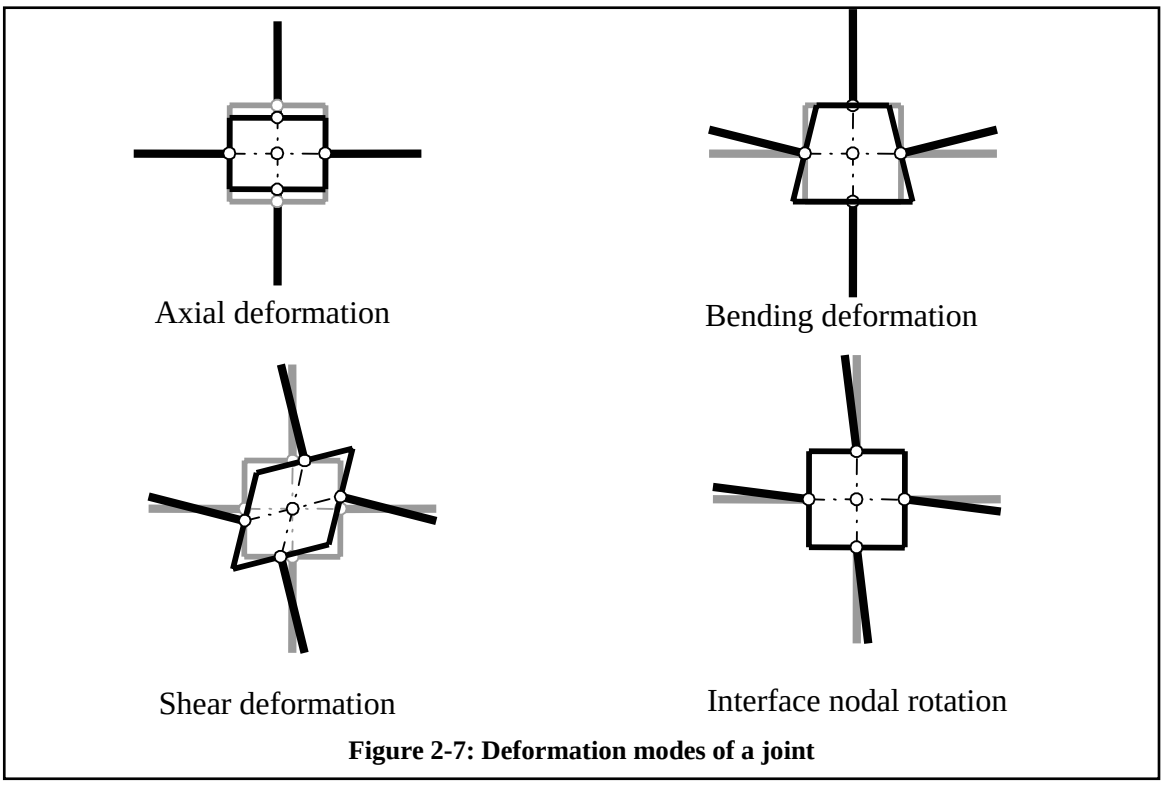

Figure 2-7: Deformation modes of a joint

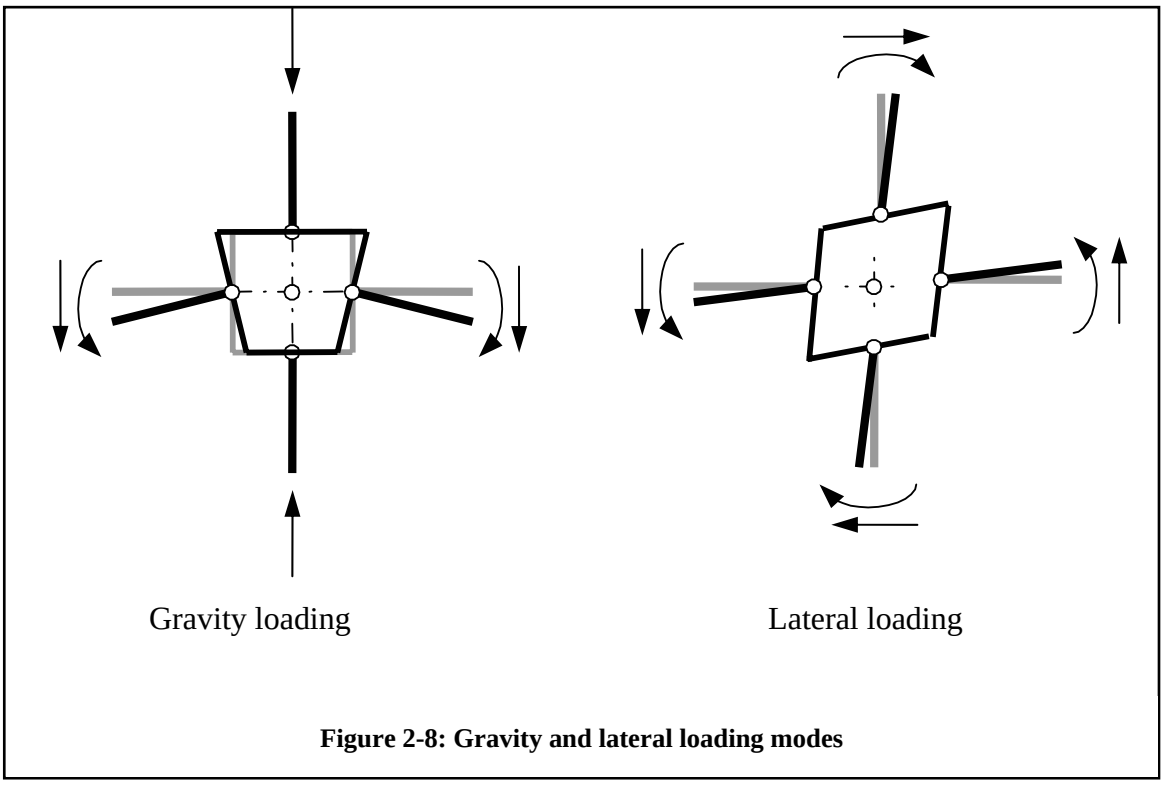

Figure 2-8: Gravity and lateral loading modes

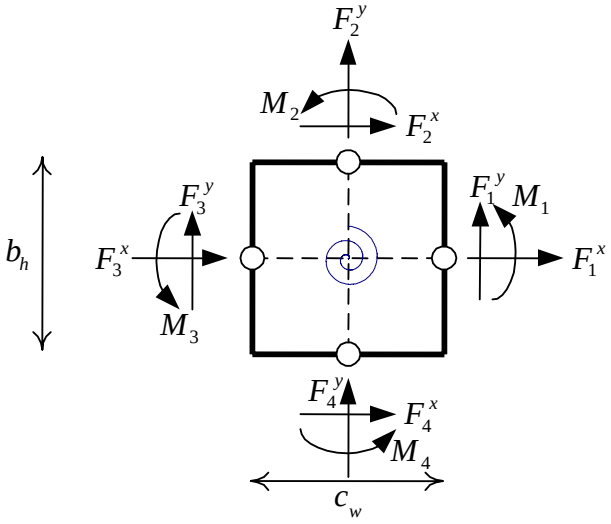

Figure 2-9: Free body diagram of the joint external forces (positive sign convention)

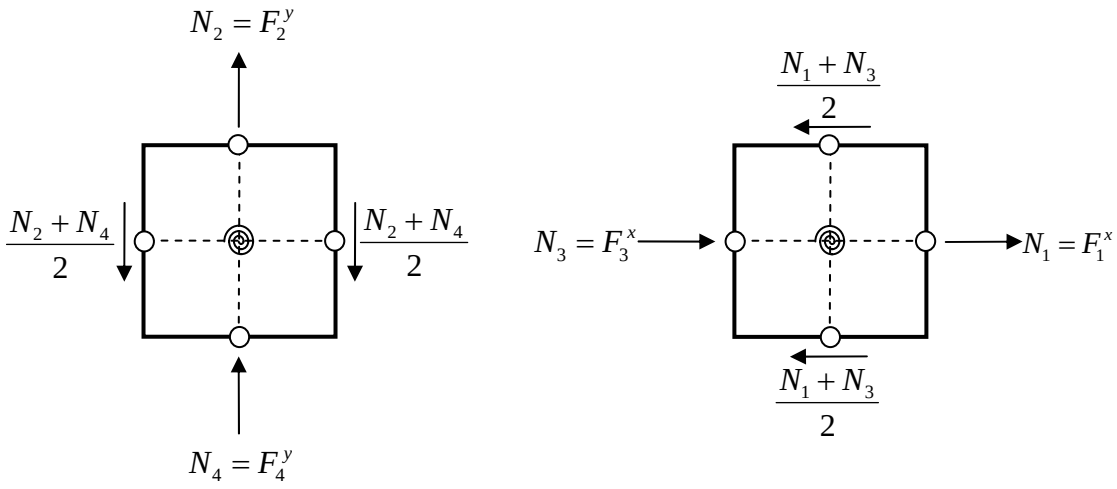

Figure 2-10: Joint load decomposition; the axial modes

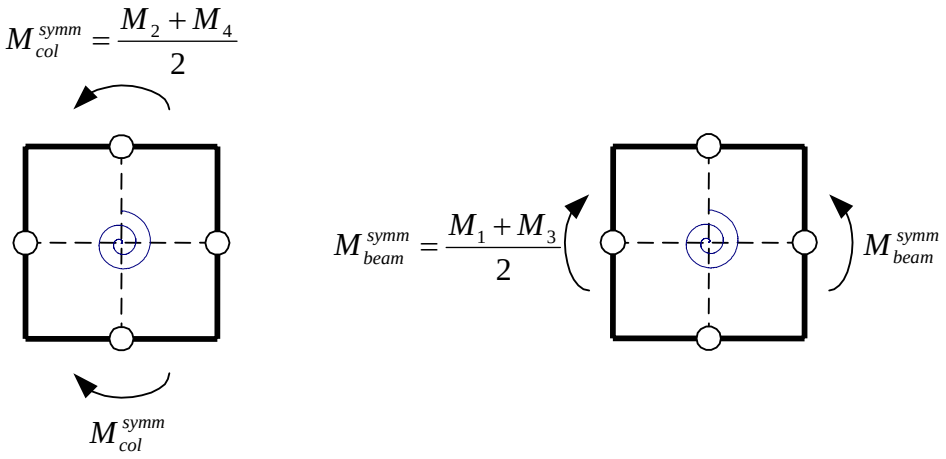

Figure 2-11: Joint load decomposition - symmetric bending modes

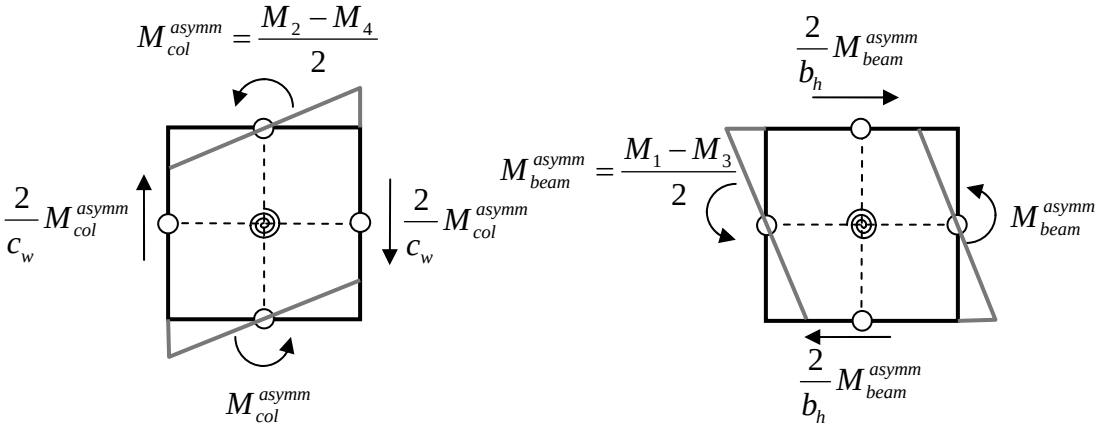

Figure 2-12: Joint load decomposition; anti-symmetric bending mode

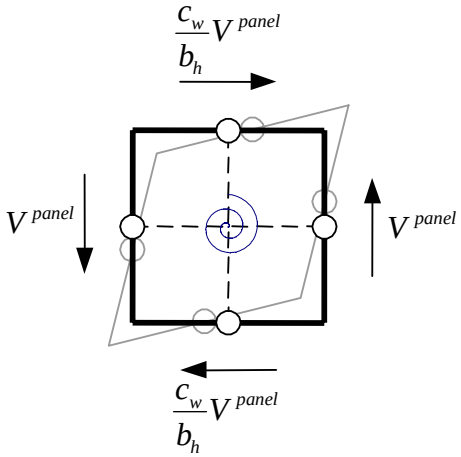

$$V^{panel} = F_1^y + \frac{F_2^y + F_4^y}{2} - \frac{M_2 - M_4}{c_w}$$

$$M_{shear}^{panel} = c_w \cdot \frac{2F_1^y + F_2^y + F_4^y}{2} - \left(M_2 - M_4\right)$$

Figure 2-13: Joint load decomposition; the pure shear mode and shear equivalent moment

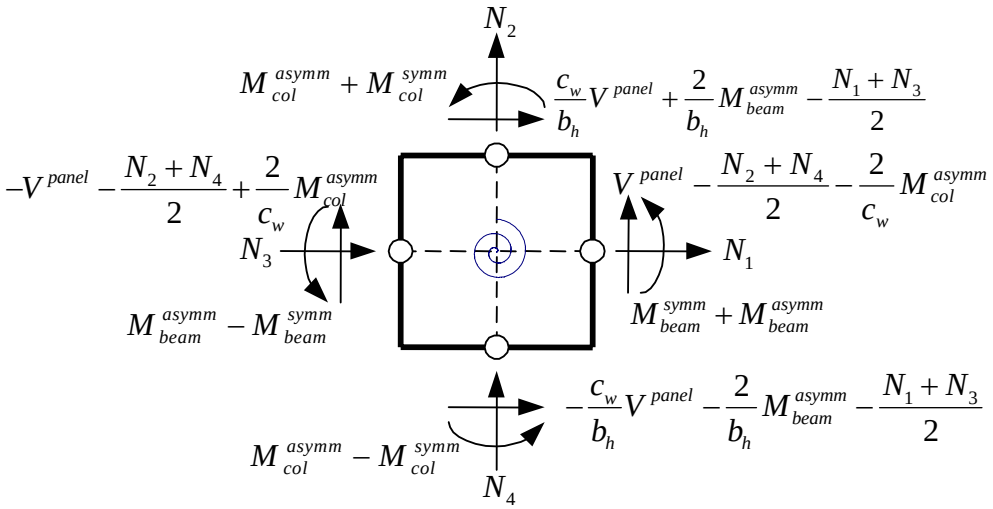

$$\sum F^x = F_1^x + F_2^x + F_3^x + F_4^x = 0$$

$$\sum F^y = F_1^y + F_2^y + F_3^y + F_4^y = 0$$

$$\sum M = M_1 + M_2 + M_3 + M_4 + \frac{c_w}{2}F_1^y - \frac{b_h}{2}F_2^x - \frac{c_w}{2}F_3^y + \frac{b_h}{2}F_4^x = 0$$

Figure 2-14: The joint equilibrium equations

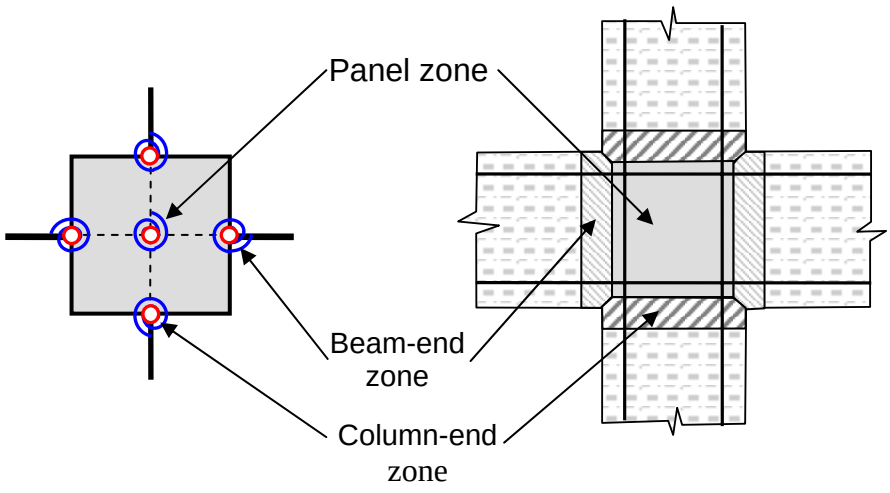

Figure 2-15: The joint zones represented by rotational springs

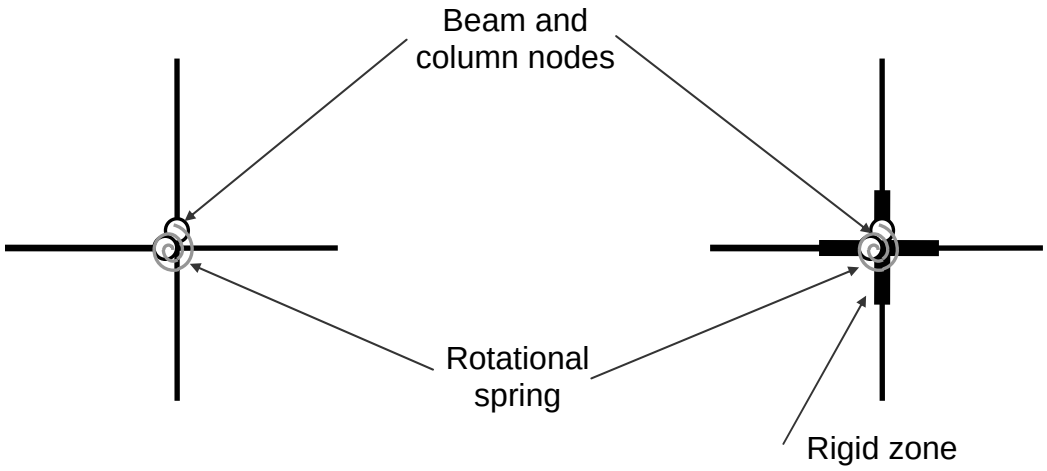

Figure 2-16: Previously proposed joint models

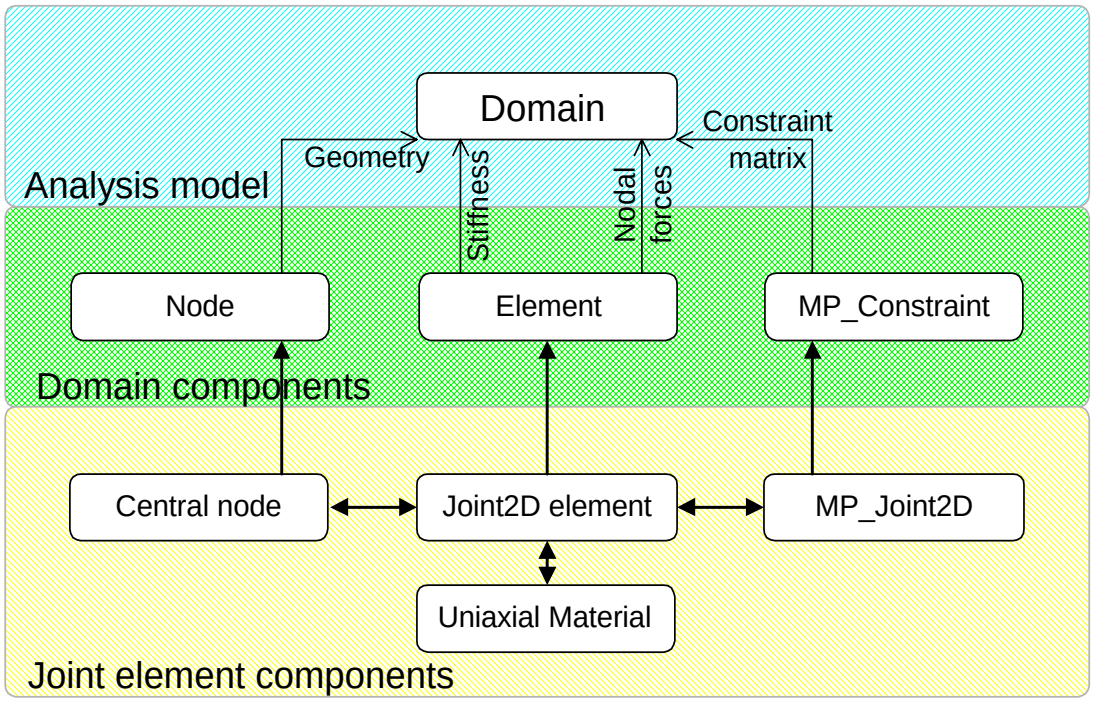

Figure 2-17: Joint element in OpenSees

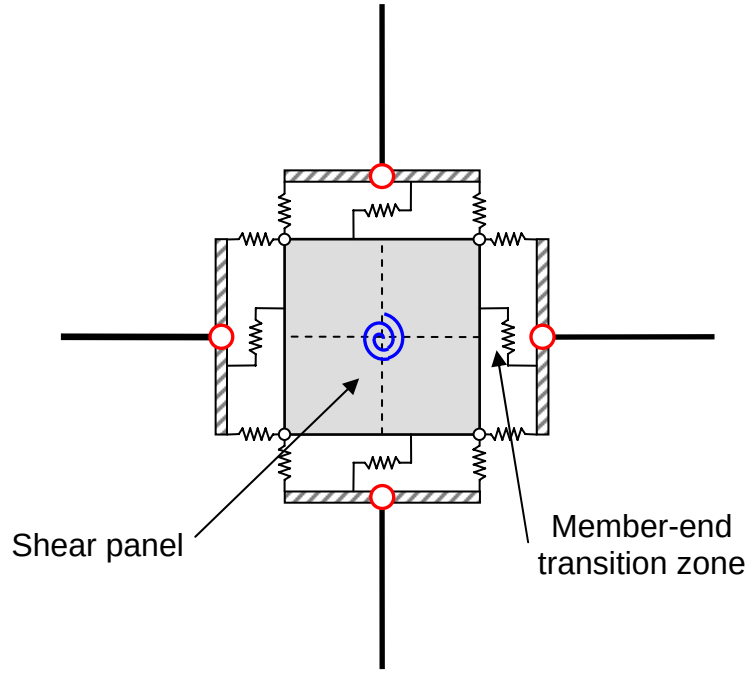

Figure 2-18: Joint model with transition elements (Lowes and Altoontash, 2003)

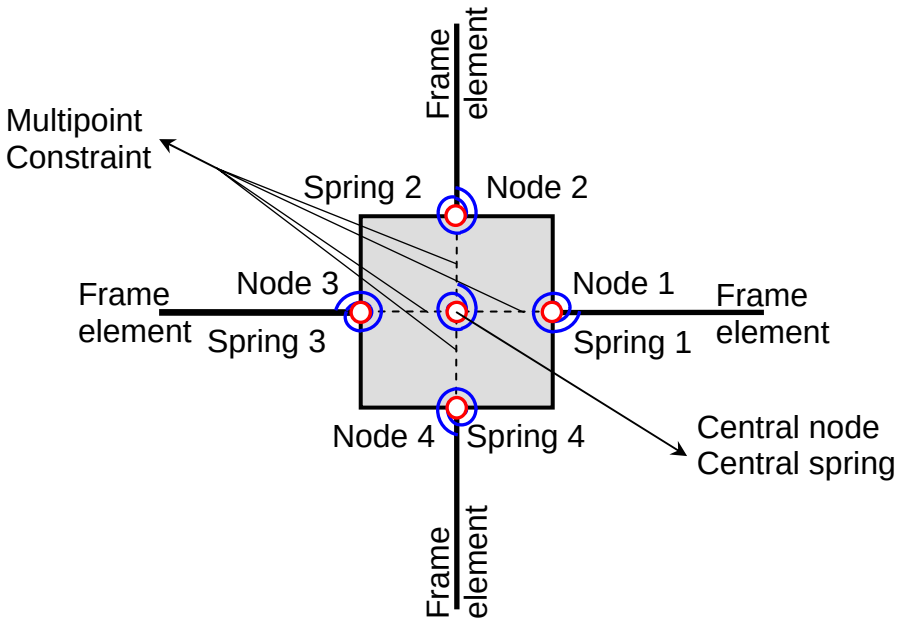

Figure 2-19: Graphic representation of the internal components of the Joint2D-5SPR element

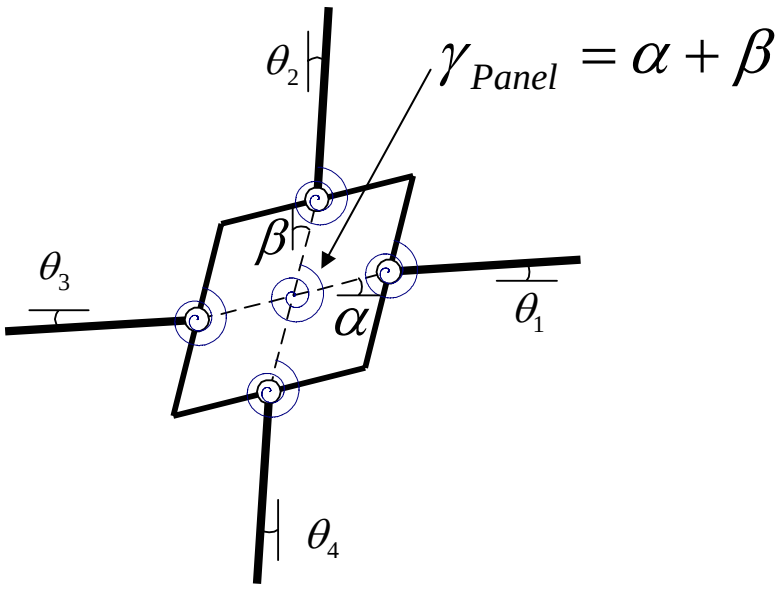

Figure 2-20: Joint2D-5SPR deformed shape with member-end rotations

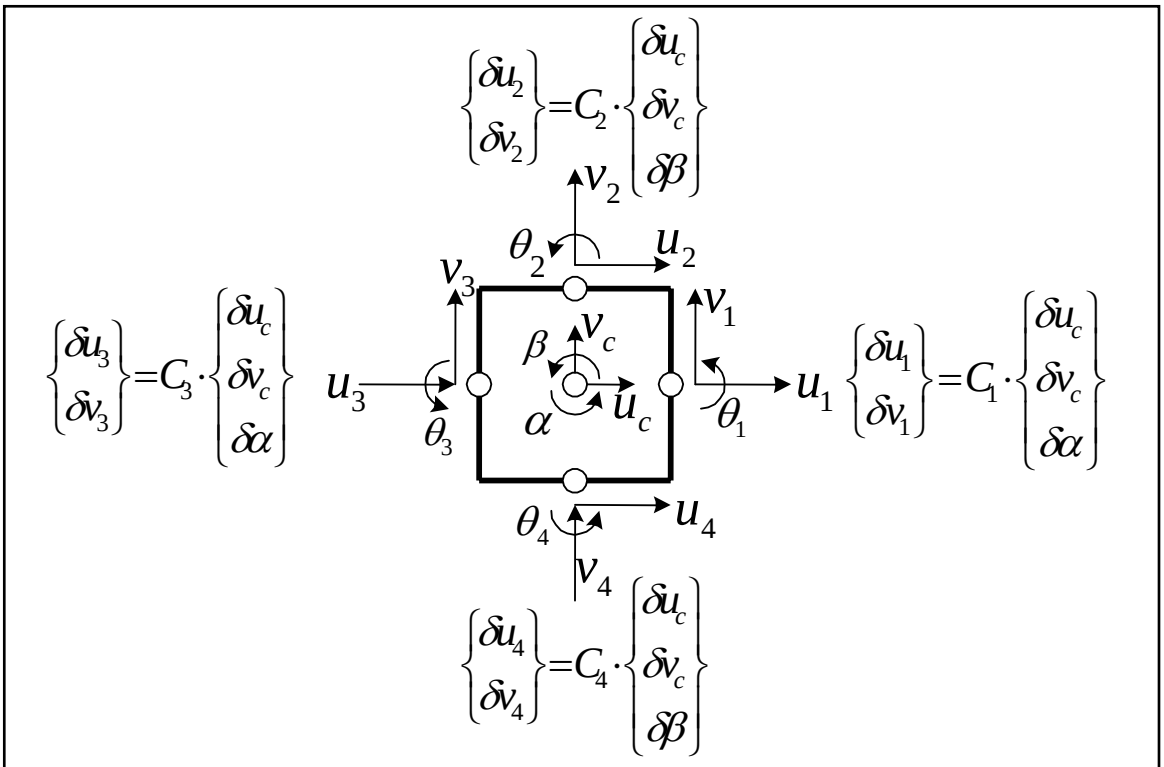

Figure 2-21: Constraint relations for the Joint2D-5SPR with rigid MERs

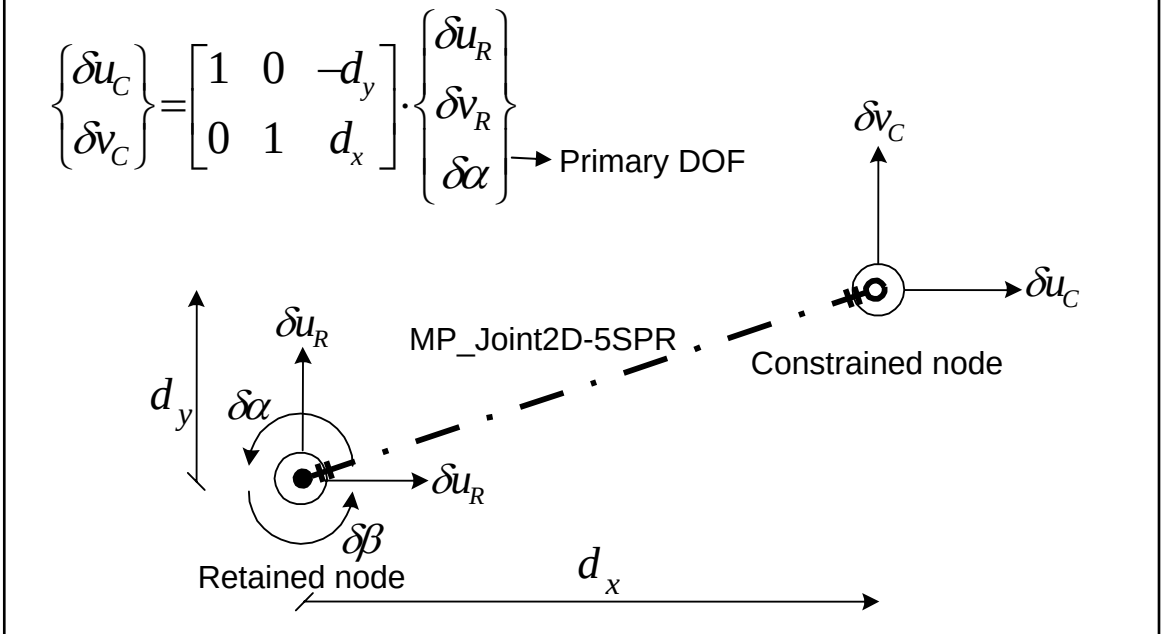

Figure 2-22: Joint2D-5SPR multipoint constraint with Member-End Rotation

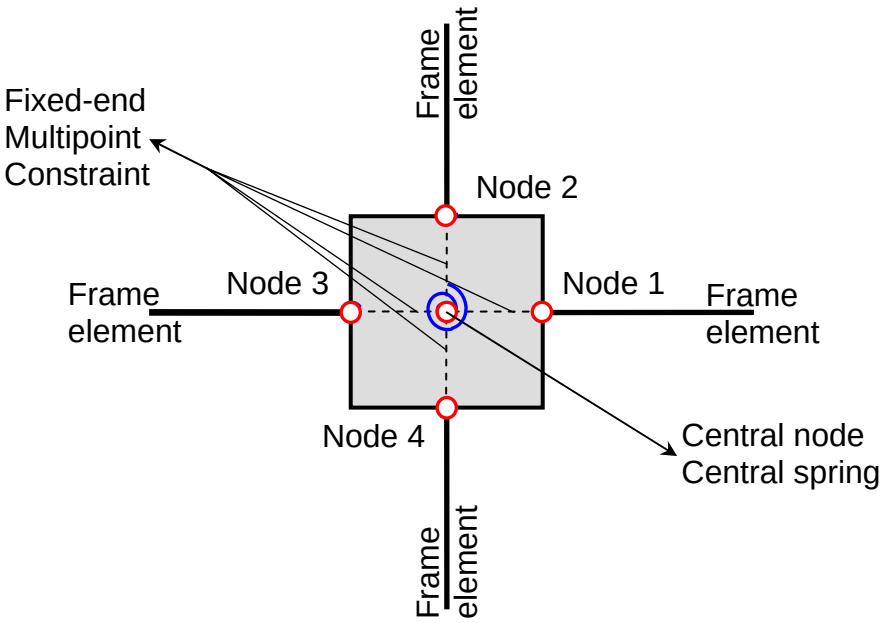

Figure 2-23: Internal components of the Joint2D-1SPR element

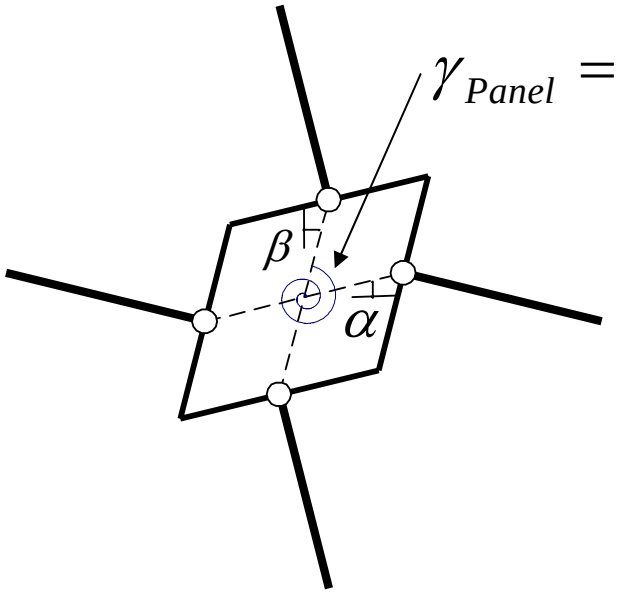

$$M_{shear}^{panel} = M\left(\gamma_{Panel}\right)$$

Figure 2-24: Joint2D-1SPR deformed shape, the shear panel moment-deformation

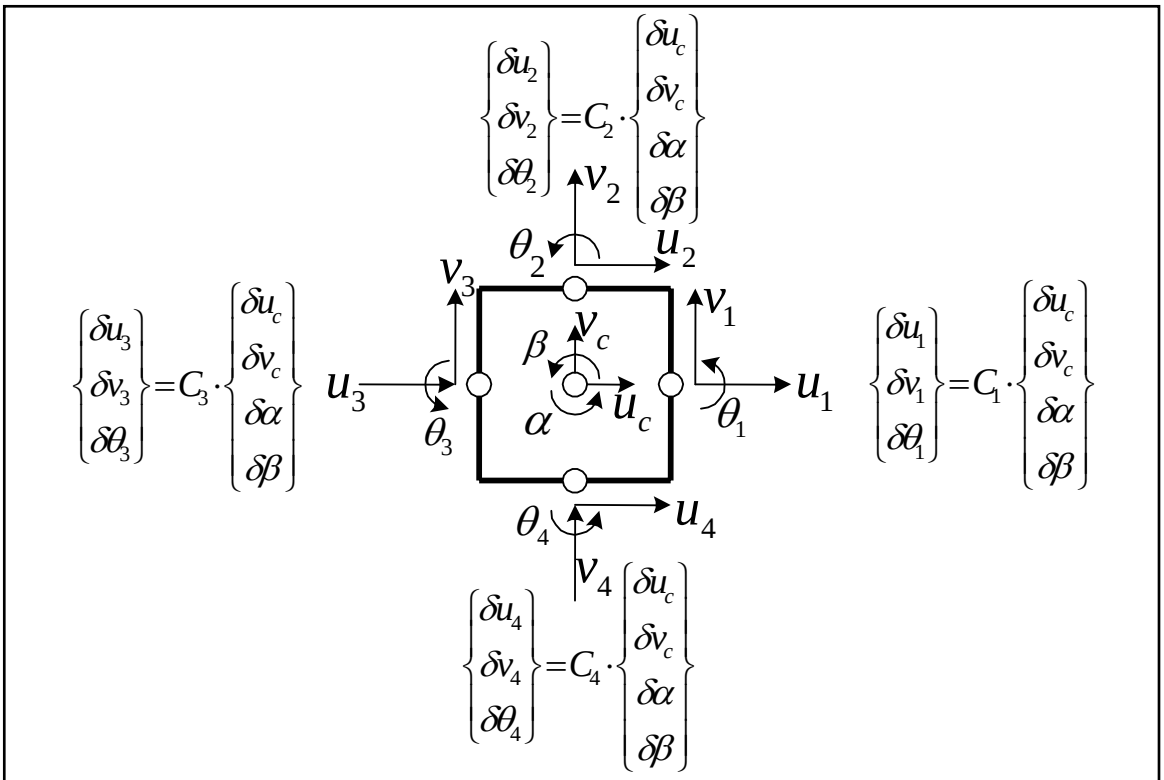

Figure 2-25: Constraint relations for the Joint2D-1SPR with rigid MERs

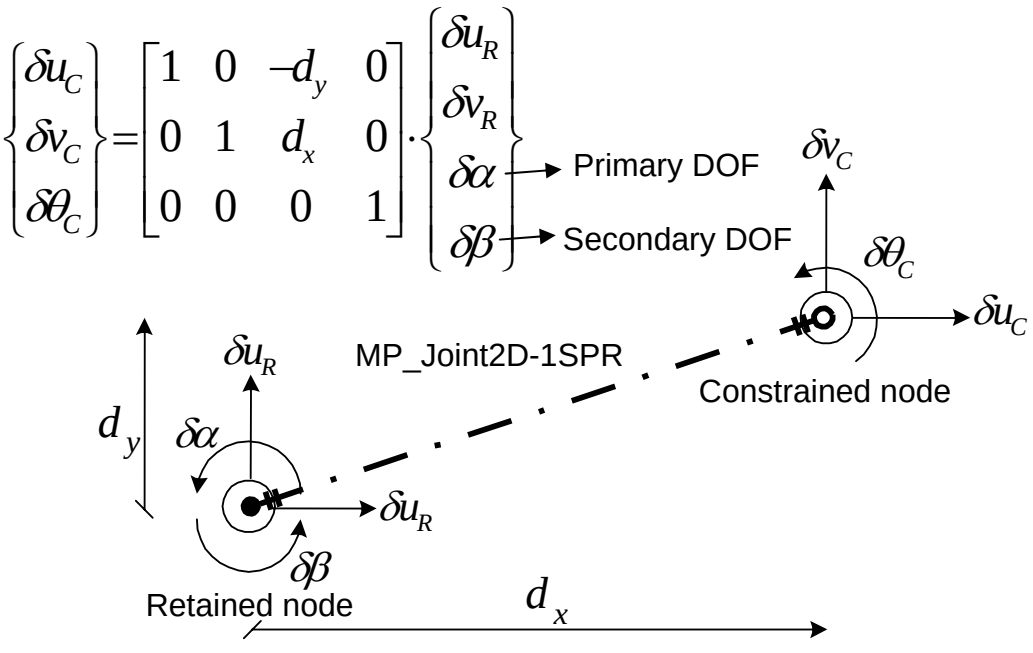

Figure 2-26: Joint2D-1SPR multipoint constraint with Member-End Rotation

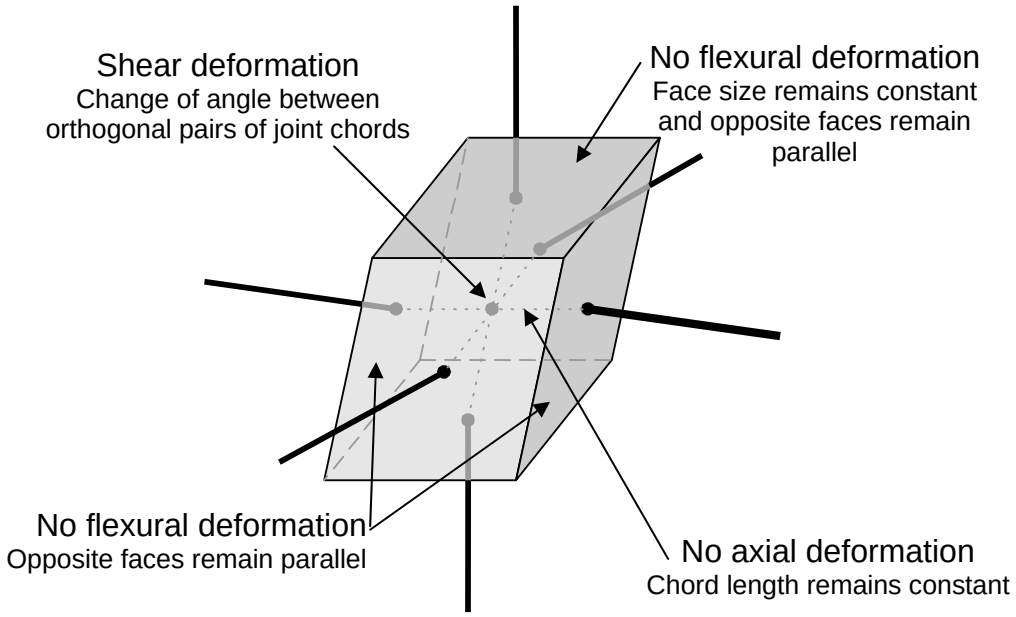

Figure 2-27: Joint3D deformed shape

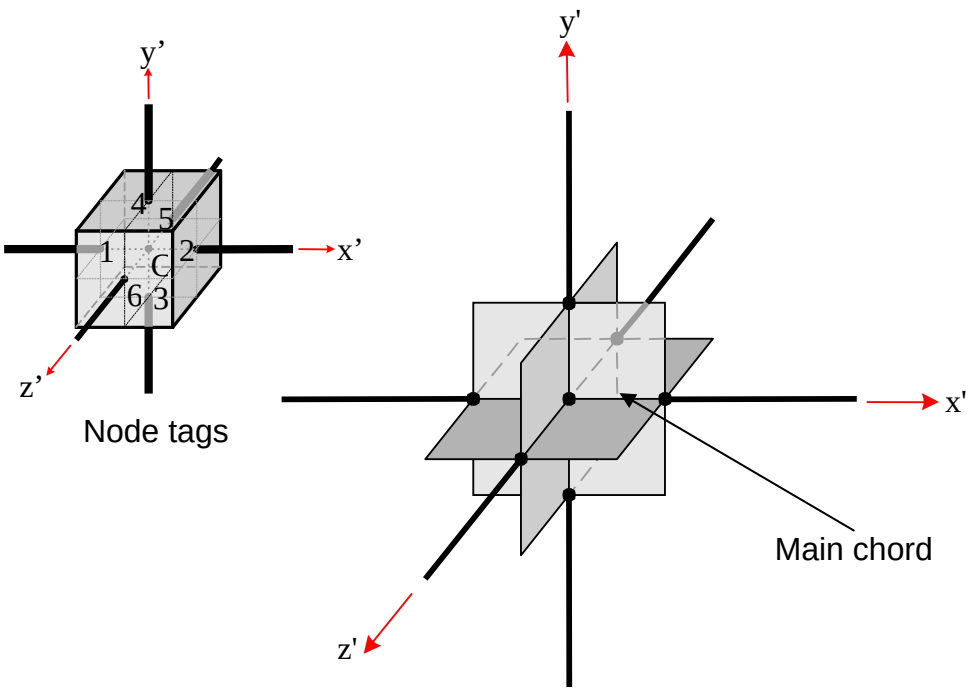

Figure 2-28: Shear block principal planes and local coordinate system

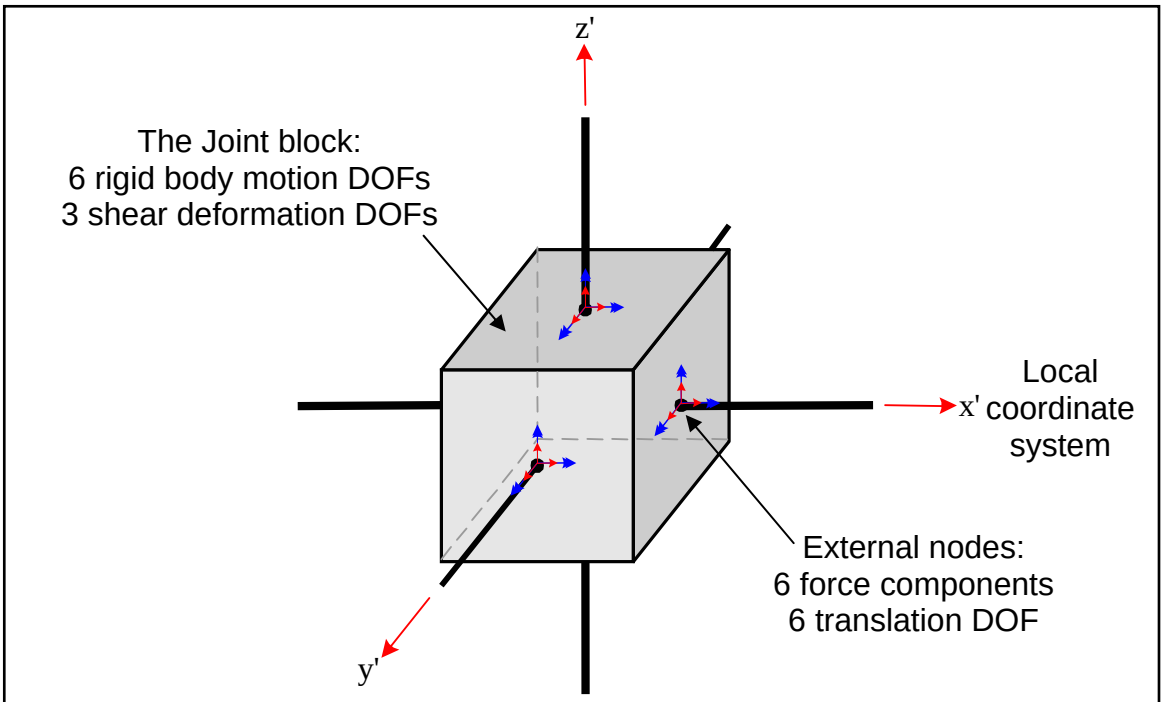

Figure 2-29: Joint3D nodal degrees of freedom/force components

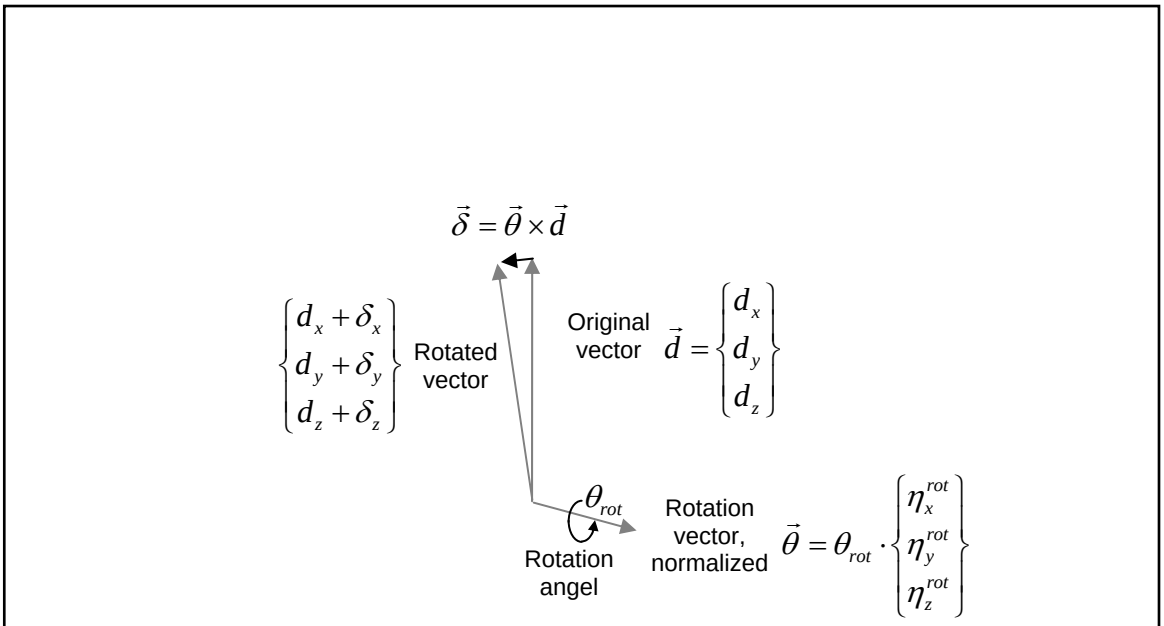

Figure 2-30: Vector rotation for infinitesimal rotations

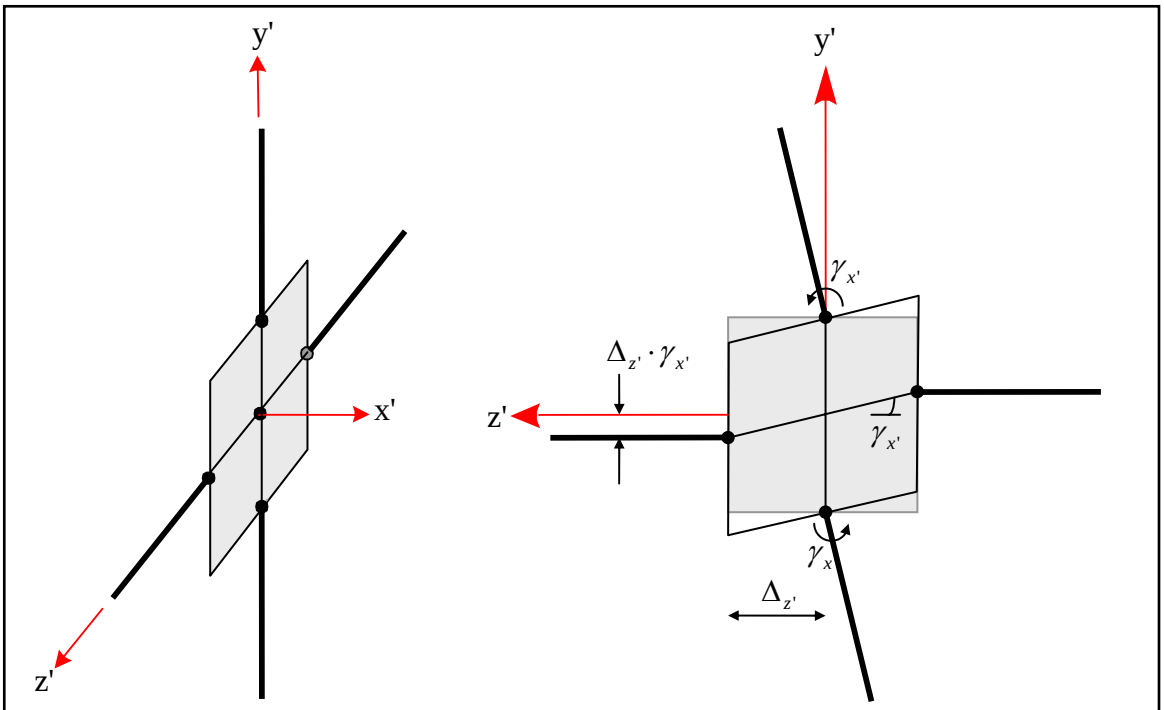

Figure 2-31: In plane deformation of a principal parallelogram

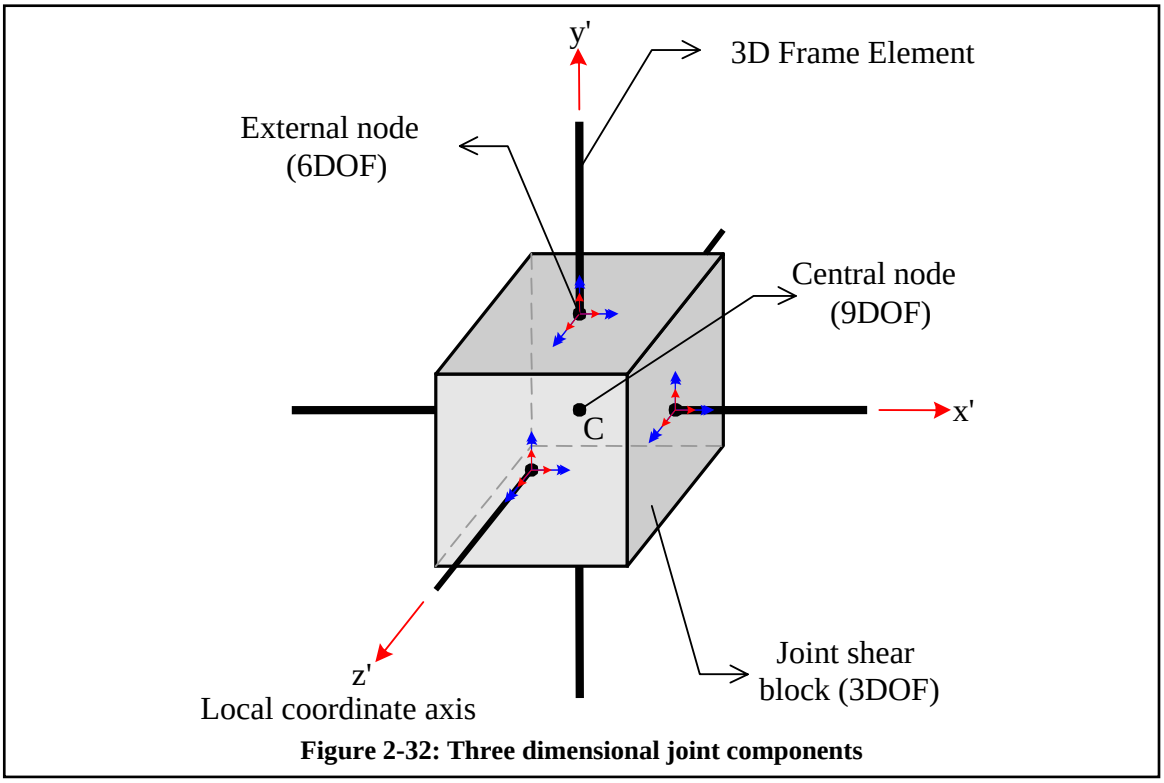

Figure 2-32: Three dimensional joint components

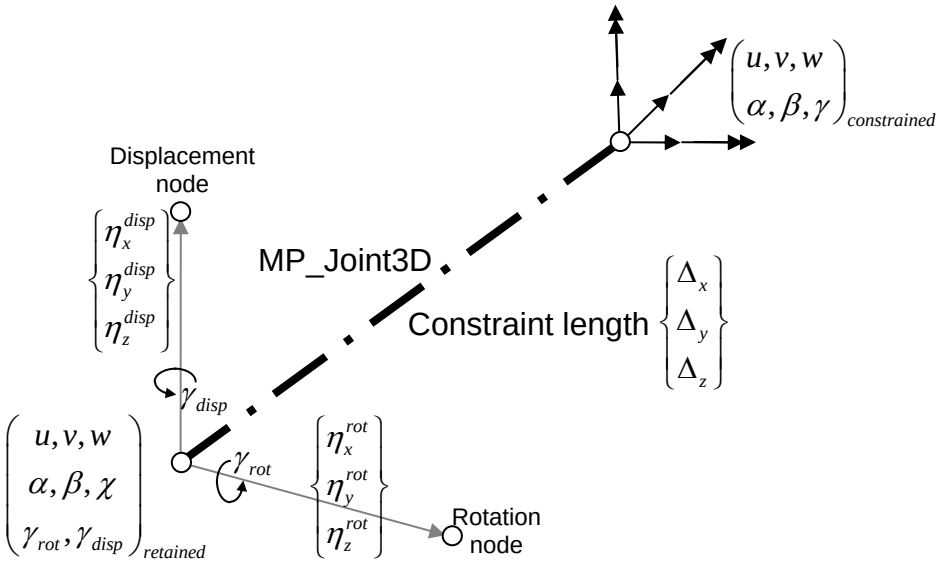

Figure 2-33: 3D multipoint constraint for the Joint3D element

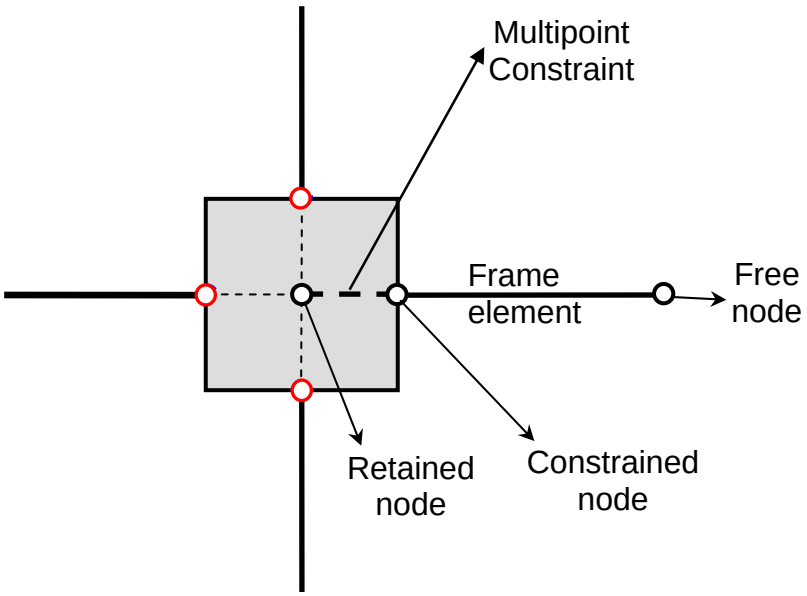

Figure 2-34: Retained, constrained and free nodes in transformation formulation

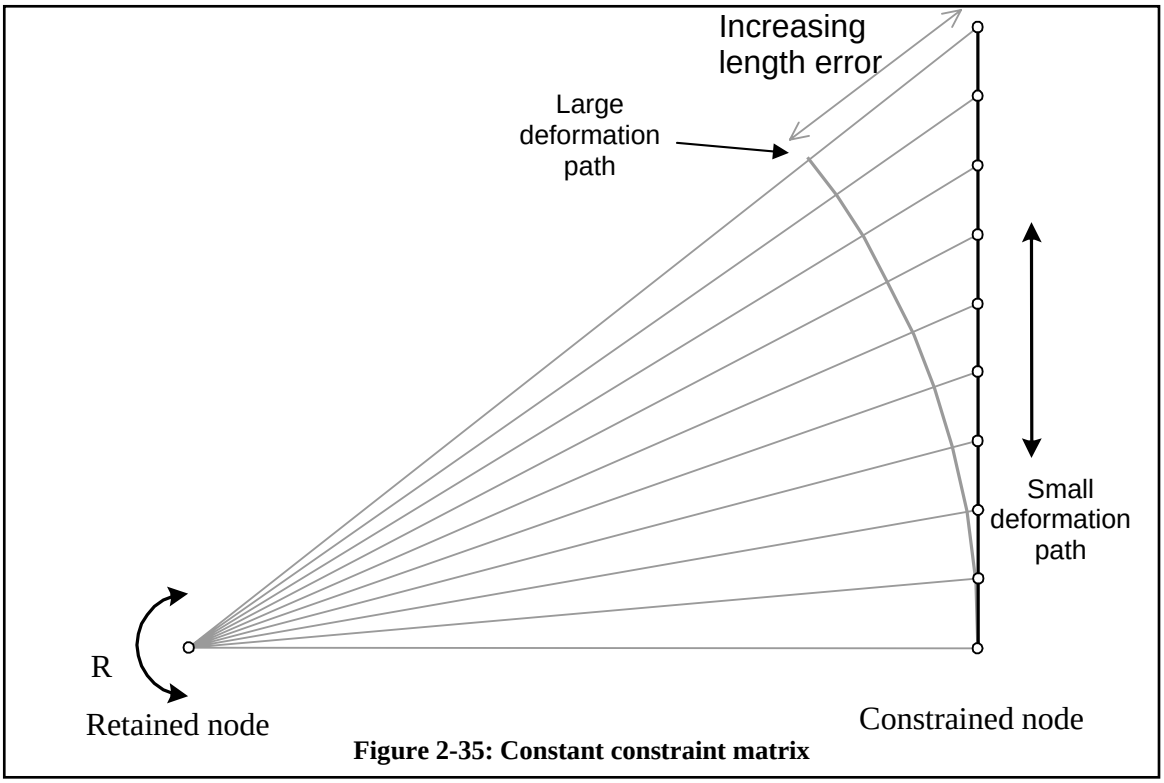

Figure 2-35: Constant constraint matrix

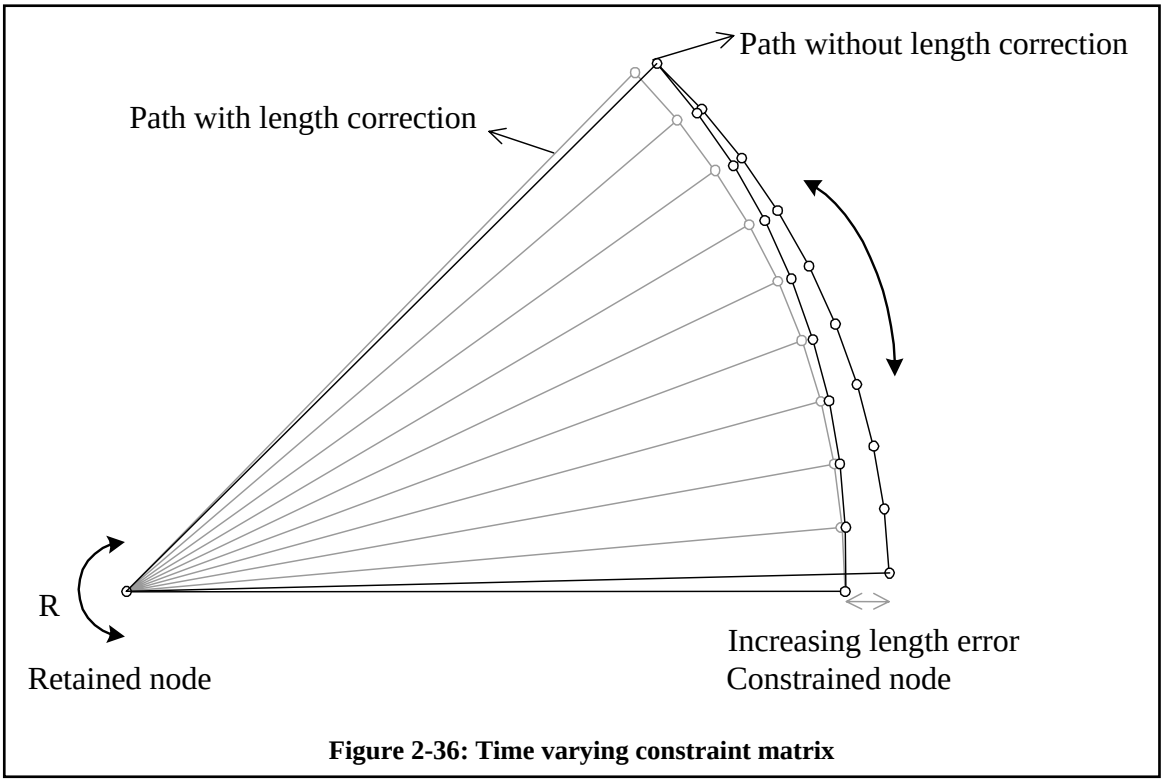

Figure 2-36: Time varying constraint matrix

3 Damage models and degrading hysteretic material models

One of the intermediate steps in the Performance Based Earthquake Engineering process involves calculation and assessment of *Damage Measures*. The *Damage Measures* are the qualitative state of the structural damage after an earthquake, which are calculated as a function of *Engineering Demand Parameters*. The decision variables (e.g. economic loss, down time, and repair time) are then determined based on the *Damage Measures*. According to the PBEE framework equation, there must be a solution to determine *DMs* analytically.

Damage evaluated through the structural analysis can be expressed on a global or component basis. Damage evaluation on a global basis is particularly appropriate for collapse assessment, whereas individual component damages are more appropriate for evaluating losses prior to collapse. The overall state of structural damage is typically calculated based on the global outputs of the analytical model, such as inter-story drift. Alternatively the global damage assessment can be aggregated based on the individual component damage. Some of the mostly used *Engineering Demand Parameters* to evaluate damage include the following:

- Parameters related to floor movement, such as floor displacement, velocity or acceleration. In modeling, these parameters are acquired as nodal displacement, velocity, or acceleration
- Inter-story drift (relative displacement between two floors).
- Parameters related to structural components, such as internal forces, or plastic deformations

The damage for individual elements is calculated based on element data such as element deformations, forces, or dissipated energy. These engineering parameters must be extracted from the solution and processed for calculating a *Damage Index*. A *Damage Model* is defined as an operator that calculates the *Damage Index* by applying a specific damage rule (e.g. Park-Ang damage model). The damage index can be recorded for

subsequent loss assessment and in some cases it may be used by the analysis components for degrading constitutive stiffness or strength parameters.

A state-of-art review by Williams et al. (1995) listed and categorized damage models for RC components as non-cumulative and cumulative damage models. The damage models rely on the force, displacement, energy or a combination of them. In this research a generic damage model is introduced into OpenSees, which casts the RC damage models in a standard form the OpenSees analysis program.

The generic damage model, or in OpenSees terms the *Damage Model class*, inputs the parameters in the form of an array and uses one of several available damage formulations to calculate the damage index (Figure 3-1). The standard input vector includes the displacement, force, unloading stiffness and plastic deformation. Elastic and dissipated energy are calculated by the damage formulation as a function of the standard input variables, while any other desired parameters can be appended to the input vector. The damage index is reported as a continuous scalar quantity; normalized to the unit scale where 0.0 corresponds to the undamaged case and 1.0 corresponds to total damage. The cumulative damage models store the history data necessary for the damage calculation.

The damage models are calibrated individually for each structural or non-structural component to serve as numerical links, relating *EDPs* to *DMs*. Damage states of structural and non-structural components are typically define qualitatively; therefore they cannot be easily aggregated to form a global damage indicator which the target decision variable can be based on. A simple solution is presented later in this chapter to integrate the component damage indices by assigning importance weights to structural components on the basis of how they correspond to the decision variable (i.e. the repair cost or the risk of collapse).

3.1 *Existing damage models for RC components*

Selecting and calibrating the right damage model for each RC component is a delicate task, which requires knowledge of the available damage models, as well as the monotonic and cyclic behavior of RC components. Damage in reinforced concrete components may

be caused by excessive deformation or by repeated load reversals. The damage in a reinforced concrete component is associated with damage to the concrete (aggregate-cement matrix), reinforcement steel (rebar yielding, fracture or buckling), bond loss, or a combination of all these elements. The damage models are categorized based on the loading types and the failure mechanisms (Williams and Sexsmith 1995).

Non-cumulative damage models: Non-cumulative damage indices use the envelope of maximum response such as component ductility or loading, as the basic variable to calculate the damage. The ductility is usually expressed in terms of curvature, rotation, strain, or deformation; while the loading envelope is defined for moments, stresses or forces. A non-cumulative damage index is calculated based on the peak value of the basic variable which is normalized by the nominal capacity of the component. Non-cumulative models are not load path dependent and they do not generally reflect the damage due to cyclic loading.

Cumulative damage models: Cumulative damage models are employed to represent the damage under cyclic loading. Accumulated plastic deformation or the hysteretic energy are commonly used for calculating cumulative damage indices. The deformation based cumulative damage models are mostly developed based on the low-cycle fatigue formulation, where large ductility excursions are sustained over many loading cycles (Banon et al. 1981; Wang and Shah 1987; Chung et al 1987; Hindi and Sexsmith 2001). Accumulation of plastic deformations has been used as the basic variable in damage indices proposed by Mehanny and Deierlein (2000). Cumulative damage model based solely on energy was introduced by Kratzig et al. (1989).

Combined damage models: These damage models consider a combination of damage due to excessive deformation and energy abortion. The combined damage model introduced by Park and Ang (1985a) is widely used due to its simplicity and the fact that calibration information is available. Some cyclic models such as Mehanny and Deierlein (2000) also include combinations of peak and cumulative effects (deformation and/or dissipated energy).

3.2 *Damage Model implementation*

The *Damage Model* is a new class introduced by the author to OpenSees. The damage model is a tagged/moveable object that is defined in the analysis domain by a tag and it is stored by elements, material models, and recorders (terms and definitions related to the OpenSees platform are described in the Appendix A). Specific types of damage formulations are introduced as subclasses of the damage model. Typical structural damage models are not rate dependent (i.e. the damage state does not dependent on the rate of loading. So, the default damage formulations implemented in this research are not rate dependent, however, the damage class keeps the options open to represent the rate dependent damage models. The damage model is introduced by the damage type, a tag, and calibrating parameters for the damage formulation (Appendix B).

Typical solution of a nonlinear structural analysis problem is involved with prediction/correction procedures, where the trial state of the system may be calculated a few times before the nonlinear solution converges. The trial state of the system is determined by using the last converged step as the start point. The trial steps will be discarded once the solution converges and the converged solution will be stored for the next step.

Elements and material models in OpenSees are all capable to store the latest converged solution as history data and calculate the trial states without altering the stored converged state. Due to the hysteretic nature of most of the damage models, the input parameters for each step are also treated as temporary trial data. The trial data is not stored and only a trial damage index is calculated. Once the solution has converged for a step, the trial data is saved as committed data.

The damage index is calculated and reported as a scalar value which is typically a combination of damage, both in positive and negative loading excursions. The rule used to combine the positive and negative damage depends on how the damage model is formulated. For some cases (e.g. degrading material characteristics) it is essential that the

positive and negative damage indices are reported separately. The *Damage Model* is capable of returning the damage for positive and negative loading excursions separately.

3.2.1 **Normalized peak**

Normalized peak is a damage model based on the maximum (envelope) value of a response parameter, which makes it a non-cumulative damage model. The *Normalized Peak* damage model can be applied to a variety of response parameters, including force, deformation, or plastic deformation. It determines the positive peak value and negative peak value of the response envelope and calculates the damage index by normalizing the peak values with respect to ultimate response threshold. The damage accumulates monotonically, and the failure is defined when the damage index reaches *1.0*. The maximum positive and minimum negative ultimate response thresholds (capacities) and the type response parameter are used to construct the *Normalized Peak* damage model. Mathematically, the index is described by the following equation:

$$DamageIndex_i = \max\left(\left|\frac{Value_i^+}{ValueU^+}\right|, \left|\frac{Value_i^-}{ValueU^-}\right|\right) \geq DamageIndex_{i-1} \qquad (3.1)$$

where $Value_i^{\pm}$ is the recorded envelope value of the response parameter at step *i*, and $ValueU^{\pm}$ is the ultimate response threshold for positive and negative excursions.

3.2.2 **Kratzig**

The Kratzig damage index is based on dissipated energy contributions, employing the maximum energy at the failure point under monotonic loading as the calibrating parameter (Kratzig 1989). The ultimate energy capacities for positive and negative monotonic loading (E_U^+ and E_U^-) are used as calibration parameters. The energy capacities of a member can be calculated analytically by using a fiber cross section model and considering criteria to define critical limit states, such as rebar rupture or concrete crushing.

The Kratzig damage formulation applies the concept of primary and follower half cycles to account for both the excursion with the maximum amplitude, and the cumulative damage of smaller excursions. The Primary Half cycle (*PHC*) refers to a half cycle with maximum deformation amplitude that enlarges the displacement envelope. Any other half cycle with smaller amplitudes will be accounted as a Follower Half Cycle (*FHC*). Figure 3-3 shows the how primary and follower half cycles are identified for a monotonically increasing loading with three cycles at each displacement level. The energy dissipation in primary and follower half cycles (e.g. E_{Si} and E_i respectively) is calculated by integrating the energy increments (Figure 3-4). The dissipated energy history for positive and negative half cycles is used to calculate intermediate damage indices:

$$DI^{+} = \frac{\sum E_{Si}^{+} + \sum E_i^{+}}{E_U^{+} + \sum E_i^{+}} \tag{3.2}$$

$$DI^{-} = \frac{\sum E_{Si}^{-} + \sum E_i^{-}}{E_U^{-} + \sum E_i^{-}} \tag{3.3}$$

where $E_U^{\pm}$ is the ultimate energy capacity in monotonic loading in positive and negative directions. The displacements (deformations) are used to keep the track of the primary and follower half cycles. Initially the displacements (deformations) of the primary half cycles are assumed to be zero for both negative and positive loading. The primary half cycle displacement increases to the displacement envelope on each loading direction as the system deforms. Energy increments are calculated for each load step as:

$$\delta E_i = \frac{1}{2}\left(F_i + F_{i-1}\right) \times \left(\Delta_i - \Delta_{i-1}\right) \tag{3.4}$$

Depending on the displacement direction, the energy increment is added to $\sum E_i^{+}$ or $\sum E_i^{-}$ as a follower half cycle, unless the displacement Δ_i exceeds the previous primary half cycle. In this case the energy increment are added to the summation of primary half cycles, i.e. $\sum E_{Si}^{+}$ or $\sum E_{Si}^{-}$.

The failure ($DamageIndex = 1.0$) occurs when the energy dissipated in primary half cycles $\sum E_{Si}$ exceeds the ultimate energy capacity E_U, as modified by the accumulation of follower half cycles in the nominator and denominator (Equations 3.2 and 3.3). The follower half cycles are included both in the nominator and the denominator, such that they contribute considerably less to the damage index.

When a combined index is defined, the positive and negative damage indices are combined as:

$$DamageIndex = \left(DI^{+} + DI^{-} - DI^{+} \cdot DI^{-} \right) \leq 1.0 \tag{3.5}$$

3.2.3 **Mehanny - Deierlein**

This damage model (Mehanny and Deierlein, 2000) is based on cumulative member ductility in the form of total plastic deformations. This damage model is inspired by the energy based damage model developed by Kratzig (1989) model and the Otes (1985) concept for capturing the cyclic damage accumulation. The maximum plastic deformation capacity in positive and negative loading (θ_{pu}^{+} and θ_{pu}^{-}) and three positive parameters (α, β, and γ) are used as the calibrating parameters.

Plastic rotation, θ_p, is chosen as the basic input to this damage model. The plastic rotation is supplied to the damage model either in the form of a pure plastic deformation or as the non-recoverable part of the elastic deformation calculated from the total deformation, force and unloading stiffness, using the following equation:

$$\theta_p = \theta_{total} - \frac{F}{K_{unloading}} \tag{3.6}$$

A half cycle is defined as a monotonic change in plastic deformation. Once the plastic deformation increment $\left(\delta\theta_p\right)$ changes direction, a new half cycle is initiated. To eliminate unnecessary cycles, all the excursions smaller than certain limits are filtered out. The Primary Half Cycle (*PHC*) refers to the half cycle with highest magnitude, while

any other half cycles with smaller amplitude are referred as a Follower Half Cycle (*FHC*). The definition of *PHC* is slightly different than the definition used for the Kratzig model. In this formulation there is a unique PHC at each point and once a new PHC occurs the former PHC will be treated as a FHC (Figure 3-5).

Damage indices for positive and negative deformations are calculated separately as:

$$DI^{+} = \frac{\left(\theta_p^{+}\big|_{currentPHC}\right)^{\alpha} + \left(\sum_{i=1}^{n^{+}} \theta_p^{+}\big|_{FHC,i}\right)^{\beta}}{\left(\theta_{pu}^{+}\right)^{\alpha} + \left(\sum_{i=1}^{n^{+}} \theta_p^{+}\big|_{FHC,i}\right)^{\beta}} \tag{3.7}$$

$$DI^{-} = \frac{\left(\theta_p^{-}\big|_{currentPHC}\right)^{\alpha} + \left(\sum_{i=1}^{n^{-}} \theta_p^{-}\big|_{FHC,i}\right)^{\beta}}{\left(\theta_{pu}^{-}\right)^{\alpha} + \left(\sum_{i=1}^{n^{-}} \theta_p^{-}\big|_{FHC,i}\right)^{\beta}} \tag{3.8}$$

where $\theta_p^{+}\big|_{currentPHC}$ and $\theta_p^{-}\big|_{currentPHC}$ are the positive and negative primary peaks and $\theta_p^{+}\big|_{FHC,i}$ and $\theta_p^{-}\big|_{FHC,i}$ are positive and negative follower peaks. As noted previously, α and β are calibrating parameters.

The failure ($DamageIndex = 1.0$) occurs when the energy dissipated the primary half cycles exceeds the ultimate energy capacity, or an infinite number of follower half cycles equalizes the nominator and denominator. The damage indices are combined as:

$$DamageIndex = \sqrt[\gamma]{\left(DI^{+}\right)^{\gamma} + \left(DI^{-}\right)^{\gamma}} \le 1.0 \tag{3.9}$$

where γ is calibrating parameter.

3.2.4 **Hysteretic energy**

The hysteretic energy damage model uses a cyclic deterioration formulation to calculate the damage index. The underlying deterioration formulation was originally proposed by Rahnama and Krawinkler (1993) as an index to reduce the material properties (e.g. strength or stiffness) at the end of a loading cycle. The deterioration formulation used herein is dependent on the dissipated energy of the last excursion and the total cumulative dissipated energy. The deterioration coefficient (β) is given as:

$$\beta_{Excursion} = \left(\frac{E_{excursion}}{E_U - \sum E} \right)^C \leq 1.0 \tag{3.10}$$

where E_U and c are specified by the user as calibration parameters. E_U is ultimate energy capacity, normally defined as a multiplier of the yield energy, i.e. $E_U = \lambda \cdot F_y \cdot \delta_y$.

The energy values are calculated by integrating energy increments, using either the total energy or the plastic energy (i.e. the recoverable or elastic energy is excluded). In cases an unloading stiffness is specified in the input, the damage is calculated based on plastic energy. $E_{excursion}$ is the energy dissipated in current cycle and once a new load cycles begins, $E_{excursion}$ is reset to zero.

When used as a deterioration mode for materials, the deterioration coefficient is used to reduce the material model stiffness and strength are reduced at the end of each half cycle, i.e. at the zero force point or when the material force switches direction. The deteriorated strength/stiffness is calculated by multiplying the last step value to the loss of $\left(1-\beta_{Excursion}\right)$. For example the yield strength at excursion i is calculated as:

$$F_Y\big|_{excursion=i} = F_Y\big|_{excursion=i-1} \times \left(1-\beta_{excursion=i}\right) \tag{3.11}$$

The hysteretic damage index is formulated to reflect the total deterioration by accounting for the cumulative cyclic deterioration. Further, the damage index is uploaded at the end

of each excursion. The relationship between the damage index after excursion *i* and cyclic deterioration parameter is expressed as:

$$\left(1-DI_i\right)=\left(1-\beta_i\right)\times\left(1-\beta_{i-1}\right)\times\ldots\times\left(1-\beta_2\right)\times\left(1-\beta_1\right) \tag{3.12}$$

This equation can be further simplified to the following,

$$\left(1-DI_i\right)=\left(1-\beta_i\right)\times\left(1-DI_{i-1}\right) \tag{3.13}$$

and, eventually to the following to give the damage index DI_i at the end of excursion *i*:

$$DI_i = DI_{i-1}+\beta_i-\beta_i\times DI_{i-1}\le 1.0 \tag{3.14}$$

The damage index value DI_i is calculated and updated at the end of each excursion.

3.2.5 **Park-Ang**

Park-Ang is a combined damage model, which was originally calculated for RC components (Park and Ang, 1985). The Park-Ang model calculates the damage index is a linear combination of the damage caused by excessive deformation, and repeated cyclic loading, captured in the form of dissipated energy. The general form of the Park-Ang damage formulation is as follows:

$$DamageIndex=\frac{\delta_{Max}}{\delta_U}+\frac{\beta}{F_u\cdot\delta_U}\int dE\le 1.0 \tag{3.15}$$

where δ_{Max} is the peak deformation, δ_U is the ultimate deformation capacity under monotonic loading, F_u is the calculated yield strength (the smaller value of the yield strength or the ultimate strength), and β is the calibration parameter for cyclic damage. The dissipated energy is calculated by integration of energy increments calculated by (3.4).

A variation of (3.15) is implemented and used in this research (Park and Ang 1985):

$$DamageIndex = \left[\frac{\delta_{Max}}{\delta_U} + \beta \int \left(\frac{\delta}{\delta_u} \right)^{\alpha} \frac{dE}{E_c(\delta)} \right] \leq 1.0 \qquad (3.16)$$

where $E_c(\delta)$ is the accumulated energy per loading cycle for the current displacement and α and β are two calibration parameters for cyclic damage.

A detailed classification of damage levels suggested by Park, Ang and Wen (1985b) is used to related the observed empirical damages and the calculated damage indices.

Table 3-1: Park-Ang damage level classifications

Damage level	Damage Index	Damage measure
I	$DI < 0.1$	No damage; localized minor cracking
II	$0.1 \leq DI < 0.25$	Minor damage; light cracking throughout
III	$0.25 \leq DI < 0.4$	Moderate damage; severe cracking, localized spalling
IV	$0.4 \leq DI < 1.0$	Severe damage; crushing of cracking, reinforcement exposed
V	$DI \geq 1.0$	Loss of element load resistance

Table 3-1 summarizes the ranges of damage indices associated with a certain damage level. This table will be later referred in Chapter 4 for damage study on the beam-column joint zone.

3.3 *Damage recorder implementation*

A nonlinear element must be able to reach the damage model and calculate its damage, where most of the existing nonlinear elements in OpenSees platform do not have a capability to calculate and report damage, other than by a simple *EDP* recorder. On the other hand, the newer elements developed in this study and future studies can be designed

to directly interact with damage index. The inability of existing elements to interact directly is resolved by an intermediate damage recorder class to access the element information and calculate the corresponding damage indices.

The nonlinear element force-deformation relationships are determined by material models or sections. Depending on the circumstances, the force, deformation and/or energy state of the sections can be used to calculate the element damage. The damage recorder is created for an element or a series of elements and uses a damage model to calculate the overall element damage or damage at certain section(s). The damage recorder is defined in OpenSees by specifying an output file, element material or section response, and a damage model. The element response is fed into the damage model at every converged step and the damage index is calculated and recorded.

3.1 *One-Dimensional Hysteretic Load-Deformation Response Model*

OpenSees uses a generic one-dimensional (uniaxial) hysteretic load-deformation model, which can be substituted by a variety of rules to facilitate the modeling process (Figure 3-6). In this research three new uniaxial material models are implemented to represent the response of the rotational springs in the joint model (both the shear panel and the member-end rotations).

The idea of changing hysteretic model by hysteretic energy of by a combination of peak deformation and hysteretic energy has been used is a variety of structural analysis computer programs (IDARC, 2004; FEDEAS, 2004; SNAP, 2003). After reviewing previous studies on hysteretic material models that can be used to represent the cyclic behavior of reinforced concrete components (Townsend, 1977; Rahnama, 1993; Mostaghel, 1999; Mettupalayam, 2000; Deng, 2000; Ibarra et. al., 2004) three hysteretic material models are selected. The selected material models (Bilinear, Clough, and Pinching) were previously developed and implemented in SNAP by Ibarra (2003) to capture the strength deterioration and cyclic deterioration. SNAP is an in-house computer program that carries out dynamic and quasi-static inelastic analysis for SDOF systems. These material models are used to model overall behavior of an RC connection or the individual mechanisms contributing to the component response (e.g. rebar pull out, bond

slip behavior, and shear behavior). As part of this research, these hysteretic materials are implemented in OpenSees with some modifications to interact with the damage models, and as will be discussed in Chapter 5, to calculate and return material response sensitivity to the modeling parameters.

As described by Ibarra (2003), the Bilinear, Clough, and Pinching material models are defined by a response envelope, an unload/reload path, and damage rules to control the degradation define the uniaxial material model. These models share a similar envelope, while the characteristics of the unloading/reloading paths are different. The four material states that define a hysteretic uniaxial material model (loading, reloading, and unloading states) are illustrated in Figure 3-7. Load-deformation paths for the loading states (states 1 and 2) in the positive and negative direction are defined by the backbone envelopes at the beginning of the analysis (undamaged model without any deterioration). The backbones can be modified during the analysis to simulate the cyclic deterioration. Whenever there is a deformation reversal, the unloading/reloading states (states 3 and 4) are redefined based on specific rules for each material model and the unloading/reloading path endpoints. The force-deformation point at which the reversal occurs defines the beginning point for the unloading/reloading state; and, the transition point to loading in the opposite direction defines the endpoint.

Hysteretic damage is simulated through deterioration in unloading stiffness (unloading stiffness deterioration), deterioration in strength achieved at previously unachieved deformation demands (strength deterioration), and deterioration in the strength developed in the vicinity of the maximum and minimum deformation demands (reloading strength deterioration). Figure 3-15 to Figure 3-17 show the impact of these three different damage modes on the hysteretic response. A generalization of the damage index is used to define hysteretic damage for the current displacement increment.

3.1.1 **Bilinear with cap**

The bilinear material model is an extension to the basic elastic-plastic hardening formulation, with additional features to model softening at large deformations and

hysteretic deterioration. The loading paths (states 1 and 2) for the bilinear material models are defined by the positive and negative envelopes shown in Figure 3-8. The envelopes are defined independently, so this material model can be used to simulate structural components with different properties in each loading direction. The monotonic behavior of the bilinear material is described by an elastic-isotropic hardening rule with a softening cap.

An optional residual strength can be specified as a minimum resistance that the model has at large deformations. The residual value is used for both positive and negative ends of the envelope. The bilinear model envelopes can be used as the generalized force-deformation relation for concrete elements, as suggested by FEMA 356 for nonlinear analysis of the reinforced concrete components.

The implementation of the bilinear material model is based on the definition of positive and negative force envelopes, since force response is limited to the maximum and minimum force values prescribed by the envelopes. The force envelopes are defined based on initial material parameters and as it will be mentioned later, they may cyclically deteriorate. The force envelopes for the bilinear material are defined by three key points. Table 3-2 is used to determine these key points for the positive envelope. Same table can be easily generated for the negative envelope.

Table 3-2: Force-deformation envelope key points

Point	Deformation/Strain	Force/Stress	Stiffness
1	$< \delta^{+}_{\min}$	$F^{+}_{res} = R \cdot F^{+}_{y}$	0
2	$\delta^{+}_{\min} = \dfrac{(\alpha_h - 1 + R) \cdot F^{+}_{y}}{\alpha_h \cdot K_{elastic}}$	$F^{+}_{res} = R \cdot F^{+}_{y}$	$\alpha_h \cdot K_{elastic}$
3	δ^{+}_{cap}	$F^{+}_{cap} = (1-\alpha_h) F^{+}_{y} + \alpha_h \cdot K_{elastic} \cdot \delta^{+}_{cap}$	$\alpha_{cap} \cdot K_{elastic}$
4	$\delta^{+}_{res} = \left(\dfrac{\alpha_{cap} - \alpha_h}{\alpha_{cap}} \right) \delta^{+}_{cap} + \dfrac{(R - 1 + \alpha_h) F^{+}_{y}}{\alpha_{cap} \cdot K_{elastic}}$	$F^{+}_{res} = R \cdot F^{+}_{y}$	0

5	$> \delta_{res}^{+}$	$F_{res}^{+} = R \cdot F_{y}^{+}$	0

The terms in Figure 3-8 and Table 3-2 are defined as follows:

$K_{elastic}$ is the initial elastic stiffness, F_y^+ is a positive value for the yield strength in positive direction, F_y^- is a negative value for the yield strength in negative direction, α_h is the isotropic hardening ratio as a fraction of elastic stiffness, R is the residual force ratio as a fraction of yield strength, α_{cap} is a negative value for the cap slope ratio as a fraction of stiffness, δ_{cap}^{+} is a positive value for the cap displacement on positive side, and δ_{cap}^{+} is a negative value for the cap displacement on negative side.

The unloading/reloading path for load reversals is simply defined as an elastic path, unloading from the reversal point with a constant stiffness to the point it intersects the backbone envelope (Figure 3-9).

An option is provided for the *Bilinear* model to modify the force envelopes after the deformation exceeds the cap deformation (δ_{cap}), i.e. the softening branch. In this case, the force envelope value for the maximum deformation is used as cut-off limit for the envelopes. Figure 3-10 shows the cap cut-off option.

For the sensitivity analysis, described later in Chapter 5), it is necessary to define the envelope in the form of a single analytical function. The multi-linear envelope is expressed analytically by using boxcar function as:

$$\begin{aligned} F_{envelope}^{+} = {} & B_{\delta_{\min}^{+},\delta_{cap}^{+}}(\delta)\cdot\left[(1-\alpha_h)F_y^{+} + \alpha_h \cdot K_{elastic}\cdot\delta\right] + \\ & B_{\delta_{cap}^{+},\delta_{res}^{+}}(\delta)\cdot\left[(1-\alpha_h)F_y^{+} + (\alpha_h - \alpha_{cap})\cdot K_{elastic}\cdot\delta_{cap}^{+} + \alpha_{cap}\cdot K_{elastic}\cdot\delta\right] + H(\delta-\delta_{res}^{+})\cdot F_{res}^{+} \end{aligned} \tag{3.17}$$

where

$$B_{a,b}(x) = \left[H(x-a) - H(x-b)\right] = \begin{cases} 1 & a \le x \le b \\ 0 & elsewhere \end{cases} \tag{3.18}$$

and the Heaviside Step Function is defined as:

$$H(x)=\begin{cases}0 & x<0\\ 1/2 & x=0\\ 1 & x>0\end{cases} \tag{3.19}$$

The tangent of the envelope is defined as:

$$\frac{\partial F_{envelope}}{\partial \delta}=B_{\delta^{+}_{\min},\delta^{+}_{cap}}(\delta)\cdot\alpha_h\cdot\delta+B_{\delta^{+}_{cap},\delta^{+}_{res}}(\delta)\cdot\alpha_{cap}\cdot\delta \tag{3.20}$$

A predictor force (or stress) for a trial deformation (or strain) is calculated assuming the step is totally elastic(3.21). The predictor force is the compared with the envelope values (3.22) to correct the force to the envelope level in case it exceeds the boundary.

$$F_{trial}=K_{excursion}\cdot(\delta_{trial}-\delta_{commited})+F_{commited} \tag{3.21}$$

$$\delta^{-}_{envelope}\le\delta_{trial}\le\delta^{+}_{envelope} \tag{3.22}$$

The unloading and reloading phases of the bilinear material model are fairly simple since a constant stiffness (slope) is assumed.

3.1.2 **Peak-oriented hysteretic material (Modified Clough)**

The monotonic loading force-deformation (stress-strain) behavior of peak oriented material models and the bilinear material are identical. The loading regime of peak oriented material models starts with an elastic-hardening plastic constitutive rule, followed with a softening section and a residual force value. Peak oriented material models have totally different unloading/reloading paths, compared with the bilinear model.

The force envelopes for peak-oriented materials are similar to the envelope used for the bilinear material model, with the only difference being that the positive envelope is zero

for negative deformations and the negative envelope is zero for positive deformations (Figure 3-11). The loading envelope is defined by five key points, which are determined based on the user input (Table 3-3).

Table 3-3: Force-deformation envelope key points

Point	Deformation/Strain	Force/Stress	Stiffness
1	0	0	
2	$\delta_y^+ = \frac{F_y^+}{K_{elastic}}$	F_y^+	$K_{elastic}$
3	δ_{cap}^+	$F_{cap}^+ = F_y^+ + \alpha_h \cdot K_{elastic} \cdot \left(\delta_{cap}^+ - \delta_y^+\right)$	$\alpha_h \cdot K_{elastic}$
4	$\delta_{res}^+ = \delta_{cap}^+ + \frac{\left(R \cdot F_y^+ - F_{cap}^+\right)}{\alpha_{cap} \cdot K_{elastic}}$	$F_{res}^+ = R \cdot F_y^+$	$\alpha_{cap} \cdot K_{elastic}$
5	$> \delta_{res}^+$	$F_{res}^+ = R \cdot F_y^+$	0

The multi-linear envelope is analytically expressed by using boxcar function (3.20) as:

$$F_{envelope}^+ = B_{0,\delta_y^+}(\delta) \cdot K_{elastic} \cdot \delta + B_{\delta_y^+,\delta_{cap}^+}(\delta) \cdot \left[F_y^+ + \alpha_h \cdot K_{elastic} \cdot \left(\delta - \delta_y^+\right)\right] + B_{\delta_{cap}^+,\delta_{res}^+}(\delta) \cdot \left[F_{cap}^+ + \alpha_{cap} \cdot K_{elastic} \cdot \left(\delta - \delta_{cap}^+\right)\right] + H\left(\delta - \delta_{res}^+\right) \cdot F_{res}^+ \quad (3.23)$$

The tangent of the envelope is defined as:

$$\frac{\partial F_{envelope}}{\partial \delta} = B_{0,\delta_y^+}(\delta) \cdot K_{elastic} + B_{\delta_y^+,\delta_{cap}^+}(\delta) \cdot \alpha_h \cdot K_{elastic} + B_{\delta_{cap}^+,\delta_{res}^+}(\delta) \cdot \alpha_{cap} \cdot K_{elastic} \quad (3.24)$$

Consider the unloading/reloading path. The unloading occurs with the unloading stiffness (normally the degraded elastic stiffness) until the force reaches zero. The reloading path is defined based on the peak points reached in previous cycles. The initial peak points are set to the yield points (point 2 in Figure 3-11), and as the material is loaded into the nonlinear region, the peak points are relocated on the loading envelope. The positive and negative peak points are identified by the peaks deformations (δ_{peak}^+ and δ_{peak}^-), and the

corresponding force envelopes (F^{+}_{peak} and F^{-}_{peak}). The reloading stiffness is calculated according to Equation (3.25) by targeting from a reloading point to the peak point. The reloading point refers to the unloaded state or the latest step where the reloading occurs.

$$K^{+}_{reloading} = \frac{F^{+}_{peak} - F_{reloading}}{\delta^{+}_{peak} - \delta_{reloading}} \tag{3.25}$$

The reloading stiffness is used to calculate the predicted force, unless the trial deformation exceeds the peak deformation, the material state switches back to the loading state and the corresponding force is calculated by the envelope.

3.1.3 **Pinching material model**

Pinching behavior often occurs due to crack opening and closing and bond-slip behavior in reinforced concrete components. The behavior of the pinching model is similar to the peak oriented material model, except the reloading branch initially points to a pinching point lower than the peak point, and once the reloading branch hits the pinching point, it will aim to the peak point. The locations of pinching points are specified by the user as a percentage of the peak points (Figure 3-13).

Two additional load-deformation target points define the state 3 (state 4) load path with pinching. The first target point reached once substantial unloading has occurred and the point at which substantial reloading occurs. For state 3 (state 4), the load developed upon unloading is defined as a fraction of the minimum (maximum) strength that can be developed. With the unloading stiffness defined, this establishes the end of the substantial unload phase. The load-deformation point at which substantial reloading occurs for state 3 (state 4) is defined as a fraction of the minimum (maximum) historic deformation demand and a fraction of the load developed at the minimum (maximum) deformation demand.

3.2 *Material parameter deterioration*

The physical behavior of reinforced concrete components, typically measured by the strength and stiffness, deteriorates under cyclic loading. The strength and stiffness deterioration is significant for members without adequate confinement, rebar bond-slip, etc. The material models are formulated to reflect the deterioration in the physical behavior. Hysteretic damage is simulated through deterioration in unloading stiffness (unloading stiffness deterioration), deterioration in strength achieved at previously unachieved deformation demands (strength deterioration), and deterioration in the strength developed in the vicinity of the maximum and minimum deformation demands (reloading strength deterioration). Figure 3-14 shows the impact of strength and stiffness deteriorations for two of the models introduced by Ibarra (2004). In the current implementation, each deterioration mode is ruled by a separate damage index, acquired from one of the damage model described primarily. The damage indices and deterioration parameters are calculated and updated at the end of each half cycle.

3.2.1 **Strength deterioration**

The strength deterioration is carried out through reducing the yield strength (Figure 3-15) according to the following:

$$F_y^+\Big|^{excursion=i} = \left(F_y^+ - R\cdot F_y^+\right)\times\left(1-DI_{str}\right)+R\cdot F_y^+ \tag{3.26}$$

The strength deterioration given by this equation is limited to a minimum strength determined by the minimum residual force defined by the user.

3.2.2 **Stiffness deterioration**

Stiffness deterioration is applied to the unloading path (states 3) by reducing the unloading stiffness (Figure 3-16). For the bilinear material model, the stiffness deterioration also extended to the reloading path (state 4) also. The minimum threshold for the deteriorated stiffness is the backbone hardening stiffness (bilinear material) or the reloading stiffness (peak oriented models).

For the bilinear model, the unloading stiffness deterioration is formulated as:

$$K_{excur} = \left(1 - DI_{stf}\right) \times \left(K_{elastic} - \alpha_h \cdot K_{elastic}\right) + \alpha_h \cdot K_{elastic} \tag{3.27}$$

or, for the peak oriented models as:

$$K_{excur} = \left(1 - DI_{stf}\right) \times K_{elastic} \tag{3.28}$$

3.2.3 **Accelerated stiffness deterioration**

The accelerated stiffness deterioration model is exclusively defined for peak oriented material models to reduce the reloading stiffness. In accelerated stiffness deterioration, the displacement component of the peak point is increased to mimic the cyclic stiffness loss by pointing to a new peak point (Figure 3-17). The new displacement of the peak point is recalculated as:

$$\delta_{peak}\Big|^{excursion=i} = \left(1 + \frac{DI_i - DI_{i-1}}{1 - DI_{i-1}}\right) \times \delta^{+}_{\max} \tag{3.29}$$

The maximum increase to the peak point displacement is limited to $2 \times \delta^{+}_{\max}$.

3.2.4 **Cap deterioration:**

The cap, or the softening section of the loading envelope, is identified by the point where the softening initiates (Point 3 in Figure 3-8 and Figure 3-11) and the cap slope. The cyclic deterioration relocates the cap branch toward the origin (Figure 3-18), without changing the cap slope. A reference force F_{capref} is used to determine the distance of the capping branch to the origin. The reference force is determined by the intersection of the cap slope and the force (y) axis. The initial the reference force is calculated for positive and negative loading as:

$$F^{\pm}_{cap\,\mathrm{Re}\,f} = F^{\pm}_{cap} - \alpha_{cap} \cdot K_{elastic} \cdot \delta^{\pm}_{cap} \tag{3.30}$$

where $F_{cap}^{\pm}$ is presented in Table 3-2 or Table 3-3.

The reference force is reduced due to deterioration:

$$F_{capref}^{\pm}\Big|^{excursion=i} = \left(1 - DI_{cap}\right) \cdot F_{capref}^{\pm}\Big|^{excursion=0} \tag{3.31}$$

The reduced reference force is used to indicate the new location of the capping branch, and the new cap displacement is determined by the intersection of the cap and the hardening slope.

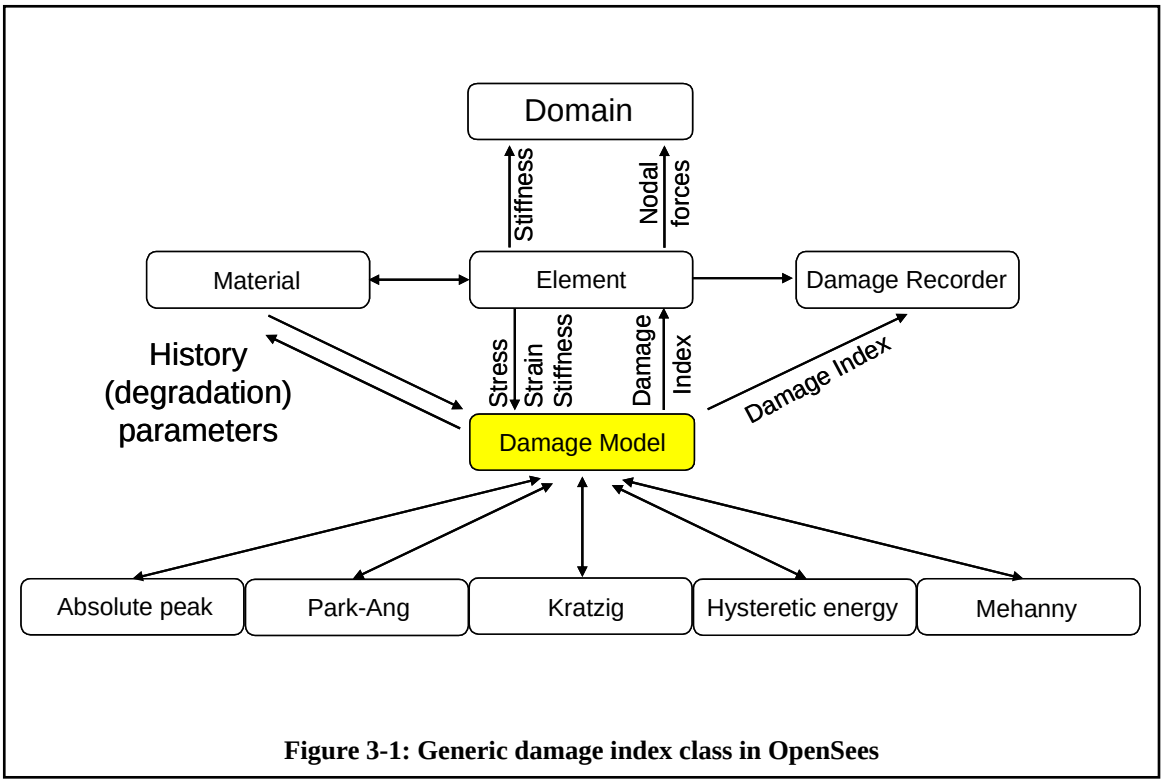

Figure 3-1: Generic damage index class in OpenSees

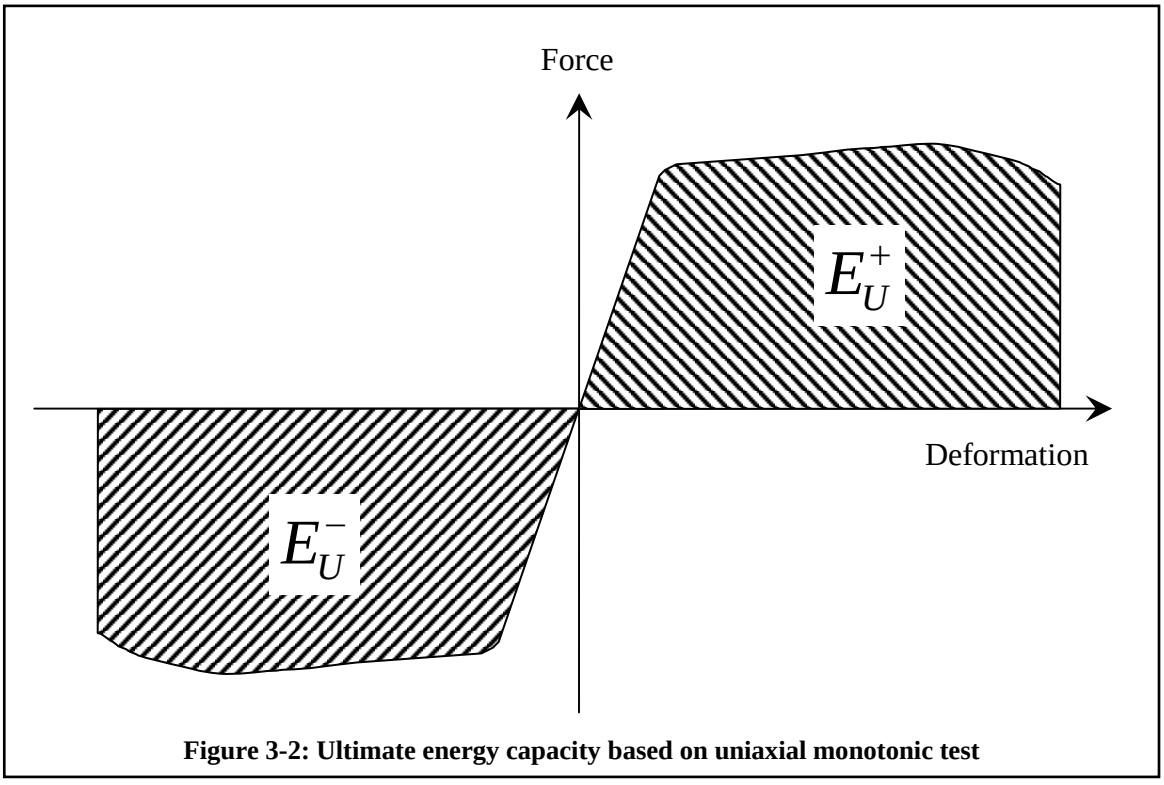

Figure 3-2: Ultimate energy capacity based on uniaxial monotonic test

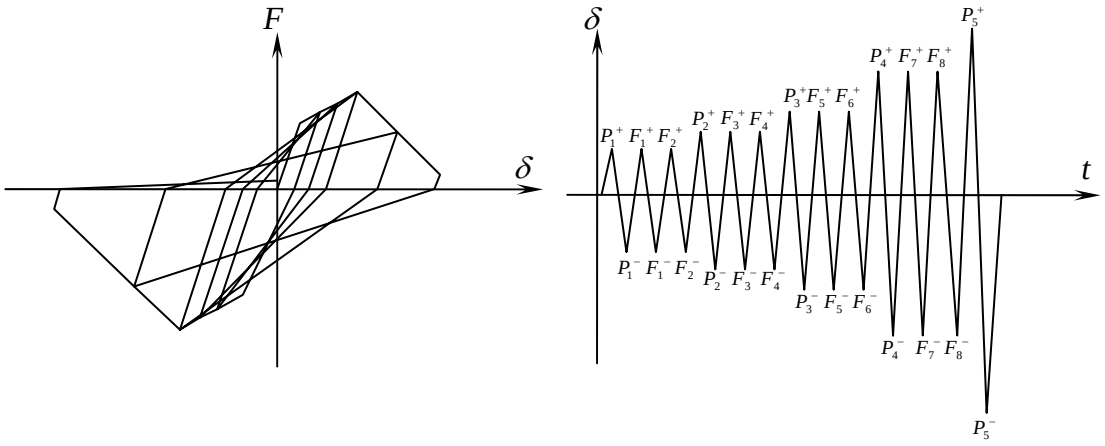

Figure 3-3: Kratzig model primary and follower half cycles

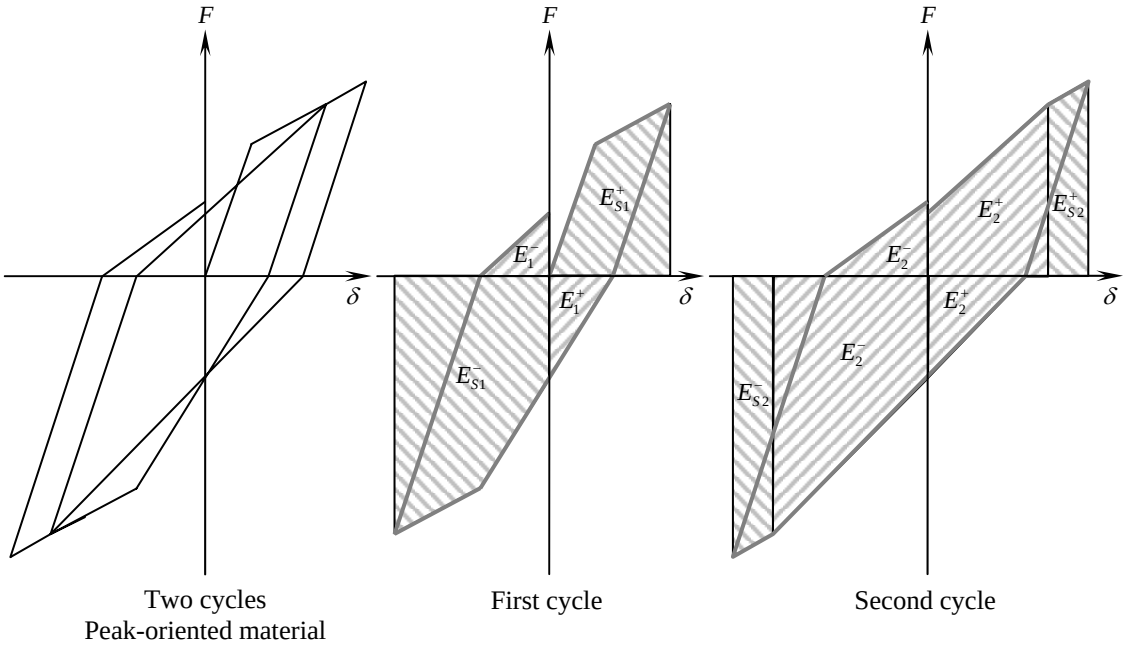

Figure 3-4: Energy calculation for Kratzig model

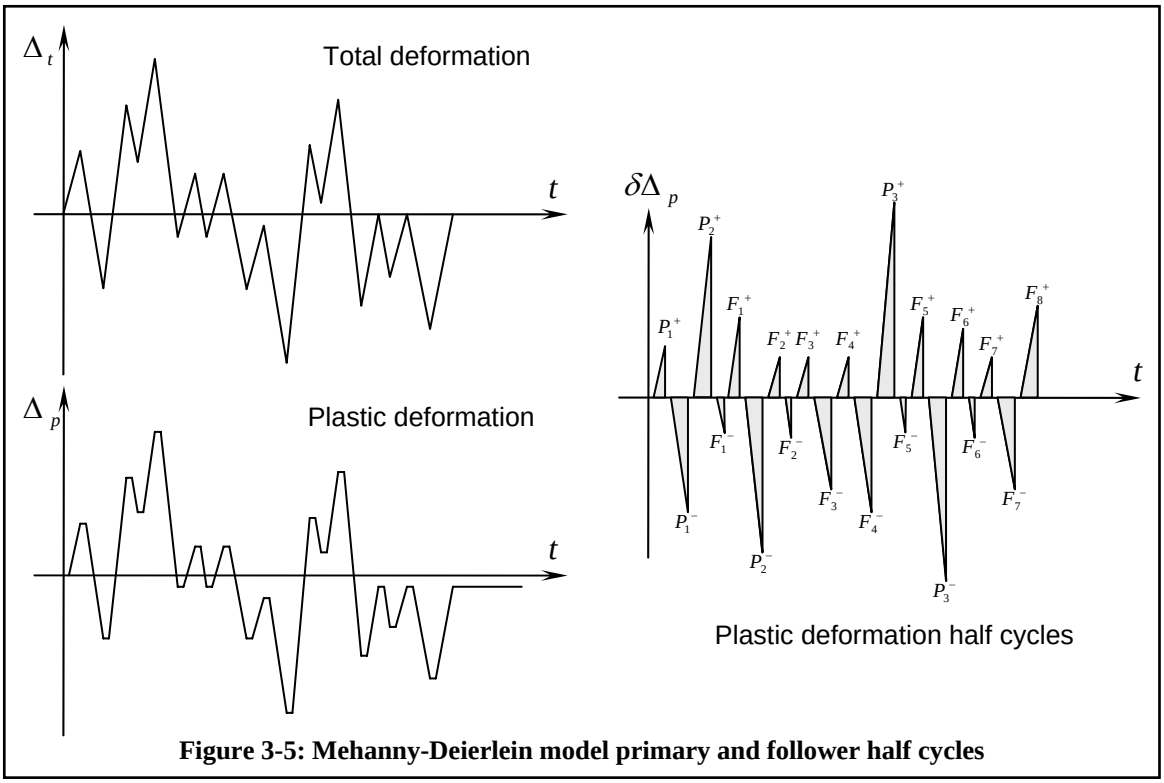

Figure 3-5: Mehanny-Deierlein model primary and follower half cycles

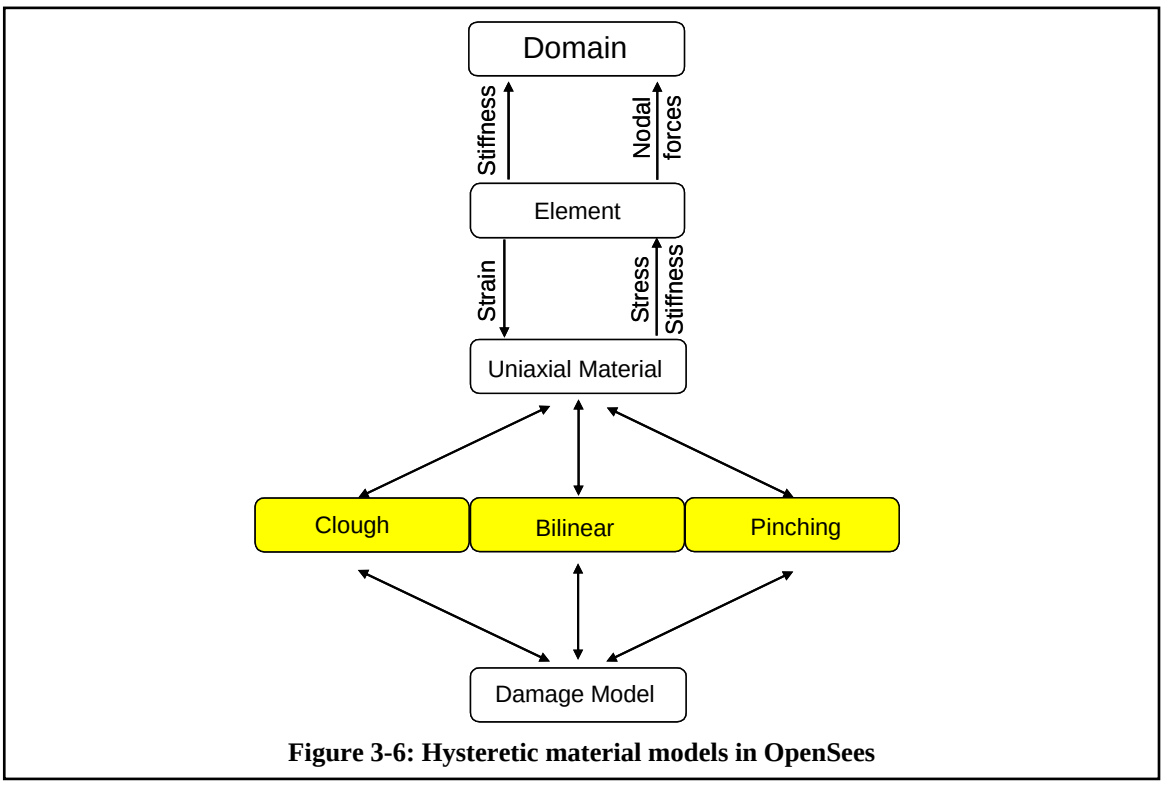

Figure 3-6: Hysteretic material models in OpenSees

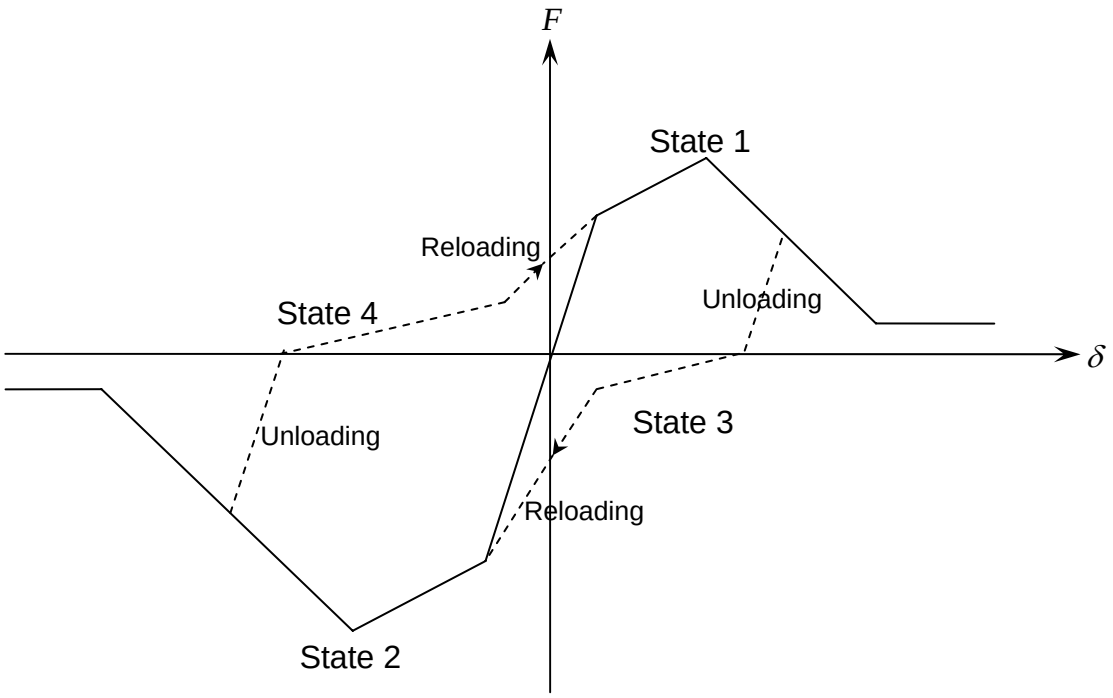

Figure 3-7: Material states for general uniaxial material (Lowes and Altoontash, 2003)

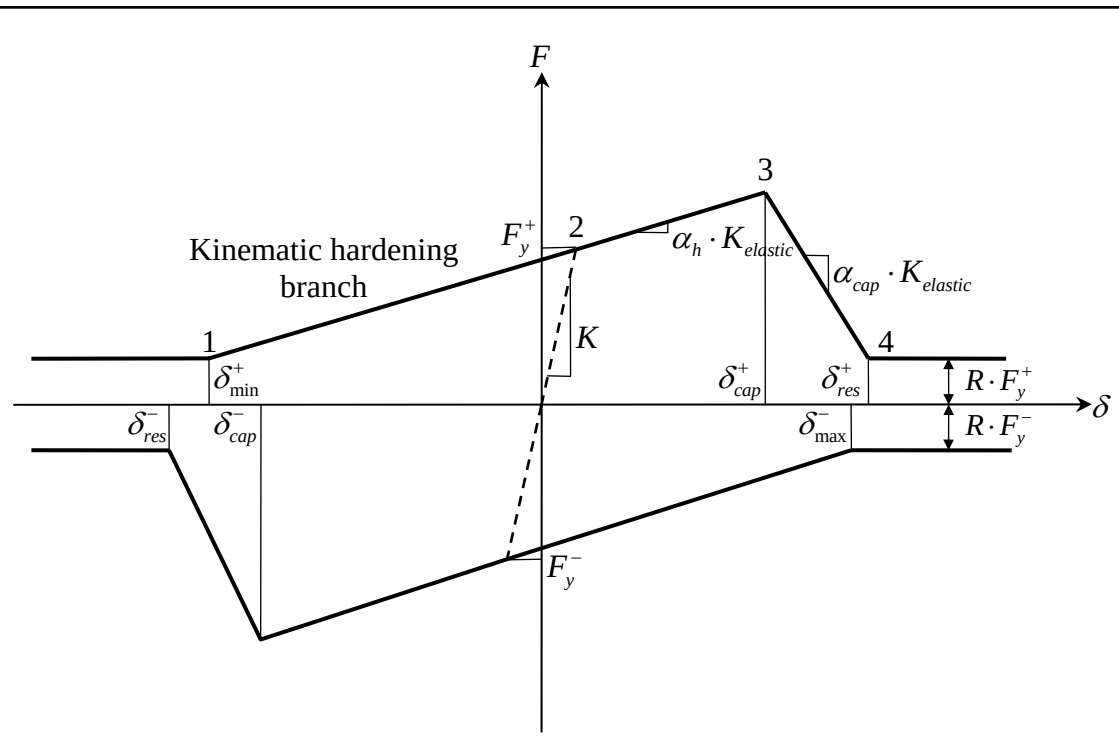

Figure 3-8: Loading envelope for bilinear model with capping

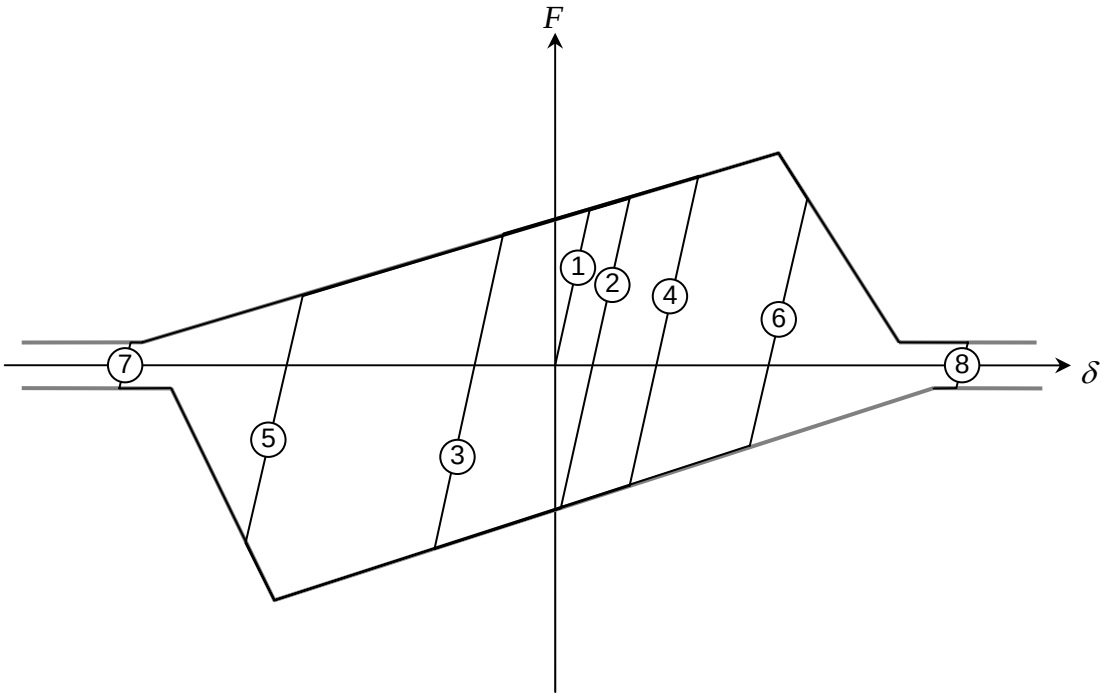

Figure 3-9: Bilinear material model

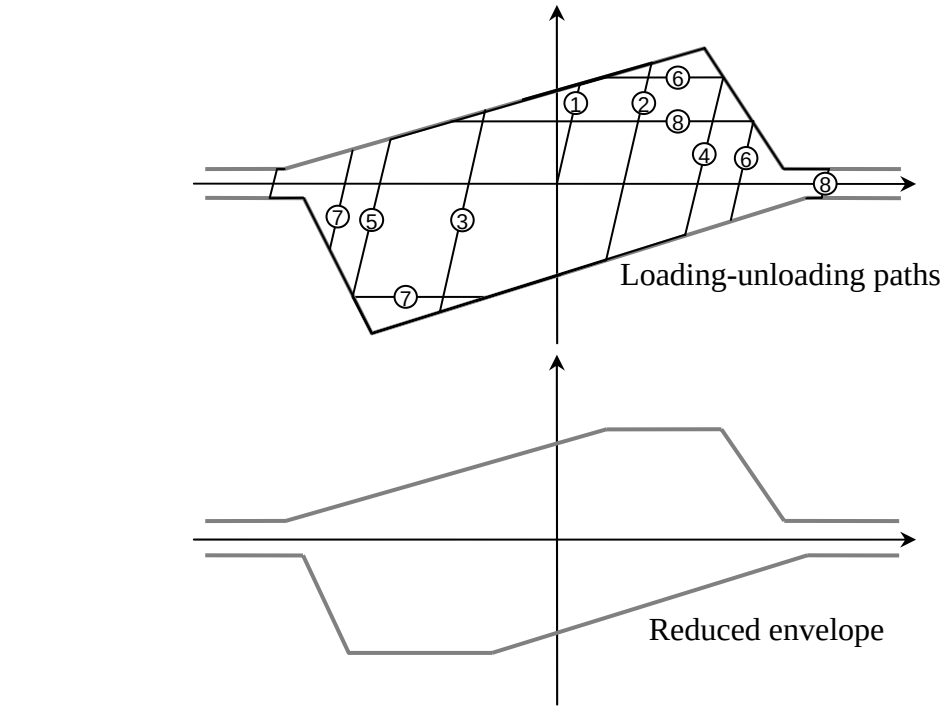

Figure 3-10: Bilinear material model with cap reduced envelopes

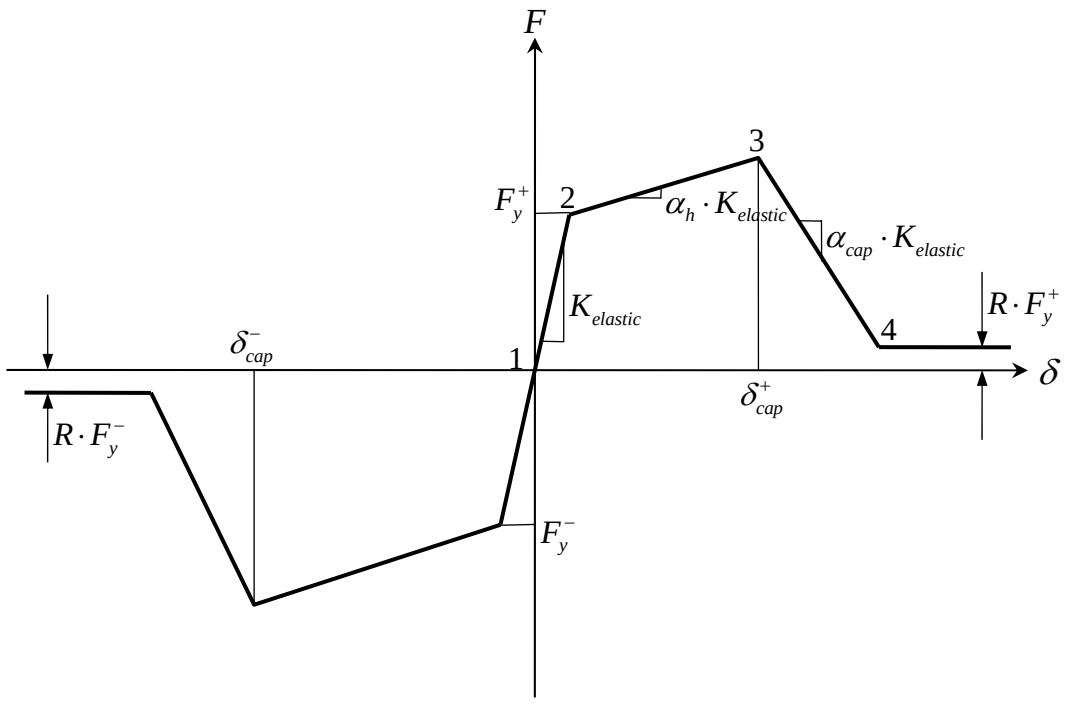

Figure 3-11: Loading envelope for peak oriented and pinching models (Ibarra 2003)

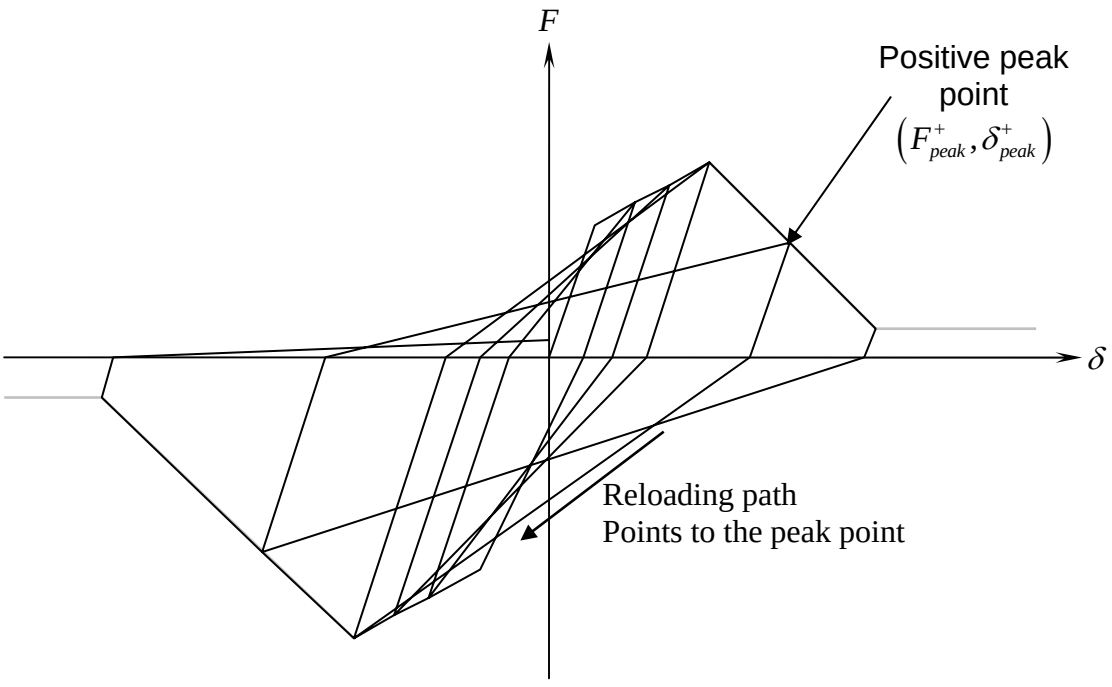

Figure 3-12: Modified Clough peak oriented material model

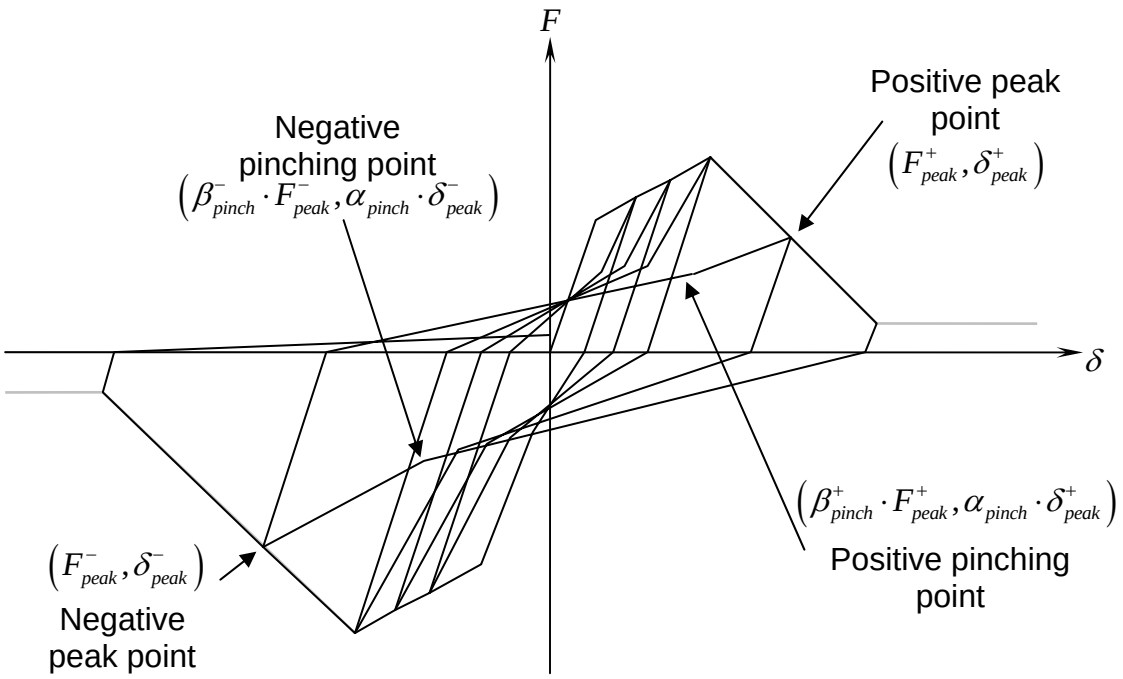

Figure 3-13: Pinching material model

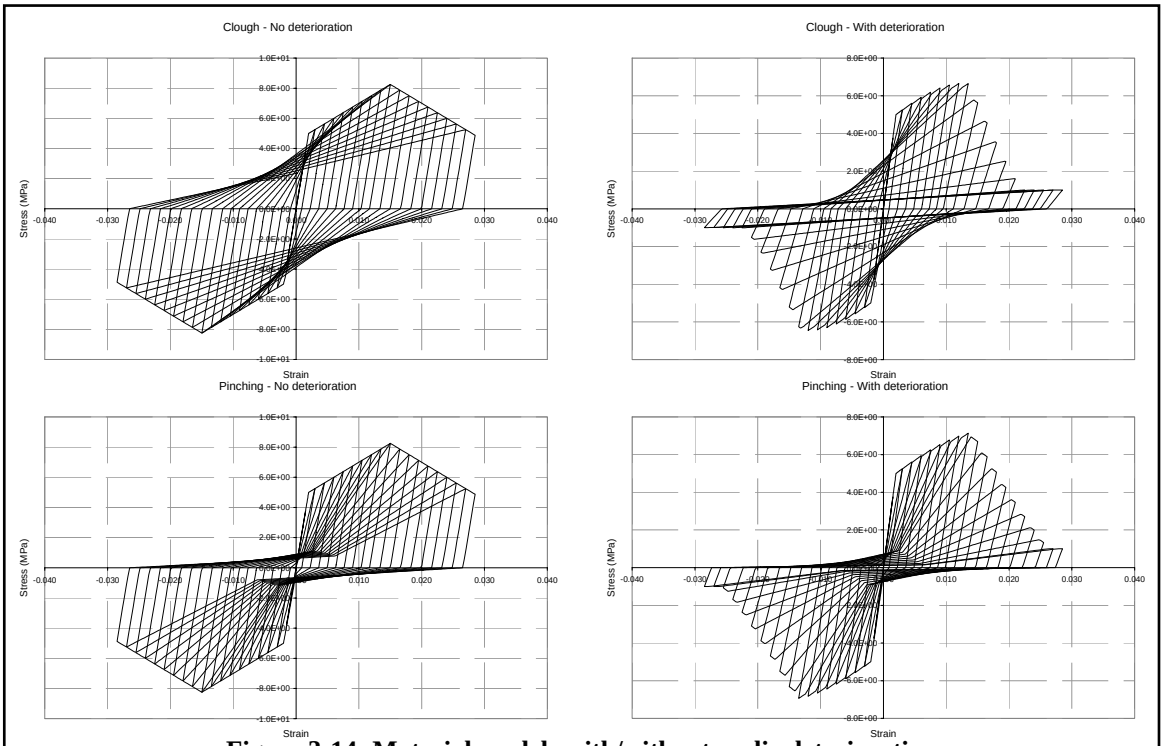

Figure 3-14: Material models with/without cyclic deterioration

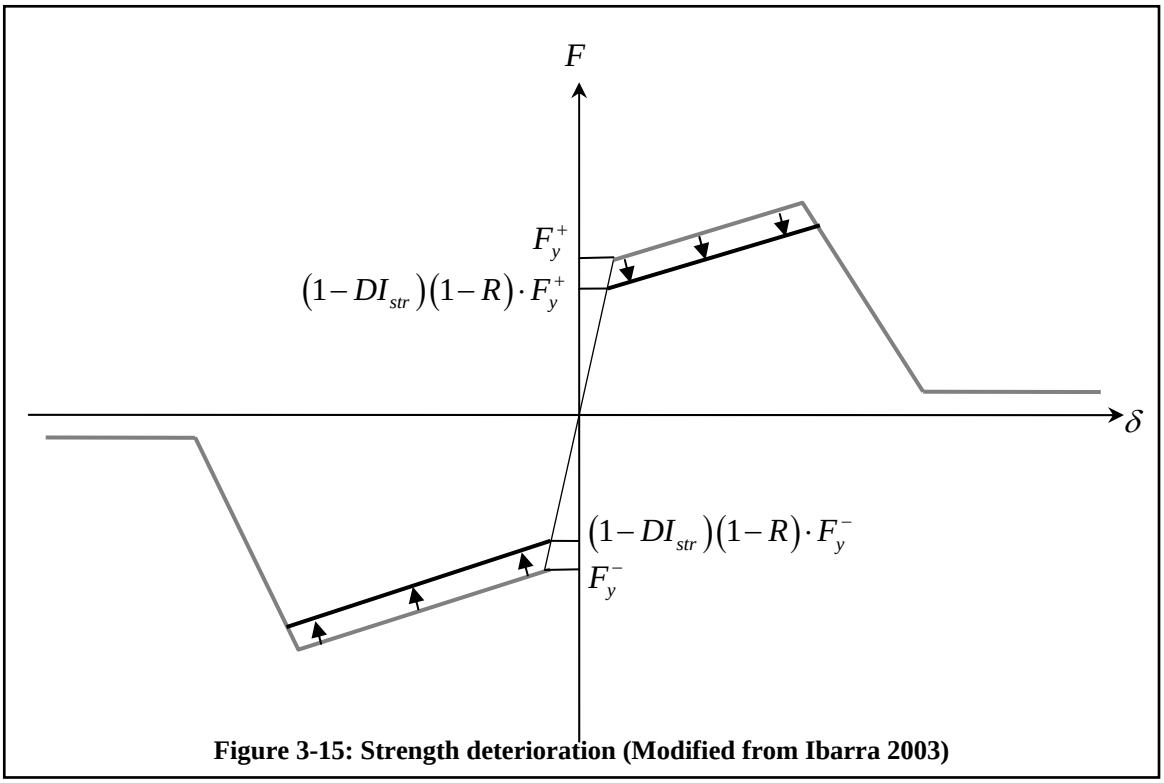

Figure 3-15: Strength deterioration (Modified from Ibarra 2003)

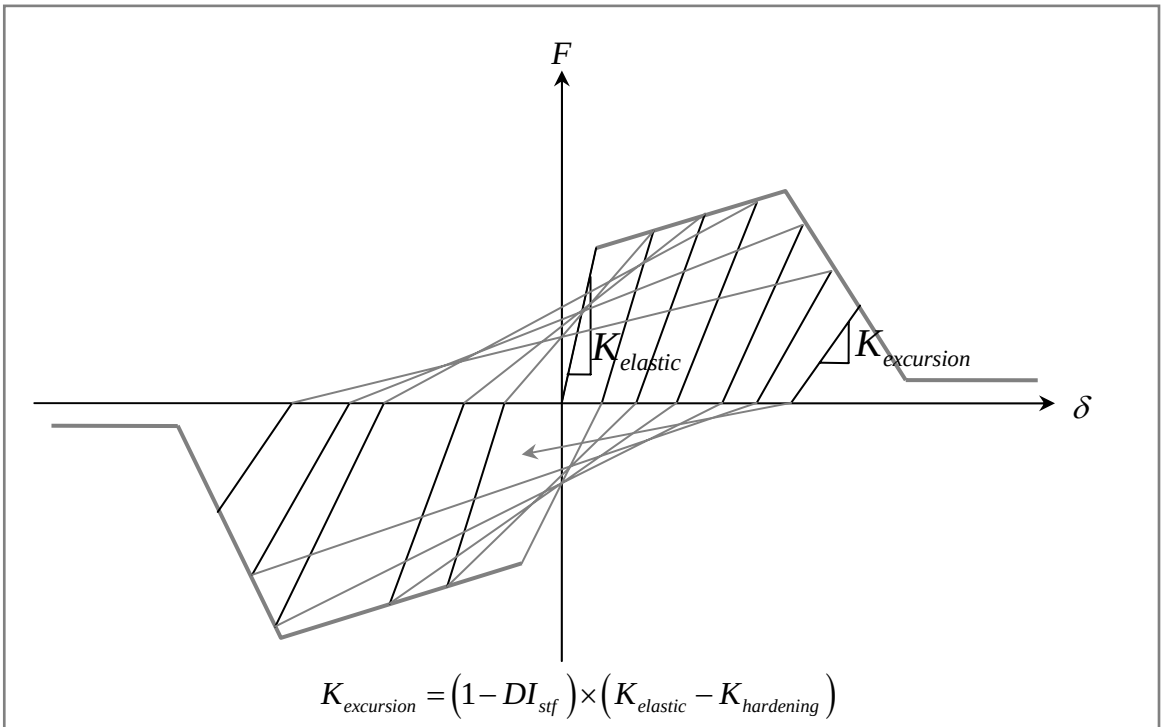

Figure 3-16: Stiffness deterioration (Modified from Ibarra 2003)

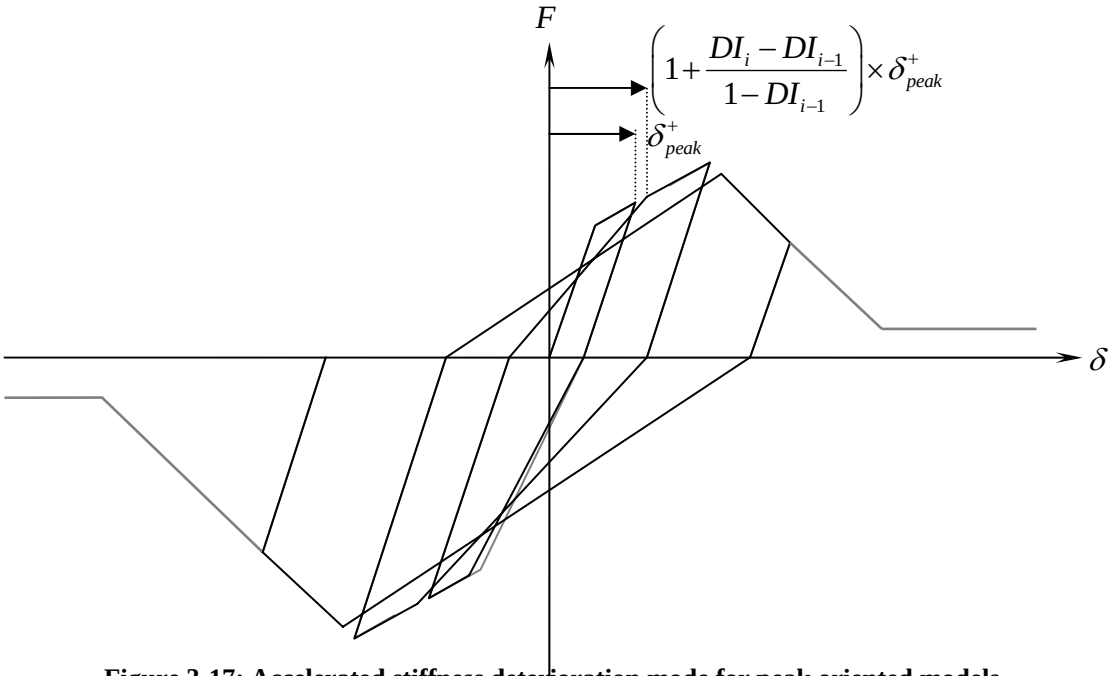

Figure 3-17: Accelerated stiffness deterioration mode for peak oriented models (Modified from Ibarra 2003)

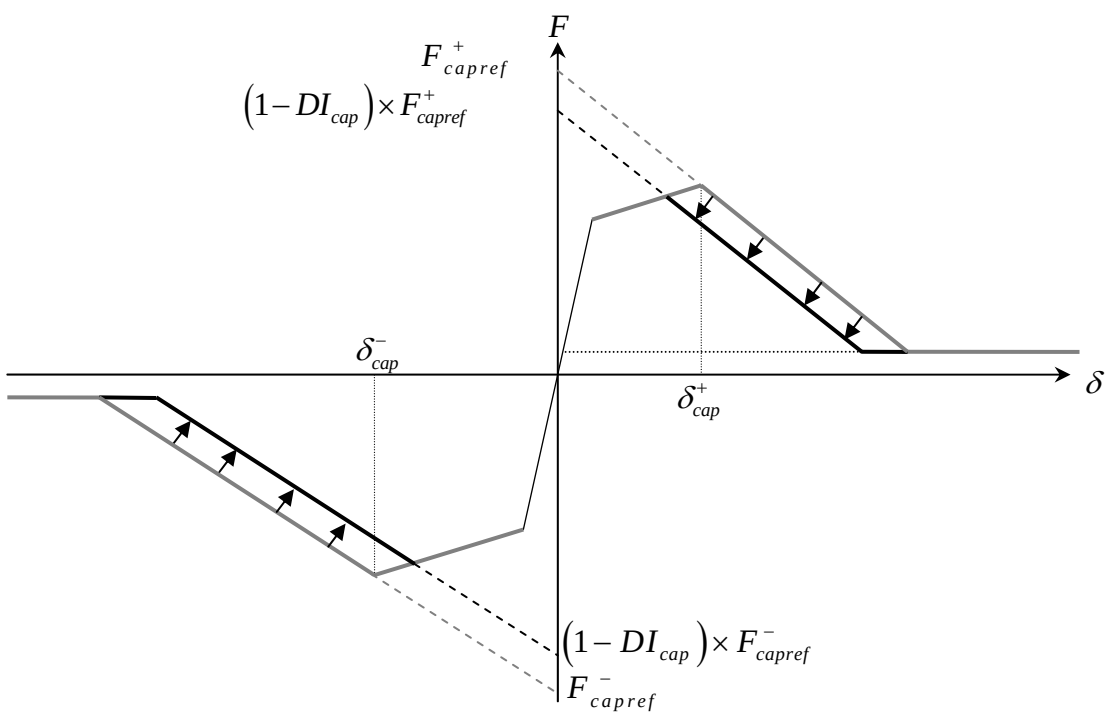

Figure 3-18: Cap deterioration (Modified from Ibarra 2003)

4 Calibrating methods and validation problems

4.1 *Versatile joint model for moment resisting frames*

As introduced in previous chapters, the simple joint element can be calibrated to simulate the joint response in different types of structural frames. This chapter begins with a brief review of three possible applications for the joint element to steel moment-resisting frames, reinforced concrete frames, or reinforced concrete-steel composite frames. The focus then shifts to the primary application of this research which is to reinforced concrete structures; and, detailed calibration information is provided for simulating RC joints through a combination of uniaxial materials applied to the Joint2D model. The formulation is verified by comparing analysis results and experimental observations.

4.1.1 Steel structures

Steel beam-column joints contribute to the structural deformation and energy dissipation of steel frames by panel zone deformation in shear mode and, for some cases, through concentrated beam end rotations. Older design provisions (e.g. AISC 1980) were based on the premise that the panel zone should remain elastic and that all inelastic deformation must occur in the beams. However, even in these cases the panel zone shear deformation has been shown to be contributing up to 30% of the overall drift of a frame (Krawinkler et al. 1971). Newer design codes allow some controlled inelastic deformation at the joint panel as well as the beams, so both the panel zone and the beams contribute to seismic energy dissipation (e.g. FEMA 267A, 1997). Reliance on the shear panel deformation for newer designs will be even more and should be considered in the analysis.

In analyzing steel joint panel zones, it is assumed that the sides of the panel zone remain straight after panel zone deforms, which results in some local plastic deformation in the columns (Krawinkler et al., 1975). Many typical models for steel joints (e.g. El-Tawil et al., 1999) assume pure shear deformation in the panel zone with straight sides and local plastic hinging (or kinking) in the column flanges. The Joint2D-1SPR element can represent this mechanism.

The unbalanced beam moments developed at the column face are chosen as the basic load parameter for characterizing the joint behavior (Krawinkler at al. 1978). The shear behavior of the panel zone is a function of the aspect ratio of the panel, the thickness of the column web and additional shear reinforcement, resistance of the elements surrounding the panel zone (column flanges and in-plane stiffeners), connecting media and loading condition at the column interfaces.

4.1.2 **Reinforced Concrete-Steel (RCS) composite structures**

Reinforced Concrete-Steel (RCS) structures refer to composite systems with reinforced concrete columns and steel beams. Beam-column joints in RCS frames are usually configured with a steel beam that is embedded and runs continuously through the reinforced concrete columns. The relative rotation of the beams and columns in lateral loading is resisted by two mechanisms, shear deformation of the embedded part of the beam and bearing deformation at the contact parts of the beam and column. Research has been done on behavior and modeling the beam-column joints in RCS frames (Deierlein and Kanno, 1994). A shear panel is proposed as an analytical model for RCS joints with beams and columns rigidly framed to the panel (Mehanny and Deierlein, 2000b). The shear and bearing mechanisms are modeled by two uniaxial materials in series (representing the panel shear distortion and the relative rotation of the beams and columns due to the bearing deformation mode). By employing the series spring material in OpenSees, Cordova and Deierlein (2004) have used the Joint2D-1SPR model to simulate RCS joints.

4.1.3 **Reinforced concrete structures**

The joint element is able to model shear deformation of the panel zone in RC joints, as well as the effects of bond slip or bar pullout at the beam-joint interface. The calibration process in this study is modeled after the American Concrete Institute joint committee (ACI 352-R02) provisions for the beam-column joints. The following limitations of the ACI provisions are assumed in this study: normal weight concrete in the joints, beam width is smaller than column width, and the beam and column centerlines are coincident.

Irregular design cases which do not satisfy these assumptions are listed in Chapter 6 as suggestions for future research. The calibration process is based on previous analytical and experimental studies and design guidelines (FEMA 356 and ACI 352-R02) to define the load-deformation response of the shear panel on the basis of material properties and joint geometry.

4.2 *Reinforced concrete joint calibration*

Gravity loading of a frame usually applies little joint shear due to small unbalanced moments at opposite sides of a joint, while lateral loading results in significant unbalanced moments and large joint shear (Figure 4-1). In particular, earthquake loading of a joint may result in substantial shear loading of the joint panel into inelastic zone. The shear forces acting on the joint panel zone are usually transferred as a combination of direct shear and the moment induced shear.

Direct shear refers to the shear force in a beam/column element, which is directly transferred to the shear panel (Figure 4-2). The transfer mechanism for direct shear is the same as the mechanism in beams or columns, i.e. friction stresses, aggregate interlock and dowel action. The shear deformation at the interface zone is minimal due to large section increase at the intersection of the frame member and the joint, and due to extra confinement provided by the adjacent members framed to the joint. Few data are available for use in evaluating a stiffness relationship for interface shear (Lowes and Altoontash, 2003). However as the interface deformations are assumed to be small, this deformation mode is not addressed in the proposed model.

The moment acting on an external face of a joint can be expressed as a tensile-compressive force couple, and the shear force induced by this force couple is referred to as the moment induced shear. The compressive component of the force couple is applied as compressive stress in the concrete and the rebar, while the tensile component is typically applied as tension in the rebar(s). The tensile component is transferred partly through bond stress between the flexural reinforcement and the shear panel, and partly though the compression at the opposite side of the joint (see Figure 4-3). The latter

mechanism (compression) tends to dominate once the bond-transfer mechanism deteriorates due to high bond stresses combined with severe cyclic loading. Degradation of the bond transfer leads to the slip which causes extra flexibility at the beam to joint interface. The member-end rotational springs are calibrated to represent the extra flexibility induced by the bond slip. Calibration of this mechanism is sensitive since even after just a few high magnitude cycles, severe bond degradation is likely. A pinching type material model best represents the bond-slip. Calibrating this model is complicated due to complexity of bond-slip mechanism; therefore some approximations and assumptions are necessary to provide a practical way to calibrate this model (Lowes et al., 2003b).

Using the joint equilibrium expressions, the direct shear and moment induced shear are superimposed and applied to the shear spring. The joint panel response is modeled through a constitutive relationship expressed in terms of shear force versus deformation. According to experimental and analytical data, this response can be represented by a peak oriented hysteretic model with pinched reloading path (Lowes et al., 2003a). The constitutive parameters for this material model are calibrated on the basis of the panel shear capacity and design details.

The initial approach for characterizing the shear-panel response was evaluating the experimental results. However, there are relatively few data sets available for joints with different ranges of material properties, geometries, reinforcement details, and cyclic load histories. Additionally, the approaches and instrumentation layouts used to measure the shear deformation, bond-slip, flexural yielding in beams and columns, and other highly localized deformations in the joint are not consistent between the available investigations. The considerable number of parameters influencing the joint response and lack of detailed experimental information to capture the influence of every individual parameter on the cyclic joint behavior makes it difficult to develop a unique calibration formula to provide an accurate response prediction for a joint with varying design configurations. On the other hand, there are analytical approaches that can help characterize the behavior of joint components within an acceptable range of experimental data.

In the current study, an algorithm is presented to derive the constitutive model for the shear panel, based on Modified Compression Field Theory (MCFT) (Vecchio and Collins, 1986) with some modifications to better define the envelope of shear stress versus strain of the joint core. The analytical and experimental data provided by Stevens et al. (1991) are used to define the cyclic response. The proposed procedure allows a user to calculate the constitutive parameters for a hysteretic material model, based on the material properties, the joint geometry, and joint reinforcing steel ratio (Figure 4-4).

The joint response depends on the material behavior (i.e. elastic and nonlinear behavior of steel and concrete), physical dimensions of the joint, design details and confinement provided at the joint core, and the reinforcing bar anchorage length and details. Experimental and analytical parametric studies (Filippou et al., 1984; Durrani and Wight, 1985; Ehsani and Wight, 1985; Bonacci and Pantazopoulou, 1993; Pantazopoulou and Bonacci, 1994) provide some useful information on the parameters that may influence the RC beam-column joint behavior.

4.2.1 **Shear behavior and the panel zone**

For beam column joints in a two-dimensional frame, the joint panel experiences planar shear loading. The major failure mechanisms observed in the laboratory tests are listed as yielding or fracture of transverse reinforcements, crushing of the concrete in compression, or slipping on the crack face. These failure mechanisms are captured and simulated by Modified Compression Field Theory (Vecchio et al., 1986). The Modified Compression Field Theory (*MCFT*) in the original form developed by Vecchio and Collins (1986) only characterizes the monotonic response of joint panel and the response envelope for cyclic loading. The MCFT is recommended to characterize the global response of reinforced-concrete panels subjected to uniform shear and uniform shear plus axial load.

The *MCFT* was later used for developing a constitutive model for RC finite element analysis (Stevens et al., 1991) and the theory is extended to Disturbed Stress Field Model for cracked reinforced concrete elements (Vecchio, 2000; Vecchio et al., 2001). The

MCFT assumes that the principal concrete stress direction coincides with the direction of principal strain, and the concrete compressive strength is reduced due to coexisting tensile strain in the normal direction (Figure 4-5). The *MCFT* is appropriate for use in defining the response of the shear panel since the panel zone shear behavior is determined by the response of previously cracked concrete carrying compression in the direction of the principal compressive stress and by the response of reinforcing steel carrying tension across concrete cracks that open in the direction of the principal tensile stress (Lowes 2002). These response mechanisms are incorporated into the *MCFT*. The analytical models used to verify the *MCFT* (Lowes 2003b) exhibit damage patterns and failure modes similar to those observed in joint test specimens (Lehman et al 2004, Pantelides 2002). The *MCFT* defines the shear-panel response as a function of concrete and steel material properties and vertical and horizontal ratios of the joint reinforcement.

Application of the *MCFT* to generate an envelope to the shear response history requires the introduction of some extra assumptions on the joint core response. The *MCFT* defines a plane stress constitutive model in which there is coupling between normal (axial) and shear response. The joint model is developed assuming that all joint loads, including column axial load, are transferred through the joint core.

The *MCFT* in the form proposed by Vecchio and Collins (1986) is extended to simulate the response under cyclic loading (Stevens et al., 1991); however the modifications by Stevens impose some level of sophistication that does not warrant the expected simplicity of a practical model for the joint simulation. For this study, the response envelope is derived by using *MCFT*, and experimental data provided by Stevens et al. (1991) are used to determine the unload–reload path. Concrete compressive strength is also reduced using the factor proposed by Stevens et al. (1991). A concrete tensile stress-strain response model is derived from the Stevens data (1991) and used in the current implementation of the *MCFT*.

Calibration of the material for the joint panel is not complete without characterization of the reversed-cyclic history. The cyclic behavior must represent a highly pinched stress-strain history due to the opening and closing of cracks in the confined reinforced

concrete. This behavior can be represented by the pinching uniaxial material model with unloading response defined to be equal to the initial stiffness and the reloading pinching point defined to occur at a shear strain equal to approximately 25% of the maximum hysteretic shear strain demand and shear strength. The Stevens data (1991) show an extremely pinched shear stress–strain history. This behavior is represented using the one-dimensional material model with parameters defined as follows:

- Unloading stiffness assumed to be equal to the initial stiffness
- The shear stress at which reloading occurs is defined to be zero
- The break point on the reloading path (the pinching point) is located at 25% of the peak-point deformation and 25% of the peak-point shear stress

MFCT calculates the panel response based on the concrete material properties, vertical and horizontal steel ratios in the joint panel, steel reinforcement material properties, and axial load on the joint panel. The application of *MCFT* requires the introduction of several assumptions regarding the axial and flexural response of the beam-column joint. It is assumed that all the unbalanced flexural load is transferred as shear through the joint.

Computing the shear-force versus deformation backbone: A computer program in MATLAB was developed for calculating the shear-force versus deformation backbone for reinforced concrete joints. The iterative method used in this procedure is based on the MCFT with some modifications and new assumptions. The variables used as input variables for calibrating the hysteretic material model for the joint panel can be summarized as:

P_{ver} Vertical gravity force on the joint (KN)

S_x Maximum distance of x reinforcement (M)

S_y Maximum distance of y reinforcement (M)

ρ_x Reinforcement ratio along x direction

ρ_y Reinforcement ratio along y direction

f_c' Concrete compressive strength (KPa)

E_c Concrete elastic modulus (KPa)

f_{yx} Yield stress for reinforcement along x direction (KPa)

f_{yy} Yield stress for reinforcement along y direction (KPa)

E_s Steel elastic modulus (KPa)

α_h Steel hardening ratio

a Maximum aggregate size (mm)

The MCFT algorithm was originally introduced by (Vecchio et al. 1986). In this research, the original algorithm is modified to capture the softening, using a displacement (deformation) controlled approach. The shear deformation (strain) is monotonically increased and the Newton-Raphson method (or for the softening branch the modified Newton method with initial tangent) is used to calculate the horizontal and vertical normal strains. The concrete material follows the modified Kent-Park model (Kent and Park, 1971) and the steel is assumed to be elastic-hardening plastic. The overall shear stress of the joint panel is assumed to be equal to the concrete shear. After convergence at each shear strain level, a check is performed to determine the possible shear failure mode (rebar yielding at the crack face, concrete failure in compressive mode, or slip along the crack face).

In this algorithm, horizontal and vertical stresses of σ_x and σ_y are assumed to be constant and they are determined from the external loading condition. γ_{xy} is the independent variable increasing form zero up to a limit point defined by one of the failure modes. ε_x and ε_y are calculated through an iterative modified Newton algorithm to satisfy the force boundary conditions. The outcome of this algorithm is the shear stress (τ_{xy}) envelope of the panel. The $\tau_{xy} - \gamma_{xy}$ in the MCFT is used to represent $V_{xy} - \gamma_{xy}$, assuming the shear stress and strain is uniform through the joint.

The MCFT algorithm for determining the $v - \gamma$ envelope (modified from Vecchio and Collins, 1986):

Step 1) Calculate the force boundary values and the initial values for ε_x and ε_y by the following equation:

$$f_x = \frac{P_{hor}}{A_{gx}} \tag{4.1}$$

$$f_y = \frac{P_{ver}}{A_{gy}} \tag{4.2}$$

$$\varepsilon_x = 0 \tag{4.3}$$

$$\varepsilon_y = \frac{P_{ver}}{A_{gy}.\left(1-\rho_{sy}\right).E_C + A_{gy}.\rho_{sy}.E_S} \tag{4.4}$$

where P_{hor} and P_{ver} are the horizontal (beam) and vertical (column)axial forces, A_{gx} and A_{gy} are the column and beam gross cross section areas, f_x and f_y are average horizontal and vertical normal stresses, and ε_x and ε_x are average joint panel horizontal and vertical strains, respectively (Figure 4-6), and other terms are input variables as defined previously .

Step 2) Initialize the shear strain $\gamma_{xy} = 0$

Step 3) Calculate the principal strains (ε_1 and ε_2) and the crack angle θ

$$\varepsilon_1 = \frac{\varepsilon_x + \varepsilon_y}{2} + \sqrt{\left(\frac{\varepsilon_x - \varepsilon_y}{2}\right)^2 + \left(\frac{\gamma_{xy}}{2}\right)^2} \tag{4.5}$$

$$\varepsilon_2 = \frac{\varepsilon_x + \varepsilon_y}{2} - \sqrt{\left(\frac{\varepsilon_x - \varepsilon_y}{2}\right)^2 + \left(\frac{\gamma_{xy}}{2}\right)^2} \tag{4.6}$$

$$\theta = \frac{1}{2} arctg \frac{\gamma_{xy}}{\varepsilon_x - \varepsilon_y} \tag{4.7}$$

Step 4) The average stress in concrete is derived for both the maximum and minimum principal strains.

For tension where $\varepsilon_1 > 0$:

- Prior to cracking when $\varepsilon_1 \le \varepsilon_{cr} = \frac{f_{cr}}{E_c} = 0.5 \times 10^{-4}$

$$f_{c2} = E_C . \varepsilon_1 \tag{4.8}$$

- After cracking when $\varepsilon_1 > \varepsilon_{cr}$

$$f_{c1} = \frac{f_{cr}}{1 + \sqrt{200 \varepsilon_1}} \tag{4.9}$$

For compression where $\varepsilon_2 < 0$

$$f_{c2} = f_{c2\max} \left[2 \left(\frac{\varepsilon_2}{\varepsilon_c'} \right) - \left(\frac{\varepsilon_2}{\varepsilon_c'} \right)^2 \right] \tag{4.10}$$

Where $f_{c2\max}$ for the given perpendicular strain ε_1 is:

$$\frac{f_{c2\max}}{f_c'} = \frac{1}{0.8 - 0.34 \frac{\varepsilon_1}{\varepsilon_c'}} \le 1.0 \tag{4.11}$$

ε_c' is a negative quantity, usually chosen $\varepsilon_c' = -0.002$.

Step 5) The stress in the horizontal (f_{sx}) and vertical (f_{sy}) reinforcing bars is calculated based on an elastic-plastic kinematic hardening plastic material model. Taking account of the signs, the model is described as:

$$f_{sx} = E_S \cdot \varepsilon_x \le f_{yx} + \alpha_h \cdot E_S \cdot \left(\varepsilon_x - \frac{f_{yx}}{E_S} \right) \tag{4.12}$$

$$f_{sy} = E_S \cdot \varepsilon_y \le f_{yy} + \alpha_h \cdot E_S \cdot \left(\varepsilon_y - \frac{f_{yy}}{E_S} \right) \tag{4.13}$$

Step 6) The concrete stresses in the global (*x*-*y*) coordinate system (f_{cx} and f_{cy}) is determined based on Mohr's stress transformation equations:

$$f_{cx} = \frac{f_{c1} + f_{c2}}{2} + \frac{f_{c1} - f_{c2}}{2} \cos 2\theta \tag{4.14}$$

$$f_{cy} = \frac{f_{c1} + f_{c2}}{2} - \frac{f_{c1} - f_{c2}}{2} \cos 2\theta \tag{4.15}$$

Step 7) Compute the trial horizontal and vertical stresses in the shear panel and check the convergence criteria:

$$f_x^{Trial} = f_{cx} + \rho_{sx}.f_{sx} \tag{4.16}$$

$$f_y^{Trial} = f_{cy} + \rho_{sy}.f_{sy} \tag{4.17}$$

If both $\left| f_x^{Trial} - f_x \right| < tol.f_x$ and $\left| f_y^{Trial} - f_y \right| < tol.f_y$, then the convergence conditions are satisfied and the Modified Newton-Raphson loop is terminated, and the process goes to step 10. Otherwise, the process continues to the next step.

Step 8) Recalculate the strains in global coordinate system

$$\varepsilon_x^{new} = \varepsilon_x^{old} + \frac{f_x - f_x^{Trial}}{\left(1 - \rho_{sx}\right) E_c + \rho_{sx}.E_s} \tag{4.18}$$

$$\varepsilon_y^{new} = \varepsilon_y^{old} + \frac{f_y - f_y^{Trial}}{\left(1 - \rho_{sy}\right) E_c + \rho_{sy}.E_s} \tag{4.19}$$

Step 9) Proceed to step 3 to recalculate the stresses and strains (step 3 to 8) with new values for horizontal and vertical strains.

Step 10) It is assumed that the entire shear stress (τ_{xy}) is carried by the concrete (implying $\tau_{sx} \approx 0$ and $\tau_{sy} \approx 0$), so:

$$\tau_{xy} \approx \tau_{cxy} = \frac{f_{c1} - f_{c2}}{2} \sin 2\theta \tag{4.20}$$

Step 11) Check for rebar yielding at the crack face, and calculate the shear (τ_{ci}) and normal compression stress (f_{ci}) on the crack:

$$\Delta f_{c1} = f_{c1} - \rho_{sx} \cdot \left(f_{yx} - f_{sx} \right) \tag{4.21}$$

If $\Delta f_{c1} \le 0$, then $\tau_{ci} = 0$ and $f_{ci} = 0$

If $\Delta f_{c1} > 0$, then $C = \frac{\Delta f_{c1}}{\tan\theta} - 0.18 \cdot v_{ci\max}$

If $C \le 0$, then $f_{ci} = 0$ and $\tau_{ci} = \frac{\Delta f_{c1}}{\tan\theta}$

where $v_{ci\max}$ is defined in equation (4.33). Otherwise:

$$A = \frac{0.82}{v_{ci\max}} \tag{4.22}$$

$$B = \frac{1}{\tan\theta} - 1.64 \tag{4.23}$$

$$f_{ci} = \frac{-Bb\sqrt{B^2 - 4AC}}{2A} \tag{4.24}$$

$$\tau_{ci} = \frac{\left(f_{c1} + \Delta f_{c1} \right)}{\tan\theta} \tag{4.25}$$

Calculate reinforcement stresses at crack face f_{sycr} and f_{sxcr}:

$$f_{sxcr} = f_{sx} + \frac{\left(f_{c1} + f_{ci} - v_i / \tan\theta \right)}{\rho_{sx}} \tag{4.26}$$

$$f_{sycr} = f_{sy} + \frac{\left(f_{c1} + f_{ci} + v_i / \tan\theta \right)}{\rho_{sy}} \tag{4.27}$$

If $f_{sycr} > f_{yy}$ yielding of the x-reinforcements at the crack face governs.

Step 12) Check for concrete failure in compressive mode.

If $f_{c2\max} > f_c' \cdot \frac{1}{0.8 - 0.34\frac{\varepsilon_1}{\varepsilon_c'}}$ the panel has failed in the compressive mode

Step 13) Check the slip along the crack face mechanism:

Determine the crack control characteristics of x and y reinforcements:

$$S_{mx} = 1.5 \times S_x \tag{4.28}$$

$$S_{my} = 1.5 \times S_y \tag{4.29}$$

Calculate the average crack width:

$$S_\theta = \frac{1}{\frac{\sin\theta}{S_{mx}} + \frac{\cos\theta}{S_{my}}} \tag{4.30}$$

$$w = \varepsilon_1 \times S_\theta \tag{4.31}$$

Calculate average tension in the concrete f_{c1}:

$$k = 1.64 - \frac{1}{\tan\theta} \geq 0 \tag{4.32}$$

$$\tau_{ci\max} = \frac{\sqrt{f_c'}}{0.31 + 21\dfrac{w}{a+16}} \tag{4.33}$$

f_{c1} has an upper limit. If $f_{c1} > \tau_{ci\max}\left(0.18 + 0.3k^2\right)\tan\theta + \rho_{sx}\left(f_{yx} - f_{sx}\right)$ the failure has happened due to slip on crack face.

Step 14) Increment the γ_{xy} and restart from step 3.

Step 15) Plot the calculated values of shear stress τ_{xy} versus shear strain γ_{xy}.

This algorithm used in sections 4.4 and 4.5 to analytically determine the parameters of the material model that represents the shear panel behavior. Figure 4-7 shows a typical application of the MFCT for modeling the beam-column joints in a frame (Section 4.4.2), where the results are used to define a multi-linear envelope for the shear panel material model. In addition to defining the response envelope, the probable shear failure mode is also be determined by using the MCFT algorithm, e.g. rebar yielding at the crack face, concrete failure in compressive mode, or slip along the crack face mechanism.

4.2.2 **Member-end rotation**

The member-end rotational springs are calibrated to capture the effects of reinforcing bar yielding and bond slip in the joint. A simple, yet practical calibration procedure is presented here to determine the moment-rotation properties of the member-end springs. It is assumed that adequate development length is provided for the reinforcing bar to prevent complete pull-out. Ideally the joint size is larger than the development length of the reinforcement bars and complete anchorage is provided within the joint, but typically the joint sizes is not sufficient enough and the beams are anchored into the opposing beam framing into the connection, Or in exterior or continuum joints, the beam are installed with a 90 degree hook.

4.2.2.1 *Bond slip*

A constitutive model is developed to define the load-deformation history of the bond-slip springs that simulate inelastic anchorage-zone response (Figure 4-8). One possible approach for defining the bar stress–slip relationship is to use data from experimental testing of joint subassemblies. However, there are relatively few experimental investigations that accurately report bar slip data. Experimental measurement of bar slip requires a relatively sophisticated instrumentation setup and the adoption of a definition as to what constitutes slip. Measurement of experimental bar stress requires the use of steel strain gauge data and an assumed hysteretic material model or an assumption about the stress distribution across the beam or column cross section. These factors limit the availability of experimental data, the objectivity of the available data, and the generality of a model developed on the basis of these data. Given this situation, in the current study, a model is developed using data from experimental testing of anchorage-zone specimens and assumptions about the bond-stress distribution within the joint. This approach enables the use of a much larger data set and provides a bar-stress versus slip model that can be generally applied in general for simulating joint response.

Average bond strength values are defined on the basis of experimental data provided by previous investigations. Average bond strength values for regions where the reinforcing bar is elastic are computed using the empirically defined maximum bond strength for elastic reinforcement, the bond-stress versus slip model proposed by Eligehausen et al. (1983), and the assumption that zero to maximum bond strength is developed along the elastic length.

Four different average bond strength values are proposed for the four different bond zone conditions that may develop within the joint (Table 4-1). The results of the experimental investigation by Eligenhausen et al. (1983) are used as a basis for defining the bond strength for an elastic reinforcing bar loaded in tension. For a beam longitudinal reinforcing bar anchored in a joint and stressed in tension to a level that does not exceed the yield stress, the concrete in the vicinity of the bar is expected to carry compression or tension with limited crack width (Figure 4-8). Such anchorage-zone conditions are not

expected to reduce bond strength significantly from values obtained in classical bond studies, such as the Eligenhausen study (1983), that use specimens with short anchorage lengths and initially undamaged anchorage zone concrete.

Table 4-1: Average bond stress

Notation	$\mu_{average}(MPa)$	Steel strain	Description
μ_{te}	$2.0\sqrt{f_c'}$	$0 < \varepsilon_s \le \varepsilon_y$	Tension-Elastic
μ_{tp}	$0.5\sqrt{f_c'}$	$\varepsilon_s > \varepsilon_y$	Tension-Post yield
μ_{ce}	$3.1\sqrt{f_c'}$	$-\varepsilon_y \le \varepsilon_s < 0$	Compression-Elastic
μ_{cp}	$3.1\sqrt{f_c'}$	$\varepsilon_s < -\varepsilon_y$	Compression-Post yield

Figure 4-9 shows the proposed bar-stress versus slip envelope (Lowes and Altoontash, 2002) as well as envelopes computed from experimental data provided by the case of monotonic loading. Cyclic response extension of the monotonic bar-stress versus slip history for the case of reversed-cyclic loading requires calibration of the unload–reload path and the hysteretic damage rules (Lowes et al. 2002):

- **Unloading stiffness:** assumed equal to the elastic stiffness.

- **Residual bar stress:** computed assuming that a uniform residual bond stress of $0.15\sqrt{f_c'}(MPa)$ $(1.6\sqrt{f_c'}(psi))$ to represent data provided by Eligehausen et al. (1983).
- **Slip at which reloading occurs as a fraction of maximum historic slip:** defined to be 0.25 to represent Eligenhausen et al. (1983) and Hawkins (1982) data.
- **Force at which reloading occurs as a fraction of the force developed at the maximum historic slip:** defined to be 0.25 to represent Eligenhausen et al. (1983) and Hawkins et al. (1982) data.

4.2.2.2 *Rebar pull out*

The crack opening at the beam/joint interface (causing member-end rotations) is related to the bond-slip behavior. The envelope to the bar-stress versus slip relationship is developed through a bond-slip formulation with several simplifying assumptions. The first assumption is that there is uniform bond stress along the anchored length of a reinforcing bar that remains elastic and along the length of the reinforcing bar that is loaded beyond its yield stress (though the magnitude of bond stress is different in each region). Second, slip is assumed to define the relative movement of the reinforcing bar with respect to the concrete at the face of the joint. The slip is calculated as a function of the strain distribution along the bar. Third, the bar is assumed to exhibit zero slip at the point of zero-bar stress (i.e. once full development length is achieved). This approach is similar to that used by Filippou and Popov (1984), and Mazzoni (1997).

Figure 4-8 shows an idealization of the bond stress and resulting bar stress distribution for an anchored bar loaded beyond yield. Parameters identified in Figure 4-8 are defined in the following paragraph. Employing the simplifying assumptions described previously, the bar-stress versus slip relationship is defined as outlined bellow:

The first step of this procedure involves formulating the pullout behavior of a single rebar and then it observes the behavior in a reinforced concrete section. The rebar is assumed to be completely bounded in concrete, and the reinforcement steel is assumed to be elastic-hardening plastic. The slip is calculated separately for the rebar pre-yielding and post-yielding states, where the bar stress is defined as:

$$\sigma_s = \begin{cases} E \cdot \varepsilon & \varepsilon \le \varepsilon_y \\ \sigma_y + \alpha \cdot E \cdot \left(\varepsilon - \varepsilon_y\right) & \varepsilon > \varepsilon_y \end{cases} \tag{4.34}$$

Pre-yielding: For the pre-yielding case where $\sigma_s \le \sigma_y$ the tensile force of the rebar is balanced by the bond force along the stress penetration depth. The stress penetration length, L_d is the length that stress of the rebar is completely transferred to the concrete

and it is assumed to be totally anchored. The reinforcement bar tensile force is calculated for average bond stress as:

$$F_s = \sigma_s \times \frac{\pi \cdot D^2}{4} = \mu_{te} \cdot \pi \cdot D \cdot L_d \tag{4.35}$$

where, μ_{te} is determined on Table 4-1, D is the bar diameter, and L_d is the development length of the bar to transfer the tension to concrete through bond stress. Equation (4.35) can be rearranged to calculate L_d as:

$$L_d = \frac{F_s}{\mu_{te} \cdot \pi \cdot D} = \frac{\sigma_s \cdot D}{4\mu_{te}} \tag{4.36}$$

Based on equilibrium, it is possible to calculate the rebar stress at any location (x) from the anchorage point by integrating the bond stress from:

$$\sigma_s\big|_x = \frac{4\mu_{te} \cdot x}{D} \tag{4.37}$$

where x is the distance from the anchorage point. The bar strain at this location is calculated as:

$$\varepsilon_s\big|_x = \frac{4\mu_{te} \cdot x}{E_s \cdot D} \tag{4.38}$$

The *slip* is defined as the deformation in the reinforcement bar at the crack face. The slip is calculated by integrating the bar deformation:

$$slip = \int_0^{L_d} \varepsilon_s\big|_x \, dx = \frac{2\mu_{te} \cdot L_d^2}{E_s \cdot D} = \frac{2F_s^2}{\mu_{te} \cdot E_s \cdot \pi^2 \cdot D^3} \tag{4.39}$$

For convenience, the following constant is defined for the pre-yield rebar slip relationship: for convenience of formula presentation.

$$C_{te} = 0.5\pi^2 \cdot \mu_{te} \cdot \alpha E_s \cdot D^3 \tag{4.40}$$

Using this, the slip can be expressed as:

$$slip = \frac{F_s^2}{C_{te}} \quad F_s \le F_y \tag{4.41}$$

Post-yielding: The post-yielding case is more complicated since there are two levels of bond resistance (μ_{te} and μ_{ty}) with their associated bond lengths (L_d and L_{yd}). The bar stress and bond lengths are calculated by the following:

$$F_s = \sigma_s \times \frac{\pi \cdot D^2}{4} = \mu_{te} \cdot \pi \cdot D \cdot L_{ed} + \mu_{ty} \cdot \pi \cdot D \cdot L_{yd} \tag{4.42}$$

$$L_d = L_{ed} + L_{yd} \tag{4.43}$$

Where $L_{ed} = \frac{F_y}{\mu_{ts}.\pi.D}$ and $L_{yd} = \frac{F_s - F_y}{\mu_{ty}.\pi.D}$

Based on equilibrium, it is possible to calculate the rebar stress at any location (x) from the anchorage point:

$$\sigma_s\big|_x = \begin{cases} \dfrac{4\mu_{te}.x}{D} & x \le L_{ed} \\ \dfrac{4\mu_{ty}}{D}(x - L_e) + \sigma_y & L_{ed} < x \le L_{ed} \end{cases} \tag{4.44}$$

$$\varepsilon_s\big|_x = \begin{cases} \dfrac{4\mu_{te}.x}{E_s.D} & x \le L_{ed} \\ \dfrac{4\mu_{ty}}{\alpha.E_s.D}(x - L_e) + \dfrac{\sigma_y}{E_s} & L_{ed} < x \le L_{ed} \end{cases} \tag{4.45}$$

$$slip = \int_0^{L_d} \varepsilon_s\big|_x dx = \int_0^{L_{ed}} \frac{4\mu_{te}.x}{E_s.D} dx + \int_{L_{ed}}^{L_d} \left[\frac{4\mu_{ty}}{\alpha.E_s.D}(x - L_e) + \frac{\sigma_y}{E_s} \right] dx \tag{4.46}$$

$$slip = \frac{2\mu_{te} \cdot L_{ed}^2}{E_s \cdot D} + \frac{2\mu_{ty}}{\alpha \cdot E_s \cdot D}\left(L_d^2 - L_{ed}^2\right) - \frac{2\mu_{ty} \cdot L_e}{\alpha \cdot E_s \cdot D}\left(L_d - L_{ed}\right) + \frac{\sigma_y}{E_s}\left(L_d - L_{ed}\right) \quad (4.47)$$

Another constant is defined for post-yield rebar slip relationship:

$$C_{ty} = 0.5\pi^2 \cdot \mu_{ty} \cdot \alpha E_s \cdot D^3 \quad (4.48)$$

$$slip = \frac{F_y^2}{C_{te}} + \frac{1}{C_{ty}}\left[F_s^2 + (1-2\alpha)F_y^2 + (2\alpha - 2)F_s \cdot F_y\right] \quad F_y < F_s < F_u \quad (4.49)$$

The resulting slip-rebar force relationships are plotted and simplified to a bilinear model. For the case of development length greater than the width of the joint, when the rebar is anchored into the opposing frame member, the deterioration of bond strength within the joint zone will be much more severe under cyclic loading due to the shear damage at the panel zone. In this case, it may be appropriate to assume reduced bond strength for the full length of rebar embedded in the joint (i.e. the bond stress for the post yielding state), which results in more flexibility for the member-end rotation springs. Based on the calibration study on cases with slip as the dominant failure mechanism, it is suggested to reduce the post-yield average bond stress.

The bar-stress versus slip relationship defined by the bilinear model monotonically increases. However, experimental data indicate that bond strength deteriorates once a slip limit is exceeded (Eligenhausen et al., 1983), and it is assumed that the bond strength deteriorates once slip exceeds 3 mm (0.1 in.), and post peak stiffness is defined equal to 10% of the initial stiffness. These assumptions are consistent with the results of previous studies (Eligenhausen et al., 1983; Lowes, 1999).

Constitutive rules for the member-end rotation springs are derived by using a modified fiber section analysis that accounts for the bond-slip behavior.

4.2.2.3 *Modified section for the rotation at the connection face*

The moment-rotation diagram of the beam or column interface is derived by a fiber section model analysis. It is assumed that the beam (or column) is connected to a reinforced concrete support. This reinforced concrete support provides confinement for the concrete and complete development lengths for the longitudinal reinforcements, so as to limit deformations to the pull-out effects. The computational results of the fiber analysis are then used to calibrate a uniaxial material model or to develop a section that represents the effects of rebar pull-out.

The calibration process requires a series of modifications to the beam or column fiber sections to represent the bar pull-out mechanisms. The section analysis is performed on a unit length section, where the section displacements are equal to the strains and the curvatures are identical with the rotations. The calculated curvatures must then be scaled to the effective stress dissipation depth, so that the unit length section represents the actual rotation.

The effective depth of the section is defined as the depth that the effects of the axial stresses due to bending are totally dissipated through bond transfer. Based on calibration studies, the development length of the embedded reinforcement bars is recommended as the effective depth. The actual member-end rotation mechanism is compared with the analytical equivalent section (Figure 4-10), where L_{eff} is assumed to be:

$$L_{eff} = \frac{F_u - F_y}{\mu_{ty} \cdot \pi \cdot D} + \frac{F_y}{\mu_{ts} \cdot \pi \cdot D} \tag{4.50}$$

where $F_u = A_s \cdot \sigma_u$ is the reinforcement bar ultimate tensile force.

A bilinear (steel) uniaxial material model is used for the rebar pull-out. The material properties are derived based on the bar pull-out formulation and a scaling factor for the effective stress. The stress-pullout deformation plot of a rebar is calculated based on the

formulation derived in the previous section. The relationship can be represented by a bilinear model which must be scaled for the unit-length section analysis.

The equivalent stiffness based on the pull-out can be calculated as:

$$K_{slip} = \frac{F_{rebar}}{\Delta_{pullout}} = \frac{\sigma_{rebar} \cdot A_{rebar}}{\Delta_{pullout}} \tag{4.51}$$

where K_{slip} is an average stiffness for the bar pull-out mechanism. The slip mechanism occurs along the development length. If the slip-force relation for the pull-out mechanism is defined in a stress-strain domain, the equivalent elastic modulus is calculated as:

$$E_{slip} = \frac{\sigma_{rebar}}{\varepsilon_{slip}} = K_{slip} \cdot \frac{L_{developement}}{A_{rebar}} \tag{4.52}$$

The fiber section formulation allows analyzing a unit-length fiber section to compute the moment-curvature relationships. The moment-rotation a reinforced concrete member with the development length is modeled by an equivalent unit-length fiber section. The stiffness of the materials used in the equivalent section must be scaled in such a way that the deformations are correctly calculated. The unit-length model and the original RC section with the development length have equal force, hence, force scaling is not required. The scaled stiffness is calculated, assuming both models have equal stress for equal deformation:

$$\Delta = \varepsilon_{devlength} \cdot L_{devlength} = \varepsilon_{unit} \cdot L_{unit} \tag{4.53}$$

so the strain of the unit-length fiber model is calculated as:

$$\varepsilon_{unit} = \frac{\varepsilon_{devlength} \cdot L_{devlength}}{L_{unit}} \tag{4.54}$$

For both models to have equal stresses, it is assumed:

$$\sigma = E_{devlength} \cdot \varepsilon_{devlength} = E_{unit} \cdot \varepsilon_{unit} \tag{4.55}$$

By combining equations (4.54) and (4.55) the equivalent elastic modulus for the unit-length model is calculated as:

$$E_{unit} = E_{devlength} \cdot \frac{L_{unit}}{L_{devlength}} \tag{4.56}$$

The pullout stiffness can be implemented to the unit-length model as:

$$E_{unit} = K_{slip} \cdot \frac{L_{developement}}{A_{rebar}} \cdot \frac{L_{unit}}{L_{developement}} = K_{slip} \cdot \frac{L_{unit}}{A_{rebar}} \tag{4.57}$$

The concrete fibers of the modified section are defined by a concrete uniaxial material with properties for fully confined concrete. The stiffness of the concrete materials is also modified for the unit-length section by scaling the strains of the concrete material model:

$$\varepsilon_{unit} = \varepsilon_{concrete} \cdot \frac{L_{developement}}{L_{unit}} = \varepsilon_{concrete} \cdot DepthRatio \tag{4.58}$$

where ε_{unit} is the scaled strain, and $\varepsilon_{concrete}$ is the original concrete strain. This scale will be used for both the maximum, and the ultimate concrete strains.

The *Depth Ratio* will be used to modify the material properties of the unit-length fiber model, where as the *Depth Ratio* is defined as:

$$DepthRatio = \frac{L_{developement}}{L_{unit}} \tag{4.59}$$

Tri-linear material models are fitted to the moment-curvature results of the modified section analysis. These materials are then used to represent the member-end rotation spring property.

4.3 *Calibrating the damage models*

Calibration of the damage model is based on experimental observation of components under both monotonic and cyclic loading. The first step in this process is to choose a damage model suitable for the observed component. The response of the structural component is then used to calculate the engineering parameters that are fed to the damage model (e.g. force, deformation, and energy values). The damage state of the experimental specimen is typically based on its physical condition and its remaining capacity. A correlation between the engineering parameter and the damage index helps to determine the calibrating parameters for the selected damage model. A damage investigation is presented later in Section 4-6 to calibrate the joint damage (Figure 4-16).

The ultimate plastic deformation is determined by continuing the softening branch of the monotonic loading envelope to the total strength loss, or the failure deformation (if known). The ultimate energy for monotonic loading is determined by the integrating the area under the force-deformation diagram up to the ultimate deformation.

The calibration parameters are suggested as:

- For Park-Ang model: $\alpha = 1$ and β depends on the design detains, $\beta = 0.1$ is suggested for seismic detailed, and $\beta = 0.25$ is suggested for joints with no transverse reinforcement.
- For Mehanny-Deierlein model: $\alpha = 1$, $\beta = 1.5$, and $\gamma = 2.0$ are suggested for reinforced concrete (Mehanny and Deierlein, 2000).

4.4 *Validation problems*

4.4.1 RC beam-column subassemblies with older (pre-1970's) detailing

For verification purposes, the joint element is employed for analyzing a test series of reinforced concrete joints. In the verification/calibration process, appropriate uniaxial material models are selected and their parameters were analytically determined for Interior beam-column joints with older (pre-1970's) detailing. Test results for seven

specimens were acquired from a research team at the University of Washington. The detailed descriptions for the model details and laboratory results are documented by Walker et. al. (2004). The models are detailed to represent samples of pre-1970's design recommendation for RC joints, i.e. joint without transverse reinforcements in the joint zone. Two sets of specimens are designed for two different levels of nominal joint shear capacities. The average joint shear stress is limited to the nominal joint shear capacity calculated by Equation (4.60) or (4.61).

$$v_{j1} = \tau_1 . f_c' \tag{4.60}$$

$$v_{j2} = \tau_2 . \sqrt{f_c'} \tag{4.61}$$

The key parameters for the specimens are summarized in Table 4-2. As shown in the table, Four specimens were designed for the target shear stresses of $0.82\sqrt{f_c'}$ (MPa) and three for $1.29\sqrt{f_c'}$ (MPa).

Table 4-2: Physical properties of specimens

Specimen	$f_c'(MPa)$	$f_y\,(MPa)$	Target τ_1	Target τ_2
PEER-14	37.8	450	0.14	0.82
CD15-14	29.8	450	0.14	0.82
CD30-14	42.5	450	0.14	0.82
PADH-14	42.9	450	0.14	0.82
PEER-22	38.4	527	0.22	1.29
CD30-22	38.1	516	0.22	1.29
PADH-22	36.3	527	0.22	1.29

The specimens were subjected to four different load histories. A major feature of the experimental results is to evaluate the separate effects of the nominal joint capacity and the loading regime on the performance. The specimens for each target shear stress demand are nominally identical, though there were variations in the as-built conditions. For example, the material test shows some variability in the actual material strength. Figure 4-11 shows the test setup for the interior joint subassemblies.

The four displacement histories (PADH, PEER, CD15, and CD30) are illustrated in Figure 4-12. The Pulse Asymmetric Displacement History (PADH) displacement history begins with a positive half cycle to the maximum extend of deformation (5% drift) in the experimental study. The PADH loading protocol was intended to reflect the pulse characteristics of a near-fault ground motion. Response to the PADH history proved to be a rich source of information for developing behavioral rules for analytical models, which require a monotonic envelope and information about response to asymmetric load cycles. The PEER displacement history consists of increasing cyclic deformations with three cycles at each deformation level. CD15 and CD30 consisted of many cycles at Constant Displacement amplitude of ±1.5% or ±3.0% drift, with the goal of determining the effect of a long duration earthquake. In the CD15 history the constant displacement cycles were followed by a series of asymmetric cycles intended to demonstrate the effect of loading in one direction on the strength in the other. These cyclic load histories are used to validate the joint model and select and calibrate a damage index for the joint response.

The normalized measured joint shear stress versus joint shear strain is plotted for all seven specimens Figure 4-13. The MCFT algorithm (moment equivalent shear is calculated by multiplying the shear stress to the joint volume) is used to define the material parameters for the shear panel (Figure 4-14).

The MCFT has a major limitation for problems with no transverse reinforcement in the panel zone. Once the tensile stress in concrete exceeds the cracking stress, there will not be any tensile resistance. In such cases, the panel will immediately crack along the diagonal and the MCFT algorithm will not converge. For beam-column joints the problem is different since even without transverse joint reinforcement, the longitudinal reinforcement provides some resistance and holds the joint panel together. In this sense, the longitudinal reinforcement acts as transverse reinforcement. The beam and column longitudinal reinforcements at the perimeter of the shear panel also provide some confinement to the concrete panel.

Based on the calibration study performed on the joints without transverse reinforcement, it is proposed to consider **40%** to **50%** of the beam or column longitudinal reinforcement

at the panel perimeter as effective transverse reinforcement that can be incorporated into the MCFT algorithm. Thus the only calibration parameter introduced for modeling the joint shear panel without transverse reinforcement is the recommended percentage of the cross sectional area of the beams or columns longitudinal reinforcement at the panel perimeter. Otherwise, all the required MCFT parameters are determined based on the physical properties of the joint. The calibration ratio of longitudinal bar participation is derived by minimizing the relative difference of the MCFT results and the measured joint strength. For the seven tests calibrated in this study, a longitudinal participation percentage of **45%** results in the minimal relative difference between the measured and calculated joint shear strength. The calculated and measured joint strengths (M_{1j} as a function of f_c' or M_{2j} as a function of $\sqrt{f_c'}$), are compared in Figure 4-15.

The backbones for the shear panel and interface rotations are derived as outlined in Section 4.3. The Pinching material model with the Park-Ang deterioration rule is used to represent shear panel and interface rotations. Specific modeling recommendations are summarized in Section 4.4.3.

The absence of transverse reinforcement within the joint zone results in the sensitivity of these specimens to cyclic loading. Therefore, the deterioration modeling parameters play a significant role in the simulated behavior. The *Park-Ang* damage model is selected after performing a damage analysis and comparing the outcomes with the *Normalized Peak* and *Mehanny* models (Figure 4-16 to Figure 4-20). The ideal cyclic damage model will return the same damage index for a given physical damage. While some discrepancies were observed for the damage models tested for this study, the inconsistencies in the damage index versus physical damage are partially due to the method used for observing the physical damage in the laboratory. The observed damages are reported at the peak of the loading cycle, which may be different with the exact damage time. For example, damage descriptor of 20% strength loss was always reported at a fixed maximum drift (5%), and thus, was biased by the chosen loading protocol.

The average coefficient of variation (*COV*) of the damage indices for a given physical damage is used to compare the damage models. The Park-Ang (*COV* 30.4%) and

Normalized Plastic Deformation (*COV* 28.8%) damage models show better agreement with the physical damage, compared to the Mehanny model (*COV* 60.2%). The Park-Ang damage model has the advantage of taking into account the cyclic damage, as well as the damage due to excessive deformation.

Displacement-based nonlinear beam-column elements with fiber sections are used to model the beams and columns. The fiber sections are aggregated form Giuffre-Menegotto-Pinto steel and Kent-Park concrete material models (refer to Section 4.4.2 for more details).

The force-deformation results for seven specimens are presented in Figure 4-21 to Figure 4-27. The results show considerably good agreement with the test results.

4.4.2 **0.7 scale two-story RC test frame**

Most analytical and experimental studies on RC joint behavior have been done on statically determinate beam-column subassemblies. To investigate the interaction of joint response with that of the overall structure, this part of the study deals with development of a detailed analytical model to present the behavior of a reinforced concrete frame. The results demonstrate the influence of the joint and member-end rotations on the overall frame behavior. This model will also be used as the testbed for the reliability studies in Chapter 5.

The frame study utilizes test data from a 0.7 scale RC frame single-bay two-story frame that was built and tested at the National Center for Research on Earthquake Engineering laboratory in Taiwan (Tsai et al., 2001). The measured records of actuator forces and floor displacements are reported. In this study, a push over, cyclic load history, cyclic displacement history, and transient time history analysis are performed.

Figure 4-28 shows the test frame, instrumentation and the actuators. The characteristics of the analytical model are summarized as:

- Two-dimensional model
- Column-base rotation is allowed by adding a zero-length section

- Nonlinear displacement-based beam-column elements with fiber sections
- Realistic material models introduced for steel and concrete, using the smooth curves rather than multi-linear material models
- Beam-column joints are represented by the Joint2D element
- Geometric nonlinear model with P-Delta effects and updating nodal coordinates
- Push over displacement-controlled analysis
- Time history analysis by applying prescribed floor displacements

Nodal tags and element connectivity for the analytical model are shown in Figure 4-29. The structural model is configured in OpenSees and in multiple files to encapsulate each part of the model for parametric investigations. All the variables are introduced in a separate file for more convenient parameter modification. The domain components and analysis objects are constructed based in these variables.

Two fiber sections are defined separately for beams and columns. The T-beam section is designed to represent beam-slab interaction, and it is constructed by the beam with two layers of reinforcement and the slab with its longitudinal bars. The concrete material properties for the cover of the beam and the slab are set for the unconfined concrete with zero tensile strength and unconfined compression strength after reaching the maximum strain. The beam core is confined by the action of the hoops, and the properties of the core concrete are calculated based on the Kent-Park models (1971), allowing some tensile strength. The physical width of the slab is large and it is likely that the whole slab is not engaged in the T-beam action. Based on the ACI recommendation (ACI-318, 2002), the effective width of the slab is assumed to be four times the beam width. The fiber sections include a large number of fibers to capture the high gradient of stresses, and strain due to crack opening effects. Approximately 50 fibers are used for strong axis bending of each section (Figure 4-30). The column section is also constructed by a confined concrete core, unconfined cover and the reinforcements distributed in the perimeter. The confined concrete core of the columns follows the modified Kent and Park stress-strain curve.

The Giuffre-Menegotto-Pinto model (FEDEAS, 2004) with isotropic strain hardening is used for all the reinforcement bars. The material model used for both cover and core concrete is constructed using uniaxial Kent-Scott-Park concrete material object with degraded linear unloading/reloading stiffness, tensile strength and linear tension softening. Figure 4-31 shows the uniaxial material model for the confined reinforced concrete.

The core concrete for both beam and column core is assumed to be confined. The parameters for the column core concrete confined by rectangular hoops are originally proposed by Kent and Park (1971) and modified by Scott et al. (1980)

The modified Kent and Park relation calculates the peak compressive stress and ultimate strain based on the following material and geometry parameters:

f_c' Concrete compressive cylinder strength (MPa)

f_{yh} Yield strength of hoop reinforcement (MPa)

ρ_s Ratio of volume of hoop reinforcement to volume of concrete core

h'' Width of concrete core measured to the outside of the hoops (mm)

s_h Spacing between hoop reinforcements (mm)

The concrete stress (f_c) is calculated for a given strain (ε_c) as:

For $\varepsilon_c \le 0.002K$

$$f_c = K \cdot f_C' \left[\frac{2\varepsilon_c}{0.002K} - \left(\frac{\varepsilon_c}{0.002K} \right)^2 \right] \tag{4.62}$$

and for $\varepsilon_c > 0.002K$

$$f_c = K \cdot f_C' \left[1 - Z_m \left(\varepsilon_c - 0.002K \right) \right] \ge 0.2Kf_c' \tag{4.63}$$

Where

$$K = 1 + \frac{\rho_s f_{yh}}{f_c'} \tag{4.64}$$

$$Z_m = \frac{0.5}{\frac{3 + 0.29 f_c'}{145 f_c' - 1000} + \frac{3}{4}\rho_s \sqrt{\frac{h''}{s_h}} - 0.002K} \tag{4.65}$$

The peak stress $\sigma_{peak} = K \cdot f_c'$ happens at $\varepsilon_{peak} = 0.002K$

The ultimate concrete compressive stress is taken as $\sigma_{ultimate} = 0.2K \cdot f_c'$, so:

$$\varepsilon_{ultimate} = \frac{0.8}{Z_m} + 0.002K > 0.004 + 0.9\rho_s \left[\frac{f_{yh}}{300}\right] \tag{4.66}$$

The tensile strength for confined concrete is

$$f_{ct} = 0.25\sqrt{f_C'} < K.f_c'\left[1 - Z_m\left(\varepsilon_c - 0.002K\right)\right] \tag{4.67}$$

The parameters for cover concrete are defined by the unconfined concrete properties where $f_{yh} = \rho_s = 0$ with no tensile strength (i.e. $f_{ct} = 0$).

The dimensions and properties used for calibrating the hysteretic material model for the joint panel can be summarized as:

The physical properties of the panel zone are fed to the modified-compression field theory algorithm and a shear versus shear-deformation relationship for the panel zone is extracted. A bilinear backbone curve with strength capping is fitted to this curve. The regression information is then used as the material model properties for the joint shear springs.

$P_{ver} = 850KN$

$S_x = 0.09m$ $\qquad$ $S_y = 0.306m$

$\rho_x = 0.0212$ $\qquad$ $\rho_y = 0.0345$

$f_{yx} = 276MPa$ $f_{yy} = 414MPa$

$E_s = 2.07 \times 10^5 MPa$ $\alpha_h = 0.1$

$f_c' = 24.157MPa$ $E_c = 2.304 \times 10^4 MPa$

$a = 19mm$

The characteristic information are applied to the rebar-pullout formulation and a constitutive model for single bar pullout is extracted for both beam and column sections. These characteristic models are used for section analysis that yields the moment-rotation relationship for the member-end rotational springs.

The beams linked to the actuators are modeled with elastic elements (elements 7 connecting nodes 9 and 10, and element 10 connecting nodes 19 and 20). The sections and material model parameters for equivalent elastic sections are calculated based on ACI318-R02 recommendations.

$f_c' = 24.03Mpa$

The specified effective stiffness coefficients for beams and columns recommended by FEMA-273 are as follows:

$$EI_{eff}\Big|_{beam} = 0.35 \cdot E_c \cdot I_g \tag{4.68}$$

$$EI_{eff}\Big|_{column} = 0.7 \cdot E_c \cdot I_g \tag{4.69}$$

Several approaches are considered for modeling the nonlinear frame behavior with distributed plasticity. The force based nonlinear beam-column element and the displacement based element are applied to the structural model.

The force based distributed plasticity frame element of OpenSees allows the user to introduce a single element with multiple sections at the location of integration points to model a beam-column member undergoing plastic deformation. This element uses a flexibility formulation that interpolates the force between the sections. The iterative

flexibility solution inside the element may encounter problems due to numerical inverting the stiffness of sections with no strength left. Adding the flexibilities and the subsequent inversion to get element stiffness may also be problematic.

The nonlinear displacement-based beam-column element of OpenSees is a more reliable choice for modeling the beams and columns. In contrast with the force based element, each beam or column member must be modeled by multiple elements for better accuracy and capturing more realistic results. Each frame member is modeled by five or six displacement-based elements to help the model achieve a well behaved and accurate result comparable to a single fore-based nonlinear element with five integrations points.

The column-base rotation is captured by a zero-length section with modified properties as described in the member-end rotational spring properties.

The initial analysis is performed for the gravity loads. Gravity nodal loads are gradually applied at the top of the columns and the element forces are stored while the time step is set to back to zero. A Newton nonlinear solution algorithm is applied and the norm of displacement increments is used as convergence measure. Since the system remains in the elastic range, there is no need for a large number of load steps. All the analysis objects for the gravity analysis are removed at this point and new objects are introduced separately for push over, time history and transient analyses.

The analysis modules for the nonlinear analysis including the following:

- Degree of freedom number generator for minimizing the bandwidth using reverse Cuthill-Mackee algorithm.
- Constraint handler for transformation or penalty formulation
- Linear equation solver for general sparse system of equation with pivoting
- Integrator for the nonlinear predictor-corrector algorithm, using the load-controlled, the displacement-controlled or the arc-length method
- Nonlinear solution algorithm using the Modified Newton algorithm, the Newton algorithm or the Newton algorithm with line-search capabilities

- Convergence criteria by testing and comparing the norm of unbalance residuals, norm of displacement increment, or the norm of energy increment
- Analysis type for static analysis or dynamic analysis with the effects of inertia forces.

The pushover analysis is performed by applying an initial load to the floor levels and increasing these loads proportionally until the structure loses its load-bearing capacity. A displacement-controlled integrator monitors the displacement increment at floor levels to let the structure reach the softening parts with reasonable convergence rate. To achieve convergence in cases where the system cannot meet the tolerance criteria, the displacement increment size is reduced and the initial stiffness is used for the Newton algorithm.

The displacement controlled nonlinear analysis is performed by importing the lateral displacement (at the actuator level) histories from the input files and imposing the displacements to the nodes at each floor level. The analysis starts with a Newton algorithm and lowest level of convergence tolerance. To guarantee the solution convergence, the solution algorithm may be switched to either the Newton method with initial stiffness, the Krylov-Newton method, or the Newton method with line search. In cases where none of the nonlinear solution algorithms can solve the problem, it is necessary to increase the tolerance temporarily for a single step. The robust combination of nonlinear solution algorithms helped achieving convergence for the analysis. The results of the displacement controlled nonlinear analysis (Figure 4-35 and Figure 4-36) show good agreement for the frame lateral resistance.

The force controlled nonlinear analysis is performed by importing the actuator forces from the input files, and apply forces to the nodes in the model where actuators are connected. The analysis classes are similar to the displacement-based model, i.e. beginning with the Newton algorithm and switching to the modified Newton method, Krylov-Newton, or Newton method with line search, whenever required. The integrator is set to Load-Control initially, but it switches to Arc Length method when the convergence is not achieved (softening occurs). The results of the load controlled nonlinear analysis

(Figure 4-37 and Figure 4-38) show good agreement for the frame stiffness and lateral resistance.

In the transient analysis, two earthquake acceleration records (Loma Prieta 1989 and Chi-Chi 1999 earthquakes) are applied to the system as a uniform excitation. The Newmark integration method is used for transient analysis. The transient analysis of this frame is used for the reliability study in chapter 5.

4.4.3 **Recommendations for improving the analysis models:**

The observations on modeling a reinforced concrete frame in OpenSees are summarized in the following suggestions:

- For calibrating the material behavior:

  - It is noticed that the concrete does not reach its cylindrical test strength in the beams and columns, the ultimate strength of the concrete is reduced to $0.85 f_c'$, based on the Whitney's stress block. The reduced strengths are applied to the Kent-Park model for calculating the detailed material model properties.
  - The cover concrete can reach only 70% of the assumed strength of $0.85 f_c'$
  - The unloading stiffness for the concrete is reduced to 7.5% of the initial stiffness.
  - The pinching point displacement and force for the materials used in the joint element was chosen as 15% of the peak point displacement and force.

- The frame model

  - The beam and slab are modeled as a T-beam section, with the core and cover concrete separately introduced. The beam core concrete is considered confined, while the beam cover and the slab concrete are unconfined with no tensile strength.

- The effective slab width that is involved in the bending of the T-beam is chosen as the smaller value of the actual slab width and four times the beam width.

- Displacement based formulation for nonlinear frame elements was chosen and to achieve the compatibility, the beams and columns are divided to five displacement-based nonlinear elements.

- The convergence test criteria is switched to energy increments and the tolerance is reduced to 1.0e-14

4.5 *Performance levels for reinforced concrete joints*

Seismic performance of beam-column joints is studied by observing the progress structural damage, defining the damage state corresponding to each performance level, and finding an analytical approach to describe the performance quality with an engineering quantity (Pagni and Lowes, 2004). This process requires detailed experimental study on structural components (joints) with similar design and detailing. The experimental results must document the observed physical damages and the corresponding load-step, time, forces and deformations.

In this research two sets of experimental results on beam-column joints (older design) were reviewed (Pantelides et. al., 2002; Walker et al., 2004) to summarize the damage mechanisms and their corresponding damage states. Two major damage mechanisms for beam column joints are observed: (1) the damage due to bond-slip, or (2) the damage due to joint shear failure. Depending on the governing damage mechanism, the observed physical damages and their sequence are different. Five performance levels and their corresponding physical damages for both of the damage modes are summarized in Table 4-3, and Table 4-4. The performance levels in Table 4-3, and Table 4-4 are in agreement with the performance levels presented in Table 3-1 (Park et al., 1985b).

For a joint with shear damage as the dominant failure mechanism, Figure 4-39 to Figure 4-42 show the observed damage states (Walker et al., 2004). The governing parameters that are used to define a relationship between performance levels were found to be drift,

plastic deformation, joint crack width, and the joint strength coefficient. The observed joint-shear and shear-deformation are analyzed by *Normalized-Peak*, *Park-Ang*, and *Mehanny-Deierlein* damage models and the damage index history is stored. Based on the experimental report on the exact time step for each observed damage state, the corresponding damage index is singled out. So for every damage state of each specimen, a damage index is available. Some discrepancies are expected due to limitations in the damage model and due to the accuracy of experimental readings (the observed damages are reported at the end of each loading half-cycles, while in reality the damage might have happened in the middle of the half cycle), so for each performance level (damage state) a distribution of damage indices are observed.

Lognormal probability distributions are used to relate the performance level (damage state) to the calculated damage indices. Figure 4-43, Figure 4-44, and Figure 4-45 show these distributions for the *Park-Ang*, *Mehanny* and *Normalized Peak* damage models. These plots can be used to acquire the probability of occurrence of a target damage state for a given damage index (4.70), or they can be used to define the damage index range for a damage state by using a probability range (84^{th} percentile). The ideal damage model will have a smaller dispersion range for each damage state.

$$P\left(DM \left| di = DI \right.\right) \tag{4.70}$$

It is possible to use damage indices as *Engineering demand parameters* and the relationships between the damage states and damage indices fill the gap between the *Engineering Demand Parameters* and the *Damage Measures*.

Table 4-3: Observed damage states for bond related damage

Damage level	Physical damage state	Observed characteristics
I	First yielding of longitudinal reinforcement	Barely visible, initial cracking in the joint or no cracking at all
II	Full development of the bond slip mechanism	Cracking in the joint less than 0.01 in. wide
III	Significant diagonal cracking in the joint	Cracking in the joint more than 0.02 in. wide, and the extension of these cracks into the column
IV	Spalling of concrete at the corner(s) of the joint	Spalling where the beam bars were slipping
V	Total loss of lateral load carrying capacity	Collapsed

Table 4-4: Observed damage states for the shear related damage

Damage level	Physical damage state	Observed characteristics
I	First yielding of longitudinal reinforcement	Barely visible, initial cracking in the joint or no cracking at all
II	Significant diagonal cracking in the joint	Cracking in the joint more than 0.02 in. wide, and the extension of these cracks into the column
III	Full development of the joint shear mechanism	Extensive cracking in the joint and the extension of diagonal joint cracks into the column
IV	Spalling of concrete at the core of the joint	Spalling where the beam bars were slipping
V	Total loss of lateral load carrying capacity	Collapsed

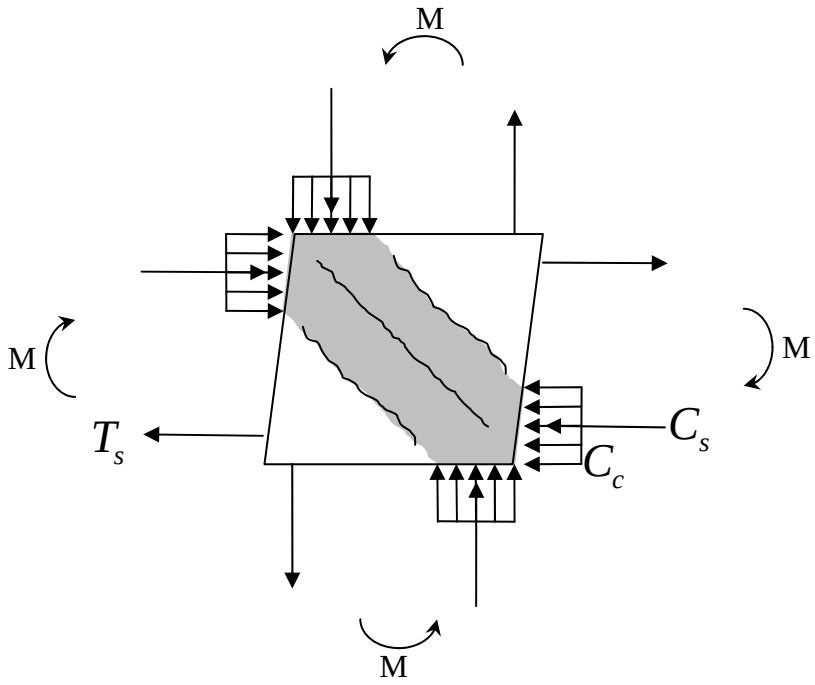

Figure 4-1: Joint shear response due to unbalanced moments

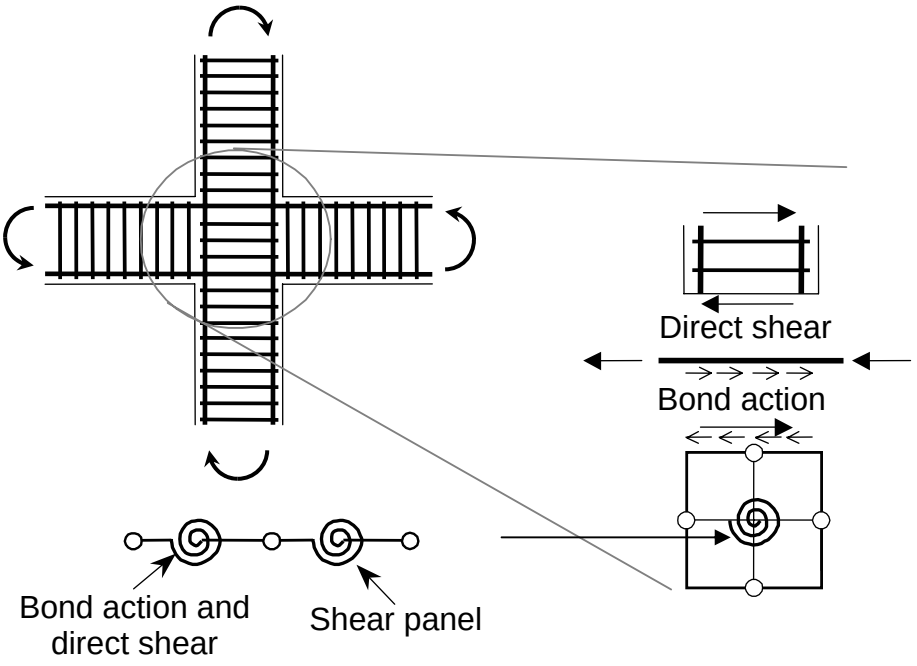

Figure 4-2: Shear force transfer mechanism in RC joints

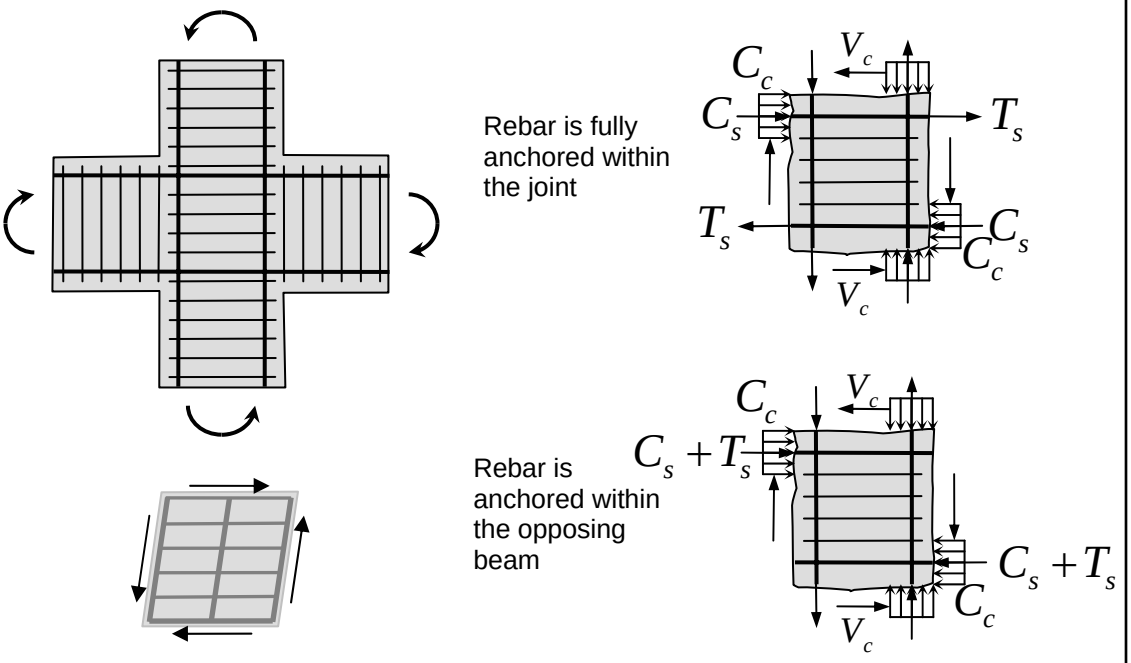

Figure 4-3: Rigid body diagram for the shear panel with/without anchorage within the joint

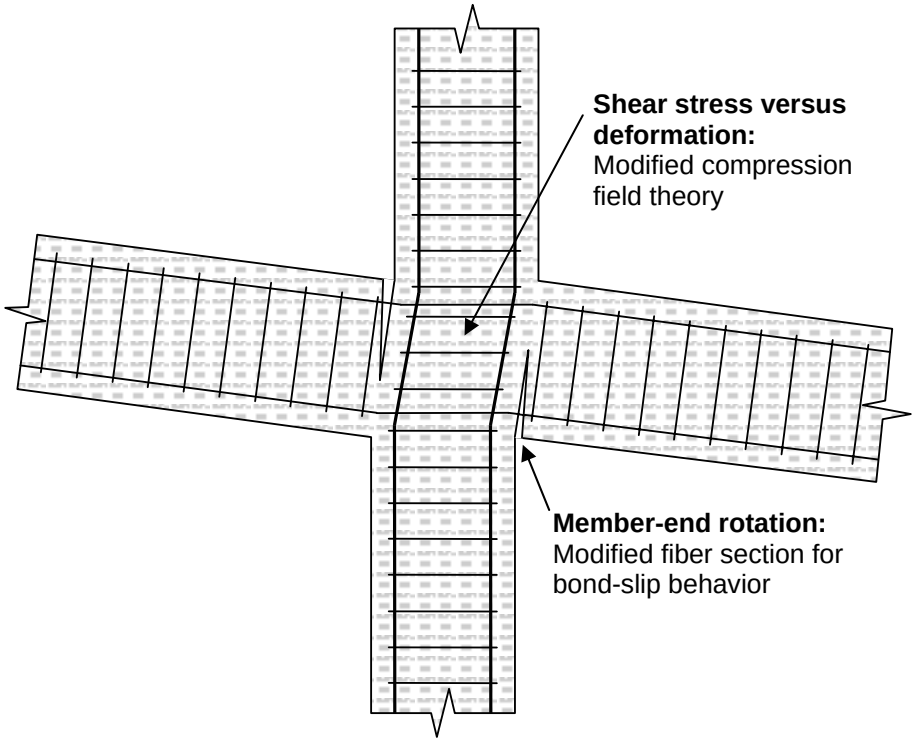

Figure 4-4: Deformed modes of reinforced concrete joint and the calibrating models

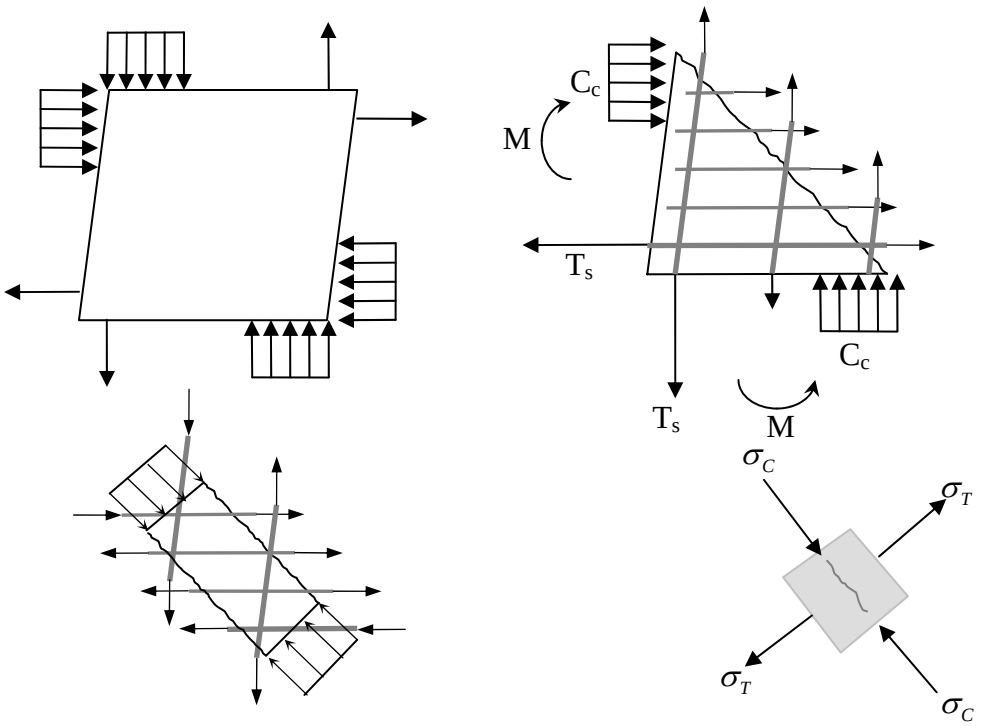

Figure 4-5: Application of Modified Compression Field Theory

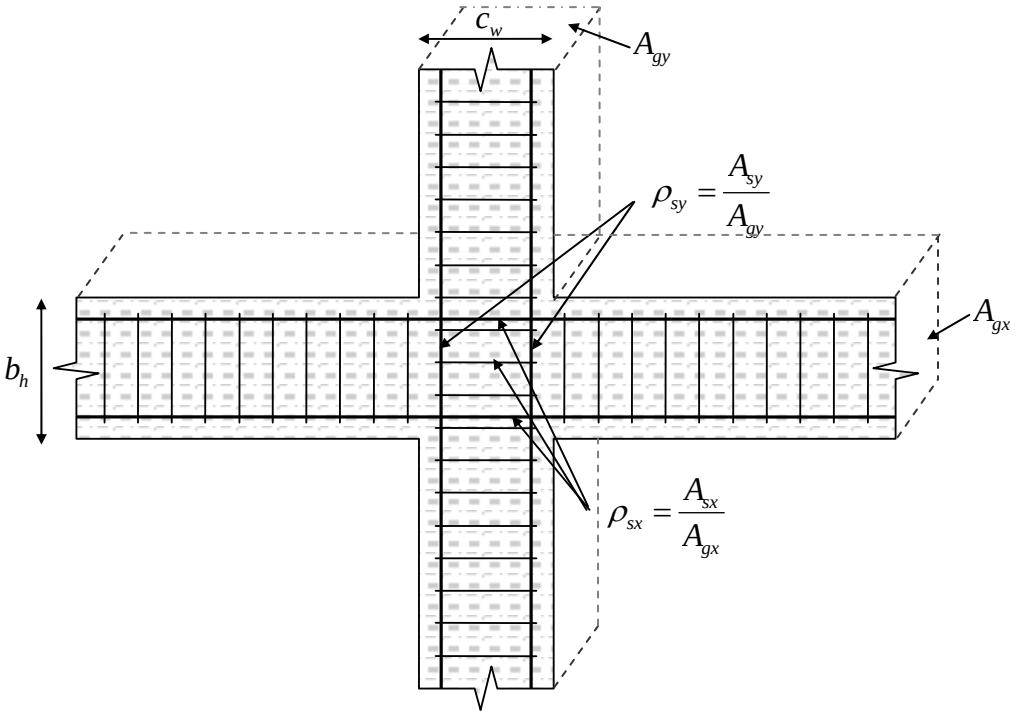

Figure 4-6: Undeformed reinforced concrete joint

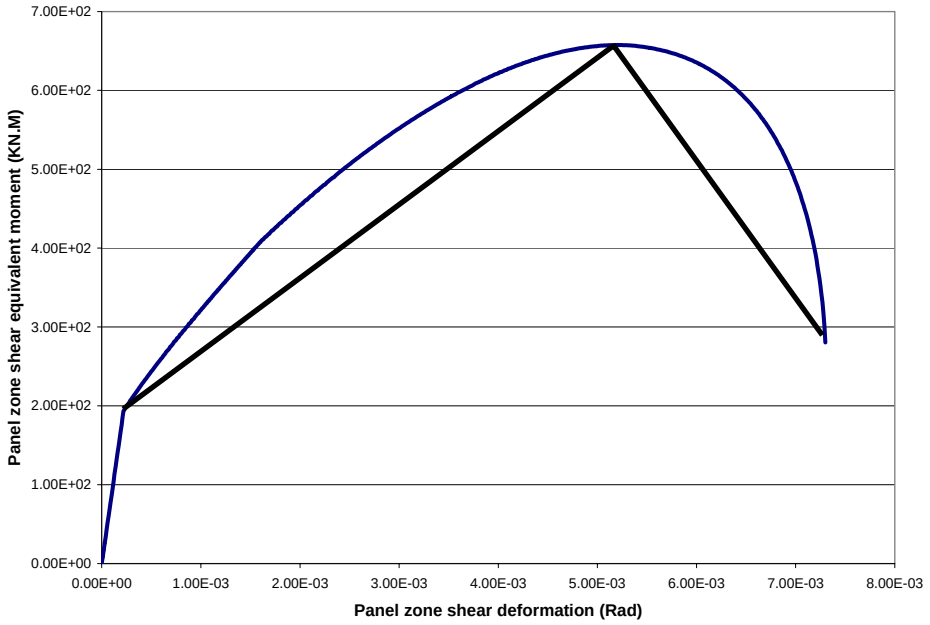

Figure 4-7: Shear panel calibration using MCFT

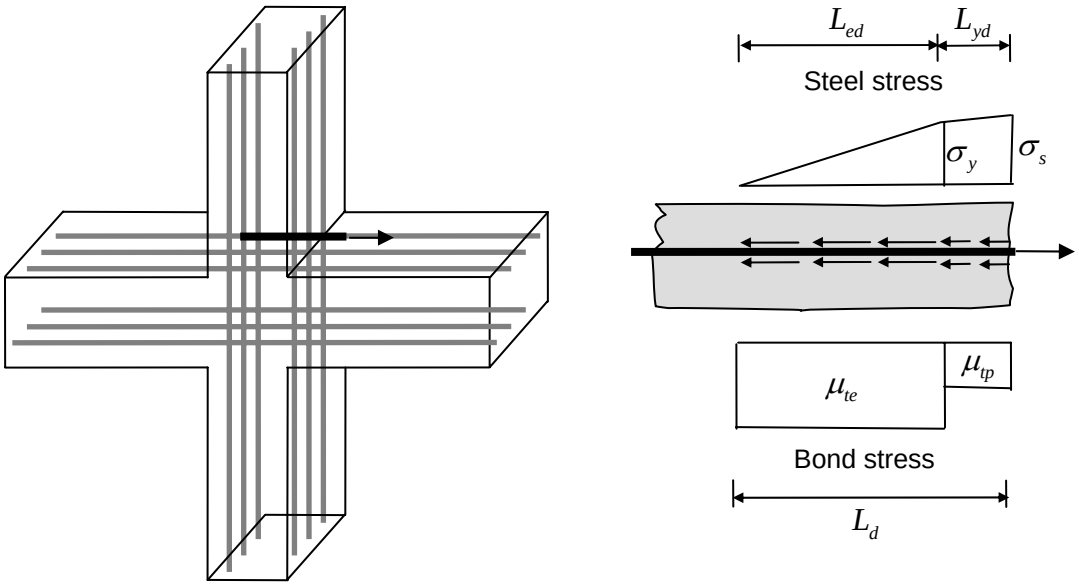

Figure 4-8: Longitudinal anchorage in the joint zone

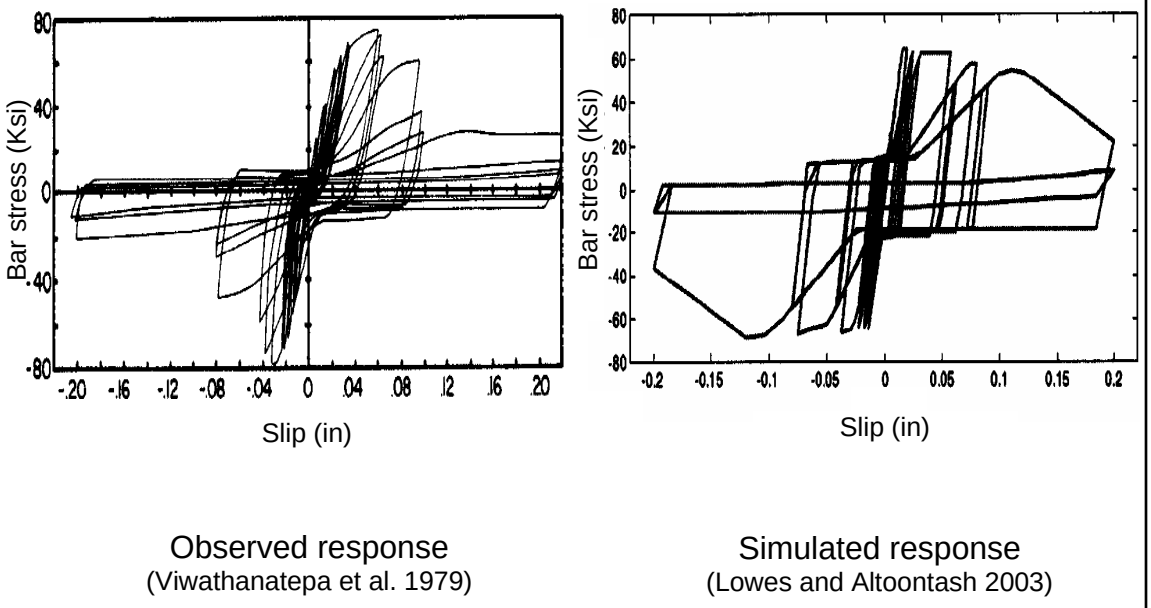

Figure 4-9: Simulated and observed bar stress versus slip for anchored reinforcing bar

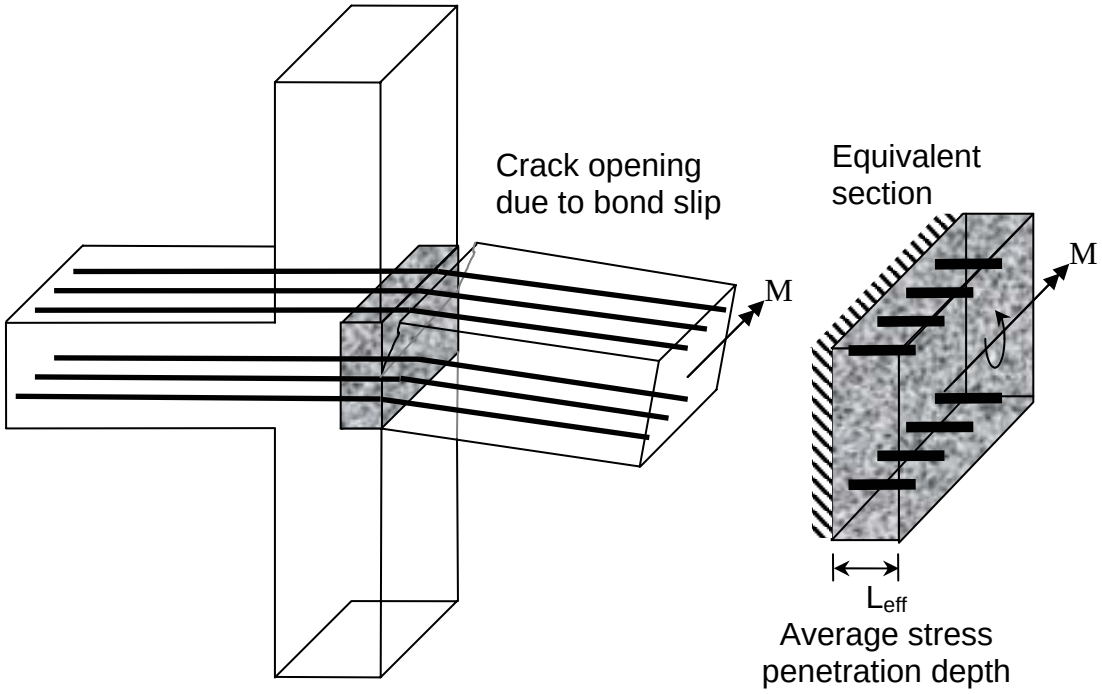

Figure 4-10: Section model for member-end rotation

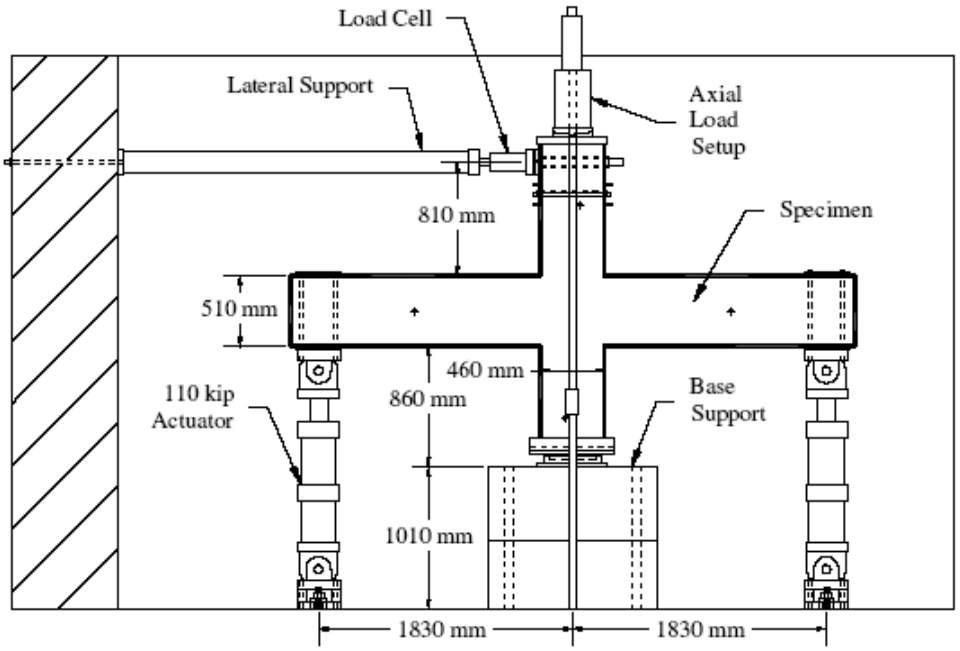

Figure 4-11: Test setup for single joint subassembly, Walker et. al. (2004)

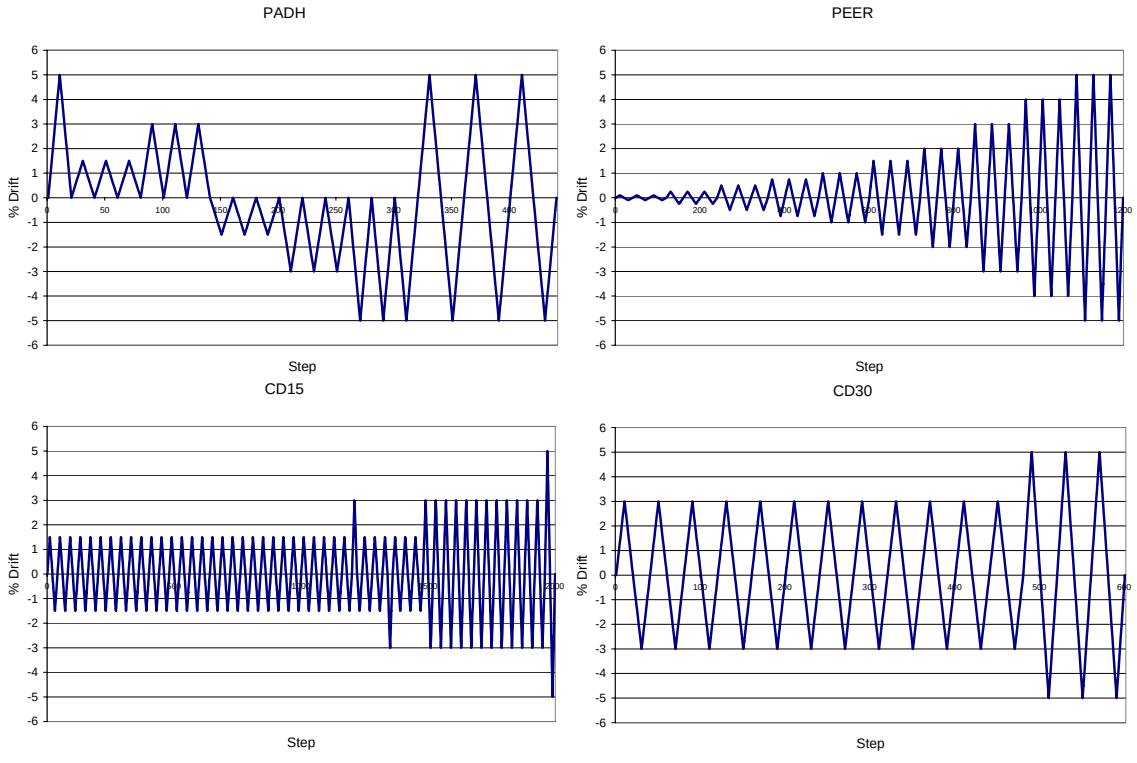

Figure 4-12: Loading protocols for the test setups, Walker(2004)

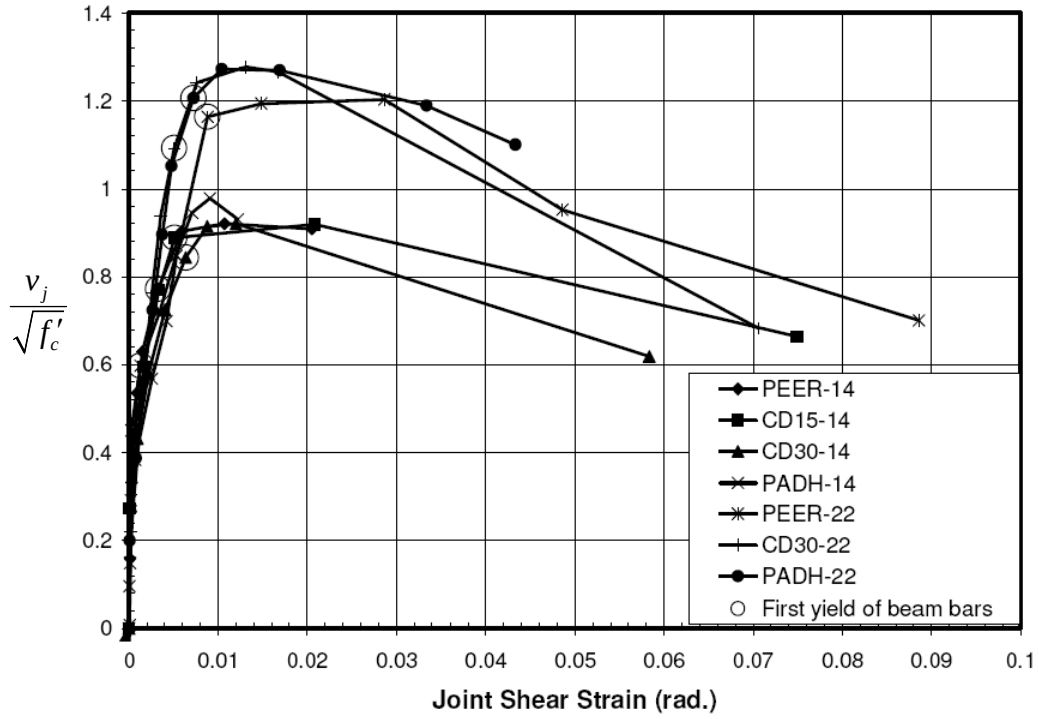

Figure 4-13: Shear panel experimental data Walker (2004)

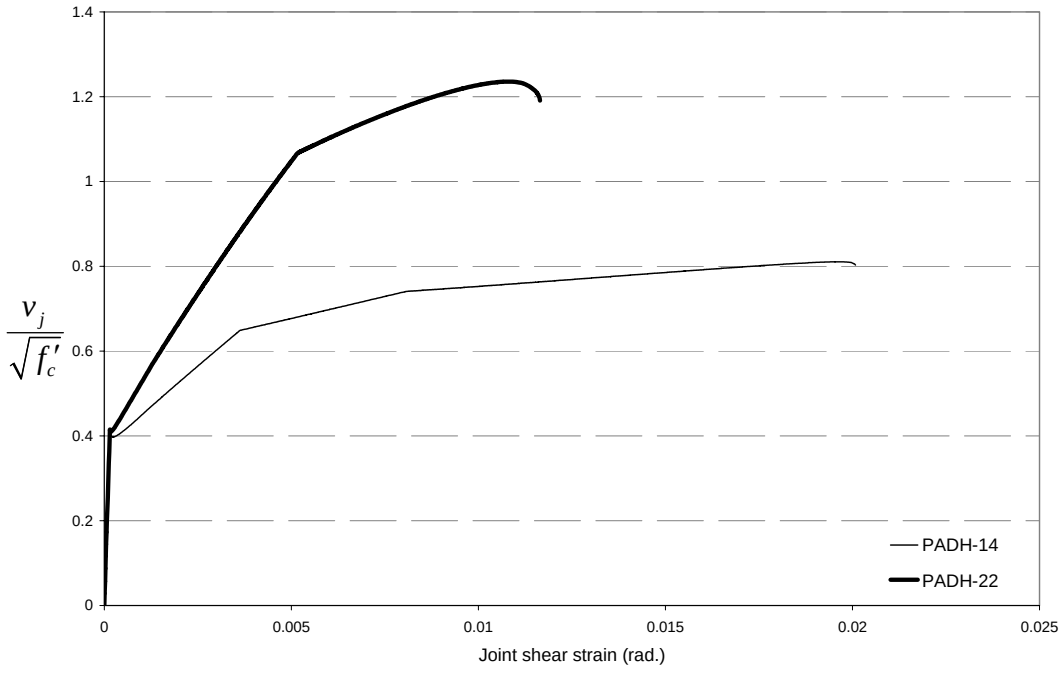

Figure 4-14: Shear panel analytical data, MCFT

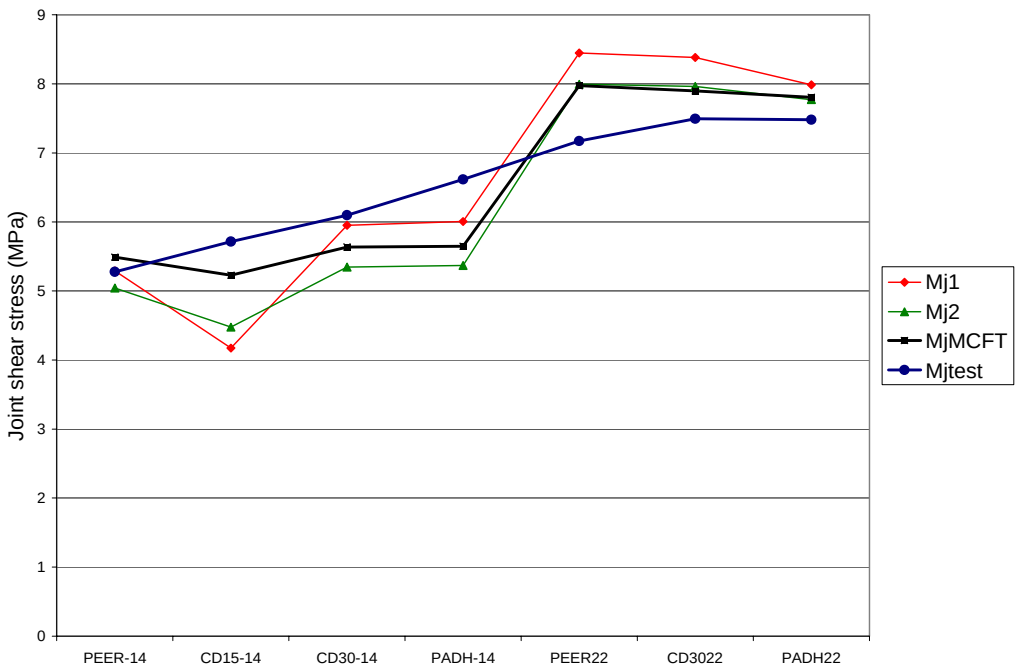

Figure 4-15: Joint shear strength, theory and experiment comparison

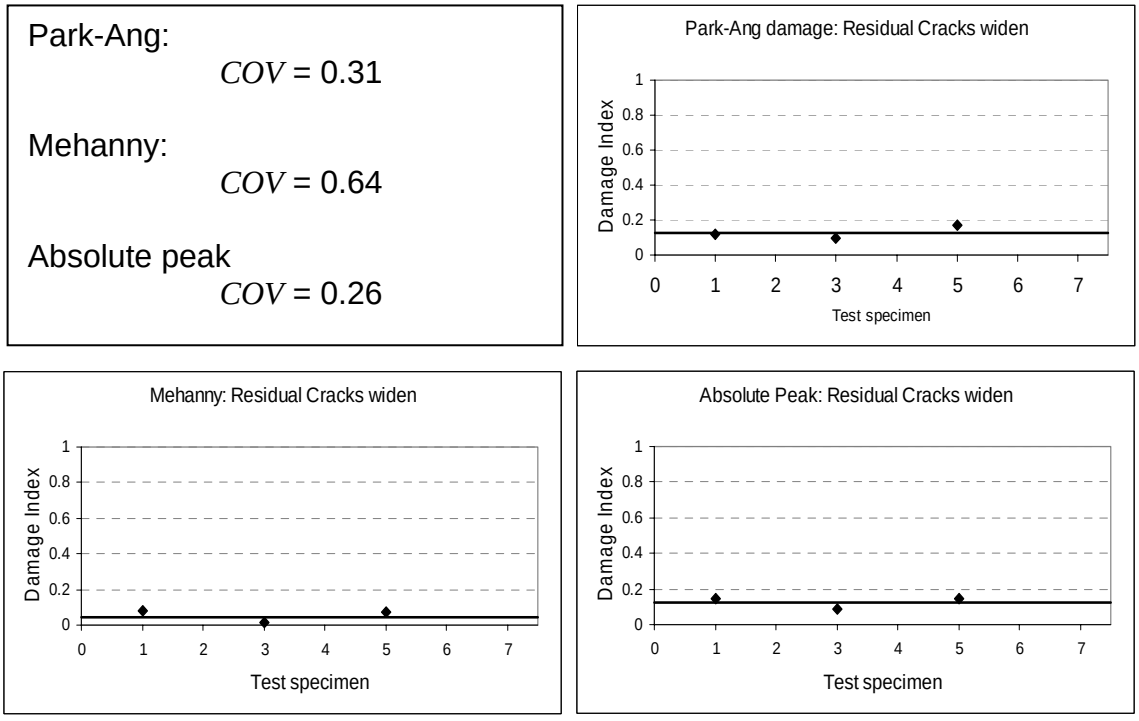

Figure 4-16: Damage model comparison, residual cracks widen

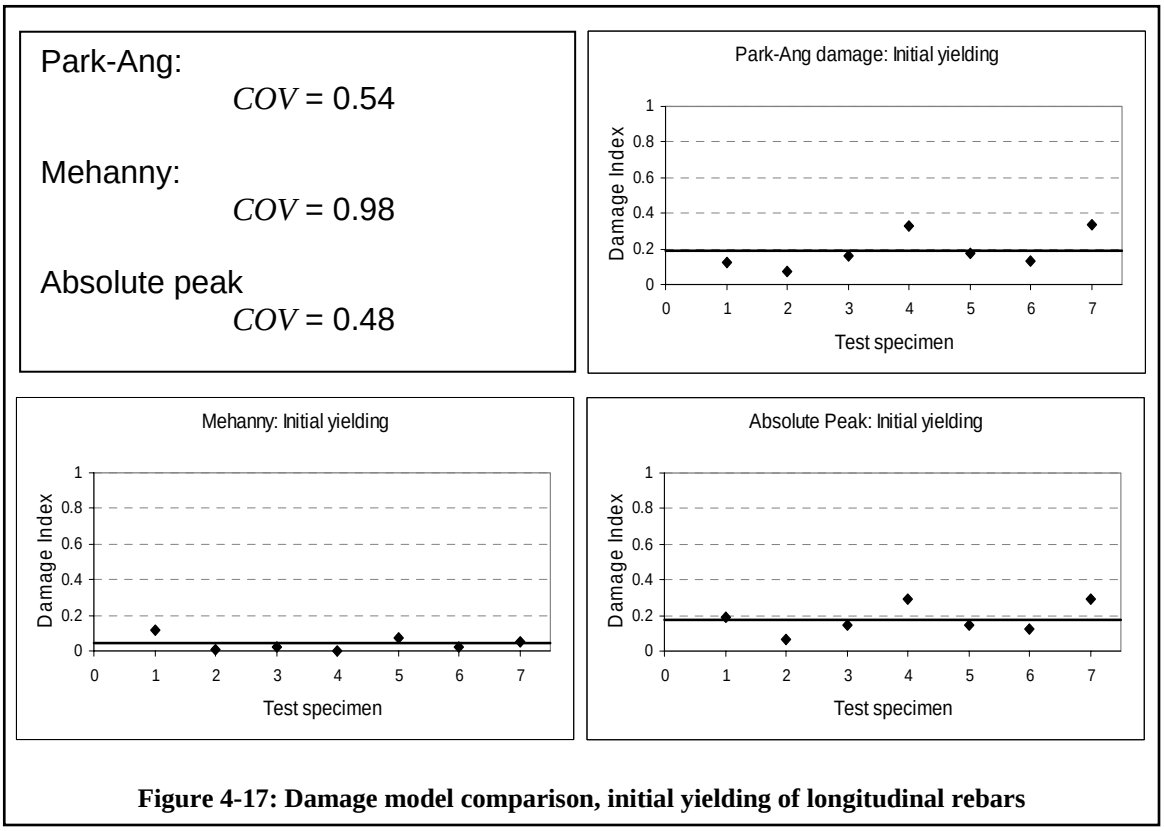

Figure 4-17: Damage model comparison, initial yielding of longitudinal rebars

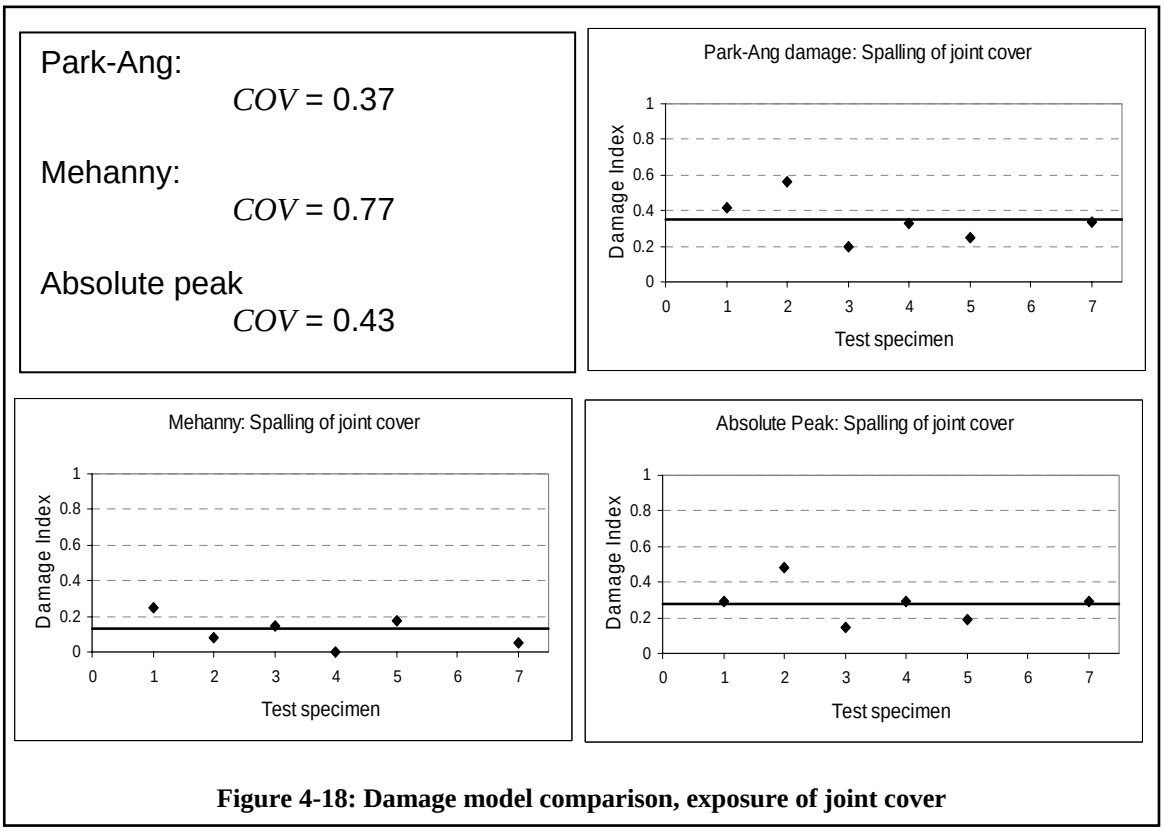

Figure 4-18: Damage model comparison, exposure of joint cover

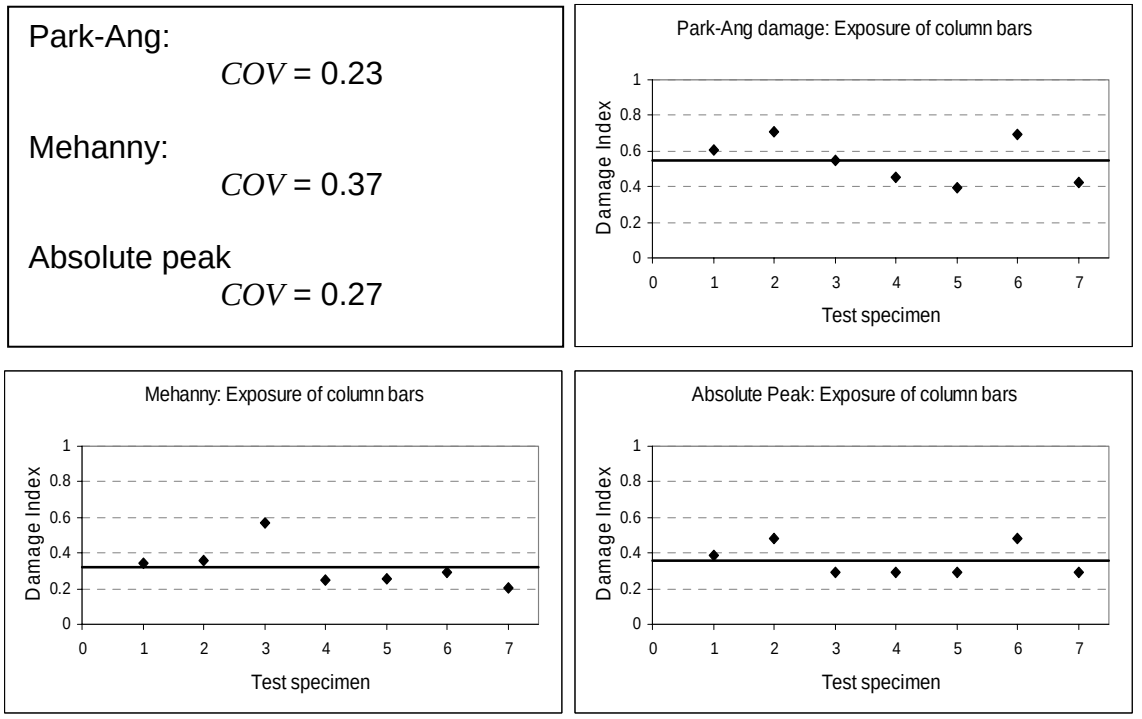

Figure 4-19: Damage model comparison, exposure of column rebars

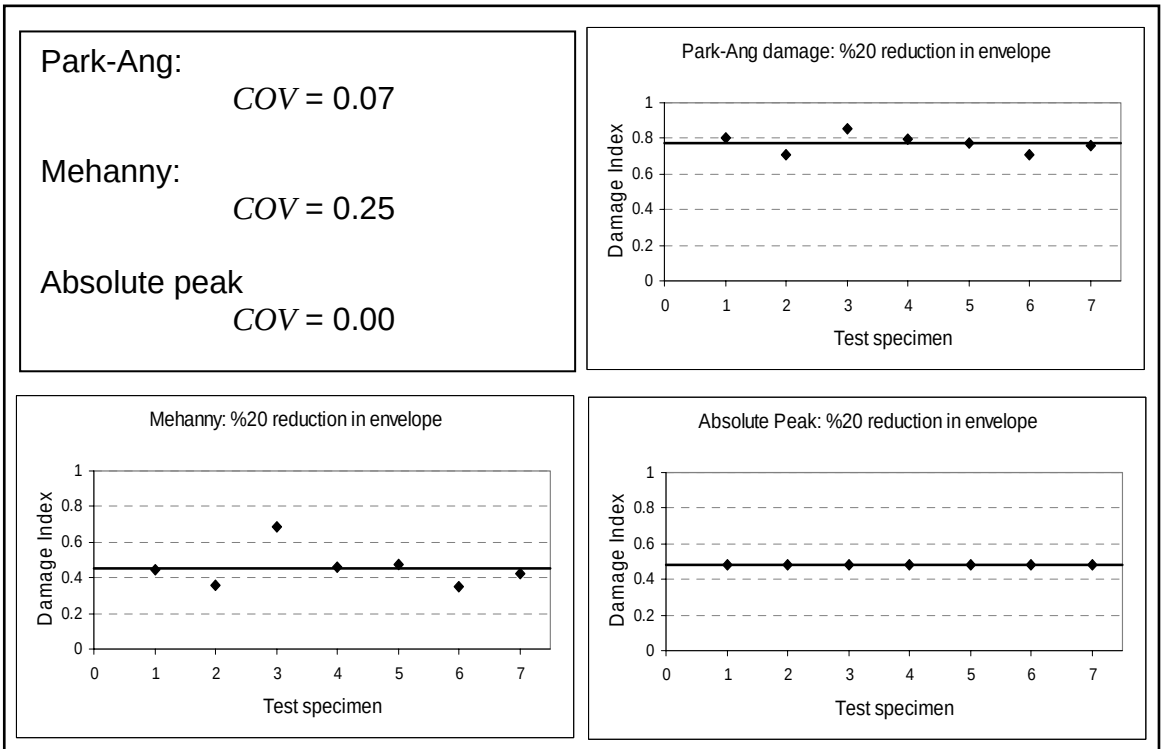

Figure 4-20: Damage model comparison, 20% reduction in envelope

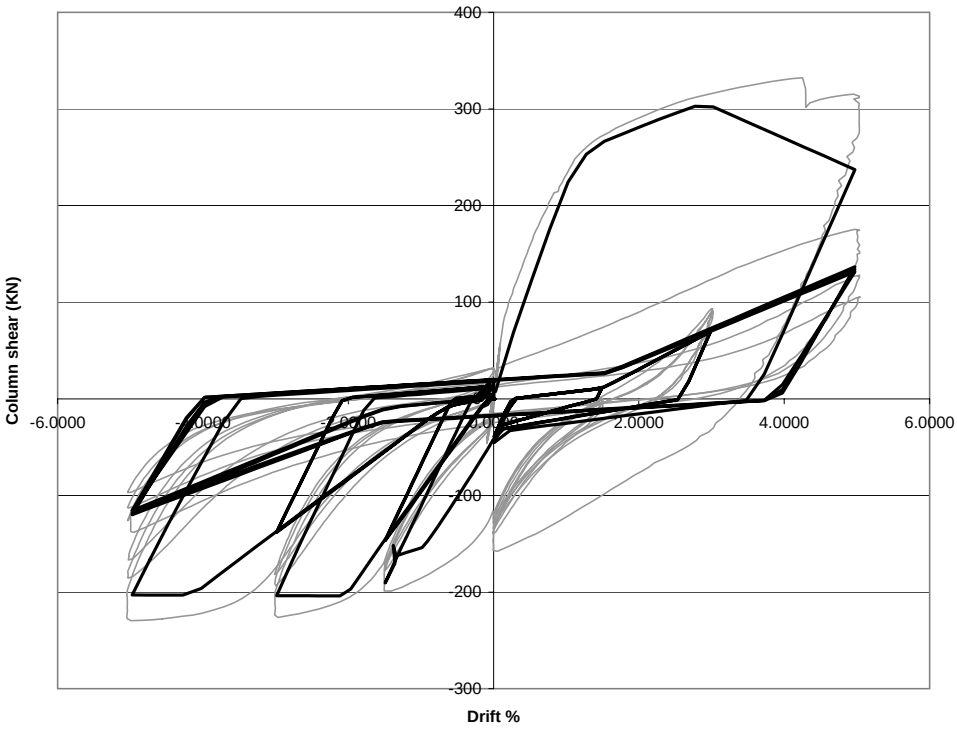

Figure 4-21: Comparison of the observed and simulated response for PADH-14 (Walker, 2004)

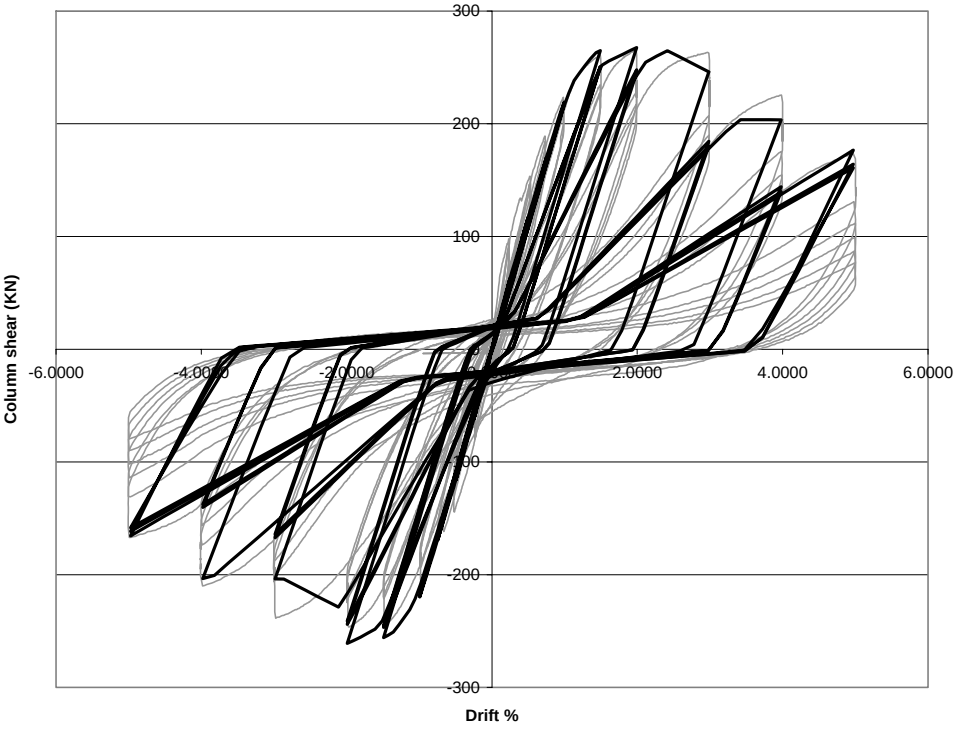

Figure 4-22: Comparison of the observed and simulated response for PEER-14 (Walker, 2004)

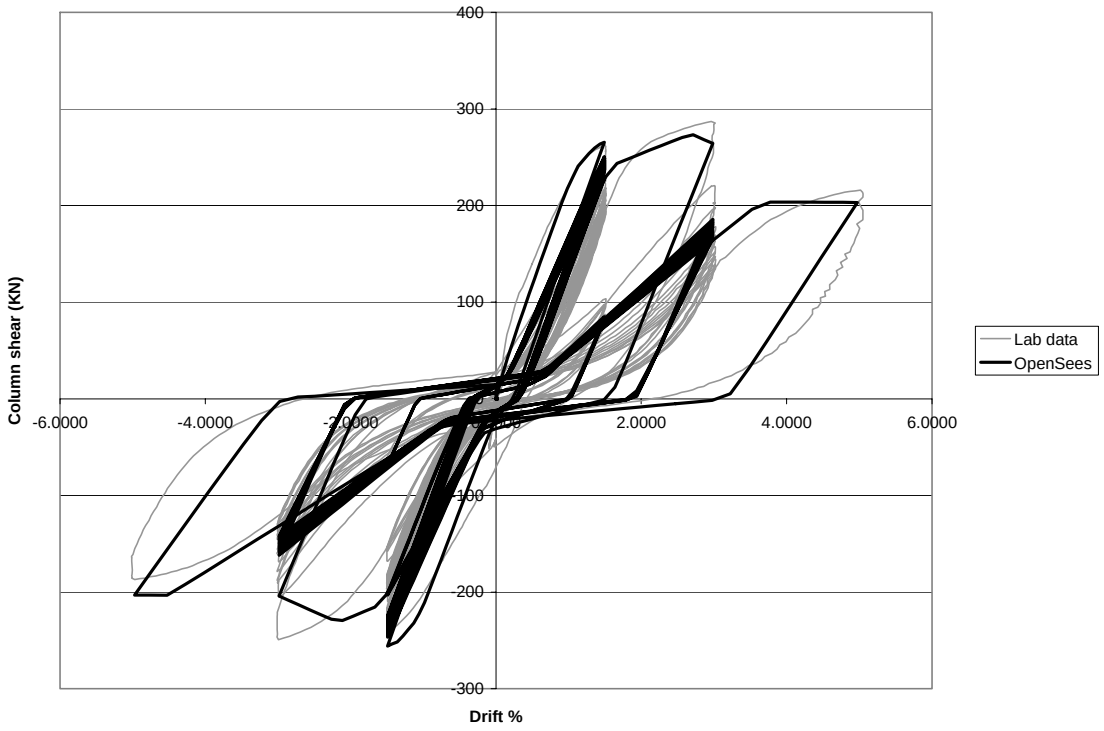

Figure 4-23: Comparison of the observed and simulated response for CD15-14 (Walker, 2004)

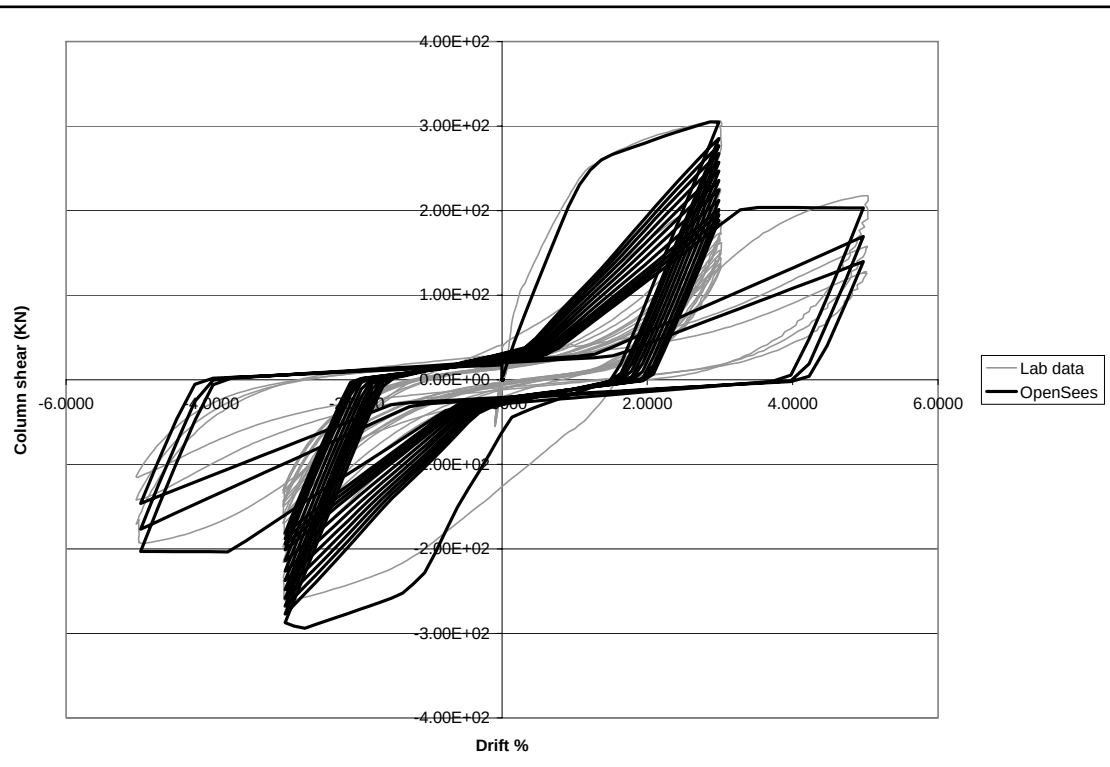

Figure 4-24: Comparison of the observed and simulated response for CD30-14 (Walker, 2004)

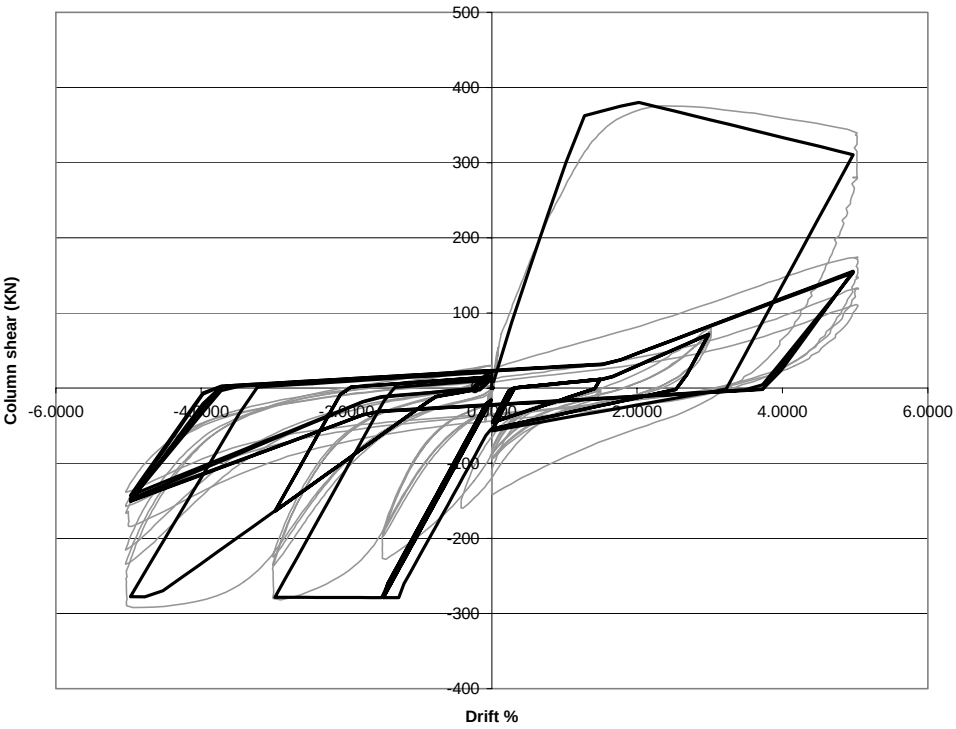

Figure 4-25: Comparison of the observed and simulated response for PADH-22 (Walker, 2004)

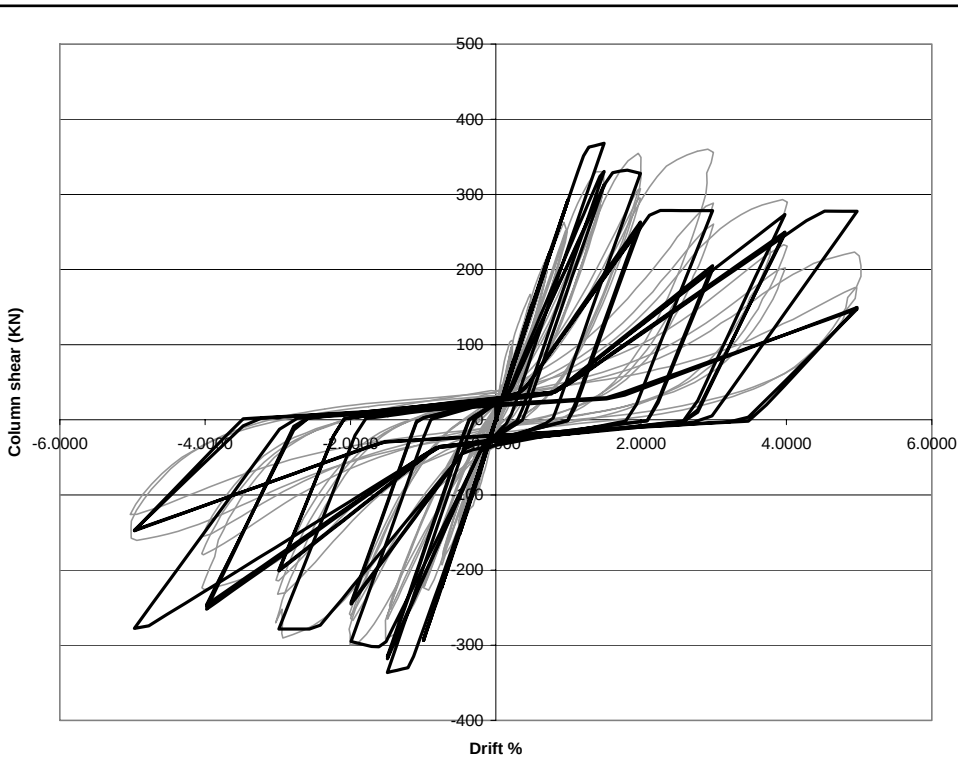

Figure 4-26: Comparison of the observed and simulated response for PEER-22 (Walker, 2004)

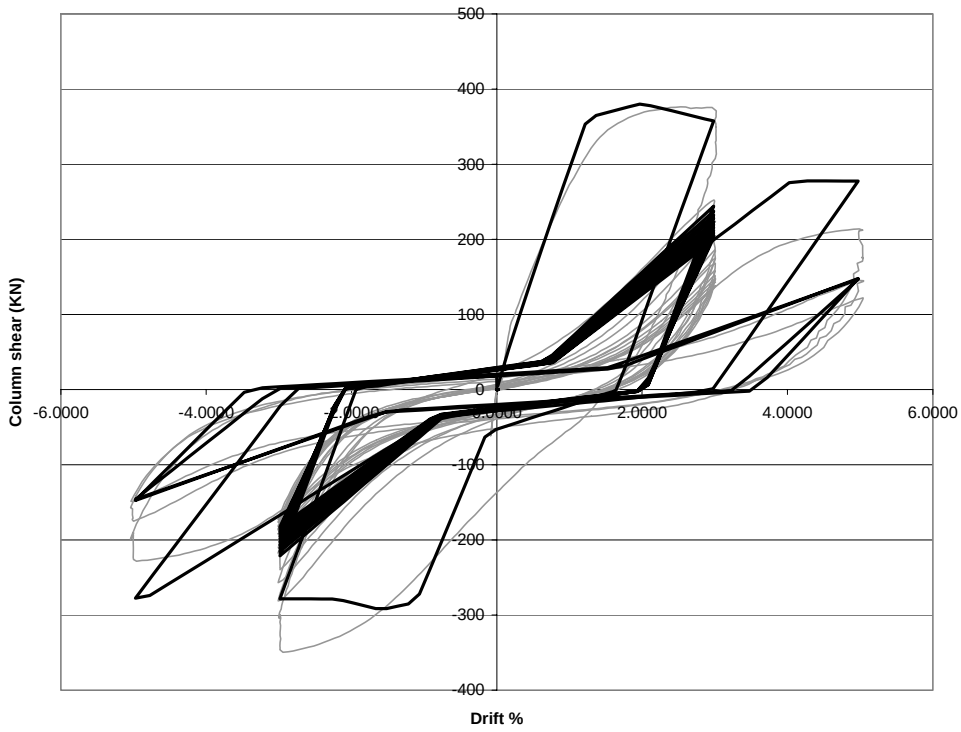

Figure 4-27: Comparison of the observed and simulated response for CD15-22 (Walker, 2004)

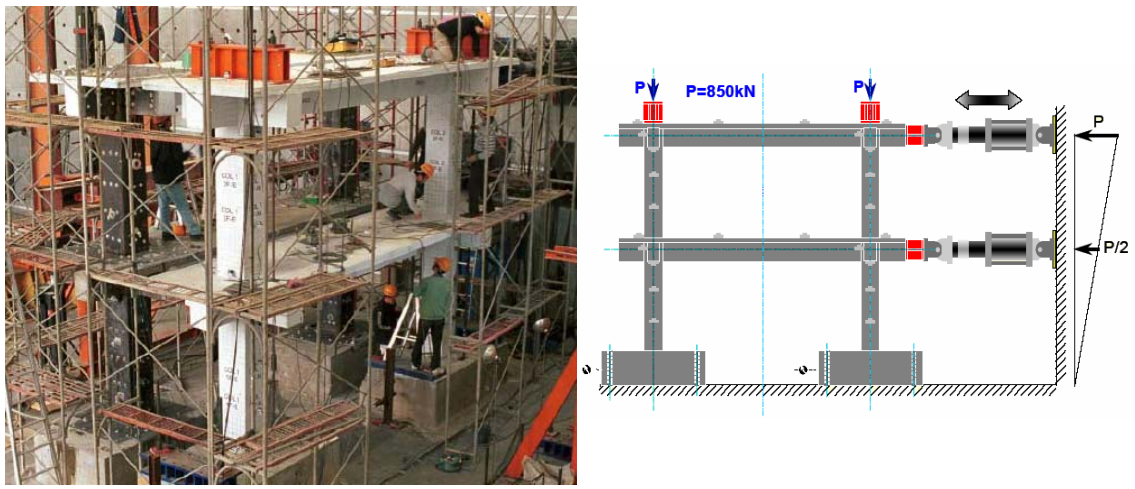

Figure 4-28: 0.7 scale RC frame test setup and instrumentation (Tsai et al., 2001)

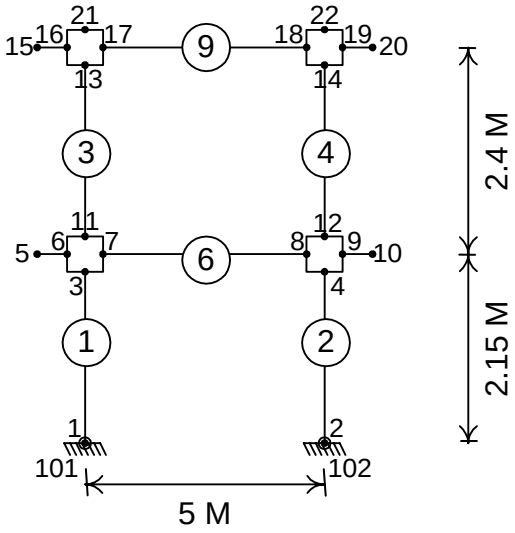

Figure 4-29: OpenSees model for the NCREE frame (Tsai et al., 2001)

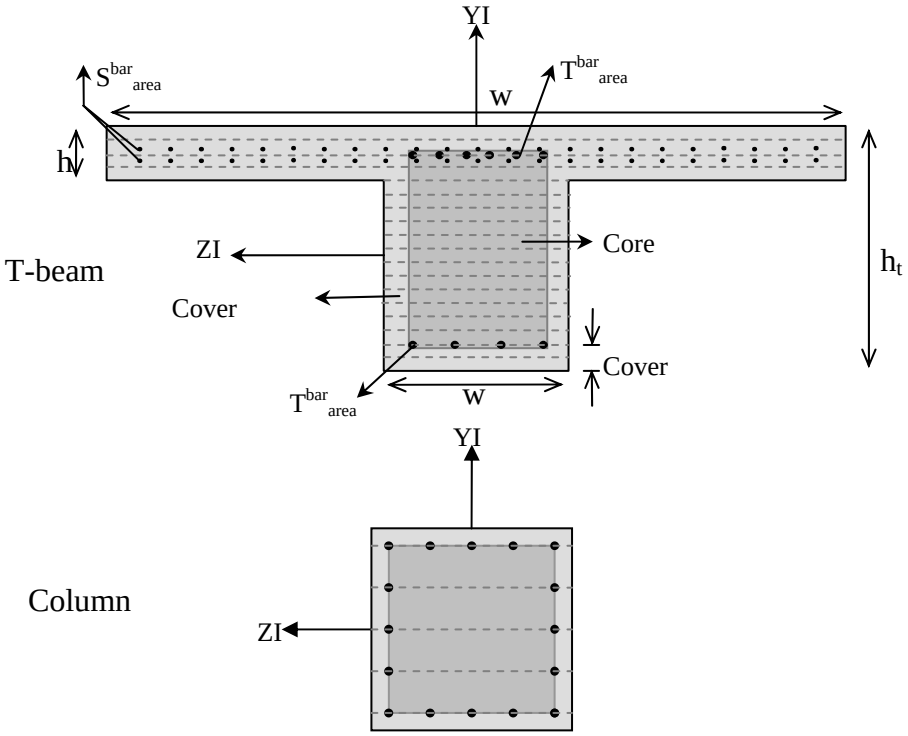

Figure 4-30: Fiber sections used in the NCREE frame model

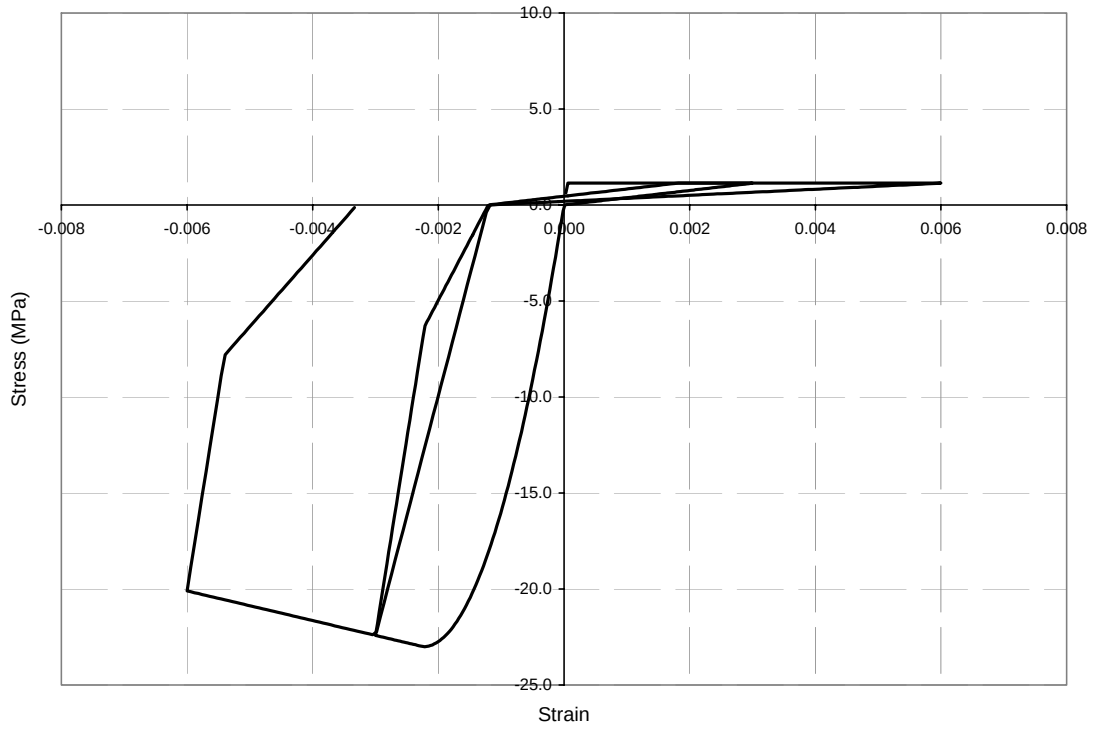

Figure 4-31: Kent-Scott-Park concrete material model

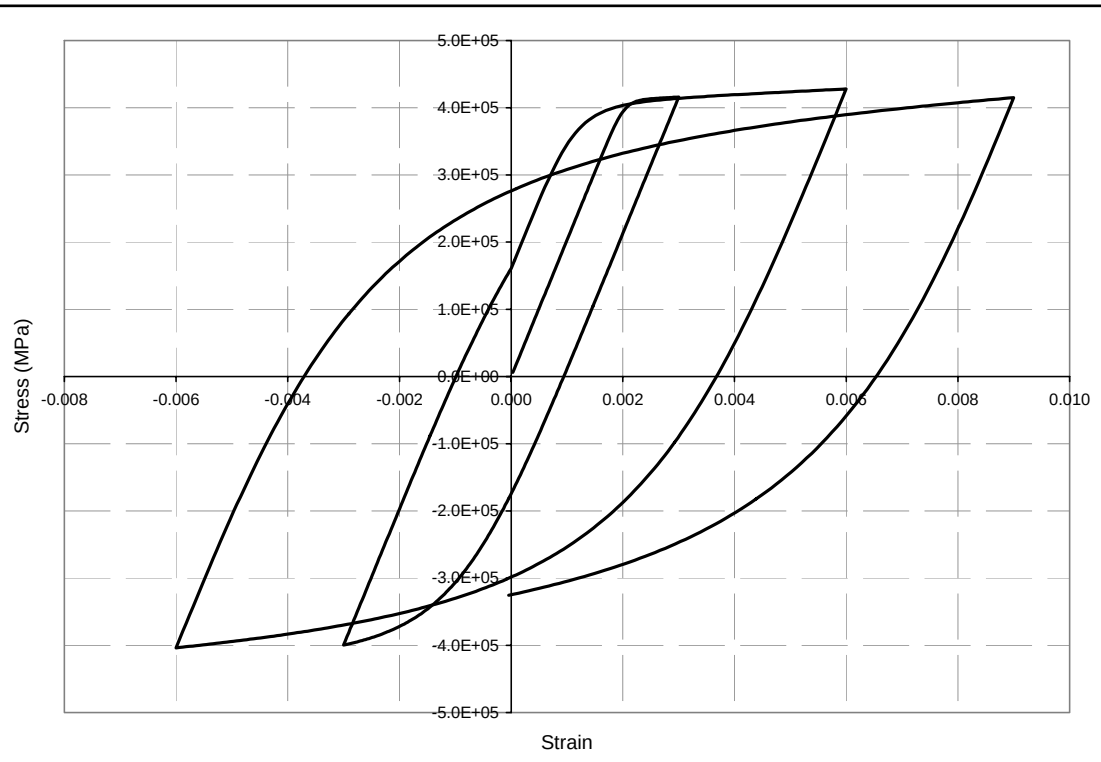

Figure 4-32: Giuffre-Menegotto-Pinto steel material model (FEDEAS, 2004)

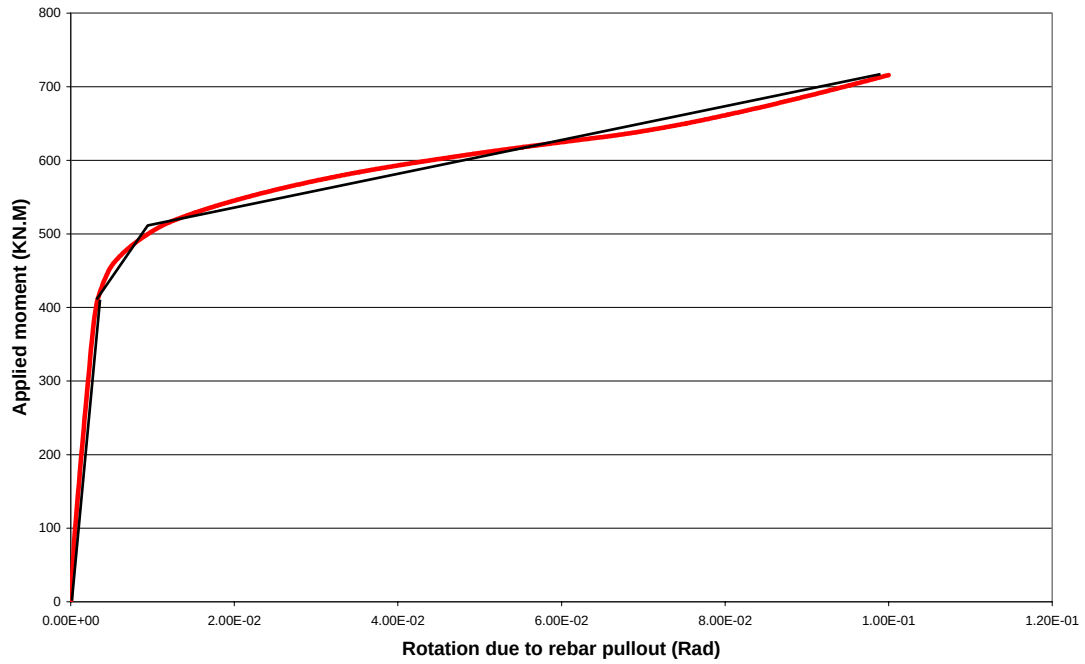

Figure 4-33: Calibrating the column-end rotation

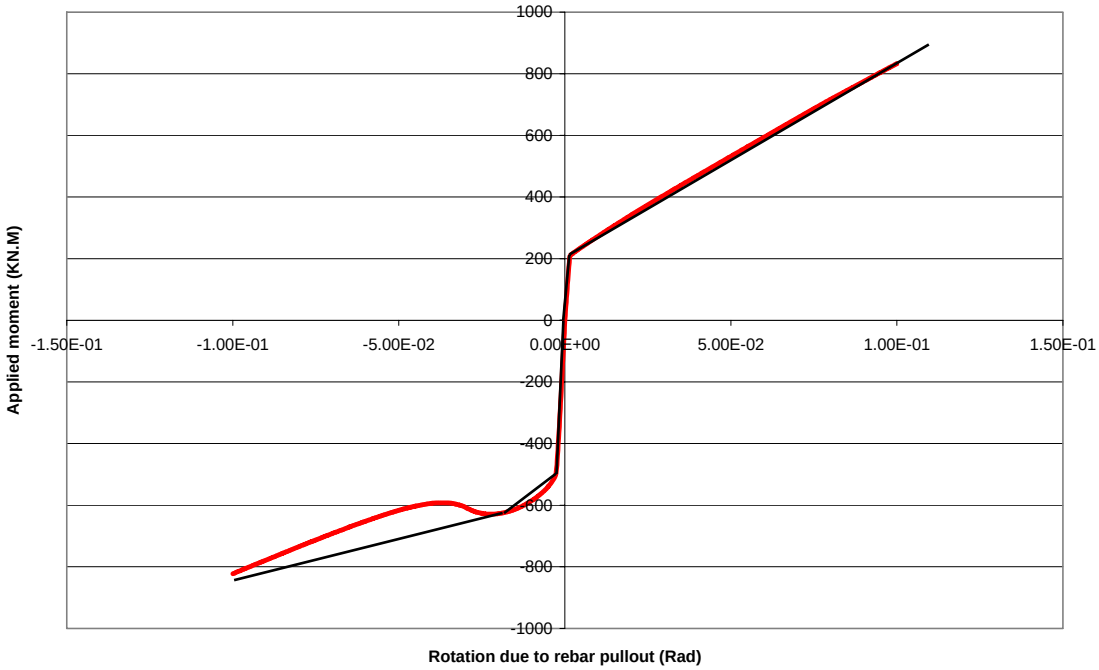

Figure 4-34: Calibrating the beam-end rotation

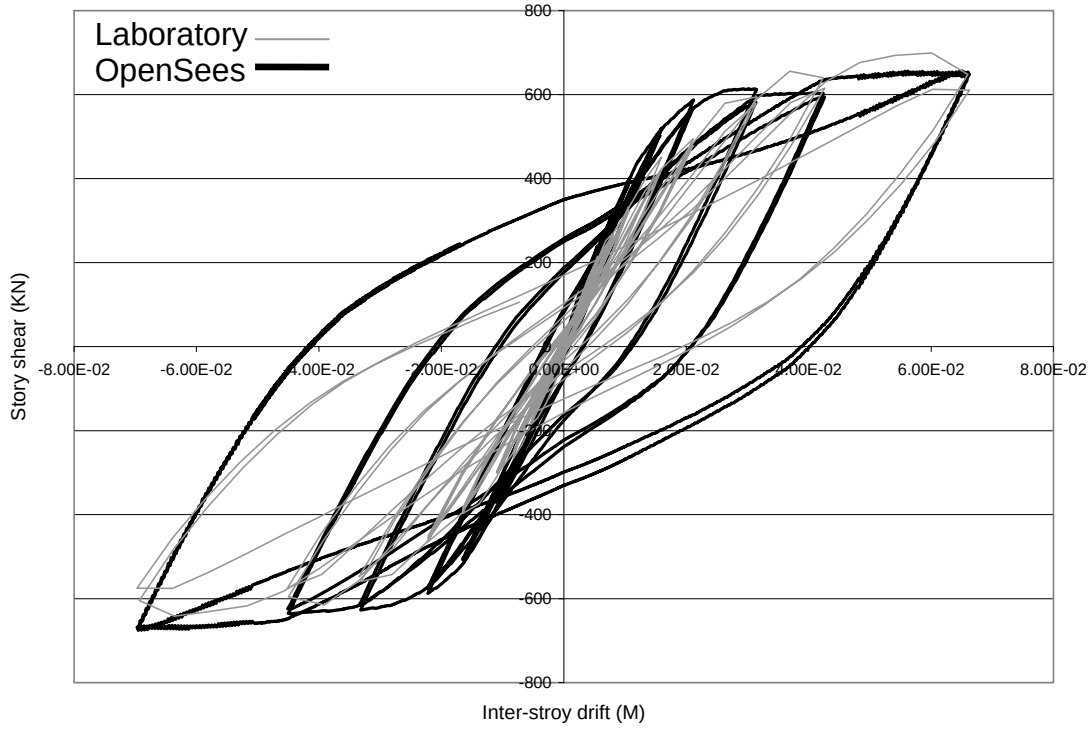

Figure 4-35: NCREE frame (Tsai et al., 2001) displacement controlled analysis: floor 1

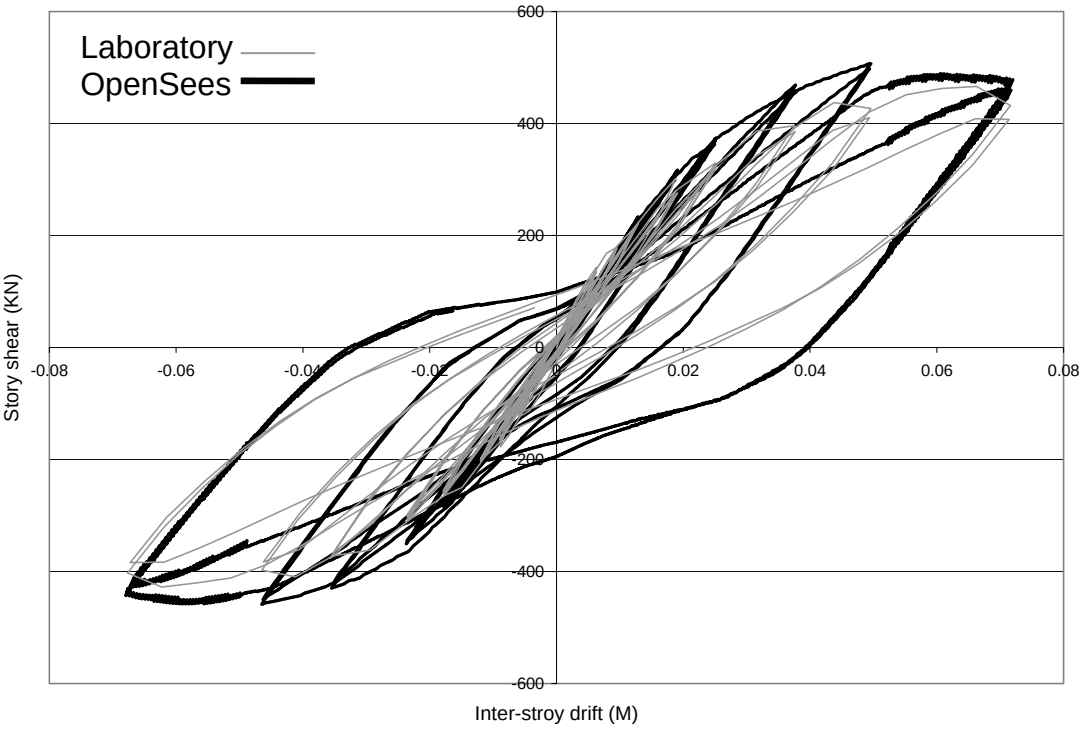

Figure 4-36: NCREE frame (Tsai, 2001) displacement controlled analysis: floor 2

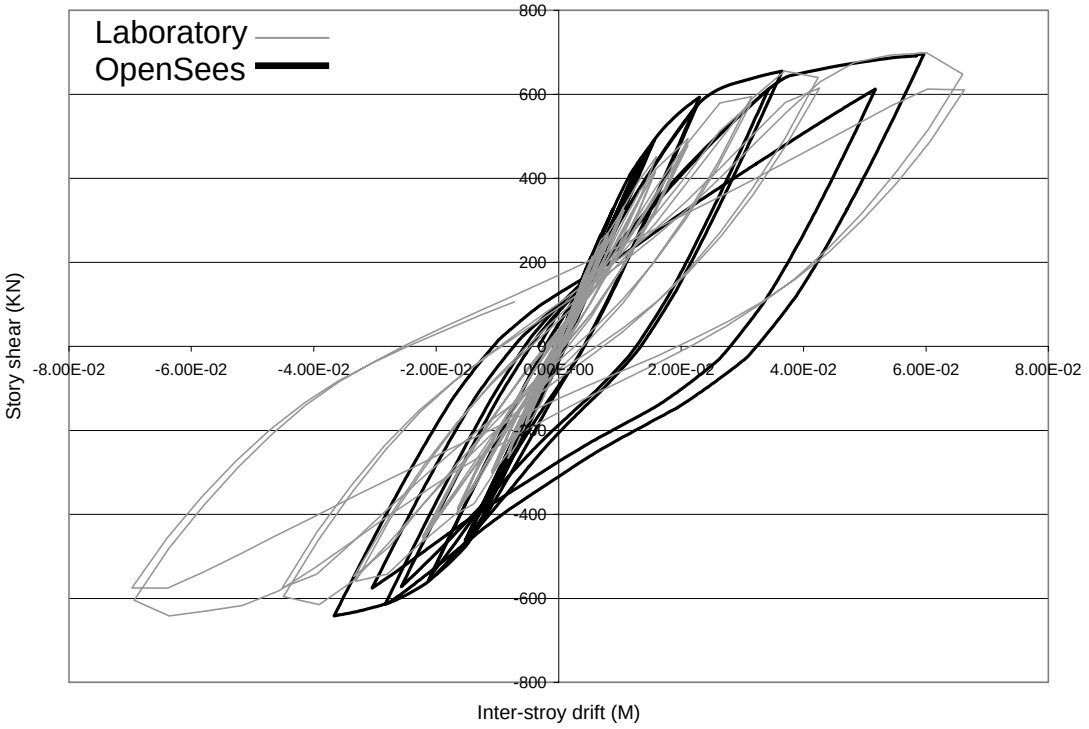

Figure 4-37: NCREE frame (Tsai, 2001) load controlled analysis: floor 1

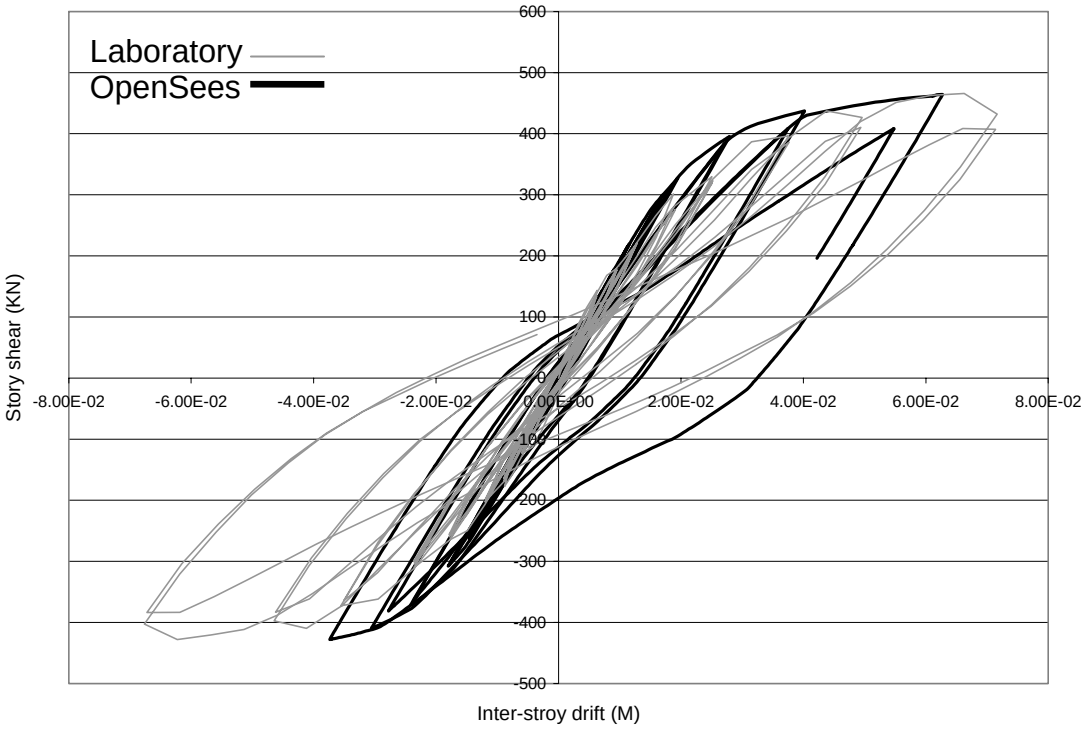

Figure 4-38: NCREE frame (Tsai, 2001) load controlled analysis: floor 2

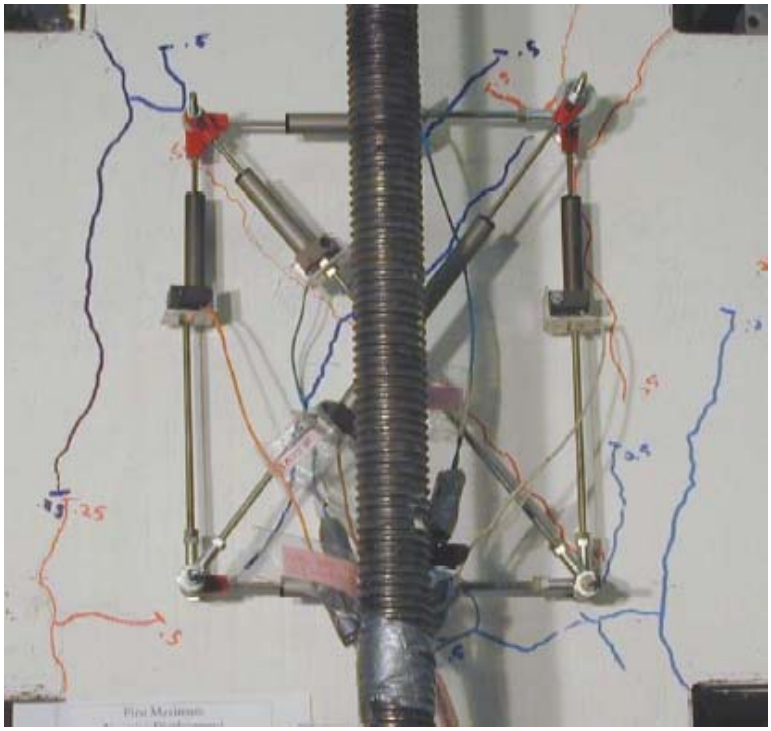

Figure 4-39: Damage levels I, first yielding of longitudinal reinforcement (Walker 2001)

Figure 4-40: Damage level II, Significant diagonal cracking in the joint (Walker 2001)

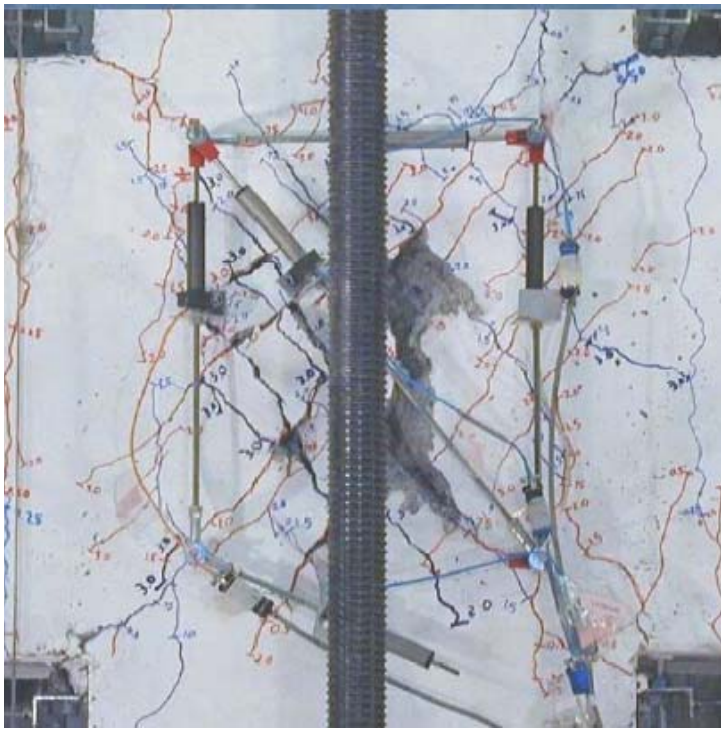

Figure 4-41: Damage level III, Full development of the joint shear mechanism (Walker 2001)

Figure 4-42: Damage Level IV, spalling of concrete at the core of the joint (Walker 2001)

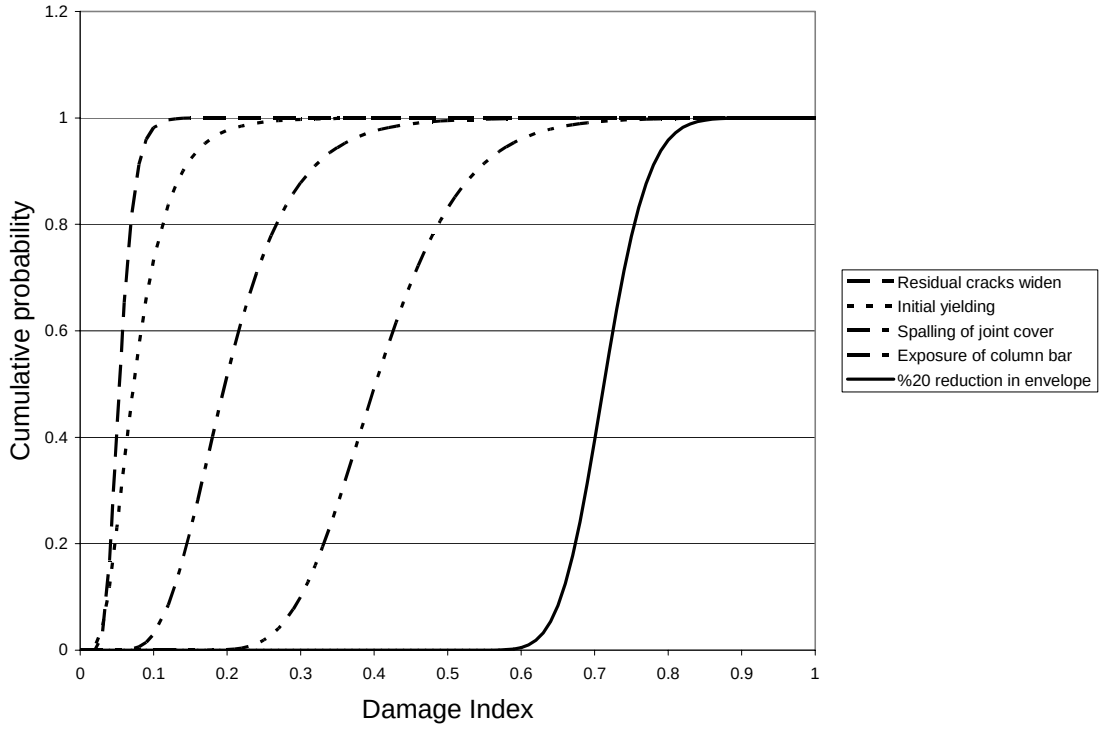

Figure 4-43: Damage index to damage measure for Park-Ang model

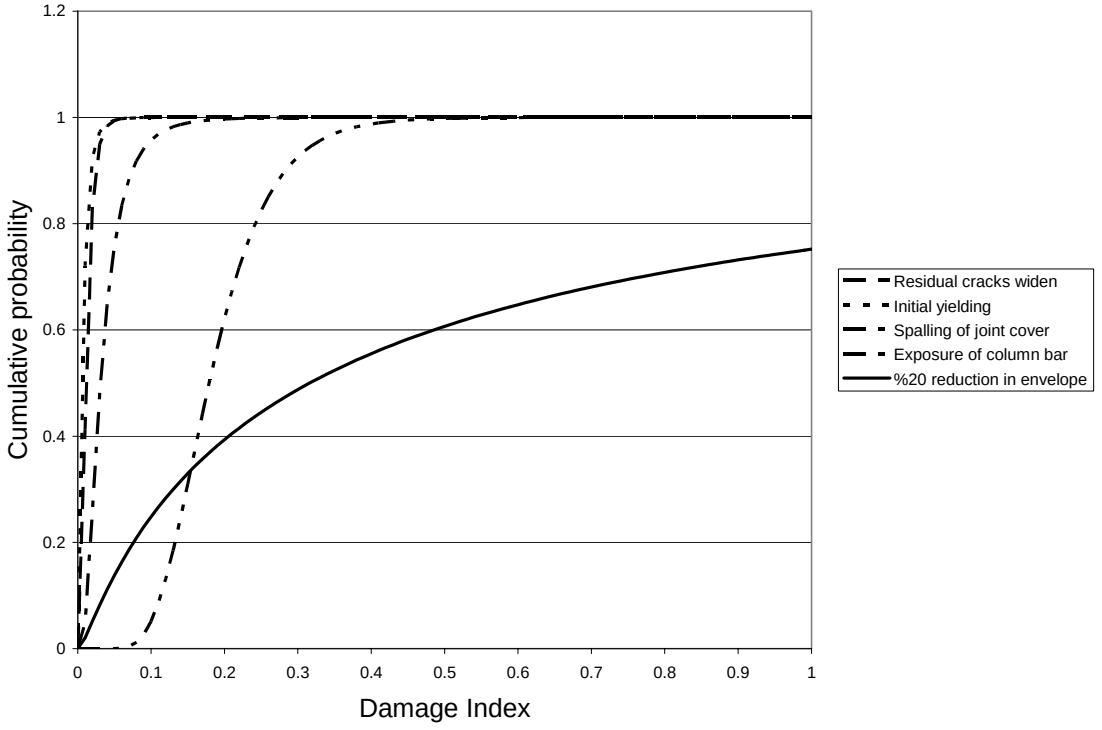

Figure 4-44: Damage index to damage measure for Mehanny model

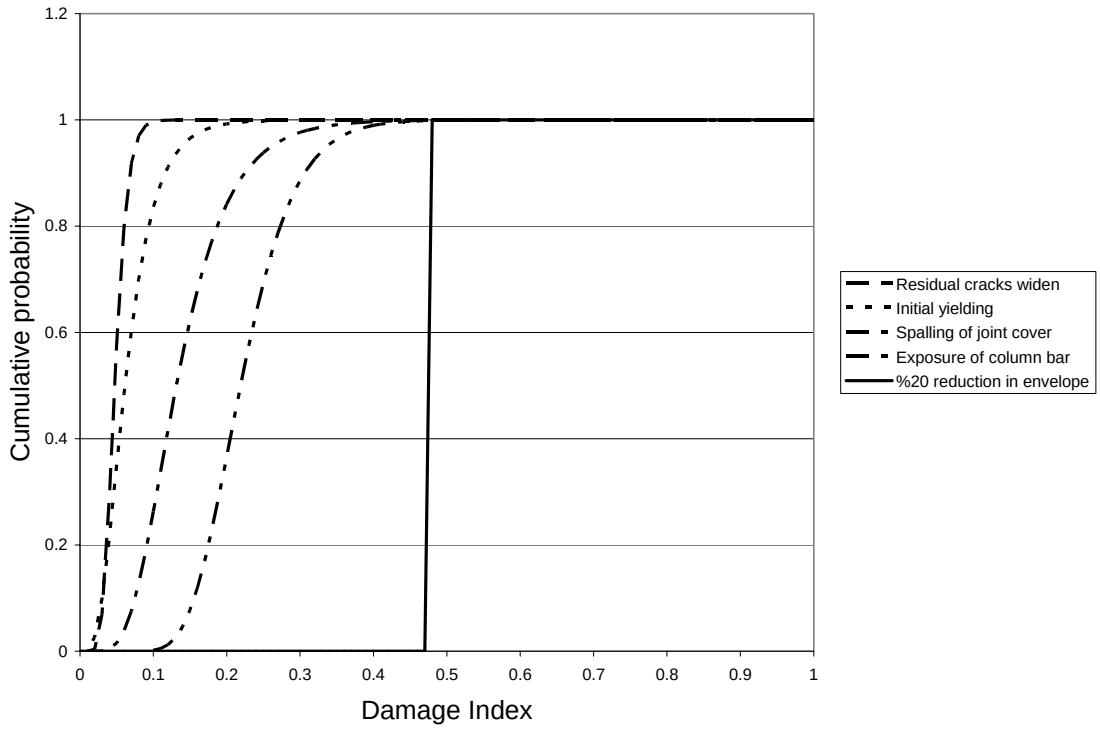

Figure 4-45: Damage index to damage measure for Normalized Peak model

5 Application to reliability studies

The goal of the performance assessment of a structure was briefly described in the introductory chapter as the estimation of the probability of exceeding a certain performance level. Quantitative representation of performance is possible by using intermediate Engineering Demand Parameters (*EDPs*) and Damage Measures (*DMs*). The major focus of this research is on developing a methodology for relating the earthquake input to the structural damage measures. The processes of finding a correlation between the decision variables (life safety, economic loss, downtime, etc.) and the damage measures are left as future research topics for others.

Previous chapters described a deterministic approach for detailed simulation of reinforced concrete structures and recording the damage in the structural components. The simulation models are typically calibrated and developed on the basis of average values of important parameters. In this chapter, methods are proposed which use the calibrated analytical models to study the effects of physical variability and modeling uncertainties on the overall performance of the system. To eliminate the effects of the ground motion uncertainty for this investigation is limited to analysis with a specified ground motion record and intensity. Thus, the methodology provides for extracting fragility curves, describing the probability of exceeding one or more damage states, conditioned on the earthquake ground motion, i.e. $P\left(DM \left| IM, ground\ motion \right.\right)$.

This chapter provides essential information for performing reliability analysis on RC frames, with focus on the role of beam-column joints. The uncertain quantities in RC modeling are reviewed and probability distributions for the joint response are aggregated from the variability in material parameters and the analytical model uncertainty. Limit-state functions are defined by limiting the damage index for individual joints. The general concept and formulation of response sensitivity is presented (Zhang and Der Kiureghian, 1991; Conte et al., 1999; Conte 2001), and the sensitivity formulation for the joint element and the hysteretic material models are derived and appended to the OpenSees models. The OpenSees reliability toolbox (Haukaas and Der Kiureghian, 2000; Haukaas,

2003a) is used to perform FORM, MVFOSM, and Monte Carlo simulations to estimate the failure (exceeding the limit-state function) probability and to derive fragility curves for individual joint damage.

5.1 *Uncertain quantities for RC components*

The expected performance of a RC structure (to a specified earthquake input) is governed by variability in the physical properties of the as-built structure (aleatory variability), as well as uncertainties in the simulation models and process (epistemic uncertainties). The discrepancy between the simulated results and the actual response of reinforced concrete frames can be formalized by defining the random variables that represent the uncertain modeling parameters.

Even after years of research on the reinforced concrete behavior analysis, there are many aspects of the behavior left unstudied. The different approaches for characterizing the RC component behavior are examples of these uncertainties. Assumptions such as effective slab width, the calibration of the shear panel, and the foundation rotation are a few samples of epistemic uncertainties in predicting the RC frame behavior. Concrete by nature is not a homogeneous material, and the quality and strength of the concrete and its bond characteristics to steel reinforcement may vary for each element of the structure.

Variables are referred to as *"Basic Random Variables"* if they are physical properties that can be observed and measured independently. Statistical information can be collected for the basic random variables, from which probability distribution functions can be derived. Material properties, member dimensions, and gravity (dead and live load) loading parameters are examples of basic variables. Engineering parameters, such as element stiffness and structural component strengths are functions of basic variables, herein referred to as *"Derived Random Variables"*. Any of the random variables can be represented by a vector:

$$X = \{x_1, x_2, \ldots, x_n\} \tag{5.1}$$

The probabilistic distribution for each random variable is selected based on the nature of uncertainty for that parameter. A comprehensive collection of random variable distributions are available in the reliability module OpenSees (see Table 5-1). The distributions are constructed based on user input, from which the OpenSees models return PDF, CDF and inverse CDF values.

Table 5-1: Random variables in OpenSees

Beta (4 parameter)	Gamma	Lognormal	Rayleigh (4 parameter)
Chi-Square	Gumbel	Normal	Uniform
Exponential	Laplace	Pareto (4 parameter)	Weibull

The Normal distribution is suggested for geometrical properties such as nodal coordinates, while the variability in the material properties is best described by a lognormal distribution (Ellingwood and Galambos, 1982). The characteristics of these two widely used probability distributions are briefly reviewed.

Normal distribution: The Normal or Gaussian distribution is a two parameter distribution model, with many convenient properties. In engineering, many random variables with unknown distributions are often assumed to be normal. This is usually a good approximation due to a characteristic of the central limit theorem, which states that the mean of any set of variables with any distribution having a finite mean and variance tends to the normal distribution (Menun 2001).

The probability distribution function (*PDF*) for the normal distribution of variable x is defined as:

$$p(x) = \frac{1}{\sigma\sqrt{2\pi}} e^{\frac{-(x-\mu)^2}{2\sigma^2}} \tag{5.2}$$

in which $x \in (-\infty, \infty)$, μ is the average and σ^2 is the variance.

The cumulative distribution function is calculated as:

$$P(x) = \frac{1}{\sigma\sqrt{2\pi}} \int_{-\infty}^{x} e^{\frac{-(t-\mu)^2}{2\sigma^2}} dt \tag{5.3}$$

The normal distribution with $\mu = 0$ and $\sigma^2 = 1$ is identified as the standard normal distribution, expressed for variable *z* as:

$$\phi(z) = \frac{1}{\sqrt{2\pi}} e^{\frac{-z^2}{2}} \tag{5.4}$$

The cumulative distribution function (*CDF*) for the standard normal distribution is calculated as:

$$\Phi(z) = \frac{1}{\sqrt{2\pi}} \int_{-\infty}^{z} e^{\frac{-t^2}{2}} dt \tag{5.5}$$

The integral (5.5) is numerically calculated and available in the form of tables or in approximate analytical functions. A general normal distribution for *x*, with arbitrary mean and standard deviation, can be converted to a standard form for *z* by changing variables to:

$$z = \frac{(x-\mu)}{\sigma} \tag{5.6}$$

Using (5.6), the CDF for the general normal distribution is calculated as:

$$P(x) = \Phi\left(\frac{x-\mu}{\sigma}\right) \tag{5.7}$$

where Φ is defined by (5.5). A linear combination of jointly independent normal random variables has a normal distribution.

$$X_1 \leftarrow N(\mu_1, \sigma_1) \quad \& \quad X_2 \leftarrow N(\mu_2, \sigma_2)$$
$$Y = X_1 + X_2 \tag{5.8}$$
$$Y \leftarrow N\left(\mu_1 + \mu_2, \sqrt{\sigma_1^2 + \sigma_2^2}\right)$$

Lognormal distribution: The lognormal is a continuous distribution in which the logarithm of a variable has a normal distribution. In contrast with the normal distribution, the lognormal distribution is skewed. The probability distribution function (*PDF*) for the lognormal distribution is defined as:

$$p(x) = \frac{1}{S \cdot x\sqrt{2\pi}} e^{\frac{-(\ln x - M)^2}{2S^2}} \tag{5.9}$$

in which $x \in [0, \infty)$, and M and S are the distribution parameters. The mean, variance are related to M and S as follows:

$$\mu = e^{M + \frac{S^2}{2}} \tag{5.10}$$

$$\sigma^2 = e^{S^2 + 2M}\left(e^{S^2} - 1\right) \tag{5.11}$$

The cumulative distribution function is calculated as:

$$P(x) = \frac{1}{S\sqrt{2\pi}} \int_0^x \frac{1}{t} e^{\frac{-(\ln t - M)^2}{2S^2}} dt \tag{5.12}$$

The cumulative distribution function of an arbitrary lognormal distribution can be calculated using the standard normal and a variable change to:

$$Z = \frac{(\ln X - M)}{S} \tag{5.13}$$

The cumulative probability is calculated as:

$$P(x) = \frac{1}{\sqrt{2\pi}} \int_{-\infty}^{\frac{\ln x - M}{S}} e^{\frac{-t^2}{2}} dt = \Phi\left(\frac{\ln x - M}{S}\right) \tag{5.14}$$

5.1.1 **Uncertainty in concrete strength**

Concrete as a construction material is subjected to significant uncertainty in compression strength and other mechanical behavior. Variations in the properties and proportions of concrete constituents and the quality of mixing, transportation and placement are major sources of uncertainty. Discrepancies in test results add to the uncertainty in the expected compressive strength, since even specimens from the same batch of concrete show different strength levels. Figure 5-1 shows the observed compressive strength for 176 normal weight concrete specimens, all of which had a nominal strength of 3000 psi (MacGregor 1997).

Many of researchers have suggested that the concrete compressive strength is a normal distribution (e.g. Mirza et al., 1979a) for concrete produced with good quality control, although for concretes with lower quality control, a lognormal distribution gives a better fit. The coefficient of variation (*COV*) of cast-in-place laboratory-cured specimens has been reported as between 15% and 20%, where approximate observed values are 12%, 15%, and 18% for precast, ready-mix in-situ, and site-mix in-situ concrete, respectively.

For design purposes, the specified compressive strength (f_c') is specified statistically as a compressive strength such that no more than permissible proportion of tests will fall bellow it (ACI-214, 2002). The required average strength to ensure the requirements for the specified compressive strength is referred to as f_{cr}'. As the *COV* is reduced (e.g. though improved quality control), the value of the required average strength can also be reduced. Figure 5-2 shows how the *COV* may affect the required average strength. For cases where a standard deviation can be established (i.e. σ is specified), the average value for compressive strength can be calculated based on Table 5-2. The average and standard deviation values for concrete compressive strength are used in the analytical model.

Table 5-2: Required average compressive strength when data are available to establish a standard deviation (ACI-318)

Specified compressive strength f_c' (psi)	Required average compressive strength f_{cr}'
$f_c' \le 5000$	Use the larger value of: $f_{cr}' = f_c' + 1.34\sigma$ $f_{cr}' = f_c' + 2.33\sigma - 500$
$f_c' > 5000$	Use the larger value of: $f_{cr}' = f_c' + 1.34\sigma$ $f_{cr}' = 0.9 f_c' + 2.33\sigma$

Depending on the quality of the concrete and the observed or selected coefficient of variation, parameters of the normal distribution for representing the concrete compressive strength is calculated.

5.1.2 **Uncertainty in steel yield strength**

The variability in the rebar yield strength is mostly caused by variation in the material itself and variation in bar area. The variation of the yield strength along a single bar is generally small, while the variability of samples from different batches may be high. A review on yield strength of reinforcing bars showed the *COV* was on the order of 1% to 4% for individual bar sizes and 4% to 7% for all bar sizes derived from one source (Mirza et al. 1979b). Test results on grade 40 and 60 steel bars showed agreement with a normal distribution within the range of 5^{th} to 95^{th} percentile, though lognormal probability distributions is suggested (Figure 5-3).

5.1.3 **Uncertainty in shear panel modeling**

The material model used to represent the joint force-deformation relationship has multiple parameters. The probabilistic features of these parameters are governed by a combination of uncertainty in the theoretical model, along with variability in the material and other modeling parameters. The physical features of the joint and construction quality (i.e. bar placements, aggregate size and type etc) also contribute to the response variability. Four modeling parameters are considered for the probabilistic study on the

joint behavior: elastic stiffness, yield shear, stiffness hardening ration, and the cap deformation.

The uncertainty in the theoretical model for calibrating the shear panel is the consequence of model limitations, the assumptions made in the process of developing the analytical model, and the assumptions made in using the model. To quantify modeling uncertainties, data from the model calibration (chapter 4) is used to estimate the relative difference between the theoretical and observed strength. Based on the available data (described bellow), the relative error follows a normal distribution.

The probabilistic function for the shear panel behavior (calculated based on Modified Compression Field Theory) is expressed as:

$$V_{theory} = V_{MCFT} + \varepsilon(v) \tag{5.15}$$

where $\varepsilon(v) \leftarrow N(0, \sigma_{error})$, so:

$$V_{theory} \leftarrow N(V_{MCFT}, \sigma_{error}) \tag{5.16}$$

The suggested coefficient of variation for the elastic stiffness, shear strength, stiffness hardening ratio, and the cap deformation is 10% based on the relative error distribution (Figure 5-4).

The effects of the variability in concrete strength f_c', steel yield stress F_y, and the column axial load are studied to determine the joint response variability to the basic random variables. A sampling simulation is performed by generating random values for f_c', F_y, and the column axial load. The random numbers are generated according to governing probabilistic distributions and within the $[\mu - \sigma, \mu + \sigma]$ range. The outcome of the Monte Carlo simulation suggests a normal distribution for the joint parameter variability with respect to the modeling parameters (Figure 5-5). The simulation is done by a *MATLAB* program, using the *MCFT* algorithm discussed in Chapter 4. The shear failure mode for the modeled joint panel was calculated as tensile yielding of the

transverse reinforcement in tension, and the model variability is mainly influenced by the variability in steel parameters.

The overall probabilistic distributions of the joint parameters are calculated by combining the model uncertainty and material variability using the conditional probability formulation (Figure 5-6). According to the results shown in Figure 5-6, the model variability is the dominant source of uncertainty in the joint model.

5.2 *Limit state boundary for RC frames with joint elements*

The structural performance requirements are enforced numerically as limit-state boundary equations. $g(X)$ is defined as the limit-state function, where X is the vector of random variables and the failure domain is defined as $g(X) \le 0$. The random variables that are involved in the limit-state function can be selected from basic or derived random variables.

The limit-state boundaries are often described by the inter-story drift for overall system performance assessment (Moehle 1997); or in terms of the local damage indices for the reinforced concrete components. The damage level of each component is calculated by the damage recorder.

Story drift: Maximum story drift or inter-story drift envelopes are widely used to characterize structural performance. There are several recommendations and limitations for the allowable story drift in reinforced concrete structures. As an example, FEMA 450 suggests allowable story drift ratio between $0.025h_{sx}$ and $0.015h_{sx}$, depending on the seismic use group. Story drift has advantage for the global performance evaluation, especially in preliminary design. However, the drifts do not directly reflect detailed information on the structural damage.

Component damage: Damage to individual components is a more accurate approach for defining the structural performance, specially for the lower performance objectives when

the collapse is not likely and the component performance objectives are more related to repair costs and the associated down-time.

The target damage index for the limit-state function is selected depending on the reliability analysis type. FORM, MVFOSM, and Monte-Carlo simulation (see Section 5.4) require a predefined limit for the damage index. In such cases the limit-state function is defined as $g\left(di - DI\right)$, where di is the calculated component damage and DI is the limit (or predefined target) value for the damage index. Where a fragility function is used, the damage index limit value varies from 0.0 to 1.0.

5.3 *Response gradients and sensitivity*

There have been several analytical and numerical studies to determine the sensitivity of the transient finite element response to the model parameters (Zhang and Der Kuireghian, 1991; Conte, 1999; Conte, 2000). In the reliability context, the response usually refers to the calculated force or deformation. The gradient of the response (or the so-called sensitivity) is defined as the variation of the response with respect to a sensitivity parameter (h). The sensitivity parameter h is one of the basic random variables such as the material properties, physical dimensions or loading parameters.

In the global sensitivity formulation by Zhang and Der Kuireghian (1991), the classic dynamical equilibrium equation is assumed, where the physical parameters of mass, damping and stiffness might be expressed as the random sensitivity parameter. The transient equilibrium equation, considering the sensitivity parameter of h, is expressed as:

$$\underline{\underline{M}}_{(h)} \cdot \underset{\sim}{\ddot{u}}_{(t,h)} + \underline{\underline{C}}_{(h)} \cdot \underset{\sim}{\dot{u}}_{(t,h)} + \underset{\sim}{R}_{\left(u_{(t,h)},h\right)} = \underset{\sim}{F}_{(t,h)} \tag{5.17}$$

where $\underset{\sim}{\ddot{u}}_{(t,h)}$, $\underset{\sim}{\dot{u}}_{(t,h)}$, and $\underset{\sim}{u}_{(t,h)}$ are the nodal acceleration, velocity and displacement vectors, $\underset{\sim}{R}_{\left(u_{(t,h)},h\right)}$ is the nonlinear internal forces ($\underline{\underline{K}}_{(h)} \cdot \underset{\sim}{u}_{(t,h)}$ for a linear system), $\underline{\underline{M}}_{(h)}$ and $\underline{\underline{C}}_{(h)}$ are the mass and damping matrices, and $\underset{\sim}{F}_{(t,h)}$ is the vector of time-variant external forces.

The dynamic equilibrium equation (5.17) is solved by integrating the solution over time, using the Newmark-beta method. The acceleration and velocity vectors of each time step $n+1$, at time $t=t_{n+1}$ are assumed to be functions of last step solution and the current displacements, described by the following equations:

$$\dot{\underset{\sim}{u}}_{n+1}=(\Delta t)\left(1-\frac{\alpha}{2\beta}\right)\ddot{\underset{\sim}{u}}_{n}+\left(1-\frac{\alpha}{\beta}\right)\dot{\underset{\sim}{u}}_{n}+\frac{\alpha}{\beta(\Delta t)}\left(\underset{\sim}{u}_{n+1}-\underset{\sim}{u}_{n}\right) \tag{5.18}$$

$$\ddot{\underset{\sim}{u}}_{n+1}=\left(1-\frac{1}{2\beta}\right)\ddot{\underset{\sim}{u}}_{n}-\frac{1}{\beta(\Delta t)}\dot{\underset{\sim}{u}}_{n}+\frac{1}{\beta(\Delta t)^{2}}\left(\underset{\sim}{u}_{n+1}-\underset{\sim}{u}_{n}\right) \tag{5.19}$$

where α and β are calibration parameters for the Newmark-beta method, and Δt is the time increment. The velocity and acceleration vectors for the current step are substituted into the main equation (5.17), in which case the dynamic equation can be written as:

$$\left(\frac{M}{\beta(\Delta t)^{2}}+\frac{\alpha C}{\beta(\Delta t)}\right)\underset{\sim}{u}_{n+1}= \\ \underset{\sim}{F}_{n}+\left(\frac{M}{\beta(\Delta t)^{2}}+\frac{\alpha C}{\beta(\Delta t)}-K\right)\underset{\sim}{u}_{n}+\left(\frac{M}{\beta(\Delta t)}+\frac{\alpha-\beta}{\beta}C\right)\dot{\underset{\sim}{u}}_{n}-\left(\frac{2\beta-1}{2\beta}M+\frac{2\beta-\alpha}{2\beta}C(\Delta t)\right)\ddot{\underset{\sim}{u}}_{n} \tag{5.20}$$

The nonlinear equation (5.20) is solved (using the Newton Raphson algorithm) for the displacement vector at the current load-step, and the velocity and acceleration vectors are calculated subsequently (equations (5.18) and (5.19)).

Equation (5.17) can be differentiated with respect to h to form the response gradients (Zhang and Der Kuireghian, 1991). Using the chain rule for derivation, the general sensitivity formulation can be derived as:

$$\frac{\partial \underline{\underline{M}}}{\partial h}\cdot\ddot{\underset{\sim}{u}}+\underline{\underline{M}}\cdot\frac{\partial\ddot{\underset{\sim}{u}}}{\partial h}+\frac{\partial \underline{\underline{C}}}{\partial h}\cdot\dot{\underset{\sim}{u}}+\underline{\underline{C}}\cdot\frac{\partial\dot{\underset{\sim}{u}}}{\partial h}+\frac{\partial \underset{\sim}{R}}{\partial \underset{\sim}{u}}\cdot\frac{\partial \underset{\sim}{u}}{\partial h}+\left.\frac{\partial \underset{\sim}{R}}{\partial h}\right|_{u}=\frac{\partial \underset{\sim}{F}}{\partial h} \tag{5.21}$$

substituting $\frac{\partial \underset{\sim}{R}}{\partial \underset{\sim}{u}} = \underline{\underline{K}}$, the sensitivity equation can be written as:

$$\underline{\underline{M}} \cdot \frac{\partial \ddot{\underset{\sim}{u}}}{\partial h} + \underline{\underline{C}} \cdot \frac{\partial \dot{\underset{\sim}{u}}}{\partial h} + \underline{\underline{K}} \cdot \frac{\partial \underset{\sim}{u}}{\partial h} = \frac{\partial \underset{\sim}{F}_n}{\partial h} - \frac{\partial \underline{\underline{M}}}{\partial h} \cdot \ddot{\underset{\sim}{u}} - \frac{\partial \underline{\underline{C}}}{\partial h} \cdot \dot{\underset{\sim}{u}} - \left. \frac{\partial \underset{\sim}{R}}{\partial h} \right|_{\underset{\sim}{u}} \tag{5.22}$$

In order to calculate the response gradients, the derivatives of model parameters ($\frac{\partial \underline{\underline{M}}}{\partial h}, \frac{\partial \underline{\underline{C}}}{\partial h}, \left. \frac{\partial \underset{\sim}{R}}{\partial h} \right|_u$) and the displacement components on the right side of the general sensitivity formulation (5.22) must be determined. The same Newmark formulation can be used to calculate the response gradients (5.23), by solving (5.24):

$$\underset{\sim}{v} = \frac{\partial \underset{\sim}{u}}{\partial h} \tag{5.23}$$

$$\underline{\underline{M}} \cdot \dot{\underset{\sim}{v}} + \underline{\underline{C}} \cdot \underset{\sim}{v} + \underline{\underline{K}} \cdot \underset{\sim}{v} = \frac{\partial \underset{\sim}{F}_n}{\partial h} - \frac{\partial \underline{\underline{M}}}{\partial h} \cdot \ddot{\underset{\sim}{u}} - \frac{\partial \underline{\underline{C}}}{\partial h} \cdot \dot{\underset{\sim}{u}} - \left. \frac{\partial \underset{\sim}{R}}{\partial h} \right|_{\underset{\sim}{u}} \tag{5.24}$$

The process of calculating the response sensitivity is performed in three steps:

- Using a regular finite element solution for finding $\underset{\sim}{u}_{n+1}$, $\dot{\underset{\sim}{u}}_{n+1}$, and $\ddot{\underset{\sim}{u}}_{n+1}$
- Calculating the stress sensitivity for the given deformation $\left. \frac{\partial \underset{\sim}{R}}{\partial h} \right|_u$
- Calculating the strain sensitivity $\frac{\partial \underset{\sim}{u}}{\partial h}$ or $\underset{\sim}{v}$

For static analysis, equation (5.24) is expressed as:

$$\underline{\underline{K}} \cdot \underset{\sim}{v} = \frac{\partial \underset{\sim}{F}_n}{\partial h} - \left. \frac{\partial \underset{\sim}{R}}{\partial h} \right|_{\underset{\sim}{u}} \tag{5.25}$$

The stress sensitivity is computed at the element and material levels, and the results are then assembled to form the stress resultant sensitivity term of $\left. \frac{\partial \underset{\sim}{R}}{\partial h} \right|_{\underset{\sim}{u}}$.

5.3.1 **Resultant force sensitivity at element level**

In the finite element formulation, the global resultant forces are calculated by assembling the element forces, and the sensitivity can be formulated in the same manner:

$$\underset{\sim}{R}_{(\underline{u},h)} = \sum_{elements} \underset{\sim}{R}^{element} \tag{5.26}$$

Thus the global sensitivity is first calculated at element level and then assembled to form the global sensitivity vector.

$$\frac{\partial \underset{\sim}{R}_{(\underline{u},h)}}{\partial h} = \sum_{elements} \frac{\partial \underset{\sim}{R}^{element}}{\partial h} \tag{5.27}$$

$\underset{\sim}{R}^{element}_{\left(\underline{u}_{(t,h)},h\right)}$ is calculated by applying the chain derivative rule, where the element response derivative is calculated as:

$$\underset{\sim}{R}^{e}_{\left(\underline{u}^{e}_{(t,h)},h\right)} = \frac{\partial \underset{\sim}{R}^{e}}{\partial \underset{\sim}{u}^{e}} \cdot \frac{\partial \underset{\sim}{u}^{e}}{\partial h} + \left.\frac{\partial \underset{\sim}{R}^{e}}{\partial h}\right|_{u} \tag{5.28}$$

where the superscript *e* refers to individual elements. Initially, the so-called force sensitivity of each element is calculated for a given nodal deformation $\left.\frac{\partial \underset{\sim}{R}^{e}}{\partial h}\right|_{\underline{u}}$. This resultant force sensitivity, $\left.\frac{\partial \underset{\sim}{R}^{e}}{\partial h}\right|_{\underline{u}}$, is required for calculating the global response sensitivity, i.e. $\underset{\sim}{v} = \frac{\partial \underset{\sim}{u}}{\partial h}$. The strain sensitivity $\frac{\partial \underset{\sim}{u}^{e}}{\partial h}$ is then input to the element sensitivity routine to calculate the complete gradient.

The resultant force sensitivity should be defined for each element. In this research the focus is on defining the procedure for the beam-column joint. The gradient of beam-column joint nodal rotations with respect to the sensitivity parameter is directly related to the sensitivity of the material model response. The following equations describe the

material (force-deformation) sensitivity expressions for the three joint models implemented in this research:

For Joint2D-1SPR:
$$\left.\frac{\partial \underset{\sim}{R}}{\partial h}\right|_u = \begin{Bmatrix} \left.\frac{\partial m_\alpha}{\partial h}\right|_{\theta_\alpha} \\ -\left.\frac{\partial m_\alpha}{\partial h}\right|_{\theta_\alpha} \end{Bmatrix} \tag{5.29}$$

For Joint2D-5SPR:
$$\left.\frac{\partial \underset{\sim}{R}}{\partial h}\right|_u = \begin{Bmatrix} \left.\frac{\partial m_1}{\partial h}\right|_{\theta_1} \\ \left.\frac{\partial m_2}{\partial h}\right|_{\theta_2} \\ \left.\frac{\partial m_3}{\partial h}\right|_{\theta_3} \\ \left.\frac{\partial m_4}{\partial h}\right|_{\theta_4} \\ \left.\frac{\partial m_\alpha}{\partial h}\right|_{\theta_\alpha} \\ -\left.\frac{\partial m_\alpha}{\partial h}\right|_{\theta_\alpha} \end{Bmatrix} \tag{5.30}$$

For Joint3D:
$$\left.\frac{\partial \underset{\sim}{R}}{\partial h}\right|_u = \begin{Bmatrix} \left.\frac{\partial m_{\gamma x'}}{\partial h}\right|_{\theta_{\gamma x'}} \\ \left.\frac{\partial m_{\gamma y'}}{\partial h}\right|_{\theta_{\gamma y'}} \\ \left.\frac{\partial m_{\gamma z'}}{\partial h}\right|_{\theta_{\gamma z'}} \end{Bmatrix} \tag{5.31}$$

where m is the moment resultant for uniaxial materials representing joint force-deformation relationships. All three of these require calculation of the response gradient at material level $(m-\theta)$.

5.3.2 **Response gradient at material level**

The response gradient at the material level is defined as the force (stress) derivative with respect to the sensitivity parameter. The sensitivity parameter, h, is selected from the model key parameters that define the loading envelopes (Table 3.3). Depending on the material state for the current step, the response sensitivity depends on the loading/unloading/reloading path sensitivity.

In OpenSees, the gradient functions have already been implemented (Haukaas, 2003b) for uniaxial Steel01, concrete01, hardening and Bouc-Wen material models. Based on the modeling recommendations in Chapter 4, three hysteretic material models were implemented as part of this research for joint elements. In this section, the force gradient functions are derived for the Bilinear, Clough and pinching material models.

The force (stress) gradient for material models is calculated based on the same systematic definitions used for calculating material force (stress) and stiffness. The material state (as described in chapter 2) is first determined and the sensitivity is calculated based on the material state.

For loading state of the material (states 1 and 2), the response sensitivity directly depends on the loading envelope sensitivity. In Chapter 3, the loading envelope for the peak oriented material modes is described as:

$$\begin{aligned} F_{envelope}(\delta) &= B_{0,\delta_y^+}(\delta)\cdot K\cdot\delta + B_{\delta_y^+,\delta_{cap}^+}(\delta)\cdot\left[F_y^+ + \alpha_h\cdot K\cdot\left(\delta-\delta_y^+\right)\right] \\ &+ B_{\delta_{cap}^+,\delta_{res}^+}(\delta)\cdot\left[F_{cap}^+ + \alpha_{cap}\cdot K\cdot\left(\delta-\delta_{cap}^+\right)\right] + H\left(\delta-\delta_{res}^+\right)\cdot F_{res}^+ \end{aligned} \tag{5.32}$$

Employing the chain-rule, the complete derivative of the force-deformation envelope (equation(5.32)) with respect to the sensitivity parameter is calculated as:

$$
\begin{aligned}
&\frac{\partial F_{envelope}}{\partial h} = \frac{\partial B_{0,\delta_y^+}(\delta)}{\partial h}\cdot K\cdot\delta + B_{0,\delta_y^+}(\delta)\cdot\frac{\partial K}{\partial h}\cdot\delta + B_{0,\delta_y^+}(\delta)\cdot K\cdot\frac{\partial\delta}{\partial h}\\
&+\frac{\partial B_{\delta_y^+,\delta_{cap}^+}(\delta)}{\partial h}\cdot\left[F_y^+ + \alpha_h\cdot K\cdot\left(\delta-\delta_y^+\right)\right]\\
&+B_{\delta_y^+,\delta_{cap}^+}(\delta)\cdot\left[\frac{\partial F_y^+}{\partial h}+\frac{\partial\alpha_h}{\partial h}\cdot K\cdot\left(\delta-\delta_y^+\right)+\alpha_h\cdot\frac{\partial K}{\partial h}\cdot\left(\delta-\delta_y^+\right)+\alpha_h\cdot K\cdot\left(\frac{\partial\delta}{\partial h}-\frac{\partial\delta_y^+}{\partial h}\right)\right]\\
&+\frac{\partial B_{\delta_{cap}^+,\delta_{res}^+}(\delta)}{\partial h}\cdot\left[F_{cap}^+ + \alpha_{cap}\cdot K\cdot\left(\delta-\delta_{cap}^+\right)\right]\\
&+B_{\delta_{cap}^+,\delta_{res}^+}(\delta)\cdot\left[\frac{\partial F_{cap}^+}{\partial h}+\frac{\partial\alpha_{cap}}{\partial h}\cdot K\cdot\left(\delta-\delta_{cap}^+\right)+\alpha_{cap}\cdot\frac{\partial K}{\partial h}\cdot\left(\delta-\delta_{cap}^+\right)+\alpha_{cap}\cdot K\cdot\left(\frac{\partial\delta}{\partial h}-\frac{\partial\delta_{cap}^+}{\partial h}\right)\right]\\
&+\frac{\partial H\left(\delta-\delta_{res}^+\right)}{\partial h}\cdot F_{res}^+ + H\left(\delta-\delta_{res}^+\right)\cdot\frac{\partial F_{res}^+}{\partial h}
\end{aligned}
\tag{5.33}
$$

The derivative (5.33) is separately expressed for the force (stress) sensitivity and (strain) sensitivity as:

$$
\frac{\partial F_{envelope}}{\partial h} = \left.\frac{\partial F_{envelope}}{\partial h}\right|_{\delta} + F_{envelope}\cdot\frac{\partial\delta}{\partial h} \tag{5.34}
$$

The derivatives of a continuous function multiplied by a boxcar or step function are calculate using chain derivative rule, as:

$$
y_{\left(x_{(h)},h\right)} = H_{(x)}\cdot f_{\left(x_{(h)},h\right)} \tag{5.35}
$$

$$
\frac{\partial y(x)}{\partial h} = \frac{\partial H(x)}{\partial h}\cdot f(x) + H(x)\cdot\frac{\partial f(x)}{\partial h} \tag{5.36}
$$

The derivative of the step function is zero, except for the neighborhood of the step, where it is represented by a Dirac delta function (Δ_D):

$$
\frac{\partial H(x)}{\partial h} = \frac{\partial x}{\partial h}\cdot\Delta_D(x) \tag{5.37}
$$

$$\frac{\partial H\left(x-c\right)}{\partial c}=-\Delta_D\left(x-c\right) \tag{5.38}$$

where c is a constant value. For the boxcar function,

$$z_{\left(x_{(h)},h\right)}=B_{a,b}\left(x\right)\cdot f_{\left(x_{(h)},h\right)} \tag{5.39}$$

$$\frac{\partial z\left(x\right)}{\partial h}=\frac{\partial B_{a,b}\left(x\right)}{\partial h}\cdot f\left(x\right)+B_{a,b}\left(x\right)\cdot\frac{\partial f\left(x\right)}{\partial h} \tag{5.40}$$

where the derivative of boxcar function is defined as:

$$\frac{\partial B_{a,b}\left(x\right)}{\partial h}=\frac{\partial\left(x-a\right)}{\partial h}\cdot\Delta_D\left(x-a\right)-\frac{\partial\left(x-b\right)}{\partial h}\cdot\Delta_D\left(x-b\right) \tag{5.41}$$

Using the derivative definitions for the boxcar and the step functions, the force (stress) sensitivity components of (5.34) are derived as:

$$\begin{aligned}
&\left.\frac{\partial F_{envelope}}{\partial h}\right|_{\delta}=\frac{\partial\delta_y^+}{\partial h}\cdot\Delta_D\left(\delta-\delta_y^+\right)\cdot K\cdot\delta+B_{0,\delta_y^+}\left(\delta\right)\cdot\frac{\partial K}{\partial h}\cdot\delta\\
&+\left[\frac{\partial\delta_{cap}^+}{\partial h}\cdot\Delta_D\left(\delta-\delta_{cap}^+\right)-\frac{\partial\delta_y^+}{\partial h}\cdot\Delta_D\left(\delta-\delta_y^+\right)\right]\cdot\left[\sigma_y^+ +\alpha_h\cdot E\cdot\left(\delta-\delta_y^+\right)\right]\\
&+B_{\delta_y^+,\delta_{cap}^+}\left(\delta\right)\cdot\left[\frac{\partial F_y^+}{\partial h}+\frac{\partial\alpha_h}{\partial h}\cdot K\cdot\left(\delta-\delta_y^+\right)+\alpha_h\cdot\frac{\partial K}{\partial h}\cdot\left(\delta-\delta_y^+\right)-\alpha_h\cdot K\cdot\frac{\partial\delta_y^+}{\partial h}\right]\\
&+\left[\frac{\partial\delta_{res}^+}{\partial h}\cdot\Delta_D\left(\delta-\delta_{res}^+\right)-\frac{\partial\delta_{cap}^+}{\partial h}\cdot\Delta_D\left(\delta-\delta_{cap}^+\right)\right]\cdot\left[F_{cap}^+ +\alpha_{cap}\cdot K\cdot\left(\delta-\delta_{cap}^+\right)\right]\\
&+B_{\delta_{cap}^+,\delta_{res}^+}\left(\delta\right)\cdot\left[\frac{\partial F_{cap}^+}{\partial h}+\frac{\partial\alpha_{cap}}{\partial h}\cdot K\cdot\left(\delta-\delta_{cap}^+\right)+\alpha_{cap}\cdot\frac{\partial K}{\partial h}\cdot\left(\delta-\delta_{cap}^+\right)-\alpha_{cap}\cdot K\cdot\frac{\partial\delta_{cap}^+}{\partial h}\right]\\
&-\frac{\partial\delta_{res}^+}{\partial h}\cdot\Delta_D\left(\delta-\delta_{res}^+\right)\cdot F_{res}^+ +H\left(\delta-\delta_{res}^+\right)\cdot\frac{\partial F_{res}^+}{\partial h}
\end{aligned} \tag{5.42}$$

The displacement (strain) sensitivity components of (5.34) are derived as:

$$\begin{aligned}\frac{\partial F_{envelope}}{\partial \delta} &= \left[\Delta_D(\delta) - \Delta_D\left(\delta - \delta_y^+\right)\right]\cdot K\cdot\delta + B_{0,\delta_y^+}(\delta)\cdot K \\ &+\left[\Delta_D\left(\delta - \delta_y^+\right) - \Delta_D\left(\delta - \delta_{cap}^+\right)\right]\cdot\left[F_y^+ + \alpha_h\cdot K\cdot\left(\delta - \delta_y^+\right)\right] + B_{\delta_y^+,\delta_{cap}^+}(\delta)\cdot\alpha_h\cdot K \\ &+\left[\Delta_D\left(\delta - \delta_{cap}^+\right) - \Delta_D\left(\delta - \delta_{res}^+\right)\right]\cdot\left[F_{cap}^+ + \alpha_{cap}\cdot K\cdot\left(\delta - \delta_{cap}^+\right)\right] + B_{\delta_{cap}^+,\delta_{res}^+}(\delta)\cdot\alpha_{cap}\cdot K \\ &+\Delta_D\left(\delta - \delta_{res}^+\right)\cdot F_{res}^+\end{aligned} \tag{5.43}$$

Equations (5.42) and (5.43) show occasional discontinuities or infinite values due to the presence of delta functions. These discontinuities are due to sharp corners of the multi-linear material models. One solution to this problem is by developing smooth material models and thereby avoiding the sharp corners. The other solution, which is applied to the material models in this research, involves using the following numerical approximation for the step function:

$$\begin{aligned}H(x) &= \lim_{t\to 0}\frac{1}{2}\left(\tanh\left(\frac{x}{t}\right)+1\right) \\ \frac{\partial \tanh}{\partial x} &= \sec h^2(x) \\ \sec h(x) &= \frac{2}{e^x + e^{-x}} \\ \delta(x) &= \lim_{t\to 0}\frac{1}{2}\sec h^2\left(\frac{x}{t}\right)\end{aligned} \tag{5.44}$$

The sensitivity parameters for the peak-orientated materials are derived as a function of variations in the elastic modulus, yield strength (stress), hardening slope, capping displacement (strain) and the cap slope. The derivatives are separately calculated with respect to the material sensitivity parameters.

These derivatives are appended to the material models as envelope sensitivity functions, for the loading states (states 1 and 2 according to the definitions in Chapter3). Equations (5.45) to (5.49) describe the force sensitivity to the six key parameters (K, F_y, δ_{cap}, α_h, α_{cap} and R).

$$\left.\frac{\partial F_{envelope}}{\partial K}\right|_{\varepsilon} = -\delta_y^+ \cdot \delta \cdot \Delta_D\left(\delta-\delta_y^+\right) + B_{0,\delta_y^+}\left(\delta\right)\cdot\delta$$
$$+\delta_y^+ \cdot \left[\delta_y^+ + \alpha_h \cdot \left(\delta-\delta_y^+\right)\right]\cdot \Delta_D\left(\delta-\delta_y^+\right) + B_{\delta_y^+,\delta_{cap}^+}\left(\delta\right)\cdot\alpha_h\cdot\delta$$
$$+\left(1-R-\alpha_h\right)\cdot\delta_y^+\cdot\left[\frac{F_{cap}^+}{\alpha_{cap}\cdot K}+\left(\delta-\delta_{cap}^+\right)\right]\cdot\Delta_D\left(\delta-\delta_{res}^+\right) \tag{5.45}$$
$$+B_{\delta_{cap}^+,\delta_{res}^+}\left(\delta\right)\cdot\left[\left(\alpha_h-\alpha_{cap}\right)\cdot\delta_{cap}^+ - \alpha_h\cdot\delta_y^+ + \alpha_{cap}\cdot\delta\right]$$
$$-\left(1-R-\alpha_h\right)\cdot\delta_y^+\cdot R\cdot\frac{\delta_y^+}{\alpha_{cap}}\cdot\Delta_D\left(\delta-\delta_{res}^+\right)$$

Figure 5-7 illustrates the envelope sensitivity to elastic stiffness (K).

$$\left.\frac{\partial F_{envelope}}{\partial F_y^+}\right|_{\varepsilon} = \delta\cdot\Delta_D\left(\delta-\delta_y^+\right) - \left[\delta_y^+ + \alpha_h\cdot\left(\delta-\delta_y^+\right)\right]\cdot\Delta_D\left(\delta-\delta_y^+\right)$$
$$+B_{\delta_y^+,\delta_{cap}^+}\left(\delta\right)\cdot\left(1-\alpha_h\right)$$
$$+\left[\frac{F_{cap}^+}{\alpha_{cap}\cdot K}+\left(\delta-\delta_{cap}^+\right)\right]\cdot\left(R-1+\alpha_h\right)\cdot\Delta_D\left(\delta-\delta_{res}^+\right) \tag{5.46}$$
$$+B_{\delta_{cap}^+,\delta_{res}^+}\left(\delta\right)\cdot\left(1-\alpha_h\right)$$
$$-\frac{\left(R-1+\alpha_h\right)}{\alpha_{cap}\cdot K}\cdot F_{res}^+\cdot\Delta_D\left(\delta-\delta_{res}^+\right) + H\left(\delta-\delta_{res}^+\right)\cdot R$$

Figure 5-8 shows the envelope sensitivity to yielding force (F_y).

$$\left.\frac{\partial F_{envelope}}{\partial \alpha_{cap}}\right|_{\varepsilon} = -\frac{\left(R-1+\alpha_h\right)\cdot\delta_y^+ - \alpha_h\cdot\delta_{cap}^+}{\alpha_{cap}^2}\cdot\left[F_{cap}^+ + \alpha_{cap}\cdot K\cdot\left(\delta-\delta_{cap}^+\right)\right]\cdot\Delta_D\left(\delta-\delta_{res}^+\right)$$
$$+B_{\delta_{cap}^+,\delta_{res}^+}\left(\delta\right)\cdot K\cdot\left(\delta-\delta_{cap}^+\right) + \frac{\left(R-1+\alpha_h\right)\cdot\delta_y^+ - \alpha_h\cdot\delta_{cap}^+}{\alpha_{cap}^2}\cdot\Delta_D\left(\delta-\delta_{res}^+\right)\cdot F_{res}^+ \tag{5.47}$$

$$\left.\frac{\partial F_{envelope}}{\partial R}\right|_{\varepsilon} = \frac{F_y^+}{\alpha_{cap}\cdot K}\cdot\left[F_{cap}^+ + \alpha_{cap}\cdot K\cdot\left(\delta-\delta_{cap}^+\right)\right]\cdot\Delta_D\left(\delta-\delta_{res}^+\right)$$
$$-\frac{F_y^+\cdot F_{res}^+}{\alpha_{cap}\cdot K}\cdot\Delta_D\left(\delta-\delta_{res}^+\right) + H\left(\delta-\delta_{res}^+\right)\cdot F_y^+ \tag{5.48}$$

$$\left.\frac{\partial F_{envelope}}{\partial \delta_{cap}^{+}}\right|_{\varepsilon} = \left[F_y^+ + \alpha_h \cdot K \cdot \left(\delta - \delta_y^+\right)\right] \cdot \Delta_D\left(\delta - \delta_{cap}^+\right) +$$

$$+\left[\left(1 - \frac{\alpha_h}{\alpha_{cap}}\right) \cdot \Delta_D\left(\delta - \delta_{res}^+\right) - \Delta_D\left(\delta - \delta_{cap}^+\right)\right] \cdot \left[F_{cap}^+ + \alpha_{cap} \cdot K \cdot \left(\delta - \delta_{cap}^+\right)\right] \qquad (5.49)$$

$$+B_{\delta_{cap}^+, \delta_{res}^+}(\delta) \cdot \left(\alpha_h - \alpha_{cap}\right) \cdot K - \left(1 - \frac{\alpha_h}{\alpha_{cap}}\right) \cdot F_{res}^+ \cdot \Delta_D\left(\delta - \delta_{res}^+\right)$$

Figure 5-9 illustrates the envelope sensitivity to cap displacement (δ_{cap}).

$$\left.\frac{\partial F_{envelope}}{\partial \alpha_h}\right|_{\varepsilon} = B_{\delta_y^+, \delta_{cap}^+}(\delta) \cdot \left(K \cdot \delta - F_y^+\right)$$

$$+\frac{F_y^+ - K \cdot \delta_{cap}^+}{\alpha_{cap} \cdot K} \cdot \left[F_{cap}^+ + \alpha_{cap} \cdot K \cdot \left(\delta - \delta_{cap}^+\right)\right] \cdot \Delta_D\left(\delta - \delta_{res}^+\right) \qquad (5.50)$$

$$+B_{\delta_{cap}^+, \delta_{res}^+}(\delta) \cdot \left(K \cdot \delta_{cap}^+ - F_y^+\right) - \frac{F_y^+ - K \cdot \delta_{cap}^+}{\alpha_{cap} \cdot K} \cdot F_{res}^+ \cdot \Delta_D\left(\delta - \delta_{res}^+\right)$$

Figure 5-10 shows the envelope sensitivity to hardening ratio (α_h).

The response sensitivity for the unloading and reloading material states (states 3 and 4 as described in Chapter 3) depends on the unloading and reloading slopes, which are different for the Bilinear, Chough, and Pinching material models. The trial force (stress) is calculated and the unloading/reloading/loading state is determined (Chapter 3). For the unloading/reloading path, the force sensitivity is calculated as:

$$\left.\frac{\partial \sigma_{\text{trial}}}{\partial h}\right|_{\delta} = \left.\frac{\partial K_{\text{unloading/reloading}}}{\partial h}\right|_{\delta} \cdot \left(\delta_{\text{trial}} - \delta_{\text{commited}}\right) + \left.\frac{\partial \sigma_{\text{commited}}}{\partial h}\right|_{\delta} \qquad (5.51)$$

where $\left.\frac{\partial K_{\text{unloading/reloading}}}{\partial h}\right|_{\delta}$ is the derivative of unloading/reloading stiffness. For reloading of the peak-oriented hysteretic models, this term is a function of the target point sensitivity (peak point or the pinching point, depending on the material type):

$$\left.\frac{\partial K^{+}_{\text{reloading}}}{\partial h}\right|_{\delta} = \frac{1}{\delta^{+}_{\text{target}} - \delta_{\text{reloading}}}\left(\left.\frac{\partial F^{+}_{\text{target}}}{\partial h}\right|_{\delta} - \left.\frac{\partial F_{\text{reloading}}}{\partial h}\right|_{\delta}\right) \tag{5.52}$$

In equation (5.52), $\left.\frac{\partial F^{+}_{\text{target}}}{\partial h}\right|_{\delta}$ is calculated by using the envelope sensitivity, and $\left.\frac{\partial F_{\text{reloading}}}{\partial h}\right|_{\delta}$ is the force sensitivity of the last committed step.

The implementation of material sensitivity requires saving the peak point and last step force sensitivity as the history variable. The current formulation does not take into account the deterioration effects.

5.4 *Reliability analysis algorithms*

Traditionally, fragility curves describe the failure (exceeding a limit-state) probability for a given earthquake intensity measure. Fragility curves mostly reflect the record to record variability for a given intensity measure, though the variability in the model response should also be considered. Typically a large sample of earthquake records are scaled to the intensity measure and applied to the structural model in the performance assessment process. Incorporating the model variability adds extensively to the computational workload, and analysis cost. The reliability analysis methods facilitate the performance assessment process.

The main objective of reliability analysis is to estimate the probability of failure to achieve a predefined performance. OpenSees reliability module presents a collection of reliability analysis algorithms (Haukaas 2003a). The reliability analysis features of OpenSees are developed in a fashion similar to the finite element analysis framework in which the model is created and it is matched up by proper analysis algorithms.

The Mean-Value First Order Second moment (MVFOSM), the First Order Reliability Method (FORM), and the Monte Carlo analysis are used in this research to compute and

verify an estimate of the failure probability, i.e. finding the probability of hitting a limit-state function.

Mean-Value First Order Second Moment analysis: The MVFOSM method is used to estimate the mean and variance of a limit-state function, or the correlation coefficient between pairs of response quantities (Menun 2002). MVFOSM method employs the mean-centered first-order Taylor series approximation of a limit-state function, which requires a single finite element solution for the mean-value of random variables and the response gradients at the random variable mean points:

$$g(X) \approx g(\mu) + \nabla g(X - \mu) \tag{5.53}$$

The first-order estimate of the mean is evaluated as the limit-state function value evaluated at the mean of the random variables:

$$E[g] \approx g(\mu) \tag{5.54}$$

and the variance is estimated as a function of response gradients:

$$Var(g) \approx \nabla g \times \Sigma \times \nabla g^T \tag{5.55}$$

where Σ is the covariance matrix of random variables vector X.

Correlation coefficients can be calculated by defining gradients for two or more performance functions are defined:

$$Cov[g1, g2] \approx \nabla g_1 \times \Sigma \times \nabla g_2^T \tag{5.56}$$

First Order Reliability Method: The FORM analysis finds the design point in the transformed uncorrelated standard normal space, and by an iterative approach, it estimates the limit-state function at the design point. The design point is defined as the point on the limit-state surface in the standard normal space with highest probability

density. The properties of the standard normal space are used to obtain an estimate the failure probability (Menun 2002).

Finding the design point can be a challenging task in nonlinear finite element reliability analysis. Some of the main challenges are observed by Haukaas (2003):

- The nonlinearities in the finite element solution are reflected to the limit-state function $g(X)$.
- Local nonlinearities in $g(X)$ may be experienced due to numerical approximations in the finite element solution (due to solution tolerances).
- Nonlinearities in the response gradient and the gradient of the limit-state function may be experienced as discussed in section 5.3.2, and numerical approximations in equation (5.44).
- The finite element analysis may not achieve equilibrium convergence, and for some realizations of the random variables it may not be possible to evaluate the performance function. This problem is likely when the reliability analysis algorithm modifies the model parameters to a non-physical configuration. This situation is anticipated in the failure domain, where gross nonlinearities in structural response are expected.

The FORM analyses attempted in this study did not converge in every instance. To derive fragility cures, it is necessary that the FORM analysis is performed multiple times for different pre-defined limit-state functions. So when an estimate for the failure probability distribution is desired, a sampling scheme may be most efficient, especially since the gradients may be costly to compute and they are not required by sampling analysis schemes.

Monte Carlo sampling/simulation analysis: The Monte Carlo Sampling method is based on generating random numbers and observing the fraction of the random numbers that cause failure. The method is useful for obtaining numerical solutions to probability problems that can not be solved analytically by reliability methods.

In the classic Monte Carlo simulation the sampling distribution is centered at the mean point, while the failure events are more likely to occur in the tail regions of probability distributions. Using random distributions centered at the mean value implies that a large number of samples are required to obtain good failure probability estimates. It is recommended the *start point* or the center point for the sampling distribution is prescribed by a previous FORM analysis (Haukaas 2003).

5.5 *Reliability analysis*

Components of a reliability analysis were discussed in the previous sections of this chapter. An OpenSees model is produced to demonstrate the application of the reliability algorithms to determine the failure probability. The reliability model is based on the validation frame model discussed in Section 4.4.2, subjected to two records from the Loma Prieta 1989 and two from Chi-Chi 1999 earthquakes.

Random modeling parameters are represented by probability distribution functions as described earlier in this chapter (e.g. concrete strength f_c', concrete strain at f_c', reinforcing bar yield stress f_y, reinforcing bar elastic modulus E, joint yield strength, joint stiffness, and joint cap deformation). The recorded joint damage indices for the time-history analysis are used to define limit-state functions (Section 5.2).

A Newmark transient analysis with sensitivity calculation (Section 5.3) is used to analytically calculate the response sensitivities. Other details of the reliability analysis model, including the probability transformation, reliability convergence check, merit function check, and step-size rule are determined as suggested by Haukaas (2003a).

Three types of reliability algorithms (Section 5.4) were applied to estimate the failure (joint damage) probability for the testbed frame subjected to the previously mentioned earthquake records. The results of a MVFOSM and Monte Carlo sampling simulation for the damage of the joint element connected to nodes 7,11,6,3 are presented in Figure 5-11. For this example, the FORM analysis did not converge, and hence, no results are available from the FORM simulation.

Figure 5-11 shows the probability distributions (MV-FOSM and MC simulation) for the joint damage index exceeding a pre-defined value, i.e.:

$$P\left\langle di > DI \,\middle|\, IM, ground\_motion \right\rangle \tag{5.57}$$

The results shown in Figure 5-7 and (5.57) could in theory be combined with *DM-DI* relationships (similar to the relations presented in Section 4.6) to complete the performance assessment process as:

$$\begin{gathered} P\left(DM \,\middle|\, IM, ground.motion\right) = \\ \int_{di} P\left(DM \,\middle|\, di = DI\right).dp\left(di > DI \,\middle|\, im = IM, ground.motion\right) \end{gathered} \tag{5.58}$$

However, appropriate *DM-DI* relationships are not available for the type of conforming construction used in this example problem. Therefore, this demonstration of the reliability tools is limited to prediction of *DI* per (5.57).

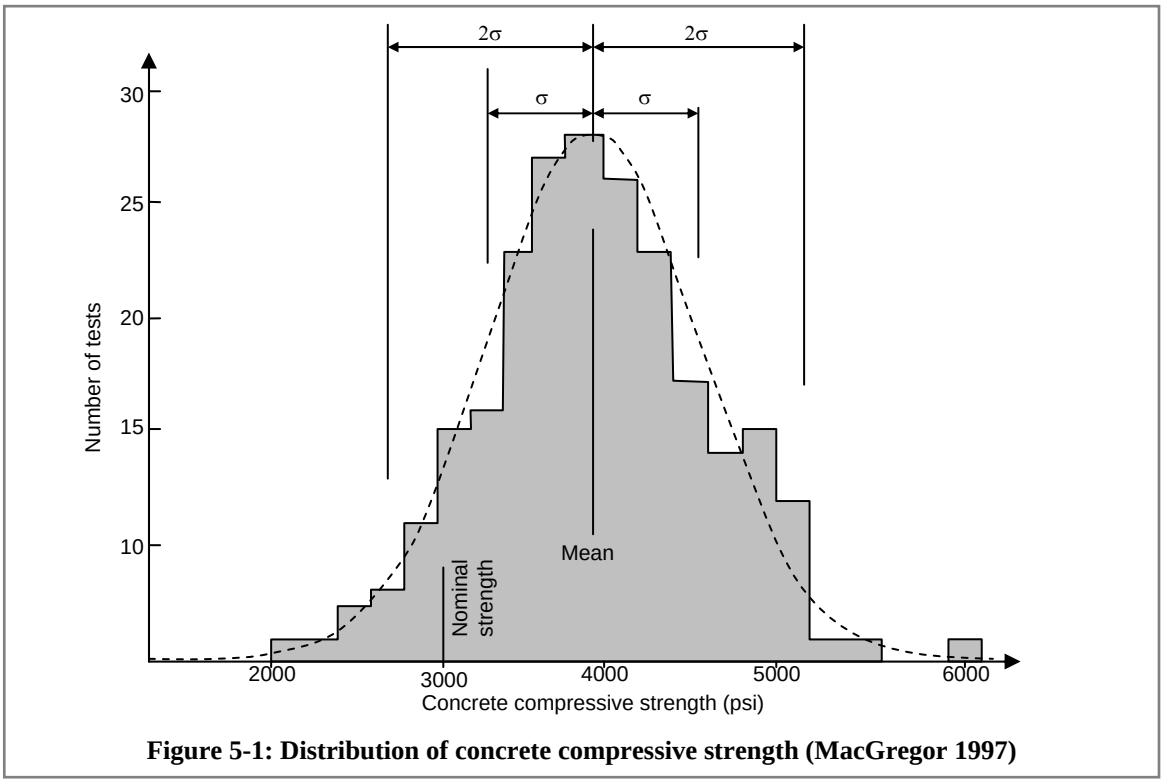

Figure 5-1: Distribution of concrete compressive strength (MacGregor 1997)

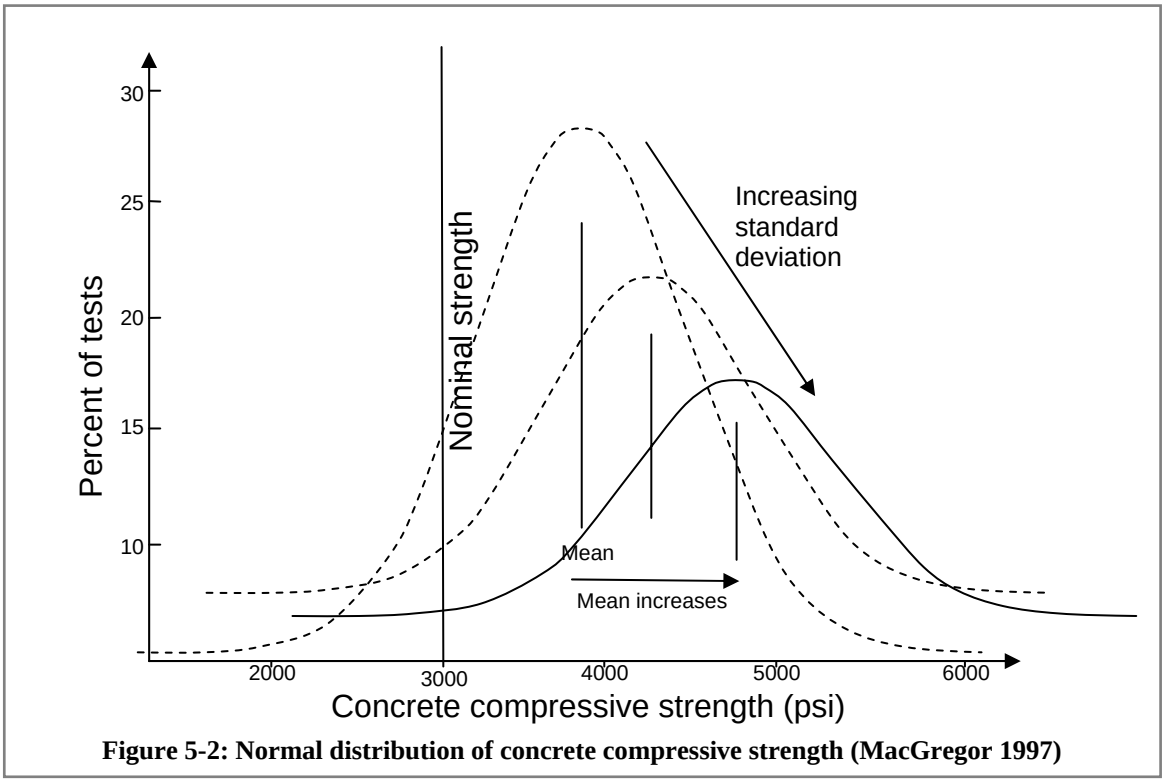

Figure 5-2: Normal distribution of concrete compressive strength (MacGregor 1997)

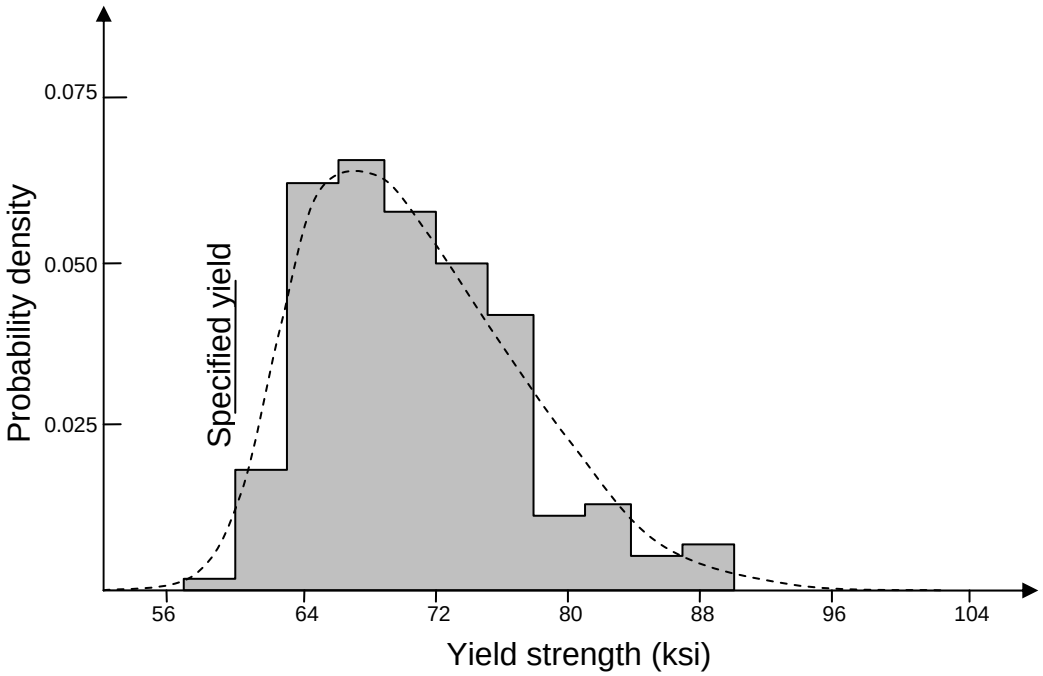

Figure 5-3: Lognormal distribution for yield strength of grade 60 steel (Al Mirza et al. 1979)

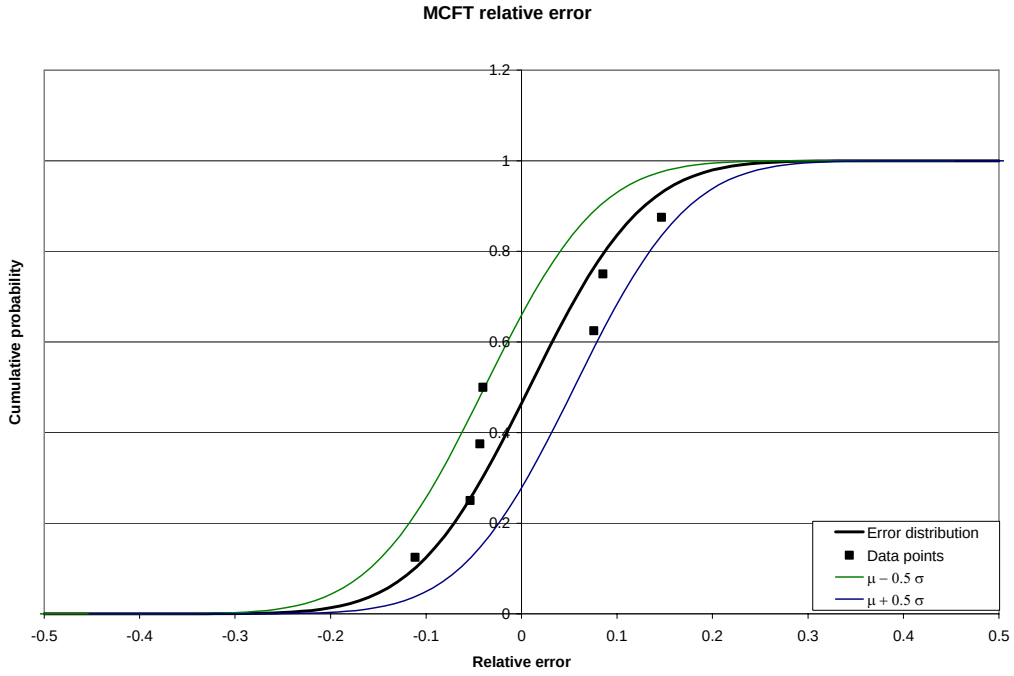

Figure 5-4: Distribution of relative error in MCFT for modeling the joint shear

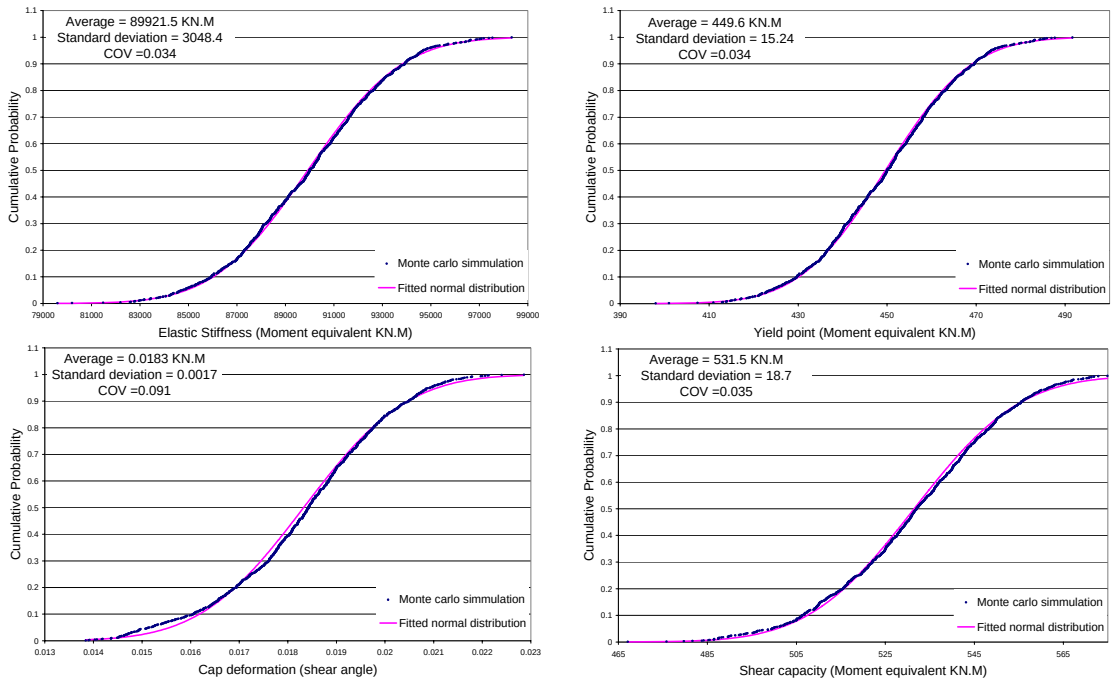

Figure 5-5: Monte Carlo simulation for PEER-14 joint shear behavior

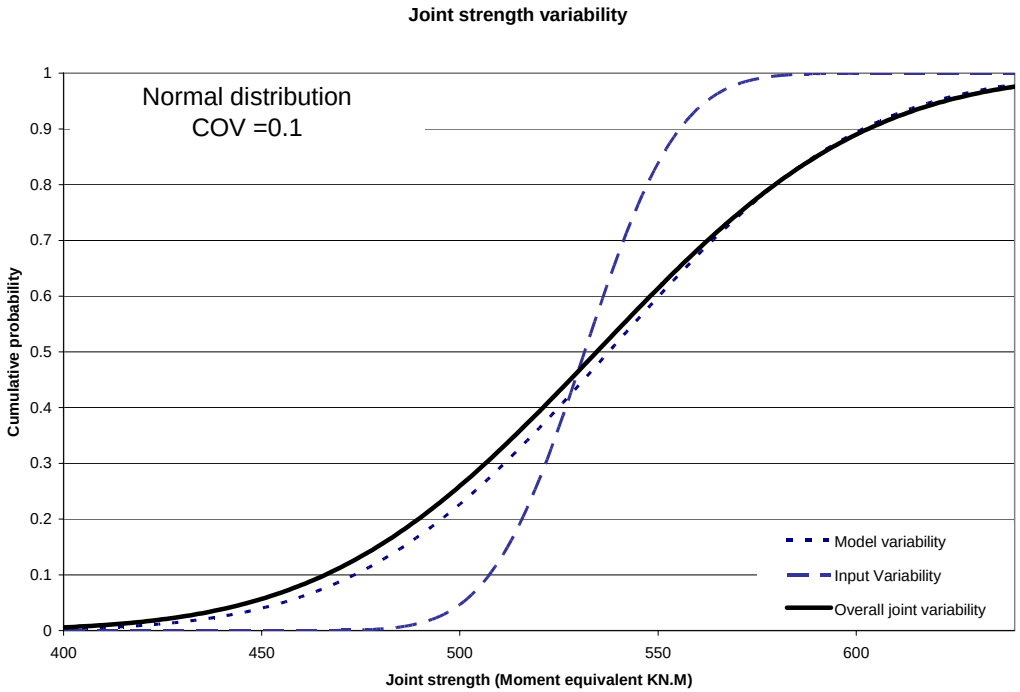

Figure 5-6: Normal distribution for the joint shear strength

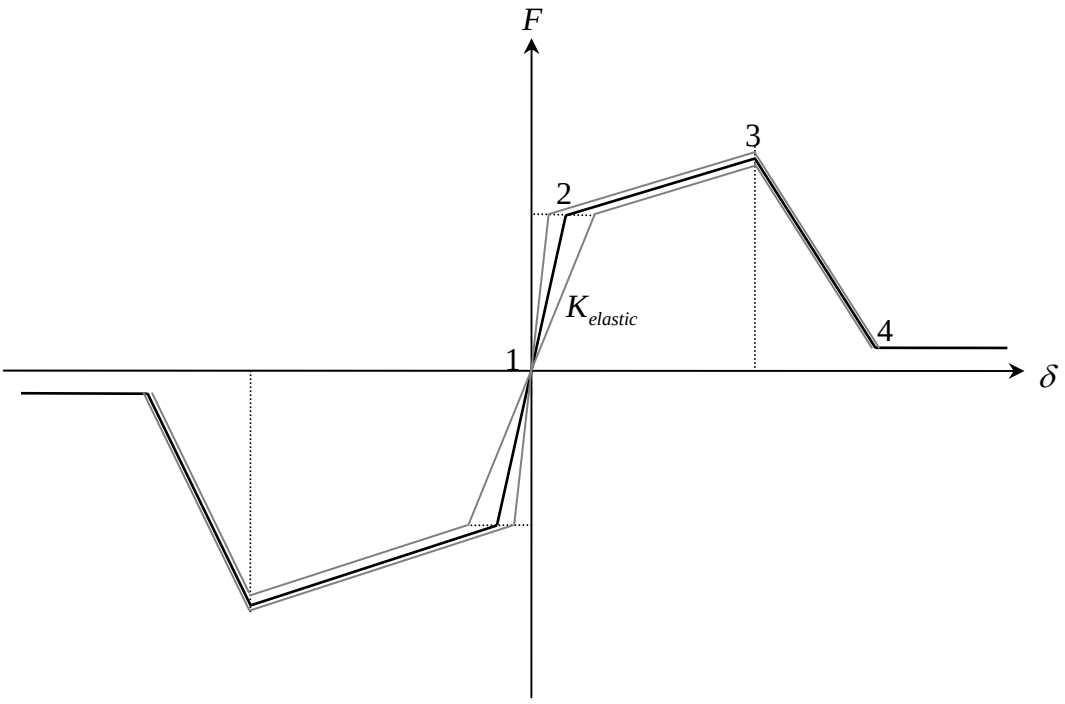

Figure 5-7: Envelope sensitivity to elastic stiffness $K_{elastic}$

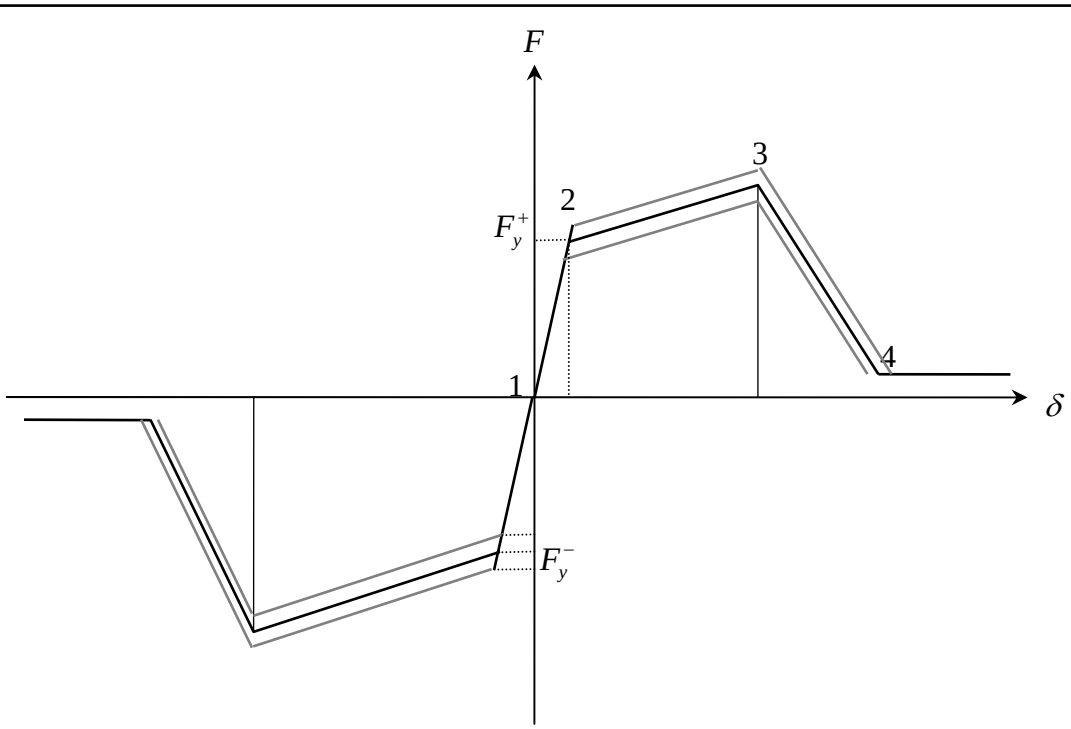

Figure 5-8: Envelope sensitivity to yielding force F_y

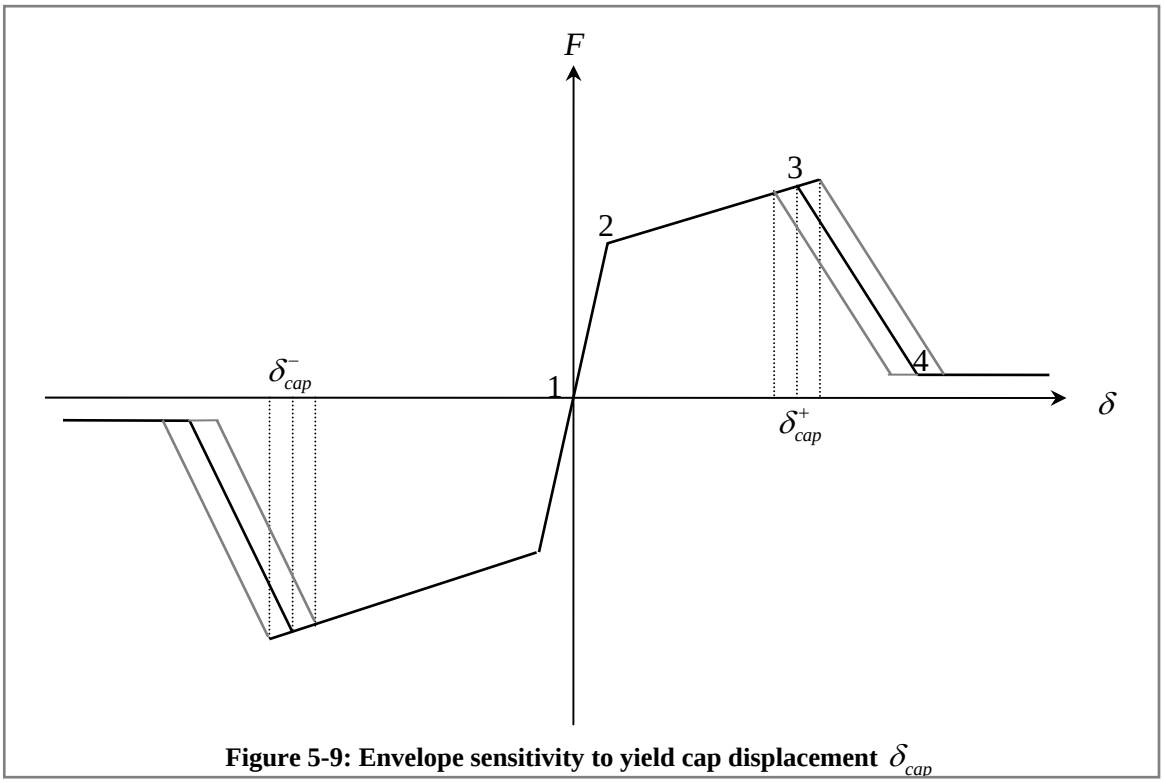

Figure 5-9: Envelope sensitivity to yield cap displacement δ_{cap}

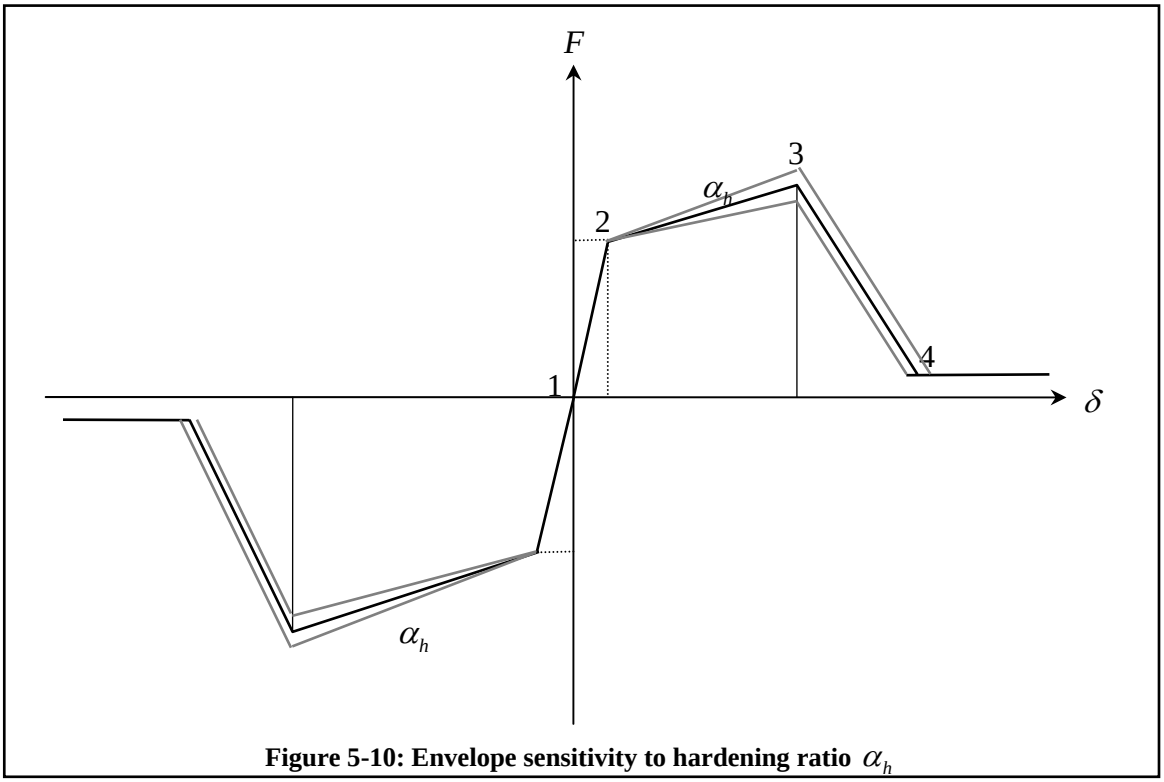

Figure 5-10: Envelope sensitivity to hardening ratio α_h

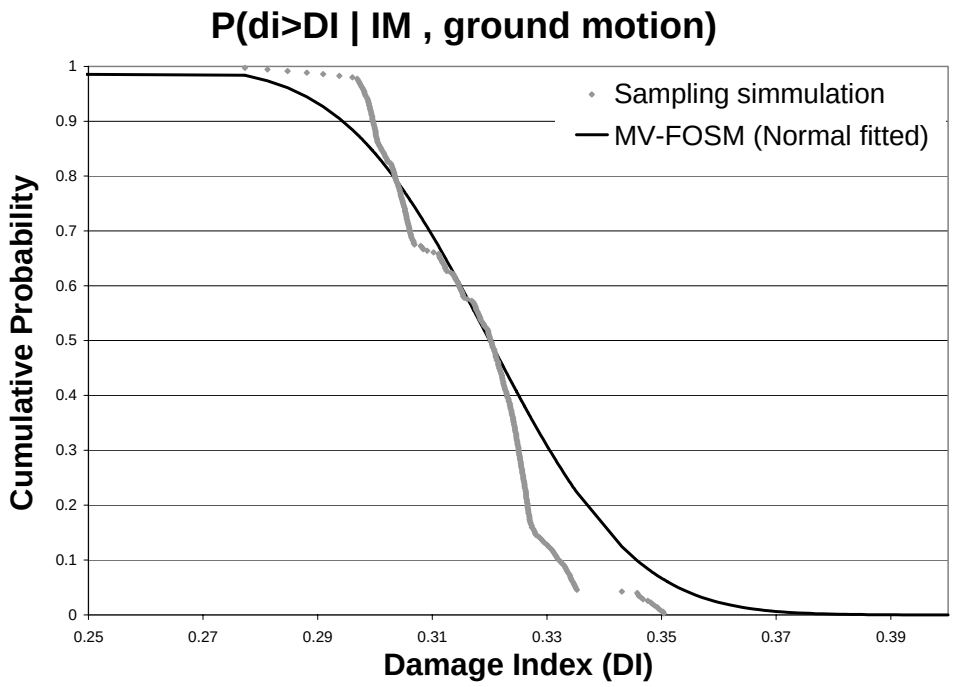

Figure 5-11: Probability analysis results for joint damage

6 Contributions and observations

This research contributes to performance based earthquake engineering by developing analytical tools for simulation and performance (damage) assessment of reinforced concrete beam-column joints within the context of a probabilistic framework. New models are formulated, implemented, and calibrated in the OpenSees platform for simulation of beam-column joints, evaluation of component damage measures, and calculation of sensitivity parameters for semi-automated reliability analyses. These models facilitate calculation of conditional probabilities of exceeding specified component damage measures during a nonlinear time history analysis. Example problems are used to demonstrate application of the damage simulation and reliability tools.

6.1 *Development, implementation, and calibration of OpenSees models for RC joints*

Analytical formulations for modeling 2D and 3D reinforced beam-column joints were derived, considering both shear distortions in the joint panel and concentrated rotations at the interfaces between the joint and adjacent beam/columns. The modeling process distinguishes between the generic finite-deformation kinematics and hysteretic response models that are unique to reinforced concrete joints. The hysteretic response model for joint shear is formulated based on modified compression field theory, and the interface model incorporates calibrated equations for bond-slip and deterioration under cyclic loading.

One of the main challenges in developing the generic joint model involved formulating kinematic equations, including the effects of large deformations. Compatibility equations were derived based on large-deformation theory, taking into account natural and rigid-body joint deformations in an incremental piecewise-linear approach. In the models developed in this investigation, accurate modeling of large deformations includes a corrector scheme applied to kinematic constraint relationships to avoid spurious joint deformations that would otherwise accumulate under large cyclic rotations.

Implementation of the joint elements in OpenSees required a detailed study of the *Object Oriented* architecture of OpenSees, so as to properly interact with existing object models for analysis (e.g., constraint handlers, material models, recorders, etc.). This development required close collaboration with the OpenSees development team. Beam-column joint elements implemented through this research are being used by a number of researchers to model RC and composite RCS frames. Feedback from the users contributed significantly to the enhancement of the proposed models.

6.2 *Development of hierarchical models for processing engineering demand parameters and damage indices*

The concept of *Damage model* was introduced to OpenSees as a new class. As a new generic class, the *Damage model* provides a framework for the introduction of several types of damage models. The damage model is used by a number of OpenSees components (elements, material models and recorders) to serve two primary functions: (1) providing a damage recorder; and (2) providing a history variable to track damage accumulation during the analysis. Selection of a unique and inclusive input/output for the generic *Damage Model* was challenging since the higher level classes need to communicate with the *Damage Model* for sending the required information.

A damage recorder was created to act as an interface between elements and damage models to extract the element damage indices and record them to an output file. Finding a global solution for element internal information was a challenge. Assuming that the damage models are mainly used to calculate damage for nonlinear elements, a and that nonlinear elements are formulated based on either uniaxial material models or sections as force-deformation relationship, so the element damage calculation is focused on the materials or sections. Element damage recorders acquire force-deformation data from the material/section models used in the element to calculate the element damage. Output of damage recorders is used as a new parameter in limit-state functions for component performance assessment.

A brief study was performed on selecting and calibrating the cyclic damage and damage states for the limited available experimental results. The resulting damage level probability is presented as a function of the component damage index.

6.3 *Demonstration of simulation, damage models, and reliability tools in application*

Key aspects of modeling uncertainty for the joint element were examined and the essentials for performing a reliability analysis were provided, including the definition of random variables, limit-state functions, and the response sensitivity. Formulation and implementation of the response sensitivity equations for the hysteretic material models were another contribution.

The new reliability and simulation models were applied to calculate the probability of reaching Various damage states (*DM*) in a *RC* subassembly for a specified input ground motion. The reliability analysis algorithms were exercised for two records form the Loma Prieta 1989 and two from Chi-Chi 1999 earthquakes to derive the fragility curves for individual RC components. The combination of the joint damage fragility curves and the damage index to damage measure curves are used determine the conditional probability of exceeding a pre-defined damage measure for a given ground motion record.

6.4 *Future work*

The new damage indices in OpenSees provide a framework to use the damage models as history parameters to control stiffness/strength degradation. As an example, the damage indices have already been used as a degradation factor in the generalized hinge beam-column elements implemented in OpenSees by Kaul (Kaul and Deierlein 2004). Other standard models could similarly make use of the new damage indices and damage models.

Application of the damage indices can also be extended to non-structural components by introducing non-structural components to the OpenSees simulation framework. The non-

structural elements may or may not affect the structural system response, but they nevertheless would access to the analysis results (such as nodal displacements or accelerations) to calculate and record the damage index for non-structural components.

The modeling RC beam-column joints can be enhanced in a number of ways. There is also need for further calibration studies to refine the joint models. Some possible improvements and extensions to the current models are listed as:

The joint element could be enhanced for:

- Cases with insufficient anchorage of beam reinforcement within the joint and the potential for complete bond loss. The joint model could be modified to transfer a portion of unbalanced moment directly from one beam to the opposing one, by connecting the nodal rotations of opposing node through an additional rotational spring.
- Using fiber sections instead of uniaxial materials to link the adjacent frame elements to the joint for more detailed calibration.
- Interactive effects of varying axial load on the shear panel and pullout behavior.
- Three dimensional cases where the beam centerline does not pass through the column centroid, i.e. eccentric beam-column joints.

More information on joint behavior is required for:

- The interaction of the shear panel damage and bond-slip behavior.
- Slab-column joints and the effect of the slab width on the outcome.
- Precast structures with discrete beam/column connections.
- Detailed laboratory test on the joint response under cyclic loading, with precise data collection on the joint deformations and internal forces.
- Biaxial bending and torsion transfer mechanism in the space frame joints.
- Reinforced concrete-steel beam-column joints.
- Connections with new “engineered” fibers.

Detailed damage study on

- Cyclic performance of both poorly and adequately detailed joints, i.e. joints with/without adequate confinement and development length.
- Most damage indices take into account cumulative damage, but few consider loading history (same damage is predicted, regardless of the sequences of the loading cycles). A lot more experimental and analytical research is needed to develop damage models that take into account the loading history.
- Damage models and damage calculator for shear damage in frame elements.

Bibliography

ACI 214 (2002). “Evaluation of Results of Tests Used to Determine the Strength of Concrete”. *American Concrete Institute, Committee 214*, ACI 214R-02.

ACI 318 (2002). “Building Code Requirements for Structural Concrete and Commentary”. *American Concrete Institute, Committee 318*, 2002, 443 pp.

ACI 352 (2002). “Recommendations for design of beam-column joints in monolithic reinforced concrete structures”. *American Concrete Institute, Committee 352*, ACI 352R-02.

ACI 352 (1976). “Recommendations for design of beam-column joints in monolithic reinforced concrete structures”. *American Concrete Institute, Committee 352*, ACI 352R-76.

Alameddine, F. and Ehsani, M. R. (1991). “High-strength RC connections subjected to inelastic cyclic loading”. *Journal of Structural Engineering*, 117, 3, Mar. 1991, pages 829-850.

Alath, S. and Kunnath, S. K. (1995). “Modeling inelastic shear deformation in RC beam-column joints”. Engineering Mechanics: *Proceedings of 10th Conference: University of Colorado at Boulder, Boulder, Colorado, May 21-24*, 1995, American Society of Civil Engineers, New York, Vol. 2, 1995, pages 822-825.

Altoontash, A. and Deierlein G. G.,(2003). “A Versatile Model for Beam-Column Joints”. *Proceedings of 2003 Structures Congress & Exposition, May 29 - May 31*, Seattle, WA.

Anderson, J. C., and Townsend, W. H. (1997). “Models for reinforced concrete frames with degrading stiffness”. *Journal of Structural Division, American Society of Civil Engineers*, 103(ST12), 1433–1449.

Banon, H., Biggs, J. M., and Irvine, H. M. (1981).”Seismic damage in reinforced concrete frames”. *Journal of the Structural Division, American Society of Civil Engineers*. Vol. 107, no. ST9, pp. 1713-1729. Sept. 1981

Beres, A., Pessiki P.P., White R. N. and Gregely P. (1996). “Implications of experiments on the seismic behavior of gravity load designed RC beam-to-column connections”. *Earthquake Spectra*, 12, 2, May, 1996, pages 185-198.

Bonacci, J. F., and Pantazopoulou, S. J. (1993). ‘‘Parametric investigation of joint mechanics.’’ *ACI, Structural Journal,* 90(1), 61–71.

Bracci, J. M., Reinhorn, A. M. and Mander, J. B. (1995). “Seismic resistance of reinforced concrete frame structures designed for gravity loads: performance of structural system”. *ACI Structural Journal*, 92, 5, Sept.-Oct. 1995, pages 597-609.

Chung, Y. S., Meyer, C., and Shinozuka, M. (1987). “Seismic damage assessment of reinforced concrete members”. *National Center for Earthquake Engineering Research*, 1987. 1 vol.

Conte, J. P. , Vijalapura P. K. and Meghella M. (1999). “Consistent finite element sensitivities in seismic reliability analysis”. *Proceedings of 13th ASCE Engineering Mechanics Division Conference, The Johns Hopkins University, Baltimore, Baltimore*, MD, June 13-16, 1999.

Conte, J. P. (2001). “Finite element response sensitivity analysis in earthquake engineering”. *Earthquake Engineering Frontiers in the New Millennium: Proceedings of the China-U.S. Millennium Symposium on Earthquake Engineering, Beijing, 8-11 November 2000*, A. A. Balkema, Lisse, The Netherlands, 2001, pages 395-401.

Cordova, P., Lai, W. C., Chen, C. H., and Tsai, K. C. (2004). “Pseudo-Dynamic Test Of Full Scale RCS Frame: Part 2 – Analysis and Design Implications”. *Proceedings of the 13th world conference on earthquake engineering, Aug 1-6, 2004, Vancouver, B.C., Canada.*

Cornell, C. A. and Krawinkler, H. (2001). “A framework for performance-based seismic design”. *2001: A Structural Engineering Odyssey: Proceedings of the 2001 Structures Congress and Exposition, May 21-23, 2001, Washington, D.C.* [electronic resource]; 2 pages pp. 2001

Deierlein, G. G., Krawinkler, H., and Cornell, C. A. (2003) “A framework for performance-based earthquake engineering”. *Proceedings of the 2003 Pacific Conference on Earthquake Engineering [electronic resource]*, 2003, 8 pages.

Deng, C. G., Bursi, O. S. and Zandonini, R. (1999). “A hysteretic connection element and its applications”. *Computers & Structures*, 78, 1-3, Nov. 2000, pages 93-110.

Der Kiureghian, A. (1996). “Structural reliability methods for seismic safety assessment: a review”. *Engineering Structures*, 18, 6, June 1996, pages 412-424.

Dube, J.-F., Pijaudier-Cabot, G., and La Borderie, C. (1996). “Rate dependent damage model for concrete in dynamics”. *Journal of Engineering Mechanics*, 122, 10, Oct. 1996, pages 939-947.

Durrani, A. J. and Wight, J. K. (1985). “Behavior of interior beam-to-column connections under earthquake-type loading”. *Journal of the American Concrete Institute,* 82, 3, May-June 1985, pages 343-349.

Ehsani, M. R. and Wight, J. K. (1985). “Effect of transverse beams and slab on behavior of reinforced concrete beam to column connections”. *Journal of the American Concrete Institute*, 82, 2, Mar.-Apr. 1985, pages 188-195.

Ehsani, M. R. and Wight, J. K. (1985). “Exterior reinforced concrete beam-to-column connections subjected to earthquake type loading”. *Journal of the American Concrete Institute*, 82, 4, July-Aug. 1985, pages 492-499.

El-Metwally, S. E. and Chen, W. F. (1988). “Moment-rotation modeling of reinforced concrete beam-column connections”. *ACI Structural Journal*, 85, 4, July-Aug. 1988, pages 384-394.

El-Tawil, S., Vidarsson E., Mikesell T. and Kunnath K. (1999). “Inelastic behavior and design of steel panel zones”. *Journal of Structural Engineering*, 125, 2, Feb. 1999, pages 183-193.

El-Tawil, S. and Deierlein G. G. (2001). “Nonlinear analysis of mixed steel-concrete frames, I: Element formulation”. *Journal of Structural Engineering* (New York, N.Y.). Vol. 127, no. 6, pp. 647-655. June 2001.

Ellingwood, B. and Galambos, T. V. (1982). “Probability-based criteria for structural design”. *Structural Safety*. Vol. 1, no. 1, pp. 15-26. Sept. 1982.

Eligenhausen, R., Popov, E. P., and Bertero, V. V. (1983). ‘‘Local bond stress-slip relationships of deformed bars under generalized excitations.’’ *Earthquake Engineering Research Council (EERC)* Rep. No. 83/23, Univ. of California, Berkeley.

Elmorsi, M. , Kianoush, M. R. and Tso, W. K. (1998). “Lightly reinforced beam column joint model for frame analysis”. *Proceedings, Sixth U.S. National Conference on Earthquake Engineering [computer file], Earthquake Engineering Research Inst., Oakland, California*, 1998, 11 pages.

Fajfar, P. and Gaspersic, P. (1996). “The N2 method for the seismic damage analysis of RC buildings”. *Earthquake Engineering & Structural Dynamics*, 25, 1, Jan. 1996, pages 31-46.

FEDEAS (2004). Aug. 1, <http://www.ce.berkeley.edu/~filippou/Research/fedeas.htm>

FEMA-356 (2000), “Prestandard and Commentary for the Seismic Rehabilitation of Buildings”, Federal Emergency Management Agency, Washington, DC.

FEMA-450 (2004), “Recommended Provisions for Seismic Regulations for New Buildings and Other Structures”, Federal Emergency Management Agency, Washington, DC.

Filippou, F. C. and Popov, E. P. (1984). “Hysteretic behavior of reinforced concrete beams and joints”. *Proceedings of the Eighth World Conference on Earthquake Engineering, Prentice-Hall, Inc., Englewood Cliffs, New Jersey, 1984*, pages 821-828, Vol. V, Copyright with Earthquake Engineering Research Inst., El Cerrito, California.

Fleury, F., Merabet, O. and Reynouard, J.-M (1996). “A new semi-local approach for the finite element modeling of interior R/C beam-column joints”. *Eleventh World Conference on Earthquake Engineering [Proceedings], Pergamon, Elsevier Science Ltd., [Oxford, England], 1996*, Disc 1, Paper No. 478.

Fleury, F., Reynouard, J. M., and Merabet, O. (2000). ‘‘Multicomponent model of reinforced concrete joints for cyclic loading.’’ *Journal of Engineering Mechanics*, 126(8), 804–811.

Florez-Lopez, J. (1995). “Simplified model of unilateral damage for RC frames”. *Journal of Structural Engineering*, 121, 12, Dec. 1995, pages 1765-1772.

Gardoni, P. , Der Kiureghian, A. , and Mosalam, K.M. (2002). ”Probabilistic models and fragility estimates for bridge components and systems”. *Pacific Earthquake Engineering Research Center, University of California*, 2002. 164 pages pp.

Gentry, T. R. and Wight, J. K. (1994). “Wide beam-column connections under earthquake-type loading”. *Earthquake Spectra*, 10, 4, Nov. 1994, pages 675-703.

Hawkins, N. M., Lin, I. J., and Jeang, F. L. (1982). “Local bond strength of concrete for cyclic reversed loadings.” *Bond in concrete*, P. Bartos, ed., Applied Science Publishers Ltd., London, 151–161

Haukaas, T. and Der Kiureghian, A. (2000). “An object-oriented platform for finite element reliability analysis”. *8th ASCE Specialty Conference on Probabilistic Mechanics and Structural Reliability*.

Haukaas T. (2003a). “User’s guide for reliability and sensitivity analysis in OpenSees”. “http://www.ce.berkeley.edu/~haukaas/OpenSees-Reliability/opensees_reliability.pdf”

Haukaas, T. (2003b). “Software framework for finite element reliability and sensitivity analysis of hysteretic degrading structures”. Ph.D. Dissertation, University of California at Berkeley, Department of Civil and Environmental Engineering.

Higashi, Y. and Ohwada, Y. (1969). “Failing behaviors of reinforced concrete beam-column connection subjected to lateral load”. Tokyo, 1969, [11] pages.

Hindi, Riyadh A. and Sexsmith, Robert G. (2001). “A proposed damage model for RC bridge columns under cyclic loading”. *Earthquake Spectra*, 17, 2, May 2001, pages 261-290.

Ibarra, L., Medina, R., and Krawinkler, H. (2004). “Hysteretic models that incorporate cyclic strength deterioration and stiffness degradation”, *Earthquake Engineering and Structural Dynamics* (submitted).

Ibarra, L. F., and Krawinkler, H. (2004). “Global Collapse of Deteriorating MDOF Systems”. *Proceedings of the 13th world conference on earthquake engineering, Aug 1-6, 2004, Vancouver, B.C., Canada.*

Ibarra, L. (2003) “Global collapse of frame structures under seismic excitation”. Ph.D. Dissertation, Stanford University, Department of Civil and Environmental Engineering.

IDARC (2004). August 1, <http://civil.eng.buffalo.edu/idarc2d50/>

Kanno, R. and Deierlein, G. G. (1994). “Cyclic behavior of joints between steel beams and reinforced concrete columns”. *Structures Congress XII: Proceedings of Papers Presented at the Structures Congress '94, Atlanta, GA, April 24-28, 1994*; pp. 1137-1142.

Kaul, R. (2004) “Object Oriented Development of Strength and Stiffness Degrading Models for Reinforced Concrete Structures”. Ph.D. Dissertation, Stanford University, Department of Civil and Environmental Engineering.

Kent, D. C. and Park, R. (1971).” Inelastic behavior of reinforced concrete members with cyclic loading”. *Bulletin of the New Zealand Society for Earthquake Engineering.* Vol. 4, no. 1, pp. 108-125. Mar , 1971.

Kratzig, W. B., Meyer, I. F. and Meskouris, K. (1989). “Damage evolution in reinforced concrete members under cyclic loading.” *Proceedings of 5th International Conference On Structural Safety and Reliability, ASCE New York*, Vol. II, 795-802

Krawinkler, H., Bertero, V. V. and Popov, E. P. (1975). “Shear behavior of steel frame joints”. *Journal of the Structural Division*, ASCE, 101, ST11, Nov. 1975, pages 2317-2336, Proc. Paper 11717.

Krawinkler, H. (1998). “Issues and challenges in performance based seismic design”. *Structural Engineering World Wide 1998* [computer file], Elsevier Science Ltd., Oxford, England, 1998, Paper T178-3.

Krawinkler, H. and Miranda, E. (2004). “Performance-Based Earthquake Engineering”. Chapter 9 of *Earthquake Engineering: From engineering seismology to performance based engineering*, edited by Y. Bozorgnia, and V. Bertero, CRC press.

Kunnath, S. K., Mander, J. B. and Fang, L. (1996). “Parameter identification for degrading and pinched hysteretic structural concrete systems”. *Engineering Structures*, 19, 3, Mar. 1997, pages 224-232.

Kunnath, S. K. (1998). “Macro-model based nonlinear analysis of reinforced concrete structures”. *Structural Engineering World Wide 1998* [computer file], Elsevier Science Ltd., Oxford, England, 1998, Paper T101-5.

Lehman, D., Walker S., Stanton, J., Moehle, J., Sezen, H., Pantelides, C., Clyde, C., Reaveley, L., and Robertson, I. (2004). “Performance characterization of non-ductile reinforced concrete frame components”. *Pacific Earthquake Engineering Research Center report*, 2004 (submitted).

Leon, R. T. and Jirsa, J. O. (1986). “Bidirectional loading of R.C. beam-column joints”. *Earthquake Spectra*, 2, 3, May 1986, pages 537-564.

Leon, R. T. (1989). “Interior joints with variable anchorage lengths”. Journal of *Structural Engineering*, 115, 9, Sept. 1989, pages 2261-2275.

Lowes, L.N. and Altoontash, A.,(2003a). “Modeling the response of reinforced concrete beam-column joints.”. *Journal of Structural Engineering ASCE*, Vol. 129, No. 12, December 2003, pages 1567-1729.

Lowes L.N., Mitra N., and Altoontash A. (2003b). “A Beam-Column Joint Model for Simulating the Earthquake Response of Reinforced Concrete Frames”. *Pacific Earthquake Engineering Research Center report*, 2003-10, 66 pages.

Lowes, L.N. and Altoontash, A. (2002a). “Modeling the Response of RC Building Beam-Column Joints Subjected to Earthquake Loading.”. *Proceedings of the 7NCEE: 21-26 July 2002 Boston, MS. July 2002.*

Lowes, L.N. and Altoontash, A. (2002b). “Modeling the Response of RC Beam-Column Joints.”. *Performance of Structures: from Research to Design, Proceedings of the 2002 Structures Congress*.

Lowes, L.N. (2001) “Finite element analysis of RC beam-column bridge connections.” *Modeling of Inelastic Behavior of RC Structures Under Seismic Loads, American Society of Civil Engineers, Reston, Virginia*, 2001, pages 276-296

MacGregor, J. G. (1988). “Reinforced concrete: mechanics and design”. Prentice Hall, 1988. 799 pages pp.

MATLAB. (2004). August 1, <http://www.mathworks.com>

Mazzoni, S. (1997). ‘‘Design and response of lower-level beam-column joints in ductile reinforced-concrete double-deck bridge frames’’ Ph.D. dissertation, University of California, Berkeley.

McKenna, F. and Fenves, G. L. (2002). “http://opensees.berkeley.edu. The OpenSees command language primer". Department of Civil and Environmental Engineering, University of California, Berkeley, CA.

McKenna, F., Fenves, G. L., and Scott, M. H. (2002). “Open system for earthe-quake engineering simulation, http://opensees.berkeley.edu". Pacific Earthquake Engineering Research Center, University of California, Berkeley, CA.

McKenna, F. T. (1997). “Object-oriented finite element programming: Frameworks for analysis, algorithms and parallel computing". PhD thesis, University of California, Berkeley, CA.

Mehanny, S. S. F. and Deierlein, G. G. (2000). “Seismic damage and collapse assessment of composite moment frames”. *Journal of Structural Engineering*, 127, 9, Sept. 2001, pages 1045-1053.

Mehanny, S. S. F. and Deierlein, G. G. (2000b). “Modeling and assessment of seismic performance of composite frames with reinforced concrete columns and steel beams”. *The John A. Blume Earthquake Engineering Center*, 2000. 442 pages.

Menun C. (2001). “Probabilistic Models in Civil Engineering”. Class handouts, Stanford University, Autumn 2001-02

Menun C. (2002). “Structural Reliability”. Class handouts, Stanford University, Spring 2001-02

Moehle J. P. (2003). “A framework for developing performance-based earthquake engineering”. *Proceedings of the International Conference on Advances and New Challenges in Earthquake Engineering Research (ICANCEER), August 15-20*, 2002, Harbin and Hong Kong, China: Hong Kong Volume, 2003, page 67 pp.

Moehle J. P. (1997). “Displacement-based seismic design: a compromise between simple and comprehensive”. *The EERC-CUREe Symposium in Honor of Vitelmo V. Bertero, January 31-February 1, 1997,* Berkeley, California. 1997.

Mostaghel, N. (1999). “Analytical description of pinching, degrading hysteretic systems”. *Journal of Engineering Mechanics*, 125, 2, Feb. 1999, pages 216-224.

Naito, C.J., Moehle, J.P. , and Mosalam, K.M. (2001). “Experimental and computational evaluation of reinforced concrete bridge beam-column connections for seismic performance”. *Pacific Earthquake Engineering Research Center*, University of California, 2001. 232 pages pp.

OpenSees. (2004). August 1, <http://opensees.berkeley.edu/>

Otani, S. (1974). “Inelastic analysis of reinforced-concrete frame structures”. *Journal of structural division of American Society of Civil Engineers*, 100(ST7), 1433–1449.

Pagni C. A., and Lowes L. N. (2004). “Tools to enable prediction of economic impact of earthquake damage in older RC beam-column joints”. *International Workshop on Performance-Based Seismic Design, June 28 to July 2004, Bled, Slovenia.*

Pantazopoulou, S. J. and Bonacci, J. F. (1994). “On earthquake-resistant reinforced concrete frame connections”. *Canadian Journal of Civil Engineering*, 21, 2, Apr. 1994, pages 307-328.

Pantelides, C. , Hansen J. , Nadauld J. , Reavely L. (2002) “Assessment of reinforced concrete building exterior joints with standard details”. *PEER-2000/18, Berkeley:* Pacific Earthquake Engineering Research Center, University of California, July 2002

Park, Y. J., and Ang, A. H. S. (1985a). “Mechanistic seismic damage model for reinforced concrete”. *Journal of Structural Engineering*, 111, 4, Apr. 1985, pages 722-739.

Park, Y. J., Ang, A. H. S. and Wen, Y. K. (1985b). “Seismic damage analysis of reinforced concrete buildings”. *Journal of Structural Engineering*, 111, 4, Apr. 1985, pages 740-757.

Park, R., and Ruitong, D. (1988). “A comparison of the behavior of reinforced-concrete beam-column joints designed for ductility and limited ductility.” *New Zealand National Society Earthquake Engineering Bulletin*, 21(4), 255–278.

Paulay, T., Park, R. and Priestley, M. J. N. (1978). “Reinforced concrete beam-column joints under seismic actions”. *Journal of the American Concrete Institute,* 75, 11, Nov. 1978, pages 585-593, Title No. 75-60.

Paulay, T. (1989). “Equilibrium criteria for reinforced concrete beam-column joints”. *ACI Structural Journal*, 86, 6, Nov.-Dec. 1989, pages 635-643.

Porter, K., Beck, J., and Shaikhutdinov, R. (2002). “Investigation of sensitivity of building loss estimates to major uncertain variables for the Van Nuys Testbed”. *Pacific Earthquake Engineering Research Center report*, 2002-03, 41 pages.

Rahnama, M. and Krawinkler, H. (1993). “Effects of soft soil and hysteresis model on seismic demands”. *BLUME-108*, John A. Blume Earthquake Engineering Center, Stanford, California, July 1993, 238 pages.

Scott, R. H. (1996). “Intrinsic mechanisms in reinforced concrete beam-column connection behavior”. *ACI Structural Journal,* 93, 3, May-June 1996, pages 336-346.

Scott, B. D., Park, R., and Priestly, M. J. N. (1980). “Stress-strain relationships for confined concrete : rectangular sections”. Dept. of Civil Engineering, University of Canterbury, 1980. 106 leaves pp.

Shiohara, H. (2001). “New model for shear failure of RC interior beam-column connections”. *Journal of Structural Engineering*, 127, 2, Feb. 2001, pages 152-160.

Sivaselvan, M. V. and Reinhorn, A. M. (2000). “Hysteretic models for deteriorating inelastic structures”. *Journal of Engineering Mechanics*, 126, 6, June 2000, pages 633-640.

Soleimani, D., Popov, E. P. and Bertero, V. V. (1979). “Hysteretic behavior of reinforced concrete beam-column subassemblages”. *Journal of the American Concrete Institute,* 76, 11, Nov. 1979, pages 1179-1195, Title No. 76-48.

Stevens, N. J., Uzumeri, S. M., and Collins, M. P. (1991). ‘‘Reinforced concrete subjected to reversed-cyclic shear—Experiments and constitutive model.’’ *ACI Structural Journal,* 88(2), 135–146.

Tsai, K. C., Loh, C.H., Lin, K.C., and Chen, C.H. (2000), “Cyclic load tests of 0.7 scale 2-story RC frames retrofitted with steel jackets”. *National Center for Research on Earthquake Engineering* (NCREE)

Townsend, W. H. and Hanson, R. D. (1977). “Reinforced concrete connection hysteresis loops”. *Reinforced Concrete Structures in Seismic Zones, SP-53, American Concrete Institute,* Detroit, 1977, pages 351-370.

Uma, S. R. and Prasad, A. M. (1996). “Analytical modeling of R/C beam column connections under cyclic loads”. *Proceedings of Eleventh World Conference on Earthquake Engineering* [], Pergamon, Elsevier Science Ltd., [Oxford, England], 1996, Disc 4, Paper No. 1869.

Vecchio, F. J., and Collins, M. P. (1986). ‘‘The modified-compression field theory for reinforced-concrete elements subjected to shear.’’ *Journal of American Concrete Institute,* 83(2), 219–231.

Vecchio, F. J. (2000). “Disturbed stress field model for reinforced concrete: formulation”. *Journal of Structural Engineering* (New York, N.Y.). Vol. 126, no. 9, pp. 1070-1077. Sept. 2000.

Vecchio, F. J. et al. (2001). “Disturbed stress field model for reinforced concrete: validation”. *Journal of Structural Engineering* (New York, N.Y.). Vol. 127, no. 4, pp. 350-358. Apr. 2001.

Viwathanatepa, S., Popov, E. P., and Bertero, V. V. (1979). “Effects of generalized loadings on bond of reinforcing bars embedded in confined concrete blocks.’’ Report Number UCB/EERC-79/22 EERC, University of California, Berkeley, CA.

Walker, S. G. (2001). “Seismic performance of existing reinforced concrete beam-column joints”. MS thesis, University of Washington, Seattle, Washington

Walker, S., Yeargin, C., Lehman, D., Stanton J. (2004). “Seismic performance of reinforced concrete beam-column joints without joint reinforcement”. Submitted for publish.

Wang, M.L., Shah, S. P. (1987). “Reinforced concrete hysteresis model based on the damage concept”. *Earthquake Engineering & Structural Dynamics. (15)*, no. 8, pp. 993-1003. Nov. 1987

Williams, M. S. and Sexsmith, R. G. (1995). “Seismic damage indices for concrete structures: a state-of-the-art review”. *Earthquake Spectra*, 11, 2, May 1995, pages 319-349.

Williams, M. S., Villemure, I. and Sexsmith, R. G. (1997). “Evaluation of seismic damage indices for concrete elements loading in combined shear and flexure”. *ACI Structural Journal*, 94, 3, May-June 1997, pages 315-322.

Zhang, Y. and Der Kiureghian, A. (1991). “Dynamic response sensitivity of inelastic structures”. *UCB/SEMM-91/06*, Structural Engineering, Mechanics and Materials Program, Dept. of Civil Engineering, Univ. of California at Berkeley, Oct. 1991, 33 pages.

Appendix A

Introduction to OpenSees

OpenSees is created in a *C++ Object Oriented* environment. A brief explanation of some of the commonly used *Object Oriented* concepts will help understanding the OpenSees structure, and its features used in this research to develop analytical models. The OpenSees *Object Oriented* architecture is explained in detail by McKenna (1997).

Class: Classes are one of the building blocks of object-oriented programming, or in technical words, classes are basic units of abstraction in C++. A class is used to encapsulate the user-defined data as well as operators to access and manipulate that data. A class is a prototype that defines the variables and the methods common to all objects of a certain kind.

Object: An object is a run-time value that belongs to a class, used to store the class state. The class defines all the operations for its instances. Since the objects know what class they belong to, so they automatically know what operations they are capable of. The word "instance" is another term for "object".

Message and Method: *OOP* uses "messages" instead of function calls. Sending a message to an object causes that object to perform an operation. The receiver knows what operations it can perform, because it knows its class, and. The code corresponding to a particular message is known as the "method" for that message. A message is just a string, while the method is the code in the Stack class which is triggered by the message. The C++ specific term for method is "member function".

Constructors: Methods that are automatically called on behalf of the client whenever a new instance, be it statically or dynamically allocated, comes into scope.

Model Builder: The first step in generating a finite element analysis model is subdividing the body being studied into finite element components. A *Model Builder* object is used to create the finite element model in a running program. Each *Model Builder* object is

associated with a single *Domain* object. The model builder is responsible for generating nodes, masses, materials, sections, elements, load patterns, time series, transformations, blocks, and constraints.

Domain: The domain object is responsible for storing the objects created by the model builder object and for providing the analysis and recorder objects access to these objects. The domain holds the state of the model at time t and $t + \Delta t$.

Domain Component: The domain component class is an abstract class. Its subclasses include elements, nodes, single point constraints, multipoint constraints, nodal loads, elemental loads, etc. Each object of these types is a component of an enclosing Domain object. The domain component class provides methods to set and retrieve a pointer to the enclosing Domain object.

Analysis: The Analysis object is responsible for performing the analysis. This may vary from a simple static linear analysis to a transient non-linear analysis. In OpenSees each Analysis object is composed of several component objects, which define how the analysis is performed. The component classes consist of constraint handler, degree of freedom number, analysis model, solution algorithm, integrator, linear system of equation, and the solver. The analysis performs the calculations and solves the state of the model from state at time t to $t + \Delta t$.

Recorders: The recorder object monitors the state of a domain during an *Analysis*, writes this state to a file or to a database at selected intervals during the analysis, or plots and monitors user-defined parameters in the model during the analysis. The user defined parameter could be the displacement history at a node in a transient analysis, or the entire state of the model at each step of the solution procedure. Usually several Recorder objects are created by the analyst to monitor the analysis.

Multipoint constraints: Multi-point constraint equations are a mathematical way to impose a relationship between two or more degrees of freedom.

Constraint handlers: The *Constraint Handler* object is responsible for providing an initial mapping between the nodal degrees of freedom and equation numbers of the analysis. The *Constraint Handler* object does not handle the constraints as its name would suggest and the handling of the constraints is performed by the *Analysis* object where the constraint equations are enforced as relationships between degrees-of-freedom.

Material models: A general object which represents stress-strain relationships or force-deformation at integration points of continuum or element components. *Material Models* always belong to an element or a section.

Uniaxial Materials: A *Material Model* objects which represent single degree of freedom force-deformation (or stress-strain) relationships.

Damage Model: A general tagged object in OpenSees, which represents the damage formulation. *Damage Models* are always introduced through other *Domain Components* (e.g. elements, sections, or material models) and they do not directly interact with the *Domain*.

Appendix B

OpenSees modeling reference and command lines

B.1 *Element commands*

B.1.1 Joint2D element

Joint2D represents the beam-column joint element in a two-dimension, three-DOF domain. Both of the two-dimensional joint formulations (*Joint2D-1SPR* and *Joint2D-5SPR* as described in Chapter 2) are reached through the *Joint2D* OpenSees command as follows:

element Joint2D *tag*? *Nd1*? *Nd2*? *Nd3*? *Nd4*? *NdC*? [*Mat1*? *Mat2*? *Mat3*? *Mat4*?] *MatC*? *LrgDspTag*?

tag	An integer tag identifying the element in the domain
Nd1	An integer tag indicating the node 1
Nd2	An integer tag indicating the node 2
Nd3	An integer tag indicating the node 3
Nd4	An integer tag indicating the node 4
NdC	An integer tag indicating the central node. This tag is used for generating the internal node and must not exist in the domain or used by any other node.
[*Mat1 Mat2 Mat3 Mat4*]	A group of optional integer tags indicating the uniaxial materials for interface rotational springs in *Joint2D-5SPR* model. Use a zero tag to indicate the case that a beam-column elements is rigidly framed to the joint.
MatC?	An integer tag indicating the uniaxial material for the shear panel behavior (required for both *Joint2D-1SPR* and *Joint2D-5SPR*).
LrgDspTag?	An integer indicating the flag for considering large deformations. For small deformations and constant geometry use 0. For large deformations

and time varying geometry use 1. For large deformation, time varying geometry and length correction use 2.

The nodes must be located such that the main chords bisect, and the node tags are required to be entered in a clockwise or counter-clockwise order.

The shear panel uniaxial material model is calibrated for shear-equivalent moment versus shear distortion. In the calibration formulations the shear-equivalent moment is calculated by multiplying the joint average shear stress to the joint panel volume.

The joint element automatically generates a special central node (with an extra degree of freedom), where the user is only required to provide a new (unused) node tag for the central node.

The element connects the external nodes to the central node via multi-point constraints, and *Joint2D* must be used along with either the *Penalty*, or the *Transformation* constraint handler.

The *LrgDspTag* flag activates the geometric nonlinearity option. If the *LrgDspTag* flag is set to zero, the element uses a constant constraint matrix, for small-deformation formulation. For large deformation formulation, a non-zero value is used for *LrgDspTag*. In the large-deformation formulation, the constraint matrix is time varying and it is updated at every converged time-step.

Joint2D element has the capability to record the element damage, using *Damage Model* objects. Damage models are introduced to the joint element through the following optional command line:

element Joint2D *tag*? *Nd1*? *Nd2*? *Nd3*? *Nd4*? *NdC*? [*Mat1*? *Mat2*? *Mat3*? *Mat4*?] *MatC*? *LrgDspTag*? [-damage [*Dmg1*? *Dmg2*? *Dmg3*? *Dmg4*?] *DmgC*?]

Joint2D element recorder: Valid inquiries to the joint element include:

centralNode The displacement components of the central node

deformation	Interface rotations and the shear panel deformation
force	nodal moments and the joint panel shear-equivalent moment
size	Length of the main chords (element size)
stiffness	Joint element stiffness matrix
defoANDforce	Joint deformation components followed by the nodal moments

Example input lines:

element Joint2D 12 1 2 3 4 112 10 0

Constructs a *Joint2D* element with tag 12 that is connected to nodes 1, 2, 3 and 4. The element will generate a center node with tag 112, and it uses the uniaxial material object with tag 10 as the shear panel rotational spring. The joint element introduced here will be a joint, without rotational springs at external nodes. The generated multipoint constraint matrices will be constant and they do not include large deformations. Use *Penalty*, or *Transformation* as constraint handler.

element Joint2D 13 5 6 7 8 113 11 0 11 0 10 2

Constructs a *Joint2D* element with tag 13 that is connected to nodes 5, 6, 7 and 8. The element will generate a center node with tag 113, and it uses the uniaxial material object with tag 11 for nodes 5 and 7, and rigid connections at nodes 6 and 8 to prevent member end rotations. The generated multipoint constraint matrices will be time varying to cover large deformations and if corrects the nodal positions to maintain the initial joint size.

B.1.2 **Joint3D element user information**

Joint3D is defined in a three dimensional domain with six nodal degrees of freedom. Joint3D is connected to six nodes, where the nodes are required to be entered in the order the main chords are defined (*-x', +x', -y', +y', -z', +z'*). Since the element is developed only for symmetric joints, the external nodes must construct a parallelepiped. All six

external nodes are required for exterior or corner joints, while some nodes may or may not be connected to any beam-column element.

Three uniaxial material models characterize the three shear-deformation modes of the joint block. In most calibration formulations the average shear stress is determined, which must be applied in the form of shear-equivalent moment (by multiplying to the joint block volume).

The joint element automatically generates a central node with three extra degrees of freedom for shear deformation. The user is only required to provide a new (unused) tag number for this central node.

The element connects the external nodes to this central node via multi-point constraints, so the *Joint3D* must be used along with either *Penalty*, or *Transformation* constraint handler to allow the multi point constraints work properly.

Joint3D element is introduced to the model through a command line as:

element Joint3D *tag*? *Nd1*? *Nd2*? *Nd3*? *Nd4*? *Nd5*? *Nd6*? *NdC*? *Mat12*? *Mat34*? *Mat56*? *LrgDspTag*?

tag	An integer identifying the element tag in the domain
Nd1	An integer indicating the node 1 tag connected to column at (-x')
Nd2	An integer indicating the node 2 tag connected to column at (+x')
Nd3	An integer indicating the node 3 tag connected to column at (-y')
Nd4	An integer indicating the node 4 tag connected to column at (+y')
Nd5	An integer indicating the node 5 tag connected to column at (-z')
Nd6	An integer indicating the node 6 tag connected to column at (+z')
NdC	An integer tag for internal node (must not exist in the domain).
Matx'	An integer indicating the uniaxial material for rotational spring along x’
Maty'	An integer indicating the uniaxial material for rotational spring along y’
Matz'	An integer indicating the uniaxial material for rotational spring along z’
LrgDspTag	An integer indicating the flag for considering large deformation effects

The local *x'* axis is defined by a vector from *Nd1* to *Nd2*; *y'* form *Nd3* to *Nd4; z'* from *Nd5* to *Nd6*. The external nodes must be located such that these vectors bisect each other.

The valid queries to a *Joint3D* element when creating an element recorder are 'internalNode', 'deformation', `plasticDeformation`, 'force', 'deformationANDforce', 'size', 'stiff' and 'materials ...'.

Joint3D element recorder: The valid inquiries to a *Joint3D* element when creating an element recorder are:

internalNode	Returns the central node displacements, four degrees of freedom.
deformation	Returns the spring rotation at external nodes and at the block.
force	Returns the spring moment at external nodes and at the block.
defoANDforce	Returns the spring rotation at external nodes and at the block , followed by the forces in the same order.
plasticRotation	Returns the spring plastic rotation at external nodes and at the block, by reducing the elastic component of the rotation based on initial stiffness.
size	Returns the joint size
stiff	Returns the joint stiffness matrix

Example:

element Joint3D 12 1 2 3 4 5 6 1012 11 12 13 0

This command line constructs a *Joint3D* element with tag 12 that is connected to nodes 1, 2, 3 , 4 ,5 and 6. The element will generate a central node with tag 1012, and it uses the uniaxial material objects with tags 11 , 12 , and 13 along x', y' and z' local axes. The generated multipoint constraint matrices will not be time variant and they do not include large deformations effects.

B.2 *Damage models*

B.2.1 NormalizedPeak Damage

damageModel NormalizedPeak tag? *ValueU*$^+$? *ValueU*$^-$? *reponseType*?

tag	Integer identifier for the damage model tag
ValueU$^+$	Ultimate response threshold for positive excursions
ValueU$^-$	Ultimate response threshold for negative excursions
responseType	A string indicating the response type, chosen from “Force”, “Deformation” ,”PlasticDeformation”, “TotalEnergy”, or “PlasticEnergy”.

Example:

damageModel NormalizedPeak 1 5.0 -5.0

Creates an instance on AbsolutePeak damage model with identifier tag 1. The maximum threshold value is 5.0 and the minimum is -5.0

B.2.2 Kratzig Damage

damageModel Kratzig *tag*? E_U^+? E_U^-?

tag	Integer identifier for the damage model tag
E_U^+	Maximum energy capacity for positive monotonic loading
E_U^-	Maximum energy capacity for negative monotonic loading

B.2.3 Mehanny Damage

The Mehanny damage model is a hysteretic damage model that calculates the damage model based on the accumulation of following half cycles and the effect of the primary half cycle. The damage indices are calculated separately for positive and negative half

cycles and they are combined to the overall damage index. Alpha and Beta and Gamma are obtained through calibration to test data. This damage model is also dimensionless and it can be used for displacement/force/energy based damage analysis problems.

damageModel Mehanny *tag*? α? β? γ? θ_{pu}^{+}? θ_{pu}^{-}? tol_{abs}? tol_{rel}? μ^{+}? μ^{-}?

tag	Integer identifier for the damage model tag
α	Calibration parameter for primary half cycles contribution
β	Calibration parameter for summation of follower half cycles contributions
γ	Calibration parameter for combining positive and negative damage
θ_{pu}^{+}	Plastic deformation capacity in positive loading
θ_{pu}^{-}	Plastic deformation capacity in negative loading
tol_{abs}	Optional absolute tolerance value for half cycle size to filter any half cycle smaller than tol_{abs}
tol_{rel}	Optional relative tolerance value for half cycle size to filter any half cycle smaller than $tol_{rel} \times \theta_p\big\|_{PHC}$.
μ^{+}	Optional weight given to the damage index for the positive half cycles.
μ^{+}	Optional weight given to the damage index for the negative half cycles, when the positive and negative damage indices are reported separately, as follows:

$$DamageIndex^{+} = \sqrt[\gamma]{\left(DI^{+}\right)^{\gamma} + \mu^{-} \cdot \left(DI^{-}\right)^{\gamma}} \leq 1.0$$

$$DamageIndex^{-} = \sqrt[\gamma]{\mu^{+} \cdot \left(DI^{+}\right)^{\gamma} + \left(DI^{-}\right)^{\gamma}} \leq 1.0$$

Example

damageModel Combined 1 1.0 1.2 2.0 2100.0 -2100.0

B.2.4 **Hysteretic energy**

damageModel HystereticEnergy *tag*? E_U? c?

tag	An integer identifier for the damage model tag
E_U	Positive value for ultimate energy capacity, normally defined as a multiplier of the yield energy $E_U = \lambda \cdot F_y \cdot \delta_y$
c	Calibration parameter

B.2.5 **Park-Ang Damage**

damageModel ParkAng ***t****ag*? δ_U? β? F_u?

tag	Integer identifier for the damage model tag
δ_U	The ultimate deformation capacity
β	Calibration parameter for cyclic damage
F_u	Calculated yield strength

B.3 ***Uniaxial material models***

B.3.1 **Bilinear material model**

The *Bilinear* material model is defined by the elastic/unloading stiffness and the information for generating the envelope. The envelopes are identified by yield point, hardening stiffness, cap displacement, softening stiffness of the cap and a residual factor. Three optional damage models could be used to degrade the strength, stiffness and the

capping. The damage models must be introduced in advance and the tags to these damage models would be passed to the *Bilinear* material model through the command line:

uniaxialMaterial **Bilinear** tag? K_e? F_y^+? F_y^-? α_h? α_{cap}? δ_{cap}^+? δ_{cap}^-? *flagCutEnv*? R? *DmgS*? *DmgK*? *DmgD*?

tag	Integer identifier used to tag the material model
K_e	Initial elastic stiffness
F_y^+	A positive value for the yield strength in positive direction
F_y^-	A negative value for the yield strength in negative direction
α_h	Isotropic hardening ratio as a fraction of elastic stiffness
α_{cap}	A negative value for the cap slope ratio as a fraction of stiffness
δ_{cap}^+	Positive value for the cap displacement on positive side
δ_{cap}^-	Negative value for the cap displacement on negative side
flagCutEnv	A flag to establish a cut-off limit for the force once the cap is reached
R	Residual stress ratio as a fraction of yield strength
DmgS	An integer tag to the strength damage model, zero for no damage
DmgK	An integer tag to the stiffness damage model, zero for no damage
DmgD	An integer tag to the capping damage model, zero for no damage

B.3.2 **Clough material model**

The *Clough* material model is defined by the same envelope as the Bilinear. The envelopes are identified by the elastic stiffness, yield points, hardening stiffness, cap displacement, softening stiffness of the cap and a residual factor. The Clough model reloading path is peak oriented and targets for the maximum stress point. Four deterioration modes are defined for the Clough model, allowing strength, stiffness, accelerated stiffness loss and capping deterioration modes. The deterioration is originally governed by the hysteretic energy formulation, but it could be also defined by damage

models. The damage models must be introduced in advance and the tags to these damage models would be passed to the *Clough* material model through the command line:

uniaxialMaterial Clough tag? K_e? F_y^+? F_y^-? α_h? R? α_{cap}? δ_{cap}^+? δ_{cap}^-? λ_S? λ_K? λ_A? λ_D? c_S? c_K? c_A? c_D?

uniaxialMaterial CloughDamage tag? K_e? F_y^+? F_y^-? α_h? R? α_{cap}? δ_{cap}^+? δ_{cap}^-? *DmgS*? *DmgK*? *DmgA*? *DmgD*?

tag	Integer identifier used to tag the material model
K_e	Initial elastic stiffness
F_y^+	A positive value for the yield strength in positive direction
F_y^-	A negative value for the yield strength in negative direction
α_h	Isotropic hardening ratio as a fraction of elastic stiffness
R	Residual stress ratio as a fraction of yield strength
α_{cap}	A negative value for the cap slope ratio as a fraction of stiffness
δ_{cap}^+	Positive value for the cap displacement on positive side
δ_{cap}^-	Negative value for the cap displacement on negative side
λ_S	A positive ratio for calculating the ultimate energy in the hysteretic energy deterioration model, used for strength deterioration
λ_K	A positive ratio for calculating the ultimate energy in the hysteretic energy deterioration model, used for stiffness deterioration
λ_A	A positive ratio for calculating the ultimate energy in the hysteretic energy deterioration model, used for accelerates stiffness loss deterioration
λ_D	A positive ratio for calculating the ultimate energy in the hysteretic energy deterioration model, used for capping deterioration
c_S	A positive value used as the calibration exponent in the hysteretic energy deterioration model, used for strength deterioration

c_K	A positive value used as the calibration exponent in the hysteretic energy deterioration model, used for stiffness deterioration
c_A	A positive value used as the calibration exponent in the hysteretic energy deterioration model, used for accelerated stiffness loss deterioration
c_D	A positive value used as the calibration exponent in the hysteretic energy deterioration model, used for capping deterioration
DmgS	An integer tag to the strength damage model, zero for no damage
DmgK	An integer tag to the stiffness damage model, zero for no damage
DmgA	An integer tag to the accelerated stiffness loss damage model, zero for no damage
DmgD	An integer tag to the capping damage model, zero for no damage

B.3.3 **Pinching material model**

The *Pinching* material model is defined by the same envelope as the *Pinching* model. The envelopes are identified by the elastic stiffness, positive and negative yield stresses, hardening stiffness ratio, cap strains, capping softening stiffness ratio, and a stress residual factor. The *Pinching* model unloading path follows the elastic slope, while the reloading path is peak oriented and targets for a pinching point. The pinching point is determined by a ration of the peak stress and strain point. Four deterioration modes are defined for the *Pinching* model, allowing strength, stiffness, accelerated stiffness loss and capping deterioration modes. The deterioration relation is originally governed by the hysteretic energy formulation, but the current implementation allows using a different damage model for this purpose. The damage models must be introduced in advance and the tags to these damage models would be passed to the *Pinching* material model through the command line:

uniaxialMaterial Pinching tag? K_e? F_y^+? F_y^-? α_h? R? α_{cap}? δ_{cap}^+? δ_{cap}^-? β_{cap}^+? β_{cap}^-? α_{pinch}? λ_S? λ_K? λ_A? λ_D? c_S? c_K? c_A? c_D?

uniaxialMaterial PinchingDamage *tag*? K_e? F_y^+? F_y^-? α_h? R? α_{cap}? δ_{cap}^+? δ_{cap}^-? β_{cap}^+? β_{cap}^-? α_{pinch}? *DmgS*? *DmgK*? *DmgA*? *DmgD*?

tag	Integer identifier used to tag the material model
K_e	Initial elastic stiffness
F_y^+	A positive value for the yield strength in positive direction
F_y^-	A negative value for the yield strength in negative direction
α_h	Isotropic hardening ratio as a fraction of elastic stiffness
R	Residual stress ratio as a fraction of yield strength
α_{cap}	A negative value for the cap slope ratio as a fraction of stiffness
δ_{cap}^+	Positive value for the cap displacement on positive side
δ_{cap}^-	Negative value for the cap displacement on negative side
β_{cap}^+	A positive value for the positive stress pinching ratio
β_{cap}^-	A positive value for the negative stress pinching ratio
α_{pinch}	A flag to establish a cut-off limit for the force once the cap is reached
λ_S	A positive ratio for calculating the ultimate energy in the hysteretic energy deterioration model, used for strength deterioration
λ_K	A positive ratio for calculating the ultimate energy in the hysteretic energy deterioration model, used for stiffness deterioration
λ_A	A positive ratio for calculating the ultimate energy in the hysteretic energy deterioration model, used for accelerates stiffness loss deterioration
λ_D	A positive ratio for calculating the ultimate energy in the hysteretic energy deterioration model, used for capping deterioration
c_S	A positive value used as the calibration exponent in the hysteretic energy deterioration model, used for strength deterioration
c_K	A positive value used as the calibration exponent in the hysteretic energy deterioration model, used for stiffness deterioration

c_A	A positive value used as the calibration exponent in the hysteretic energy deterioration model, used for accelerated stiffness loss deterioration
c_D	A positive value used as the calibration exponent in the hysteretic energy deterioration model, used for capping deterioration
DmgS	An integer tag to the strength damage model, zero for no damage
DmgK	An integer tag to the stiffness damage model, zero for no damage
DmgA	An integer tag to the accelerated stiffness loss damage model, zero for no damage
DmgD	An integer tag to the capping damage model, zero for no damage